Portland State University
PDXScholar

Dissertations and Theses | Dissertations and Theses

1-18-2022

Inverse Modeling of Atmospheric CH_4 and $\delta^{13}C$-CH_4 Measurements from Surface Observation Sites to Understand Trends in Global Methane Emissions Over More Than Three Decades

Sayantani Karmakar
Portland State University

Follow this and additional works at: https://pdxscholar.library.pdx.edu/open_access_etds

 Part of the Atmospheric Sciences Commons, and the Biogeochemistry Commons
Let us know how access to this document benefits you.

Recommended Citation

Karmakar, Sayantani, "Inverse Modeling of Atmospheric CH_4 and $\delta^{13}C$-CH_4 Measurements from Surface Observation Sites to Understand Trends in Global Methane Emissions Over More Than Three Decades" (2022). *Dissertations and Theses.* Paper 5889.
https://doi.org/10.15760/etd.7760

This Thesis is brought to you for free and open access. It has been accepted for inclusion in Dissertations and Theses by an authorized administrator of PDXScholar. Please contact us if we can make this document more accessible: pdxscholar@pdx.edu.

Inverse Modeling of Atmospheric CH_4 and $\delta^{13}C$-CH_4 Measurements from Surface Observation Sites to Understand Trends in Global Methane Emissions over More Than Three Decades

by

Sayantani Karmakar

A thesis submitted in partial fulfillment of the
requirements for the degree of

Master of Science
in
Physics

Thesis Committee:
Christopher L. Butenhoff, Chair
Andrew L. Rice
M. Aslam K. Khalil

Portland State University
2021

© 2021 Sayantani Karmakar

ABSTRACT

Methane (CH_4) is the second most important greenhouse gas with a radiative forcing of 0.97 W/m^2 including both direct and indirect effects and a global warming potential of 28 over a 100-year time horizon. Unlike CO_2 whose rate of growth in the atmosphere has remained positive and increased in recent decades, the behavior of atmospheric methane is considerably more complex and is much less understood on account of the spatiotemporal variability of its emissions which include biogenic (e.g., wetlands, ruminants, rice agriculture), thermogenic (fossil fuels), and pyrogenic (i.e., biomass burning) sources. After sustained growth during most of the 20^{th} century, the CH_4 growth rate declined to fall from ~15 ppb/year during the 1980s to ~6 ppb/year in the 1990s to near-zero and even negative values in the early 2000s. With some surprise however, the growth rate rebounded in 2007 and annual increase in globally-averaged atmospheric methane abundance has been 7.86 ppb/year on average during the past 14 years from 2007 to 2020. During this same period the $^{13}CH_4/^{12}CH_4$ ratio of atmospheric CH_4 also declined suggesting the post-2006 CH_4 growth was caused by an increase in $^{13}CH_4$-depleted biogenic emissions. Recent papers have attributed this growth to increasing emissions from wetlands, rice agriculture, and ruminants. This work provides an additional insight into the recent behavior of atmospheric methane by performing a global three-dimensional Bayesian inversion of atmospheric CH_4 and $^{13}CH_4/^{12}CH_4$ ratios over the period 1983-2015 using NOAA Global Monitoring Laboratory (GML) CH_4 measurements obtained from surface observation sites located worldwide and the GEOS-Chem chemical transport model (CTM) at a horizontal grid resolution of $2^{o} \times 2.5^{o}$. The use of the 3-D model allowed us to exploit spatial patterns

in the global CH_4 and $^{13}CH_4/^{12}CH_4$ fields that provide additional constraints on the retrieval of the time-dependent CH_4 fluxes from 10 different methane sources such as Gas and oil, coal, livestock, waste, rice agriculture, biomass burning from C3 and C4 vegetation, and wetlands separated into 3 latitudinal zones (90^oN-30^oN, 30^oN-0^o, 0^o-90^oS) in order to reduce aggregation error and to account for isotopic measurements that indicate northern high latitude wetlands are isotopically depleted in $^{13}CH_4$ relative to tropical wetlands. Spatially re-gridded monthly varying prior emission fields were constructed from several sources and also included sinks such as reaction with OH, stratospheric loss and soil sink at the same spatial resolution. In this work, one year of monthly varying three-dimensional OH field was used in GEOS-Chem where CH_4 loss due to reaction to OH was calculated at every grid cell for each timestep. GEOS-Chem used NASA Global Modeling and Assimilation Office (GMAO) data product GEOS-5 meteorological fields available for years 2004 to 2010 and these 6 years of meteorological variables were recycled for the entire inversion time. This work follows up on previous CH_4 inversion where a $4^o \times 5^o$ horizontal grid was used for GEOS-Chem to retrieve fluxes from 1984 to 2009 with GLOBALVIEW methane measurement data. A set of sensitivity tests were conducted to assess the impact of discontinuity in the data coverage over the entire time of inversion for different observation sites on the methane flux trends.

At a higher resolution more information is extracted from the observations due to improved model skill and a smaller number of stations aggregated within model grid cells. This increases the weights of the measurements relative to the *a priori* fluxes in the inversion producing stronger observational constraints on the optimized fluxes. This work assesses

the contribution of spatial heterogeneities in the observed CH_4 record to the retrieval of global CH_4 fluxes and provides a new look into the causes of more than a decade-long growth in atmospheric methane. The comparison between the results of optimized methane emissions from this current inversion work ($2^0 \times 2.5^0$) and previously done inversion work ($4^0 \times 5^0$) up through the end of 2008 revealed some prominent differences in the emission anomalies plots of the individual source categories of gas and oil, coal, livestock, and waste and in the aggregated source categories of fossil fuels, wetlands and all biogenic.

The model simulated concentrations using the a posteriori emission estimates match remarkably well for both the long-term trend and magnitude of the observed NOAA concentrations as well as the seasonal cycle of the measurements, except a few small discrepancies. The inversion analysis indicates that the total averaged global methane emission over years 1983 to 2015 is estimated to be 530±50 Tg/year, over the decade of 2006-2015 is 543±44 Tg/year which is ~20 Tg/year more than that during previous decade, over years 2006 to 2010 it is estimated to be 539±44 Tg/year, whereas over years 2011 to 2015, it is estimated to be 547±45 Tg/year. The global methane emissions over years of 1983 to 2015 from all biogenic sources of both natural and anthropogenic origin account for ~73% of the total global CH_4 emissions. Anthro-biogenic sources contribute about 39% of the total global CH_4 emissions, whereas natural wetlands contribute about 34.5% of the total CH_4 emissions. Emissions from fossil fuels sector constitute about 18.5% of the total global CH_4 emissions and biomass burning about 8.3% of the total global CH_4 emissions.

The averaged emission estimate of emissions from all biogenic sources (both natural and anthropogenic) shows an increase of about ~25 Tg/year during 2006-2015 than that during

1994-2005, whereas the anthro-biogenic sources show highest increase in averaged emission estimate of about ~43 Tg/year during 2006-2015 than that during 1994-2005. The results of this study conclude that the major contribution of emissions from all biogenic sources both natural and anthropogenic as well as minor contribution from biomass burning may have caused the increase in global methane levels since post-2006. It is revealed that the emissions from individual source categories of livestock, wastes, coal, northern high latitude wetlands and biomass burning of C3 vegetations had increased during 2006-2015. Although a persistent increase in total methane levels was observed until the end of the study period, a shift in relative contributions from the emissions of individual source categories may have occurred since 2011 onwards. With the decline in emissions from anthro-biogenic sources of livestock and rice, northern tropical wetlands, fossil fuel source of coal and biomass burning of C4 vegetations, the increase in global methane levels since 2011 until the end of the study period may possibly be due to the contribution of increased emissions from sources of wastes, natural wetlands (southern hemisphere and northern high latitudes), fossil fuel source of gas and oil, and biomass burning of C3 vegetations globally.

The sensitivity test inversion scenarios for all of the source categories maintained the same trends of methane emissions throughout the study period as base case inversion scenarios discussed above but, in some cases, with a significantly wider range in the mean values of the emissions. Emissions from sources like fossil fuels, livestock, and wastes are more sensitive to the variation in network densities of observational sites with continuous data coverage.

This thesis is dedicated to my parents

ACKNOWLEDGEMENTS

I would like to express my sincere gratitude to my advisor Dr. Christopher L. Butenhoff for his guidance and encouragement throughout the course of my research and thesis. I thank him for his valuable suggestions and efforts to train me to perform this computation intensive work.

I would like to extend my sincere gratitude to all members of my thesis committee, Dr. Andrew L. Rice and Dr. M. Aslam K. Khalil for their support, helpful suggestions and comments.

I would like to thank the Department of Physics for providing me teaching assistantship to support my graduate studies. I am also grateful to all faculty members of the Department of Physics and other departments from whom I was privileged to learn. I would also like to thank Office secretaries at the Department of Physics for their help.

My gratitude also goes to all my dear friends and colleagues for their continuous support and encouragement.

Words are not enough to express my deepest gratitude to my parents for their support and sacrifices. I would also like to thank my sister and brother-in-law for their support and encouragement throughout my graduate study. I would like to express my thanks to my beloved husband for his continuous support, encouragement and love.

TABLE OF CONTENTS

Page

LIST OF TABLES

LIST OF FIGURES

5.6	Upper figure shows deseasonalized methane emission anomalies for all 10 source categories from inversion at $4^0 \times 5^0$ grid resolution. The base inversion results are shown with the heavy dark blue line, and the red line indicates the prior emissions. The light blue shading shows the entire range of all 53 sensitivity runs in the ensemble. The green lines are inversions where the fossil fuel emissions were fixed according to a scenario by Simpson et al. (2012) based on measurements of atmospheric ethane. The solid green line shows the inversion where all fossil fuel emissions were assigned to the gas + oil category and coal emissions and all other sources were optimized, and in the dashed green line inversion, both gas + oil and coal emissions were fixed based on a 65/35 split of the fossil fuel emissions (Ref: Rice et al., 2016). Lower figure (same as figure 5.2) shows deseasonalized CH_4 emission anomalies for all 10 separate source categories from inversion at $2^0 \times 2.5^0$ grid resolution. Black lines indicate the base inversion results. Red lines indicate anomalies in the prior emissions. Shaded colored areas represent the variations in the inversion scenarios using different observational network densities.	234
5.7	Upper figure shows deseasonalized CH_4 emission anomalies from aggregated fossil fuels, biomass burning, wetlands, all biogenic (including wetlands) and total emissions from inversion done at $4^0 \times 5^0$ grid resolution. The base inversion results are shown with the heavy darker colored lines, and the red line indicates the prior emissions. The light colored shading shows the entire range of all 53 sensitivity runs in the ensemble (Ref: Röger, 2013). Lower figure (same as figure 5.3) shows deseasonalized CH_4 emission anomalies from aggregated fossil fuels, biomass burning, wetlands, all biogenic (including wetlands), anthro-biogenic (rice, livestock and waste) and total emissions from inversion done at $2^0 \times 2.5^0$ grid resolution. Black lines indicate the standard inversion results. Red lines indicate anomalies in the prior emissions. Shaded colored areas represent the variation in the observational network density of the inversion scenarios.	235

CHAPTER 1

Introduction

1.1. Atmospheric Methane

Methane (CH_4) is the most abundant organic trace gas in the atmosphere and the most abundant greenhouse gas in the troposphere after water vapor and carbon dioxide (CO_2). Atmospheric methane is also the second most radiatively important anthropogenic greenhouse gas after carbon dioxide. Methane only makes up 0.00018% (1.8 parts per million by volume) of the atmosphere, though it traps a significant amount of heat, helping the planet remain warm and habitable. A balance between production of methane on the surface and its destruction in the atmosphere results in the amount of methane in the atmosphere. Methane forms from the decomposition of organic matter in oxygen-poor environments, such as marshes, rice paddies, or the digestive systems of cattle. It also comes from the production of fossil fuels including oil, natural gas, coal, and the combustion (burning) of carbon-based biofuels. According to the Fifth Assessment Report of the Intergovernmental Panel on Climate Change (IPCC, AR5, 2013), globally averaged surface CH_4 concentrations have risen from 722 ± 25 ppb in 1750 to 1803 ± 2 ppb by 2011. Over that time scale the rise has been predominantly due to changes in anthropogenic-related CH_4. Using the formula from Myhre et al. (1998), the radiative forcing (RF) for CH_4 from direct effect since 1750 to 2011 is 0.48 ± 0.05 W/m^2 out of 2.83 W/m^2 by well mixed greenhouse gases, with an uncertainty dominated by the radiative transfer calculation (Figure 1.1). Including indirect effects of CH_4 emissions roughly doubles its effective radiative forcing to 0.97 Wm^{-2}. The increase of RF by 0.01 Wm^{-2} since 2007 is due to the 29 ppb increase in the CH_4 mixing ratio. This is much larger than the 11 ppb increase between 2001 and 2007 and has been driven by increases in net natural and

anthropogenic emissions, but the relative contributions of the sources are not well quantified. CH_4 concentrations do vary with latitude and decrease above the tropopause; however, this variation contributes only 2% to the uncertainty in RF (Freckleton et al., 1998). Its global warming potential based on 100 years' time scale is 28 that means it traps 28 times more heat per unit mass than carbon dioxide, but based on 20 years' time horizon is 84, illustrating the potential of large changes in the burden of CH_4 to influence climate on shorter time scales (Myhre et al., 1998; Gunnar et al., 2013).

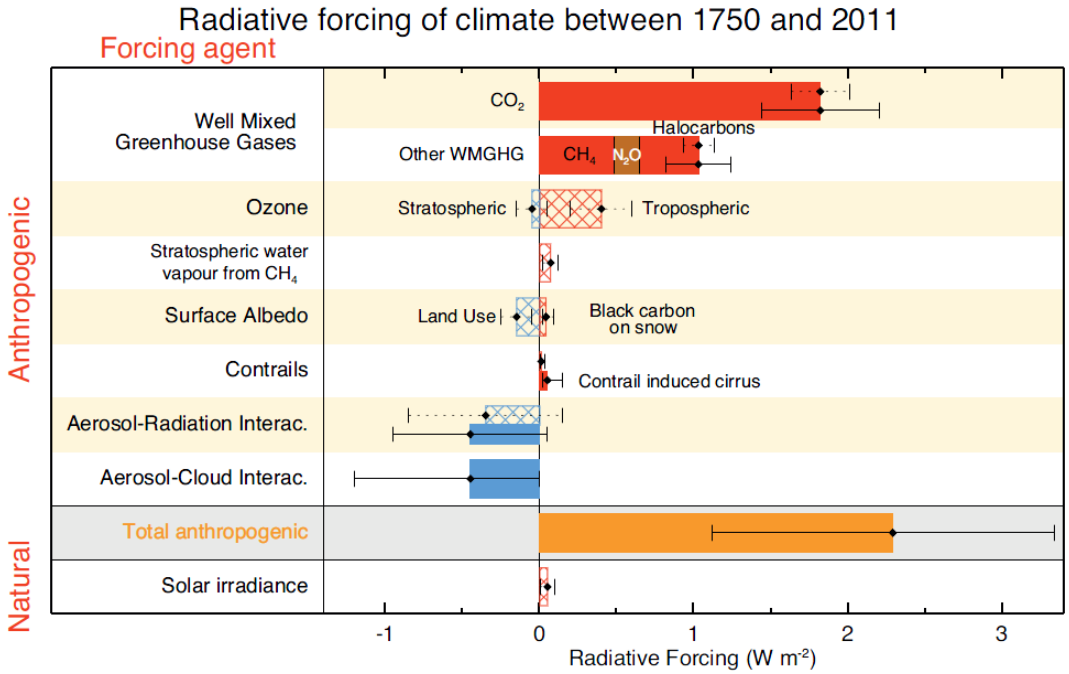

Figure 1.1: *Bar chart for RF (hatched) and ERF (solid) for the period 1750–2011. Uncertainties (5 to 95% confidence range) are given for RF (dotted lines) and ERF (solid lines) [IPCC, AR5, 2013]. In the Fifth Assessment Report (AR5) of the IPCC (2013), the term radiative forcing (RF, also called stratospherically adjusted RF, as distinct from instantaneous RF) was defined as the change in net irradiance at the tropopause after allowing for stratospheric temperatures to readjust to radiative equilibrium, while holding surface and tropospheric temperatures and state variables such as water vapor and cloud cover fixed at the unperturbed values. Effective Radiative Forcing (ERF) is the change in net downward radiative flux at the top of the atmosphere (TOA) after allowing for atmospheric temperatures, water vapor, and clouds to adjust, but with surface temperature or a portion of surface conditions unchanged.*

The effects of CH_4 on climate and atmospheric chemistry are the reason for concern over its high growth rate. Both on a molecule and a mass basis, additional methane is much more effective as a greenhouse gas than additional CO_2. Methane is also the most abundant reactive trace gas in the troposphere and its reactivity is important to both tropospheric and stratospheric chemistry. The oxidation of CH_4 by hydroxyl (OH) in the troposphere leads to the formation of formaldehyde (CH_2O), carbon monoxide (CO), and ozone (O_3), in the presence of sufficiently high levels of nitrogen oxides (NO_x). Methane is removed from the atmosphere in major amount (about 90%) by the reaction with hydroxyl radical (OH) in the troposphere and stratosphere making the atmospheric methane budget extremely sensitive to OH changes, minor reactions with atomic chlorine in the marine boundary layer and with electronically excited oxygen atoms ($O(^1D)$) in the stratosphere, and a minor but significant removal through oxidation by methanotrophic bacteria in soils (Denman et al., 2007).

Methane has a relatively short atmospheric lifetime of 8 to 11 years compared to other greenhouse gases, hence reductions in its emissions could have benefits on climate immediately, making methane an important target for efforts in mitigating climate change (Dlugokencky et al., 2011). After a decade long period of decreasing growth rate, atmospheric methane concentrations have risen in recent years raising concerns to its long-term stability. Despite much study, the factors responsible for this instability remain unclear. Large uncertainties still afflict the estimates of the relative contribution of the different methane sources and sinks to the atmospheric methane levels due in part to their variable nature. Measurements of only CH_4 mole fractions provide insufficient information

to determine definite causes of the recent rise, therefore, isotopic measurements are useful as a direct means to put powerful constraints that can help to identify specific source contributions. Thus, a reliable quantitative comprehension of the global CH_4 budget is necessary to predict future contributions of atmospheric methane to global warming and to develop effective and sensible emission strategies for its mitigation.

1.2. Distribution and Trend of Atmospheric Methane

1.2.1. Atmospheric methane record in ancient past

Ice cores with their entrapped air inclusions provide the most direct, detailed, and complete measured records of past changes in atmospheric trace-gas composition and descriptions of past climate change that are extremely valuable for comparison with modern observations. The air bubbles from ice cores revealed continuous record of atmospheric concentration of methane over the past thousands of years which are associated with climate fluctuations (e.g., Legrand et al., 1988; Chappellaz et al., 1990; Etheridge et al., 1992, 1998; Jouzel et al., 1993; Nakazawa et al., 1993; Raynaud et al., 1993; Blunier et al., 1995, 1998; Brook et al., 1996). The ice core results point to changes in sources of methane and show that methane has probably contributed, like carbon dioxide, to glacial-interglacial temperature changes (Chappellaz et al., 1990). The Vostok ice core (East Antarctica) covering the last 160,000 years included CO_2 and CH_4 greenhouse gas records, which are closely tied to Antarctic temperature variations over the last full glacial/interglacial climate

cycle (Lorius et al., 1985; Barnola et al., 1987; Jouzel et al., 1987; Chappellaz et al., 1990). The drilling of ice cores from Greenland and Antarctica allowed the extension of the record of atmospheric CH_4, CO_2 and temperature back to 420,000 years BP (Petit et al., 1999), covering four glacial-interglacial cycles. The atmospheric burdens of these two important greenhouse gases seem to have been unprecedented during the past 420,000 years with CH_4 records showing glacial-interglacial transitions rose from 320-350 ppbv up to a maximum of 650-780 ppbv (Petit et al., 1999). This atmospheric methane concentration had been less than half of the current level in the time period of 420,000 years before industrial era (Petit et al., 1999), included the period of the last glacial maximum in which CH_4 increased and decreased in phase with atmospheric temperature records at onset and end of these glacial periods (Chappellaz et al., 1993). However, results from several ice core studies supported that wetlands in response to changing climate caused the majority of CH_4 increases with rise in emissions from low-latitude, followed by higher latitude (Chappellaz et al., 1993a,b; Thompson et al., 1993; Blunier et al., 1995; Brook et al., 1996). Chappellaz et al. (1993) estimated the wetland area distribution with associated CH_4 emission for the Last Glacial Maximum (LGM, 18 kyr BP, kiloyear Before Present) and the Pre-Industrial Holocene (PIH, 9000-200 years BP). The estimates from wetland source combined with that of other biogenic sources and sink, yielded total source strengths of 120 and 180 Tg CH_4/yr for LGM and PIH, respectively, which were consistent with source estimates inferred from a photochemical model and pointed to wetland CH_4 source change as a major driving factor for increase in atmospheric CH_4 from LGM to PIH (Chappellaz et al., 1993).

During ice ages, decrease in sea level due to growing ice sheets might have caused destabilization of methane clathrates (defined as lattice structured chemical compounds in which large amounts of methane are trapped within a crystal of water in the form of solid deposits found under the sediments of the ocean floor) contained in sediments on continental shelves which in turn could lead to abrupt large-scale releases of CH_4 into the atmosphere capable of inducing a global temperature increase of up to 1-2^oC over a few decades that might have initiated the glacial termination (Thorpe et al., 1996; Dickens et al., 1997). The fractionation of nitrogen and argon isotopes at the end of the Younger Dryas cold interval, recorded in Greenland ice, demonstrated abrupt warming coinciding with the onset of a prominent rise in atmospheric methane concentration, indicated that the climate change was synchronous (within a few decades) over a region of at least hemispheric extent, but however, it was clear from the phase data that the majority of CH_4 increase was 0-30 years after the warming, thus eliminating the causal role of CH_4 in glacial-interglacial climate change, instead methane seemed to have responded to the changing climate (Severinghaus et al., 1998).

CH_4 concentrations from ice core data of Greenland and that of Antarctica over the period of Holocene to the late pre-industrial era, are compared which showed a hemispherical gradient of 24-58±10 ppbv (north polar to south polar) with larger difference during warmer climates and also indicated consistently larger emissions in the Northern Hemisphere (NH), with contrasting influences of emissions from anthropogenic sources and tropical wetlands acting to balance out the gradient (Nakazawa et al., 1993; Chappellaz et al., 1997; Etheridge et al., 1998). Several inventory studies estimated that the total natural

source of CH_4 was 190 Tg CH_4 yr^{-1} during the Late Pre-Industrial Holocene (LPIH) allowing for a soil sink of 10 Tg yr^{-1} (Chappellaz et al., 1993) and anthropogenic sources grew with estimates ranging from 7 to more than 55 Tg CH_4 yr^{-1} in the centuries leading to industrial period (Kammen and Marino, 1993; Subak, 1994). Natural emissions (predominantly wetlands), anthropogenic emissions and reaction with OH mainly contributed to the LPIH CH_4 variability with small contribution from methane exchange with the ocean (Etheridge et al., 1998). Atmospheric CO_2 levels changed almost in phase with CH_4 records during the Little Ice Age (LIA) and the Medieval Warm Period (MWP) (Etheridge et al., 1996, 1998).

1.2.2. Atmospheric Methane Concentrations since Pre-Industrial Time

Pre-industrial methane levels were investigated by several ice core studies for over last 1000 years with variation in degrees of uncertainty in air age resolution and precision in CH_4 measurement, and later in this century, observations were made from firn air and ground-based monitoring stations since 1978. First studies were published in the early 1980s clearly documenting increased levels of methane mixing ratio in the atmosphere (Rasmussen and Khalil, 1981; Fraser et al., 1981; Blake et al., 1982). The amount of methane in the atmosphere has been observed to be growing since over past 200 years, from the modern direct measurements and from the analysis of air inclusions in polar ice (Craig and Chou, 1982; Etheridge et al., 1992; Matsueda et al., 1996; Rasmussen and Khalil, 1984; Stauffer et al., 1985; Steele et al., 1992). This growth is mainly attributed to

increased human population with increased anthropogenic CH_4 sources during the agricultural period and later during the industrial period. During Preindustrial times, about 75% of the CH_4 was emitted from wetlands (Chappellaz et al., 1993), about 60% of these emissions were from the northern hemisphere (NH) and about 20% from high northern latitudes (Harriss et al., 1993). Predominantly higher methane levels were found during 1050-1250 A.D. (Etheridge et al., 1998), when temperatures of most parts of the world were higher as considered to be Medieval Warm Period, though there is debate on the existence of such generalized patterns of climate into such periods as Little Ice Age (LIA) and Medieval Warm Period (MWP) with evidence for (Keigwin, 1996; Thompson et al., 1995) and against (Hughes and Diaz, 1994) the notion. Growth in human population with more anthropogenic activities may also account for increased methane emissions before LIA such as from 1250 to 1550 A.D. (Etheridge et al., 1998). The global CH_4 levels were measured between about 675 and 850 ppb before 1800 A.D. and lower values during 1450-1660 A.D. which was suggested due to climatic forcings of the CH_4 sources (Khalil and Rasmussen, 1989). Methane levels rose immediately after 1750 A.D. with unprecedented amount, probably due to the combined effects of the emissions from the natural CH_4 sources got recovered to their pre-LIA state, and the start of major anthropogenic emissions (Etheridge et al., 1998). From 1000 to 1800 A.D. the global mean methane mixing ratio was around 695 ppb and varied about 40 ppb, simultaneously varied with climate and interpolar (N-S) differences varied between 24 and 58 ppb, furthermore, high methane growth rates were marked in the industrial period from 1945 to 1990, peaking at about 17 ppb/yr in 1981 (Etheridge et al., 1998). An average total methane source of 250 Tg/yr was calculated for 1000-1800 A.D., reaching near stabilization at about 560 Tg/yr in the 1980s

and 1990s (Etheridge et al., 1998).

The global average methane mixing ratio rose to almost 1800 ppb since the onset of the industrialization, reaching a level unknown in the last 650,000 years (Spahni et al., 2005). Direct measurements of CH_4 in the atmosphere began in 1978 (Blake et al., 1982) and global coverage was reached after 1983. Surface-based observations from four networks: National Oceanic and Atmospheric Administration (NOAA); Advanced Global Atmospheric Gases Experiment (AGAGE); Commonwealth Scientific and Industrial Research Organization (CSIRO); and University of California Irvine (UCI) show consistent changes in the global growth rate of annual CH_4 concentrations since 1980.

Most (70%) of the atmospheric CH_4 increase in the industrial era can be explained assuming the anthropogenic sources increased with the same rate as for growth of human population (Khalil and Rasmussen, 1985; Quay et al., 1988). CH_4 concentrations were increasing at almost 1% per year in the late 1970s and early 1980s (Blake and Rowland, 1988). Khalil and Rasmussen (1987, 1994a) did a top-down model analysis and found a good agreement between increasing population, agricultural emissions, and the observed rise in methane emissions over the past 200 years. Several studies based on simulations showed a decline in OH sink from pre-industrial times to 20th century with depletion of OH averaged around 10-30%, depending on the models used (Khalil & Rasmussen, 1985; Crutzen & Zimmerman, 1991; Thompson, 1992; Crutzen & Bruhl, 1993; Khalil & Rasmussen, 1994; Osborn & Wigley, 1994; Crutzen, 1995; Brasseur et al., 1998; Lelieveld et al., 1998; Wang et al., 1998).

Some studies (such as Prinn et al., 2001; Bousquet et al., 2005) estimated the temporal variations of OH concentrations in the atmosphere from 1978 to 2000 calculated using methyl chloroform as an indicator of OH trends which showed global OH trend as positive until about 1988 and then became increasingly negative after that year. One model study plotted temporal changes for both OH concentration and CH_4 emissions simultaneously from 1981 to 2000 (Khalil et al., 2007) and mentioned that changing lifetime of the changing CH_4 source was reflected in the observed pattern of emissions which is proportional to the change in OH since reaction with OH radicals control the lifetime of methane. Meanwhile, some model studies mentioned the global annual methane sources remained nearly constant from 1988 to 1997 with assumption of constant OH concentration and constant atmospheric lifetime of methane but captured the general decrease in the CH_4 growth rate observed during that time and the anomalous inter-annual fluctuations in methane growth rate during 1992-1993 after the eruption of Mt. Pinatubo in 1991 and during 1997-1998 due to contribution from wetland and boreal biomass burning emissions (Dlugokencky et al., 1994, 1998, 2001; Wang et al., 2004).

However, another study proposed that the globally averaged atmospheric methane abundance increased from 1625 ppbv during 1984 to around 1751 ppbv during 1999 and remained nearly constant through 2002 determined from an extensive network of surface air sampling sites (Dlugokencky et al., 2003). Notably, global atmospheric CH_4 burden has increased by a factor of 2.5 from its pre-industrial value, proportionately far greater than the parallel increase in CO_2, it is driven mostly by increased anthropogenic emissions from

fossil fuels, industries, agriculture including biomass burning and waste, but changes in CH_4 lifetime and meteorological feedbacks may also have played a role (Dlugokencky et al., 2011). The global anthropogenic CH_4 emissions were estimated to increase by 32 Tg since 1990, especially after 1999 as in EDGAR4 (2009) inventory (Bousquet et al., 2011). The atmospheric CH_4 level was generally stabilized from 1999 to 2006 averaged at around 1773±3 ppb (Kirschke et al., 2013). During the last decade, surprisingly the atmospheric CH_4 levels had resumed growth significantly since 2006 (Rigby et al., 2008; Dlugokencky et al., 2009; Bousquet et al., 2011; Kirschke et al., 2013; Schaefer et al., 2016; Nisbet et al., 2016). The globally averaged CH_4 dry air mole fraction in 2009 was 1794 ppb based on the US NOAA measurements (Dlugokencky et al., 2011) and reached 1799±2 ppb in 2010 (Kirschke et al., 2013). The renewed growth in atmospheric CH_4 concentration has persisted for 9 years and pace of the present methane rise is roughly 60 ppb in 9 years since the start of 2007 (Nisbet et al., 2016). Although, the factors responsible for the observed stabilization of atmospheric methane levels remain vague in the early 2000s, and the renewed rise after 2006, some conclusions were drawn with uncertainties in emission trends such as observed stabilization of methane levels between 1999 and 2006 was explained with decreasing-to-stable fossil fuel emissions, combined with stable-to-increasing microbial emissions and rise after 2006 was due to contributions both from natural wetlands and fossil fuel emissions (Kirschke et al., 2013). Most recent studies agree with the fact that this new increase is basically due to emissions from biogenic methane sources (detailed discussion in section 1.3.3.), such as may be due to climatic feedback caused thawing of Arctic permafrost and CH_4 hydrates (Dlugokencky et al., 2011), tropical wetlands (Bousquet et al., 2011; Nisbet et al., 2016), or agricultural emissions (Schaefer et

al., 2016), or may also be due to increase in fossil fuel emissions (Rice et al., 2016). Figure 1.2 presents the current globally averaged atmospheric methane record with measurement of 1888.5 ppb as in March 2021 [Reference: Ed Dlugokencky, NOAA/ ESRL (www.esrl.noaa.gov/gmd/ccgg/trends_ch4/)] which is approximately ~110 ppb increase than the methane mole fraction in the start of 2007.

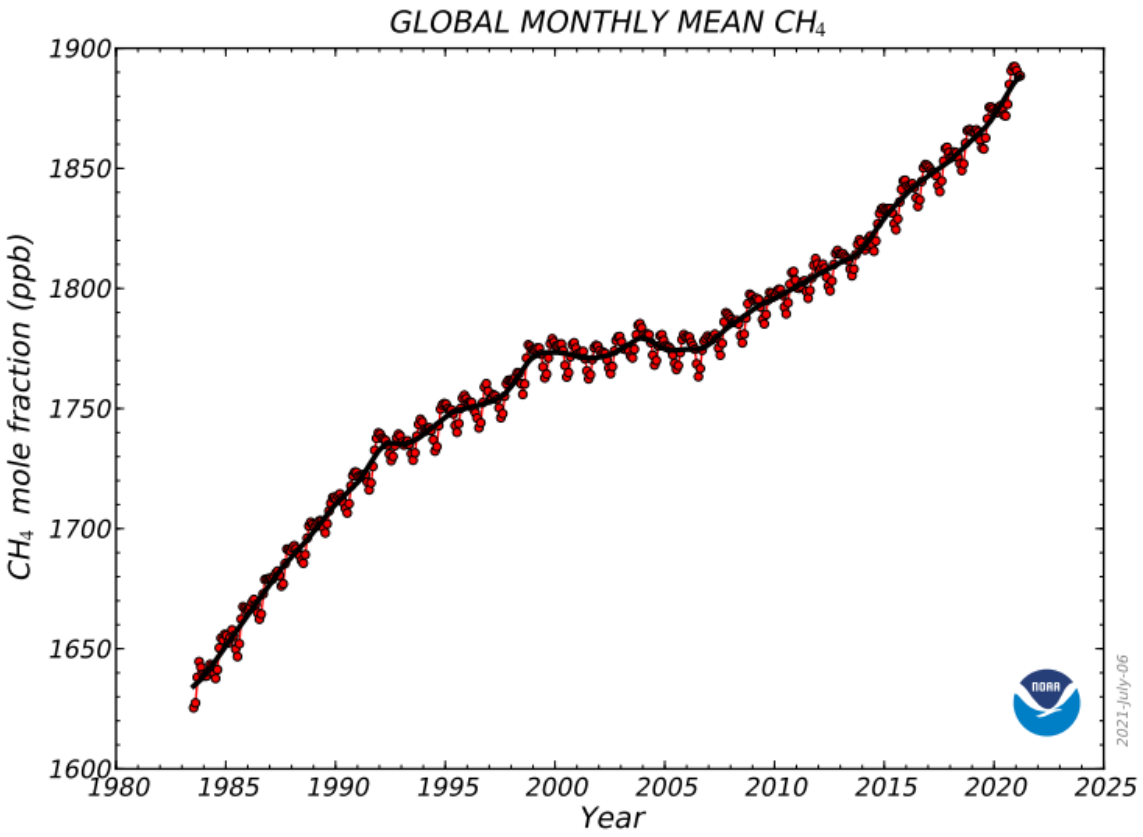

Figure 1.2: *Globally averaged monthly mean atmospheric methane abundance record since 1983 [Ed Dlugokencky, NOAA/GML (gml.noaa.gov/ccgg/trends_ch4/)]. The red line and diamonds are globally averaged monthly mean values centered on the middle of each month. The black line and squares show the long-term trend where the average seasonal cycle has been removed.*

1.3. Methane Growth Rates

1.3.1. Causes of Methane Growth Rate Changes during Past Decades

The methane growth rate averaged around 20 ppbv/year during the decade of 1970 (Blake and Rowland, 1988). The growth rate began to slow in the 1980s (Steele et al., 1992) and in the late 1992 and early 1993 there was a period of net decrease in the globally averaged CH_4 levels (Dlugokencky et al., 1998). However, the growth rate of atmospheric methane had decreased from 14 ppbv/yr (0.9%/year) in 1984 to near zero during 1999-2000 (Dlugokencky et al., 2003). The growth and decline in globally averaged annual atmospheric methane over past decades can be seen in Figure 1.3 which shows the plot summarizing the annual global increases in atmospheric methane based on globally averaged marine surface data since 1984 to 2021 [Ed Dlugokencky, NOAA/GML (gml.noaa.gov/ccgg/trends_ch4/)]. The annual increase in atmospheric CH_4 in a given year is the increase in its abundance (mole fraction) from January 1 in that year to January 1 of the next year, after the seasonal cycle has been removed, which represents the sum of all CH_4 added to, and removed from, the atmosphere during the year by human activities and natural processes [Ed Dlugokencky, NOAA/GML (gml.noaa.gov/ccgg/trends_ch4/)]. There was also report of a significant decrease in the difference between northern and southern polar zonal annual averages of CH_4 from 1991 to 1992 (Dlugokencky et al., 2003). Using a 3-D transport model, it was shown that this change is consistent with a decrease in CH_4 emissions of about 10 Tg CH_4 from north of 50^{o}N in the early 1990s which might had accelerated the global methane budget towards steady state (Dlugokencky et al., 2003).

This long term slowdown was likely tied to a change in the imbalance between methane sources and sinks, i.e., either increase in methane removal or decrease in methane emissions. Despite many theories, it remained unclear the causes of this change. Khalil and Rasmussen (1993 and 1994 a, b) reasoned for slowdown in 1980s as the methane emissions from anthropogenic sources like from agricultural activities, livestock and coal mining had leveled off in the 1980s and were not likely to contribute to the increase in atmospheric methane. Several other reasons had been suggested including reductions in natural gas release (Dlugokencky et al., 1994a), decrease in $\delta^{13}C$ enriched sources such as biomass burning in Southern Hemisphere or fossil fuel use in Northern Hemisphere (Lowe et al., 1994, 1997; Gupta et al., 1996) and wetland CH_4 production (Dlugokencky et al., 1994a), and increased CH_4 loss rates (Bekki et al., 1994). Methyl chloroform measurements inferred observed trends in the seasonal cycle of methane, and global OH concentrations which did not support a significant change in OH over the past decades (Dlugokencky et al., 1997; Prinn et al., 1995). Similarly, from the isotopic analysis over that time the growth rate of $\delta^{13}C$ was inconsistent with a substantial increase in the CH_4 sink (Etheridge et al., 1998). In contrast, Karlsdottir and Isaksen (2000) estimated the tropospheric OH had increased by about 7% or 0.43%/year from 1980 to 1996, which could have reduced the atmospheric lifetime of CH_4, but implied methane increased overall at a rate of 0.67%/year during that time when combined with observed record (Wuebbles and Hayhoe, 2002). Although the exact cause of this long-term decline in the global methane rate was unresolved, Dlugokencky et al. (1998) suggested that observation was in fact an approach to steady state, as CH_4 net emissions and sinks were nearly constant over the past two decades. Li et al. (2002) mentioned that the switch of irrigation system from continuous

flooding to mid-season drainage of rice paddies was widely implemented in China during the 1980s which was intended to conserve water and increase yields, but as an ancillary benefit, this led to significant reduction in methane emissions from rice cultivation. Suggestions from some studies involved decreasing natural emissions from wetlands might have occurred because of wet deposition of sulfates from acid rain (van Bodegom et al., 2001; Gauci et al., 2002). On the other hand, Khalil et al. (2007) noted that for methane long-term periodic cycles or events existed and influenced the observed concentrations and trends much more than any systematic increase or decrease of sources and sinks. Moreover, if the sources had increased in the past there was no environmental consequences such as increased global warming, due to the balance of sources and sinks as the extra amounts of CH_4 put into the atmosphere would be the same amounts that would have to be taken out by the increased OH to be consistent with the observed concentrations of methane during the last two decades, hence the concentrations behaved exactly as if the sources and sinks had been constant (Khalil et al., 2007). The apparent stabilization of methane growth rate in 1990s was reasoned as the decrease in CH_4 emissions due to the collapse of former USSR economy (Dlugokencky et al., 2003), also EDGAR4 (2009) showed a decrease in anthropogenic CH_4 emissions from continental Europe, but showed a contributing increase in tropical and East Asian CH_4 emissions (Bousquet et al., 2011). The low growth rate in late 1990s/early 2000s was attributed to effect of increasing anthropogenic emissions and decreasing natural wetland emissions consistent with the fact that drier conditions prevailed in various regions during that time in the Northern Hemisphere (Bousquet et al., 2006). This noteworthy slowdown of methane growth rate was not continuous but was superimposed with large inter-annual fluctuations and few short-term anomalies which are

discussed in section 1.3.2. Measurements of CH_4 growth rate jumped back up to 8-12 ppbv/yr in 1997 and 1998 and then again fell to near zero in 2000 (Dlugokencky et al., 2003), also seen in Figure 1.3. The methane growth rate decreased further (even negative as seen in Figure 1.3) during 2000-2001 (Simpson et al., 2002; Dlugokencky et al., 2003), then a small increase in 2002 with growth rate of ~2 to 7 ppb/year was observed (Dlugokencky et al., 2003). From 1999 to 2006, the globally averaged CH_4 was relatively constant (Rigby et al., 2008; Dlugokencky et al., 2011) with very low and even negative (during 2004-2005) growth rates also seen in Figure 1.3, whereas EDGAR4.1 (2009) inventory showed anthropogenic CH_4 emissions trended a small increase of 6 Tg/year during 1999-2005. A renewed increase in global CH_4 growth rate of almost 10 ppb in late 2007 was observed (Rigby et al., 2008), also seen in Figure 1.3. This rise was confirmed by all other related studies, the cause of which was inferred differently by different studies (discussed in detail in section 1.3.3.) such as a -4%±14% decrease in OH from 2006 to 2007 (Rigby et al., 2008), large scale CH_4 emissions due to rapid warming and thawing of Arctic permafrost and CH_4 hydrates (Dlugokencky et al., 2011), dominant emissions from tropical wetlands (Bousquet et al., 2011).

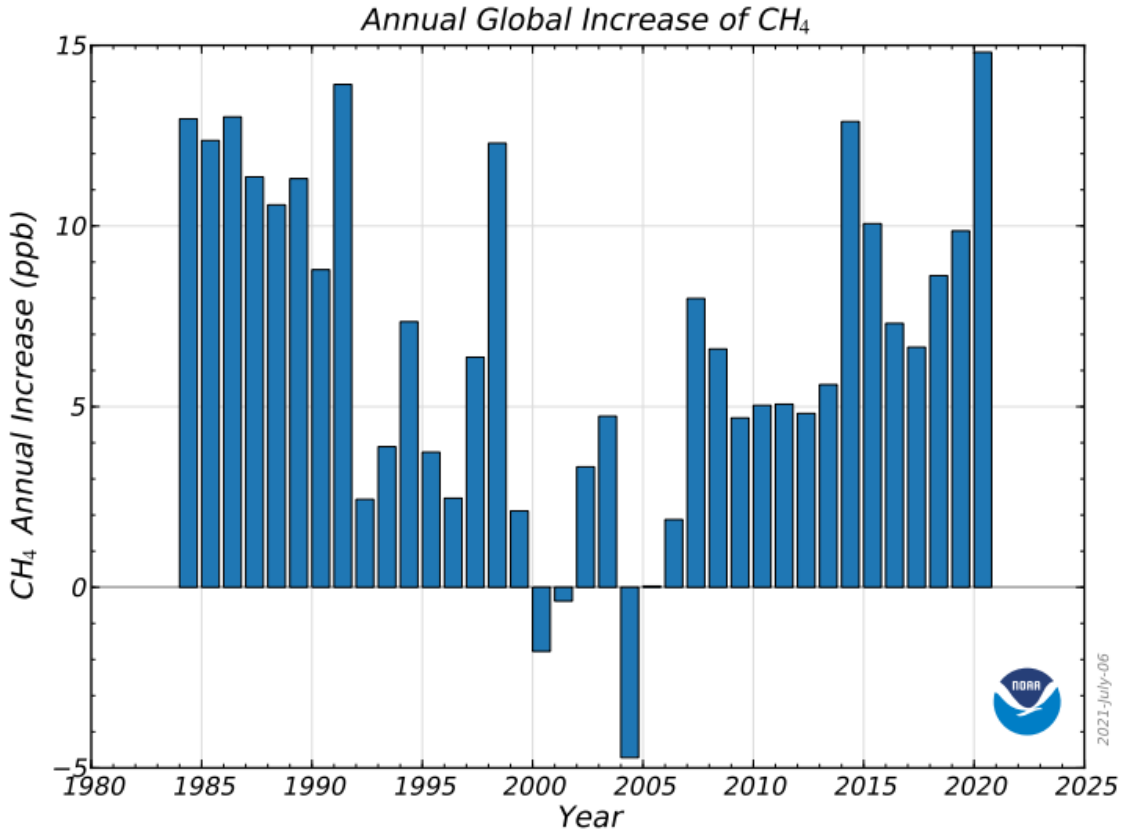

Figure 1.3: *Plot summarizing the annual global increases in atmospheric methane based on globally averaged marine surface data since 1984 [Reference: Ed Dlugokencky, NOAA/GML (gml.noaa.gov/ccgg/trends_ch4/)]. The annual increase in atmospheric CH_4 in a given year is the increase in its abundance (mole fraction) from January 1 in that year to January 1 of the next year, after the seasonal cycle has been removed.*

1.3.2. Causes of Anomalies in Methane Growth Rates as suggested by Previous Studies

The much discussed causes of the fluctuations involve anomalies observed between 1991 and 1993, between 1997 and 1998 and relatively smaller fluctuation between 2002 and 2004. During the period 1991 – 1993, the growth rate of CH_4 increased sharply after the eruption of Mt. Pinatubo in June in 1991 followed by a sudden drop in 1992 to

exceptionally low values, even less than zero and then a partial recovery during 1993 (Dlugokencky et al., 1994). Average growth rate in 1992 was about 1.8 ppbv/yr in the Northern Hemisphere, and 7.7 ppbv/yr in the Southern Hemisphere (Dlugokencky et al., 1994a, b, 1998). Many studies have suggested the eruption of Mt. Pinatubo in Philippines in June 1991 had important impacts on methane sources and sinks linked with this anomalous behavior. Dlugokencky et al. (1996) calculated ultraviolet actinic flux in the wavelength region 290–310 nm which was attenuated by ~12% immediately after the eruption due to absorption by SO_2 using a radiative transfer model, and showed that the ultraviolet flux was perturbed for up to one year because of scattering by sulphate aerosols. The production of main sink of CH_4 i.e., OH radical decreased which depends strongly on the photolysis of ozone by solar ultraviolet radiation, therefore attributed to the increased CH_4 growth rates just after the eruption. A period of net decrease in globally averaged methane levels was observed in late 1992 and early 1993. Some studies proposed the reason for short-term CH_4 drop as increase in tropospheric OH through mechanisms such as El Niño-induced increasing tropospheric water vapor, an important source of OH (Khalil & Rasmussen, 1993), or aerosol-induced stratospheric ozone depletion, causing an increase in tropospheric UV radiation and a subsequent rise in OH formation may also help explain the decrease in global growth rate (Bekki et al., 1994). Increased stratospheric temperatures following the Pinatubo eruption may have enhanced mixing of stratospheric air, resulting in low CH_4 levels, had also been proposed (Schauffler & Daniel, 1994). Discussed as possible contributors to the brief but abrupt slowing are occurrences of colder and dryer conditions in the aftermath of the eruption causing reductions in emissions from sources like tropical biomass burning due to 1991-1992 droughts in southern Africa, or decrease in

wetland emissions, or also lowered emissions from Northern Hemisphere fossil fuel sources after economic breakdown of the Former Soviet Union (Lowe et al., 1994, 1997; Dlugokencky et al., 1994b, 2001; Law & Nisbet, 1996; Hogan & Harriss, 1994; Walter et al., 2001). Observational and modeling studies constrain these theories to match the observed drop by comparing source strengths, mixing ratios, and isotopic abundances. Instead of role of atmospheric chemistry or changes in wetland emissions, a decrease in $\delta^{13}C$-enriched sources such as biomass burning in the Southern Hemisphere or fossil fuel use in the Northern Hemisphere was supported when regional mixing ratios were compared with $\delta^{13}C$ isotopic measurements (Lowe et al., 1994, 1997; Gupta et al., 1996). However, Quay et al. (1999) could not distinguish the possible impacts of changes in biogenic sources, fossil sources, and OH concentration by using isotopic measurements from six sites which were not precise enough to explain for observed slowdown in CH_4 growth rate experienced in 1992.

The growth rate of methane increased sharply during 1997-1998 to regain its level as in pre-1980, but quickly fell again. The strongest record-high El-Niño event was considered coincident with this anomaly. In El Nino events like during 1997, the response of emissions to temperature and the lag in wetland drying may in part accounted for methane growth. The increase in the growth rate of CH_4 was also attributed by competing theories such as widespread dryness causing extensive wild fires in boreal and tropical regions (Langenfelds et al., 2002; van der Werf et al., 2004; Bousquet et al., 2006), or large abnormal peat fires in Indonesia released huge amount of CH_4 from smoldering combustion (Page et al., 2002; Simmonds et al., 2005), or anomalously large emissions from wetlands (Dlugokencky et

al., 2001, 2003; Mikaloff Fletcher et al., 2004a, b), since anthropogenic emissions show gradual change with time, these abrupt year-to-year fluctuations were more likely to be influenced by natural emissions such as from wetlands and biomass burning (Bousquet et al., 2006; Chen and Prinn, 2006). However, it was found that the northern region wetland emissions decreased in 1997, followed by an increase in southern region wetland emissions in 1998 (Bousquet et al., 2006) consistent with dryer and wetter climatic conditions. A larger decrease was observed in OH concentrations during this time may be due to possible large emissions of carbon monoxide (Butler et al., 2005) and other reactive carbon compounds emitted from fires (Manning et al., 2005) could have contributed to growth in CH_4 at a faster rate (Bousquet et al., 2006). Furthermore, another study calculated the difference in CH_4 emissions and sinks which had increased by ~25 Tg/year (6.3±0.7 ppb in 1997 and 12.4±0.7 ppb in 1998), out of average total CH_4 emissions of 550 Tg/year, also suggested similar causes as increased tropical biomass burning may had affected the CH_4 sink by changing [OH] and also warm, wet conditions might had triggered more emissions from wetland regions in high northern latitudes and tropics (Dlugokencky et al., 2009).

The relatively smaller fluctuation in methane growth rate during 2002-2004 was also considered as the consequence of increase in biomass burning emissions in the Boreal and temperate North America, boreal and central Asia and Australia higher than their respective average emissions, also large emitting regions of Africa, South America and Equatorial Asia showed their respective approximate-average emissions during 2002-2003 (van der Werf et al., 2006). These emissions might be related to climate events such as 2002-2003 dry period prevailed over northern mid latitudes (Simmonds et al., 2005; Bousquet et al.,

2006). Despite the small fluctuation, the low mean of atmospheric CH_4 growth rate persisted during 2000-2003 because of the balance of increasing anthropogenic CH_4 emissions such as from fossil fuels, recovered to the early 1990s level and the significant drop in northern region wetland emissions and a decrease in OH sink in the tropics with more CH_4 removal in 2003 (Bousquet et al., 2006).

1.3.3. Causes of Increase in Methane Growth Rate since 2007 as mentioned by Previous Studies

Methane concentrations had begun to increase again since 2007 (Rigby et al., 2008), with global increase of 8.0±0.6 ppb in 2007 and 4.4±0.6 ppb in 2008 (Dlugokencky et al., 2009). The largest zonally averaged CH_4 increase of 13.7±1.3 ppb was observed in polar northern latitudes in 2007, in addition, the zonally averaged Southern Hemisphere CH_4 increase was 9.2±0.3 ppb which was more than that of 7.3±1.3 ppb for Northern Hemisphere in 2007, whereas the largest increase of 8.1±1.6 ppb was observed at low northern latitudes in 2008 (Dlugokencky et al., 2009). Several studies concluded that one main cause of increasing CH_4 levels in 2007 is a surge in natural wetland emissions in response to abnormally high temperatures in northern high latitudes, and increased rainfall over tropical wetlands during 2008-2009 and 2010-2011 (Dlugokencky et al., 2009, 2011; Bousquet et al., 2011; Bloom et al., 2010). The higher temperatures at polar northern latitudes during 2007 might had enhanced the increase in emissions from northern wetlands, but resumed low CH_4 growth rate with increase of 0.5±0.8 ppb in 2008 depicted that the Arctic had not reached the point

of sustained increase of CH_4 emissions from melting permafrost and CH_4 hydrates during 2007-2008 (Dlugokencky et al., 2009). Furthermore, two La Niña events in 2007 and 2008 might be responsible for positive anomalies in precipitation in Indonesia and eastern Amazon which might possibly had driven increased emissions from tropical wetlands and simultaneously interhemispheric transport during ENSO cool phase might had increased CH_4 growth rate in mid to high southern latitudes during 2007 (Dlugokencky et al., 2009). The average atmospheric CH_4 increase each year, i.e., growth rate, based on measurement network, showed a persistent change in emissions from Arctic wetlands of about 3 Tg $year^{-1}$ (Dlugokencky et al., 2011). Bousquet et al. (2011) investigated the distribution of sources and sinks for the 2006-2008 periods by using two atmospheric inversions and a process-based model of methane emissions by natural wetland ecosystems. They concluded that the main contributor to the global emission anomalies was a positive anomaly of tropical emissions (60–80%) for both inversions, with a share dominantly attributed to natural wetlands (2/3), and a significant contribution from high latitudes (25%) in 2007. Kirschke et al. (2013) showed that a rise in natural wetland emissions and fossil fuel emissions probably accounted for the renewed increase in global methane levels after 2006, although the relative contribution of these two sources remained uncertain. Miller et al. (2013) combined comprehensive atmospheric data, diverse datasets from the EDGAR inventory, and an inverse modeling framework to get source sectors information and to derive spatially resolved CH_4 emissions. They had estimated a mean annual US anthropogenic CH_4 budget for 2007 and 2008 of 33.4 ± 1.4 $TgCy^{-1}$ or 7-8% of the total global CH_4 source, which was a factor of 1.5 and 1.7 larger than EPA and EDGAR v4.2, respectively. They concluded that methane emissions from the animal husbandry (approximately twice) and

fossil fuel industries (4.9 ± 2.6 times) had larger greenhouse gas impacts than indicated by existing inventories, therefore, more accurate and verified emission estimates were required from across North America for assessing CH_4 sources to implement policies in regulating emissions and managing energy resources. Although the study of Miller et al. (2013) had estimated methane emissions in the USA only, but considering human and livestock population density and fossil fuel production and usage across demographic regions in the US, the estimates in their study reflected significant proportion of emission trend during 2007-2008 when compared globally. Instead, Schaefer et al. (2016) using both CH_4 mole fraction and $\delta^{13}C\text{-}CH_4$ isotopic data, concluded that the isotopic evidence demonstrated the emissions of thermogenic methane (e.g., fossil fuels and biomass burning) were not the dominant cause of the post 2007 growth, instead an increase in biogenic emissions probably from agricultural sources rather than from wetlands located outside the arctic caused the rise.

Nisbet et al. (2016) showed in most latitudinal zones of the earth, atmospheric methane mole fractions had increased sustainably since 2007, with local short-term deviations from the overall spatial pattern of growth. Rapid growth was measured in the Northern hemisphere in the Arctic and boreal zone during autumn of 2007, then dominantly been driven in the north and south of the equator in 2008 and in the southern tropics in 2010-2011. Moreover, there was an exceptional global methane increase in 2014 at all latitudes, especially in the equatorial belt was accompanied by a continuation of the recent isotopic pattern. Nisbet et al. (2016) mentioned the globally averaged mole fraction of the atmospheric methane increased by 5.7±1.2 ppb/year from 2007 to 2013. A measure of the

$\delta^{13}C\text{-}CH_4$ had shifted to more negative values since 2007. In 2014, the methane growth was extreme with value of 12.5±0.4 ppb. The isotopic evidence suggested that the methane rise was dominated by increases in biogenic emissions particularly in the tropics from expansion of tropical wetlands with strongly positive rainfall anomalies or emission from increased agricultural sources such as ruminants and rice paddies, might be due to their responses to meteorological changes. Rice et al. (2016) mentioned their inversion resulted in an increase in fugitive fossil fuel emissions since 1984 with most of its growth after year 2000. This result is consistent with some bottom-up emission inventories but not with recent estimates based on atmospheric ethane such as Aydin et al. (2011), Simpson et al. (2012). The inversions estimated a decrease in emissions from biomass burning explaining the fall of ethane abundance (Rice et al., 2016).

1.4. Methods Involved in Quantifying Atmospheric Methane

1.4.1. General Methods to Quantify Atmospheric Trace Gases

Mathematical methods are used to introduce biogeochemical observations which include measurements of concentrations of trace gases and their isotopic compositions into the modeling framework. When some information is given on the values of set of parameters, using a theoretical relationship the information of the values of some measurable quantities are obtained, then a direct or forward problem is solved, whereas, when some information is given on the values of some measurable quantities, using a theoretical relationship the

information of the values of set of parameters are obtained, then an inverse problem is solved (Tarantola and Valette, 1982). The values of the parameters are data and values of observable quantities are unknowns for a direct problem whereas, the data are the results of some measurements, and the unknowns are the values of the parameters for an inverse problem (Tarantola and Valette, 1982). Some of the most common mathematical tools used to estimate the global methane emissions are flux measurement extrapolation from regional to global scale, process modeling and inverse modeling. First two methods which are bottom-up approaches suffer from extrapolation error and process model error, respectively. Inverse modeling is the top-down approach where observations of atmospheric mixing ratios constrain the trace gas surface flux estimates to explain vaguely understood sources and sinks. Inverse modeling uses observed concentrations, chemical transport model, spatial distributions of sources and a set of priori estimates to determine optimal combination of unknown fluxes (flux refers to the different atmospheric exchange process for both sources and sinks) that match with the observational data and to help understand the source processes. General atmospheric chemical transport models are run in forward mode to compare these observations with simulation results and then discrepancies between simulation and observations lead to surface gas flux modification with reverse approach. In this approach to the problem of the large-scale sources and sinks, atmospheric observations constrain the surface fluxes needed to explain them. Inverse modeling consists of the quantification of large-scale spatial and temporal variations of sources and sinks of atmospheric trace gases like carbon dioxide, methane, and nitrous oxide.

The inverse modeling approach mentioned by Tarantola and Valette (1982), was originally applied in Geophysics to localize earthquake centers, however, in atmospheric science, it is first used by Enting (1993) and Enting et al. (1993) to study the atmospheric CO_2 cycle (Hein et al., 1997). Other estimates on atmospheric budgets for CO_2 and CH_4 interpreted the space-time distributions of concentrations in terms of space-time distributions of sources and sinks using atmospheric transport modeling (Keeling et al., 1989b; Tans et al., 1990a; Fung et al., 1991; Sarmiento and Sundquist, 1992). Inversions using 3D transport model are based on synthesis approach (Keeling et al., 1989b; Tans et al., 1990a; Fung et al., 1991) which involved seeking linear combination of source and sink processes such that the corresponding linear combination of the calculated responses matched the observations where the solution is stabilized by the spatial distributions of source components used as constraints. Other earlier synthesis inversions are done for global carbon cycle modeling (Enting and Pearman, 1987), for atmospheric CO_2 budget modeling (Enting et al., 1993, 1995), a Bayesian analysis was done where the estimation is stabilized by additional constraints in the form of independent prior estimates of source strengths. There are several studies which used inverse methods to quantify the global-scale sources of different trace gases such as for CO_2 by Keeling et al. (1989b), Enting and Mansbridge (1989), Tans et al. (1990a), Enting et al. (1995), Rayner et al. (1996), Law and Simmonds (1996), Fan et al. (1998), Kaminski et al. (1999b), Gurney et al. (2002); for CFCs by Brown (1993), Hartley and Prinn (1993), Plumb and Zheng (1996), Mulquiney and Norton (1998), Mulquiney et al. (1998); for CO by Bergamaschi et al. (2000b), Kasibhatla et al. (2002). However, in most of the studies, the fluxes are aggregated into few large regions, which has disadvantage of leading to significant biases in the estimated emissions caused by

nonhomogeneous sampling by the measurement network, thus, to efficiently compute a large number of sensitivities and to reduce the bias, an adjoint model approach was used by Kaminski et al. (1999a) for computation of the Jacobian matrix representing 3D atmospheric transport model.

1.4.2. Previous Inverse Modeling Studies on Quantifying Atmospheric Methane

Many researchers did several works by means of inverse modeling technique to estimate global CH_4 emissions and sinks, e.g., Brown (1993, 1995), Hein and Heimann (1994), Hein et al. (1997), Wang et al. (2004), Houweling et al. (1999), Mikaloff Fletcher et al. (2004a, b), Bergamaschi et al. (2005), Chen and Prinn (2006), Bousquet et al. (2006), Meirink et al. (2008b), Wecht et al. (2012). Brown (1993, 1995) performed their calculation with a 2D transport model, thereby ignoring longitudinal variability in CH_4 sources, sinks and atmospheric observations and also did not use any prior information on location or seasonality of the sources, thus reducing efficiency of atmospheric observations to deduce the emissions. The difficulty of spatial overlapping associated with using atmospheric CH_4 observations which provide information on spatial distribution of total CH_4 flux and source processes, was addressed with two inversion approaches. One approach used an inverse model which determined spatial distribution of CH_4 flux required to match the observations without differentiating the fluxes with source processes (Houweling et al., 1999), however, this process reduced uncertainty in the total CH_4 flux in Northern Hemisphere, but provided

limited knowledge on the physical processes responsible for the differences in inversion estimates and process-based estimates (Fletcher et al., 2004). Another approach used inverse models to estimate the total global CH_4 fluxes for separate source processes based on the spatial distribution of sources (Hein et al., 1997; Bergamaschi et al., 2000a, 2001) and for separate sources across large spatial regions (Chen, 2004). The estimates from these processes reduced source estimates compared to priors in source processes with larger footprints in NH and increased estimates with larger footprints in SH (Fletcher et al., 2004). Including observations of isotopic ratios in CH_4 inversions not only adds a new constraint to the underdetermined inverse problem, but it also improves partitioning of the flux estimates between source processes with similar spatial and temporal patterns but different isotopic signatures. Hein et al. (1997) reduced the uncertainties associated with source estimates using station observations of CH_4 mixing ratios and $^{13}C/^{12}C$ isotopic ratio in atmospheric CH_4 from three stations to further constrain the inversion and optimize the isotopic signatures of sources, however, only stations from NH were used and interhemispheric gradient was not included in their study (Fletcher et al., 2004). Previous inverse studies had limited use of isotopic ratios of CH_4 such as Bergamaschi et al. (2000a) used NOAA/CMDL observations data to estimate the magnitude of CH_4 sources and used isotopic data from two stations in SH and one station in NH to optimize estimate for each source process. Fletcher et al. (2004) presented first time-dependent inverse estimates of CH_4 constrained by both observations of GLOBALVIEW-CH_4 data product from NOAA (2001) and isotopic ratios from six NOAA/CMDL stations from 1998-1999 and prior estimates of the sources and sinks from IPCC (2001) report, which employed a time-dependent assimilation and source retrieval technique based on methods mentioned by

Bruhwiler et al. (2000). Fletcher et al. (2004) mentioned that their estimates were sensitive to inaccuracies in model transport and assumed isotopic signature of the sources. Their method of aggregating of sources into spatially diffused large regions also introduced source of bias known as 'aggregation error' (Kaminski et al., 1999a) since the sampling network was sparse, inaccuracies remained with unrepresented variability in the spatial pattern of the regions and imposed limitation to the understanding of source processes from the inverse estimates. In real world situation, the spatial distributions of many source processes may vary with regional temperature anomalies and other physical processes, meanwhile, grouping the sources in linear combination of spatial regions and considering the spatial pattern of emissions for each source as perfect with little or no interannual variations, eliminates the possibility of accurate diagnosis of changes in CH_4 fluxes at regional scale by using the observations (Fletcher et al., 2004). One important limitation in the inversion work of Fletcher et al. (2004) was the increased temporal noise in their inversion estimates since their basis functions reflected only one month of model transport. Errors in their flux estimates for a given month step were propagated to the next time step which meant an overestimate in the flux from one region in a given month could have led to an underestimate in the flux from that region or neighboring region in a later month, since no mechanism was included for the flux estimates from previous months to be adjusted based on the observations of the current month. Some of the observation sites such as those sampling marine air, were weakly weighted in most of the inversions because these data are influenced strongly by local sources, small-scale transport effects and other factors which are not represented effectively in a coarse resolution model such as 3D tracer transport model used by Fletcher et al. (2004) had a spatial grid resolution of 7.8^{o} latitude

by 10º longitude by nine vertical levels. The species of interest, model to be used for the inversion, sub-grid scale effects for sensitive sites, all of these determine the location of optimal observing sites, thus the network design algorithm in the inversion should have a balance between emission sensitivities and model errors and spatial resolution in determining the optimal observing sites (Chen and Prinn, 2006). Chen and Prinn (2006) addressed some of these issues by conducting an inverse modeling study incorporating 13 high frequency CH_4 observation sites [methane mole fractions measured insitu 24 to 36 times per day, e.g. Prinn et al. (2000)] and 79 low frequency CH_4 observation sites [air samples collected and mole fraction measurement done in later date, e.g. NOAA Carbon Monitoring and Diagnostics Laboratory (CMDL), 2001b] and interannual transport in atmospheric transport model, both critical to determine the CH_4 emissions in higher space and time resolution, and adapted the Kalman filter solution of interannually varying monthly fluxes. Their study optimally estimated methane emissions from regional seven seasonal and two aseasonal sources with their uncertainties from 1996 to 2001 at monthly time resolution and used the Model for Atmospheric Transport and Chemistry (MATCH) driven by National Center for Environmental Prediction (NCEP) analyzed observed meteorology at a higher horizontal resolution of ~1.8º × 1.8º which accounted for impact of synoptic and interannually varying transport on methane observations. The mismatch error or representation error arises due to coarse resolution of the model, when an observation made from a single point in space must be considered as representative of a large volume of air for the entire grid cell in the model. This error increases significantly over regions near large emitting continental sites due to local influences which is difficult to be resolved at the model resolution. Chen and Prinn (2006) assumed that the spatial

variability within a single grid cell can be related to the variability among the surrounding grid cells and estimated this error at each site using standard deviation of CH_4 mole fraction at the nine model grid cells which contain and surround each observing site. However, their deduced interannual emissions were affected more by the errors in the short-term changes in the spatial flux patterns and affected less by large-scale transport biases. Another simplification in their inversion was assumption of constant emissions from aseasonal sources such as animals, waste and energy emissions which can also change from year to year. Furthermore, using annually repeating OH field in their work involved another potential model error. Most of the works so far have used almost same set of observations to constrain methane fluxes which often disagree significantly with the estimates. For example, the variation of global emission due to biomass burning varied more than twice [~ 88 Tg/year calculated by Fletcher et al. (2004), whereas Levine et al. (2000) estimated ~52 Tg/year and IPCC (2001) reported biomass burning emission ~ 23-55 Tg/year globally] in different research works, similar comments were also true for methane emission calculation from rice paddies [Chen and Prinn (2006) calculated ~112 Tg/year globally, whereas Sass (1994) estimated global rice emissions between 25 and 54 Tg/year and Cao et al. (1996a) estimated global flux of 53 Tg/year] for different works. This significant difference in the final estimates illustrates that large uncertainties imposed by the choice of various settings are needed in the inversion process, or chemical transport model to deal with severe ill-conditioning of the inverse problem. Therefore, it is essential to study the estimated fluxes along with reliable quantification of their associated uncertainties. Röger (2013) performed an inverse modeling study, published in Rice et al. (2016), to optimize the methane emissions from ten source categories using a fixed-lag

Kalman smoother method based on descriptions in Bruhwiler et al. (2005) and Chen and Prinn (2006). They have calculated monthly mean CH_4 mixing ratios spanning 1984-2009 from the NOAA Earth System Research Laboratory (NOAA-ESRL) data product GLOBALVIEW-CH_4 (2009) by applying cubic spline fits to weekly records (221 locations and 24 ship sites) and sampling at daily frequency. They mapped the observation sites at the horizontal grid resolution of $4^{o} \times 5^{o}$ and calculated the response functions by integrating the GLOBALVIEW data product with Goddard Earth Observation System 3D Chemical atmospheric transport model (GEOS-Chem). They constructed the spatially-gridded monthly varying prior emissions from several sources and included sinks due to reaction with OH, soil uptake and stratospheric loss. Isotopic signatures of methane were introduced to their model as independent tracers to constrain and interpret temporal changes in CH_4 budget, which were obtained from several observational networks including Oregon Health and Science University (OHSU) and Portland State University (PSU) archived air measurements, White et al. (2015) at the Institute of Arctic and Alpine Research (INSTAAR), Quay et al. (1999), Tyler et al. (2007). They imposed interval constraints on the estimated fluxes based on the projection operator method by Simon and Chia (2002) and Tang and Zhuang (2011) which forced the values of the fluxes to remain positive and ensured the intra-annual variations of the fluxes from the aseasonal sources remain small, to avoid ill-conditioning of the inverse problem. They have repeated one year of monthly varying OH fields for the base inversion simulation but also conducted a sensitivity test with imposing inter-annual variability by globally scaling OH fields to match the annually varying OH concentrations derived by Prinn et al. (2005) to years after 2003 fixed at mean

OH concentrations, which resulted in increased interannual variability of wetland emissions from the tropics and little impact from wetlands at higher latitudes.

The atmospheric ethane abundance was also investigated by previous studies (Aydin et al., 2011; Simpson et al., 2012; Rice et al., 2016) which is co-emitted with methane and used along with methane observations to provide additional constraint on the methane sources such as fossil fuels, since there is large overlap between isotopic methane signatures from fossil methane sources and non-fossil methane sources. Much of this overlap exists because all fossil fuel sources are not strictly thermogenic in origin, with more than 20% of world's natural gas reserves occur due to microbial activity (Rice and Claypool, 1981; Martini et al., 1996; Curtis 2002), which makes it difficult to draw quantitative conclusions on the methane sources with only atmospheric measurements of $\delta^{13}CH_4$ at global scales (Turner et al., 2017).

Turner et al. (2017) presented a simple two-dimensional box model to investigate the cause of methane stabilization and renewed growth, the model simulated annual hemispheric concentrations of $^{12}CH_4$, $^{13}CH_4$, methyl chloroform and OH. They have used atmospheric observations of methane, $\delta^{13}CH_4$ and methyl chloroform from NOAA/ESRL, Global Atmospheric Gases Experiment (GAGE)/ Advanced GAGE (AGAGE) networks and several other sources, to constrain annual hemispheric emissions of methane, isotopic composition of the emissions, methyl chloroform emissions and OH abundance in a nonlinear, stochastic, Bayesian inversion in which they concluded the renewed growth of methane is caused likely due to decline in the OH sink.

1.4.3. Improvements in this Inverse Modeling Study

NOAA/ESRL GLOBALVIEW-CH_4 data measurements were collected by 12 laboratories, which had been smoothed, interpolated, and extrapolated to provide continuous record of CH_4 concentrations from 1984 at weekly time resolution. When there was limited measurement with incomplete data record, then the existing observations were extended based on the site climatology and observations from remote marine boundary sites at similar latitudes. The GLOBALVIEW data extension and integration processes are described in more details provided by Masarie and Tans (1995). Two extension methods were used in their study, one used deseasonalized long-term trend from a single site as a reference to individual site climatologies, referred as benchmark trend method, another method utilized measurements from many sites at similar latitudes, constructed a reference to the climatologies, referred as latitude reference method. Thus, the observations from contributing measurement sites that had been selected for conditions with sampled air expected as representative of large well-mixed air parcels, were fitted to a smoothed curve and the smoothed values were extracted from the curve sampled at regular weekly intervals. However, using these smoothed values in the inversion process introduces additional uncertainty for the seasonal sources (such as biomass burning) which are regionally more localized which may affect the air less near a distant observation site. Furthermore, these smoothed values also cannot determine the accurate magnitude of emission anomalies, interannual variability and seasonality of the sources (such as wetlands) in locations with high variance. Unfortunately, GLOBALVIEW CH_4 data also lacked widespread network coverage in the Southern Hemisphere with very few

measurement sites in South America, Africa, and Australia, which would provide less constraints on the inversion estimates with much less information and introduce substantial bias in the final optimized estimates from the Southern Hemisphere sources. NOAA/ESRL Global Monitoring Laboratory provided raw data with much better network coverage globally and increased time resolution with measurement frequency 2 times or more a day per week including uncertainties reported with each measurement. Here we present an inverse modeling study to estimate optimized emissions of methane from ten different source categories using NOAA/ESRL Global Monitoring Laboratory (GML) 'event' level data files for CH_4 and $\delta^{13}CH_4$ measurements spanning from 1980 to 2015. Initial steps included accumulation of the data and processing of the original raw data of methane mixing ratios along with their associated uncertainties to calculate weighted monthly averaged mixing ratios of CH_4 and $\delta^{13}CH_4$ at the end of each month from sampling cubic spline fits of the weighted monthly averaged mixing ratios at mid of each month which were calculated from weighted daily averaged mixing ratios of methane (more detailed description of the methods are presented in Chapter 4 of this thesis). We mapped the observation sites on a horizontal grid resolution of 2^{o} latitude by 2.5^{o} longitude to integrate with 3D global atmospheric chemical transport model GEOS-Chem. Spatially re-gridded monthly varying prior emission fields were constructed from several sources and also included sinks such as reaction with OH, stratospheric loss and soil sink at the same spatial resolution. In this work, one year of monthly varying three-dimensional OH field was used in GEOS-Chem where CH_4 loss due to reaction to OH was calculated at every grid cell for each timestep. GEOS-Chem used NASA Global Modeling and Assimilation Office (GMAO) data product GEOS-5 meteorological fields available for years 2004 to 2010 and

these 6 years of meteorological variables were recycled for the entire inversion time, since, one year of repeated meteorology has no significant impact on the results according to the sensitivity test done by Röger (2013). Isotopic $\delta^{13}CH_4$ was used as an independent tracer in the inversion to improve constraining the source estimates with the source signatures taken from previous works done by OHSU-PSU archived air measurements, White et al., (2015) at INSTAAR, Quay et al. (1999), Tyler et al. (2007). We have implemented sequential estimation of methane fluxes from observational data sets from different time steps by using fixed-lag Kalman smoother technique based on the methods described by Bruhwiler et al. (2005) and Chen and Prinn (2006). The method employed assumption of emission occurring at a time step becomes spatially well mixed and achieves a constant value after a lag time difference between emission time and observation time which was almost 6 months with GEOS-Chem chemical transport model. We have taken this lag time as 11 months and followed covariance propagation scheme with forwarding covariance of fully optimized fluxes into fluxes being estimated for current time step by including 1 month of correlations of fluxes and helped to constrain the current estimates of fluxes with measurements from subsequent time steps. To avoid ill-conditioning of the inverse problem, we imposed interval constraints using projection operator method mentioned by Simon and Chia (2002) and iterative approach by Tang and Zhuang (2011) to keep the optimized flux estimates in active set within physically sensible regions with values positive and intra-annual variations of aseasonal sources to remain small. This inverse modeling study gives insight into the understanding of spatial and temporal attribution of methane sources in the global methane budget for more than 30 years. Using spatial grid resolution as high as computationally feasible i.e., $2^{o} \times 2.5^{o}$ in this study, which had

decreased the errors caused due to aggregation of fluxes over large regions, improved the uncertainty estimates and led to more realistic posterior estimates. We also performed a series of sensitivity tests where the number of observation stations were changed in the inversions based on availability of continuous measurement record lengths. Although there was loss of information with reduced number measurement sites, but these test scenarios were included in the ensemble of fluxes from each source categories to determine the bias in the retrieved fluxes due to variable number of observation sites with continuous measurement records.

1.5. Main objectives of the study

The main objectives of the current study are as follows:

- To better understand the changing budget of atmospheric CH_4 over more than three decades.
- To perform a time-dependent retrieval i.e., inverse modeling of CH_4 fluxes spanning nearly 35 years using global surface and isotopic CH_4 measurements.
- To extend previous inversion study to year 2016 using the recent surface flask data from National Oceanic and Atmospheric Administration (NOAA) Global Monitoring Laboratory (GML) CH_4 measurements and available $\delta^{13}C$-CH_4 data.
- To implement higher grid resolution version of chemical transport model GEOS-Chem ($2^0 \times 2.5^0$ grid resolution).

- To mention the difference in the global flux estimates by inversions done using NOAA original raw data and using the GLOBALVIEW CH_4 data product.
- To determine the causes of increased methane levels in the atmosphere from 2006 onwards.
- To understand the recent trends in the global methane emissions.

1.6. Significance of this study

This work primarily focuses on inverse modeling studies of methane emissions and developing essential computer programs to perform the modeling work at Portland State University (PSU). In this thesis, we provide an insight into the recent behavior of the atmospheric methane by performing a global three-dimensional Bayesian inversion of surface CH_4 and $^{13}CH_4/^{12}CH_4$ ratios over the years 1980 - 2015 using NOAA Global Monitoring Laboratory (GML) CH_4 measurements and the GEOS-Chem chemical transport model (CTM) at a grid resolution of $2^{o} \times 2.5^{o}$. Here, a priori information is used on the magnitude of the source processes under investigation to regularize the inverse problem and impose interval constraints on the estimates to ensure physically sensible results. In this way, we derived time-dependent methane emissions consistent with atmospheric observations for this interesting time period, when the growth rate of CH_4 began a two-decade long decline and then with some surprise, rebounded in 2007 for reasons that are not well understood. The use of 3D model allowed us to exploit spatial patterns in the global CH_4 and $^{13}CH_4/^{12}CH_4$ fields that provide additional constraints on the

retrieval of the time-dependent CH_4 fluxes. This work followed up on our previous CH_4 inversion where the GLOBALVIEW CH_4 data product was used at a $4^o \times 5^o$ horizontal grid for GEOS-Chem to retrieve fluxes from 1985 to 2009, but this work used NOAA GML original raw data extending up to 2016 and at a higher horizontal grid resolution of $2^o \times 2.5^o$. At higher resolution more information is extracted from the observations due to improved model skill and a smaller number of stations aggregated within model grid cells. One of the main motivations in working with higher resolution is to reduce the model-data mismatch errors and increase the weights on the information from the observations.

1.7. Chapters Included

Chapter 1 is introduction including the factual description of methane, its role in the atmosphere as a greenhouse gas, distribution and trend of measurements of atmospheric methane over time, its growth rate over last decades, causes of growth rate anomalies as suggested by previous studies, and possible causes of increase in its growth rate since 2007 as mentioned by previous studies. Methods involved in quantifying atmospheric methane, previous inversion studies, improvements made in our study, main objectives of the study, significance and chapters included in this thesis are also included.

Chapter 2 focuses on importance of quantifying atmospheric methane, physical and chemical properties of methane, its lifetime, average mixing ratio, radiation absorption spectra, as a potential greenhouse gas, global warming potential. Sources those introduce

methane to the atmosphere, sinks those remove it from the atmosphere and its isotopes are also discussed in this chapter.

In Chapter 3, the physical and mathematical frameworks of inverse modeling are presented. The principles of Bayesian estimation and the advantages of the applied Kalman smoothing technique are being described. Furthermore, there are discussion on the incorporation of isotope data and how to impose interval constraints to guarantee physically sensible results.

Chapter 4 aims to clarify some of the so far abstractly discussed concepts by describing the implementation and setup for our inverse modeling study in more details. Description of the input data of a priori emission estimates from various methane sources and sinks are given, then the employed chemical transport model GEOS-Chem and its representation of source and sink processes are presented, next the processing of observational records are mentioned that are used to constrain the inversion estimates, and finally, the structure of the developed computer programs, and the performed sensitivity tests are discussed.

The results of our inverse modeling work of the changing methane budget are then presented and discussed in Chapter 5. Comparison of the fits between modeled concentrations and observed concentrations using a posteriori and a priori emission estimates are presented, deseasonalized emission anomalies for each source categories and aggregated categories are shown, annual seasonal cycles of estimates from seasonally varying sources are also presented and compared the results from this study with $4^{o} \times 5^{o}$ resolution model results up to 2008-2009 and also with other most recent studies. Finally,

the possible causes as revealed from our results for the post 2006 rise in global methane levels are inferred.

In Chapter 6, the overall procedure and results of this work are summarized, some conclusions are drawn based on the results and some perspectives for future improvements are provided.

CHAPTER 2

Physical and Chemical Importance of Methane in the Atmosphere

2.1. Methane in the Atmosphere

About 3.5 billion years ago, in the Earth's earlier history, the abundance of methane in the atmosphere was much higher at about 1,000 times more than the present level. The earliest methane (CH_4) and carbon dioxide (CO_2) was released into the atmosphere by volcanic activity. During this time, it is believed that the Earth's earliest life had appeared. Pavlov et al. (2003) mentioned that these first, ancient methanogenic bacteria made their metabolic living by catalyzing the reaction: $CO_2 + 4H_2 \rightarrow CH_4 + 2H_2O$, i.e., converted hydrogen and carbon dioxide into methane and water. Oxygen did not become a major content in the atmosphere until photosynthetic organisms evolved later in the Earth's history. In the absence of oxygen, methane stayed in the atmosphere longer and at higher concentrations than it does today (Pavlov et al., 2003). Methane is generally produced by microorganisms decomposing organic matter in anaerobic conditions and can be emitted from under the soil in waterlogged conditions biologically, or is produced naturally from terrestrial and marine seepages, mud volcanoes and hydrates (frozen mix of methane gas and ice formed under certain temperature and pressure) under the sea floor geologically, or from incomplete combustion of organic matter such as biomass burning, on the earth's surface and it is carried into the atmosphere by rising air in the tropics and is known as atmospheric methane. Figure 2.1 shows the global map displaying the distribution of atmospheric methane (in parts per billion by volume) near the surface of the earth based on the EDGAR and other methane emissions inventories and calculated by the atmospheric chemical transport model GEOS-Chem at horizontal grid resolution of $2^0 \times 2.5^0$ (latitude ×

longitude) using GEOS5 meteorological variables. This map is displaying the methane mixing ratio on January 01, 1990, at time 00:00 GMT on the earth surface with the concentration of methane higher near the source regions throughout the globe.

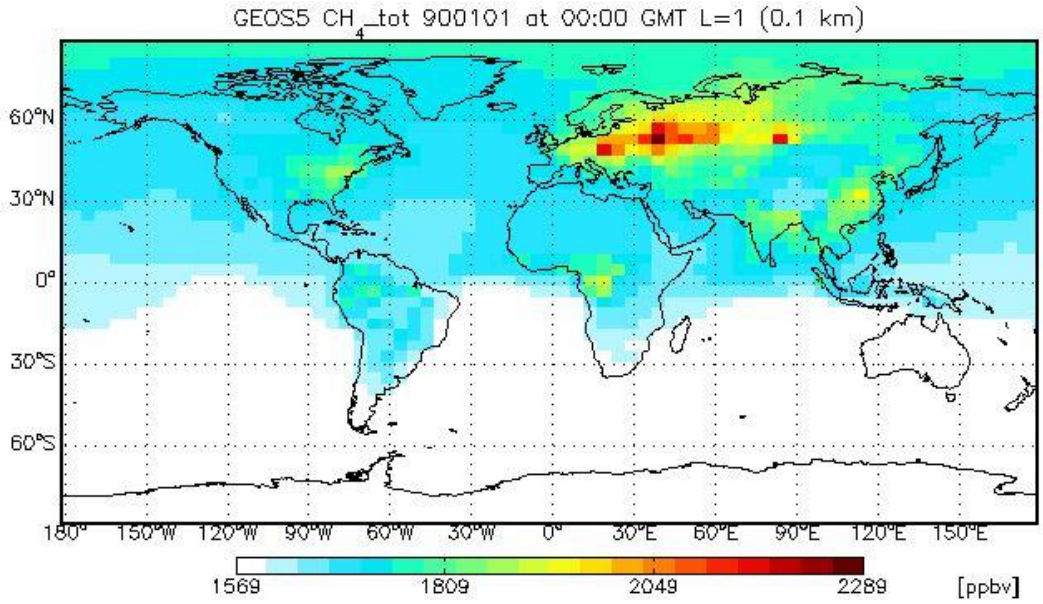

Figure 2.1: *The global map displaying the distribution of atmospheric methane (in parts per billion by volume) near the surface of the earth. It shows methane mixing ratio on January 01, 1990, at time 00:00 GMT on the earth surface with the concentration of methane higher near the source regions throughout the globe.*

2.2. Importance of Methane in the Atmosphere

2.2.1. General Properties of Methane

Structure:

Methane, the smallest hydrocarbon, is an uncolored and non-smelling gas. It has a symmetrical nonpolar structure, where the carbon atom is bonded to four hydrogen atoms in a perfectly tetrahedral arrangement (Figure 2.2).

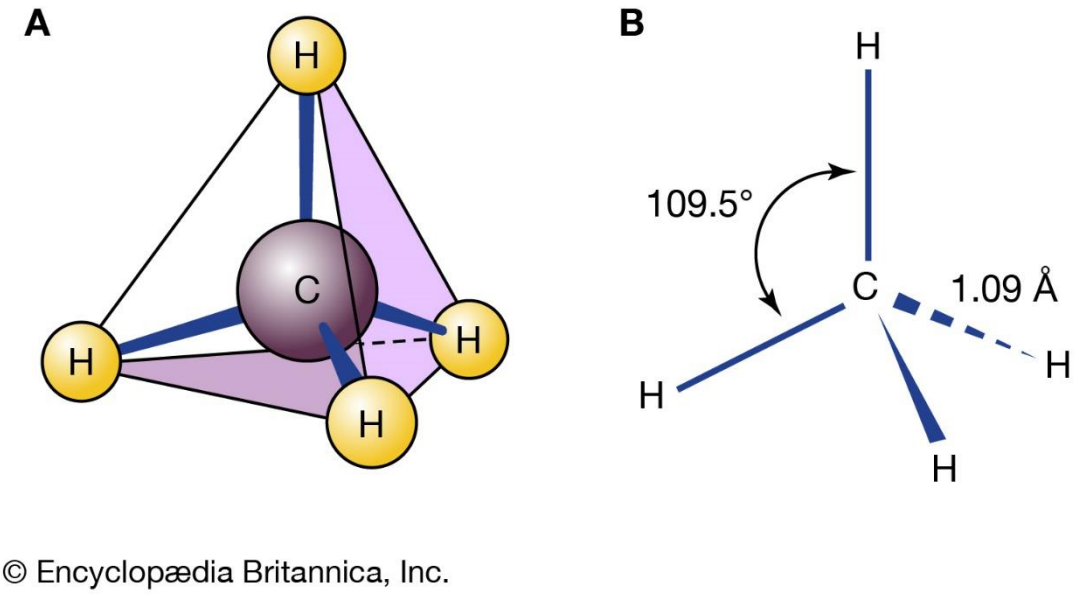

© Encyclopædia Britannica, Inc.

Figure 2.2: *CH4 molecule with four hydrogen atoms bonded to one central carbon atom shown in (a) tetrahedral structure and (b) structure with bond angle (Source: Encyclopaedia Britannica, Inc.).*

Average Mixing Ratio:

According to the Fifth Assessment Report of the Intergovernmental Panel on Climate Change (IPCC, AR5, 2013), global methane levels had risen to 1803 parts per billion (ppb) by 2011, an increase by a factor of 2.5 since pre-industrial times, from 722 ppb in 1750, the highest value in at least 800,000 years. The surface mixing ratio of CH_4 has increased by 150% since pre-industrial times (IPCC, AR5, 2013). The recent average global methane mixing ratio for the month of March 2021 is 1888.5 ppb as measured by the Global Monitoring Laboratory (GML) of the Earth System Research Laboratory (ESRL), National Oceanic and Atmospheric Administration (NOAA).

Lifetime and Seasonal Variation:

Most of the methane emissions occur in the Northern Hemisphere since all main sources (both natural and anthropogenic) are located on the land masses. Moreover, Northern Hemisphere has more land masses and thus more human population. Methane has a lifetime of 8 to 11 years, inter-hemispheric exchange time of approximately 1 year, intra-hemispheric mixing time of about 2 months and zonal mixing time of about 2 weeks which allows it to disperse globally. Thus, a latitudinal gradient and a seasonal cycle can be observed in methane mixing ratio (Figure 2.3). This variation is mainly due to the seasonal variation of methane's main sink OH radical and seasonality of emissions from sources like rice and wetlands.

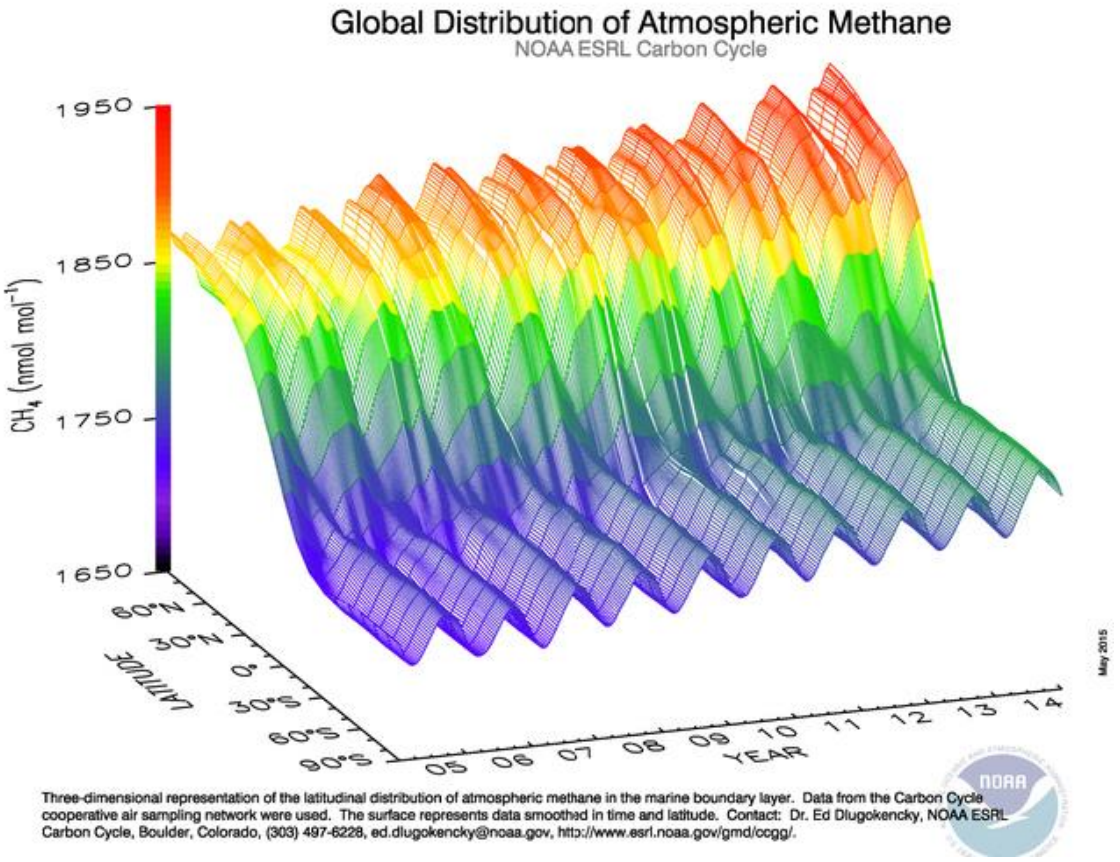

Figure 2.3: *Spatio-temporal distribution of atmospheric methane in the marine boundary layer from 2005 to 2014 showing the seasonal variations and the difference between northern and southern hemispheres [Ed Dlugokencky, NOAA ESRL GML, 2016].*

2.2.2. Methane as a Greenhouse Gas

Methane (CH_4) is an important trace gas in the earth's atmosphere. Although it only makes up 0.00018% (1.8 parts per million mixing ratio) of the atmosphere, it traps a significant amount of heat which helps earth to remain warm and habitable. Methane contributes to the greenhouse effect of the earth directly as well as indirectly as it also contributes to the

formation of other greenhouse gases (such as ozone) which have their own relative contributions to the greenhouse effect.

Radiation Absorption Spectra of Methane:

The solar energy in form of short wavelength electromagnetic radiation is transmitted from the sun to the earth. The earth loses energy by emitting long-wave electromagnetic radiation back to space at wavelengths determined by its temperature. Some of this terrestrial radiation escapes into the space and some is absorbed by the various gases in the atmosphere and radiated back to the Earth, resulting in the warming of the surface known as the greenhouse effect. Among these gases, carbon dioxide, water vapor, and ozone are the major absorbers and carbon monoxide, nitrous oxide, methane, and nitric oxide are relatively minor absorbers.

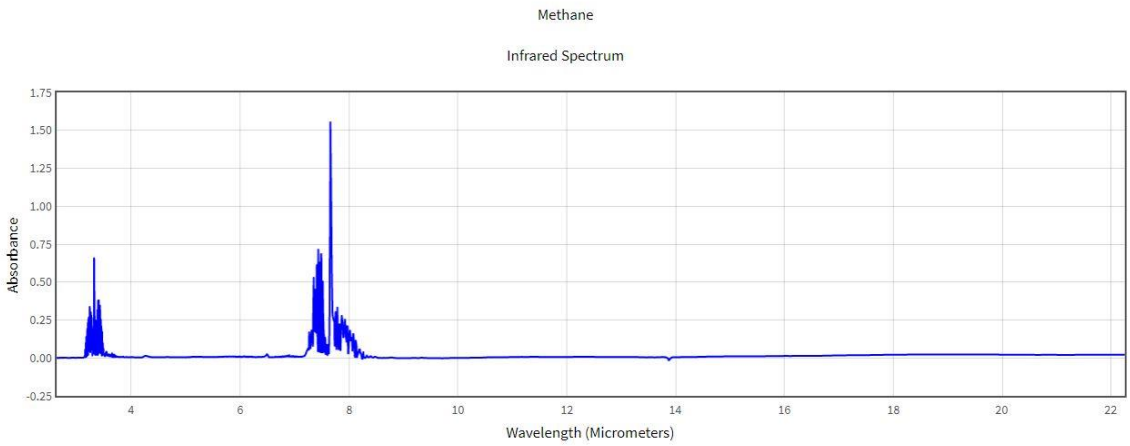

Figure 2.4: *The fraction of radiation absorbed by methane while radiating back from the surface of the earth to the top of the atmosphere as a function of wavelength. Absorption peaks of CH_4 are indicated at wavelength λ = 3.3 µm and 7.7 µm [Reference: Data from NIST Standard Reference Database 69: NIST Chemistry Web Book. https://webbook.nist.gov/chemistry].*

Methane absorbs radiation strongly at about λ = 3.3 µm and λ = 7.7 µm which are in the infra-red region (Figure 2.4). Methane molecules in the atmosphere absorb the infra-red radiation at these two wavelength regions and radiate it back to the earth surface, thus making methane a greenhouse gas in the earth's atmosphere. A low transmission value associated with a specific range of wavelengths, represents absorption bands.

Radiative Forcing:

According to IPCC AR5 (2013), the radiative forcing (RF) is conceptualized as the net change in the energy balance of the Earth system due to an imposed perturbation. It is expressed in watts per square meter averaged over a particular time and quantifies the net imbalance of energy that occurs with imposed change taking place. The instantaneous RF is the instantaneous change in net radiative flux (shortwave and longwave, in W/m^2) and

is defined in terms of flux changes at the top of the atmosphere (TOA) or at the climatological tropopause. In both IPCC Third Assessment Report (TAR) and Fourth Assessment Report (AR4), the term radiative forcing was defined as the change in net irradiance at the tropopause after stratospheric temperatures are allowed to readjust to radiative equilibrium, while surface and tropospheric temperatures and state variables such as water vapor and cloud cover are held fixed at the unperturbed values (except for the impact of aerosols on cloud albedo). Instantaneous RF or RF is not an accurate indicator of temperature response for all forcing agents, however including rapid tropospheric adjustments has the potential to characterize for drivers in the troposphere, for example, allowing quantification of forcing due to aerosol-induced changes in clouds. A forcing that accounted for rapid adjustments is termed as effective radiative forcing (ERF). Conceptually, ERF is the change in net TOA downward radiative flux after allowing for atmospheric temperatures, water vapor and clouds to adjust, but with global mean surface temperature or a portion of surface conditions unchanged. As mentioned in AR5, for well mixed greenhouse gases (WMGHG), the ERF best estimate is same as the RF, which has a value of 0.97 (0.74 to 1.20) Wm^{-2} for CH_4. The indirect effect of several emitted compounds and changes in components involved in atmospheric chemistry lead to larger RF than the RF of the compound directly. Emission of methane leads to production of ozone, stratospheric water vapor, CO_2 and importantly affects its own lifetime in the atmosphere. The RF contribution from emission of CH_4 is 0.97 Wm^{-2} which is almost twice as large as that from change in concentration of CH_4 in the atmosphere from 1750 to 2011 i.e., 0.48 (0.43 to 0.53) ± 0.05 Wm^{-2}, calculated using the formula from Myhre et al. (1998). Furthermore, emissions of CH_4 lead to stronger RF via direct CH_4 greenhouse effect which

is 0.64 Wm^{-2} than RF from abundance change of CH_4 (0.48 Wm^{-2}) because compounds such as NO_x influence the lifetime of CH_4 and reduce the abundance of CH_4 in the atmosphere. The variation of CH_4 concentrations with latitude and decrease above tropopause, contributes only 2% to the uncertainty in RF (Freckleton et al., 1998).

Global Warming Potential:

The Global Warming Potential (GWP) provides a relative measure of how much heat a greenhouse gas traps in the atmosphere. GWP is defined as the time-integrated Radiative Forcing (RF) due to a pulse emission of a given component, relative to a pulse emission of an equal mass of CO_2 [Figure 2.5 (a)]. It compares the amount of heat trapped by a certain mass of the gas to the amount of heat trapped by a similar mass of carbon dioxide. A GWP is calculated over a specific time interval, commonly 20, 100, or 500 years. The larger the GWP, the more that a given gas warms the Earth compared to CO_2 over that time. Considering the radiative and chemical contributions of methane, the Global Warming Potential of methane is 28 over 100-year time horizon and 84 for 20-year time horizon without including climate-carbon feedback and 34 over 100-year time horizon and 86 for 20-year time horizon with climate-carbon feedback [Jain et al. (2000) and IPCC AR5 (2013)]. This means that the same mass of emitted methane will be 28 times more efficient at trapping heat than that of carbon dioxide over the following 100 years. Thus, consequently, atmospheric methane contributes significantly to the human induced

radiative forcing, despite its atmospheric concentration being 200 times smaller than that of CO_2.

Global Temperature Change Potential:

The Global Temperature Change Potential (GTP) is defined as the change in global mean surface temperature at a chosen point of time in response to an emission pulse of any gas relative to that of CO_2 (Shine et al., 2005a). In comparison to GWP which is integrated with time, GTP is an end point metric which is based on temperature change for a selected year, *t*, for a component, *i*, $GTP(t)_i = AGTP(t)_i / AGTP(t)_{CO2} = \Delta T(t)_i / \Delta T(t)_{CO2}$, where AGTP is the absolute global temperature change potential giving temperature change per unit emission [Figure 2.5 (b)]. Similar to the GWP, the GTP values can also weigh the emissions of any gas in the atmosphere to get CO_2 equivalents, that means it gives surface temperature effects of the emissions relative to that of CO_2 for the chosen time horizon which affects its metric value contributing to the warming. Like GWP, the GTP formulation is also influenced by the background atmosphere and the inclusion of indirect effects of the components and feedback in the atmosphere. In contrast to the GWP, the GTP includes physical processes by accounting for climate sensitivity and the exchange of heat between atmosphere and ocean. The GTP accounts for the slow response of the deep ocean, thus prolongs the response of emissions beyond that controlled by the decay time of the atmospheric concentration. Hence, the GTP includes both the time scales for atmospheric adjustment of the component considered as well as for response of the climate

system. The GTP value for CH_4 is 67 for 20-year time horizon and 4 for 100-year time horizon with no climate-carbon feedback, however, including the feedback, it is 70 for 20-year period and 11 for 100-year period. Short-lived gases are most sensitive to the choice of the time span in metric calculation, with a change of time horizon from 20 to 100 years, for CH_4 the GWP decreases by a factor of approximately 3 and the GTP by more than a factor of 10.

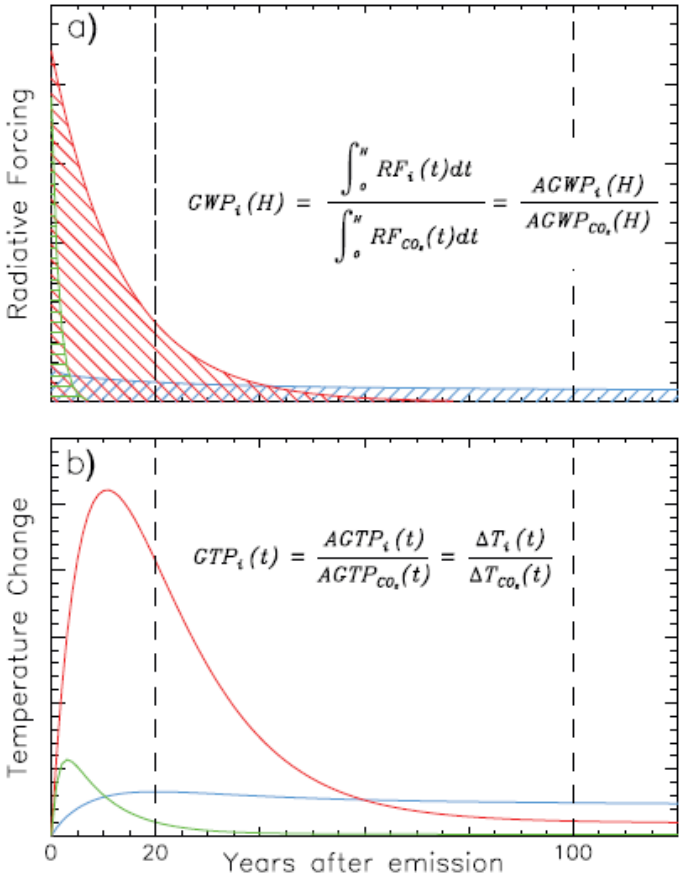

Figure 2.5: *(a) The Absolute Global Warming Potential (AGWP) is calculated by integrating the RF due to emission pulses over a chosen time horizon such as 20 or 100 years (vertical lines). The GWP is the ratio of AGWP of component 'i' over that for reference gas CO_2. The blue hatched field represents the integrated RF from a pulse of CO_2, while green and red fields represent example gases with 1.5 and 13 years of lifetime, respectively. (b) The GTP is based on the temperature response at a selected year after pulse emission of the same gases, e.g., 20 or 100 years (vertical lines) [IPCC, AR5, 2013].*

2.2.3. Oxidizing Mechanism of Methane

As the atmospheric methane increases with years, it also impacts the chemistry of the atmosphere. CH_4 as a reduced form of carbon undergoes oxidation involving sequences of reactions, and ultimately forms carbon dioxide (CO_2) and water (H_2O) as follows:

Initial oxidation of methane produces methyl radical (CH_3) which adds O_2 to form methylperoxy radical (CH_3O_2), where 'M' denotes the third body which carries off the excess energy of the reaction.

$$CH_4 + OH \rightarrow CH_3 + H_2O$$

$$CH_3 + O_2 + M \rightarrow CH_3O_2 + M$$

The methylperoxy radical (CH_3O_2) reacts with hydroperoxyl (HO_2) as:

$$CH_3O_2 + HO_2 \rightarrow CH_3OOH + O_2$$

Methyl hydroperoxide (CH_3OOH) either reacts with OH or photolyzes. The CH_2OOH radical produced then decomposes rapidly to formaldehyde (CH_2O) and OH:

$$CH_3OOH + OH \rightarrow CH_2O + OH + H_2O$$

$$CH_3OOH + OH \rightarrow CH_3O_2 + H_2O$$

$$CH_3OOH + h\nu \rightarrow CH_3O + OH$$

The methoxy radical (CH_3O) produced in previous reaction reacts rapidly with O_2:

$$CH_3O + O_2 \rightarrow CH_2O + HO_2$$

Formaldehyde produced in last reaction can either react with OH or photolyze:

$$CH_2O + OH \rightarrow CHO + H_2O$$

$$CH_2O + h\nu \xrightarrow{O_2} CHO + HO_2$$

$$CH_2O + h\nu \rightarrow CO + H_2$$

The CHO radical produced, reacts rapidly with O_2 to yield CO and HO_2:

$$CHO + O_2 \rightarrow CO + HO_2$$

CO is then oxidized to CO_2 as:

$$CO + 2O_2 \rightarrow CO_2 + O_3$$

$$CO + OH \xrightarrow{O_2} CO_2 + HO_2$$

$$HO_2 + NO \rightarrow OH + NO_2$$

$$NO_2 + h\nu \xrightarrow{O_2} NO + O_3$$

In this overall reaction sequence the C(-IV) atom in CH_4 (the lowest oxidation state for carbon) is successively oxidized to C(-II) in CH_3OOH, C(0) in CH_2O, C(+II) in CO, and C(+IV) in CO_2 (highest oxidation state for carbon). Ozone production takes place by NO_2 photolysis.

By summing all reactions in the mechanism, the following net reaction can be arrived for conversion of CH_4 to CO_2:

net: $CH_4 + 10O_2 \rightarrow CO_2 + H_2O + 5O_3 + 2OH$

net: $CH_4 + 3OH + 2O_2 \rightarrow CO_2 + 3H_2O + HO_2$

The intermediate products of these sequence of reactions influence the concentrations of other gases like ozone (O_3), carbon monoxide (CO), water vapor (H_2O) and hydroxyl radical (OH). More methane in the atmosphere decreases concentration of OH radical. This introduces a positive feedback to the greenhouse effect of these gases, since, OH radical plays an important role in the removal of many greenhouse gases including as the main sink of methane which naturally controls methane levels in the atmosphere. The increase in methane level also contributed to the increase in the tropospheric ozone concentration. Ozone in the stratosphere protects the earth from harmful ultraviolet radiation, but in the troposphere, it acts as a potential greenhouse gas (Shindell et al., 2005), a major component of smog and a toxic pollutant deteriorating human health and ecosystem.

Thus, the methane concentration affects the radiation budget of the earth's atmosphere directly and indirectly.

2.3. Global Methane Budget

The increase of atmospheric methane abundance by a factor of 2.5 since preindustrial times, pronounced the need of implementing sensible emission mitigation strategies through policies in regional as well as global level. Effective strategies to reduce methane emissions require better quantitative understanding of changes in methane sources and sinks both spatially and temporally. Several studies had published their estimates of the methane budget during last three decades since the beginning of the systematic measurement of atmospheric methane by observational networks around the globe. The IPCC AR5 (2013) used multiple atmospheric CH_4 inversion models (top-down) and process-based models and inventories (bottom-up) to provide a continuous assessment of the CH_4 budget per decade. The Fifth Assessment Report of IPCC (2013) discussed the budgets for the decades of 1980s, 1990s and 2000s and presented them in tabular form where uncertainties on emissions and sinks are listed using minimum and maximum of each published estimate for each decade. In this table, bottom-up approaches are used to attribute decadal budgets to individual processes emitting CH_4 and top-down inversions provided an atmospheric-based constraint mostly for the total CH_4 source per region, and the use of additional observations (isotopes) allowed inferring emissions per source type (IPCC, AR5, 2013). Estimates of CH_4 sinks such as through chemical loss in the

atmosphere by tropospheric OH, tropospheric chlorine and stratospheric OH and through oxidation in aerated soil, are also mentioned and listed in the table.

The global methane budget for the decade of 2000s is significant since after a decade of stable CH_4 concentration in the atmosphere since late 1990s, atmospheric measurements showed a renewed growth in the CH_4 concentration since 2007 and the drivers of this renewed growth are still debated. IPCC AR5 (2013) published global CH_4 emissions for the 2000s of 553 Tg(CH_4) yr^{-1}, with a range of 526 to 569 Tg(CH_4)/year, based on the inversion of atmospheric measurements of CH_4 from surface stations. The total loss of atmospheric methane is of 550 Tg(CH_4) yr^{-1} with a range of 514 to 560 Tg(CH_4) yr^{-1}, determining a small imbalance of about 3 Tg(CH_4) yr^{-1}, with a small growth rate of 6 Tg(CH_4) yr^{-1} observed for the 2000s, as reported in the IPCC AR5 (2013). Based on bottom-up models and inventories, IPCC AR5 (2013) published that a larger global CH_4 emissions of 678 Tg(CH_4) yr^{-1} are found, mostly because of the still debated upward re-evaluation of geological (Etiope et al., 2008) and freshwater (Walter et al., 2007; Bastviken et al., 2011) emission sources. The report also mentioned that an averaged total loss of 632 Tg(CH_4) yr^{-1} is found, by an ensemble of atmospheric chemistry models (Lamarque et al., 2013) leading to an imbalance of about 45 Tg(CH_4) yr^{-1} during the 2000s, as compared to the observed mean growth rate of 6 Tg(CH_4) yr^{-1} (Dlugokencky et al., 2011). Top-down inversions have constrained OH fields, e.g., from measurement of methyl chloroform (MCF), whereas there is no constraint applied to the sum of emissions in the bottom-up approach. Thus, top-down inversions are efficient to constrain global CH_4 emissions in the

global budget, but the mix of sources is not well resolved in the top-down inversions (IPCC, AR5, 2013).

AR5 (2013) also reported the contributions of different methane sources to the methane budget for all three decades. For the decade of 2000-2009, using bottom up approaches, the AR5 (2013) budget (range indicating the expanse of values from different literatures) estimated 177 to 284 Tg(CH_4) yr^{-1} for natural wetlands emissions, 187 to 224 Tg(CH_4) yr^{-1} for agriculture and waste (rice, animals, and waste), 85 to 105 Tg(CH_4) yr^{-1} for fossil fuel related emissions, 61 to 200 Tg(CH_4) yr^{-1} for other natural emissions including geological, termites and freshwater emissions, and 32 to 39 Tg(CH_4) yr^{-1} for biomass burning and biofuel emissions. Meanwhile, for the same decade of 2000-2009, top down inversions estimated 142 to 208 Tg(CH_4) yr^{-1} for natural wetlands emissions, 180 to 241 Tg(CH_4) yr^{-1} for agriculture and waste, 77 to 123 Tg(CH_4) yr^{-1} for fossil fuels emissions, 37 to 65 Tg(CH_4) yr^{-1} for other natural sources, and 24 to 45 Tg(CH_4) yr^{-1} for biomass burning and biofuel emissions. Anthropogenic emissions account for 50% to 65% of the total emissions, furthermore, the anthropogenic emissions related to leaks from fossil fuel industry and natural geological emissions estimated to amount to 30% of the total CH_4 emissions (IPCC, AR5, 2013).

Figure 2.6 shows the schematic diagram of the global cycle of CH_4 with annual fluxes from its various sources and sinks (IPCC, AR5, 2013).

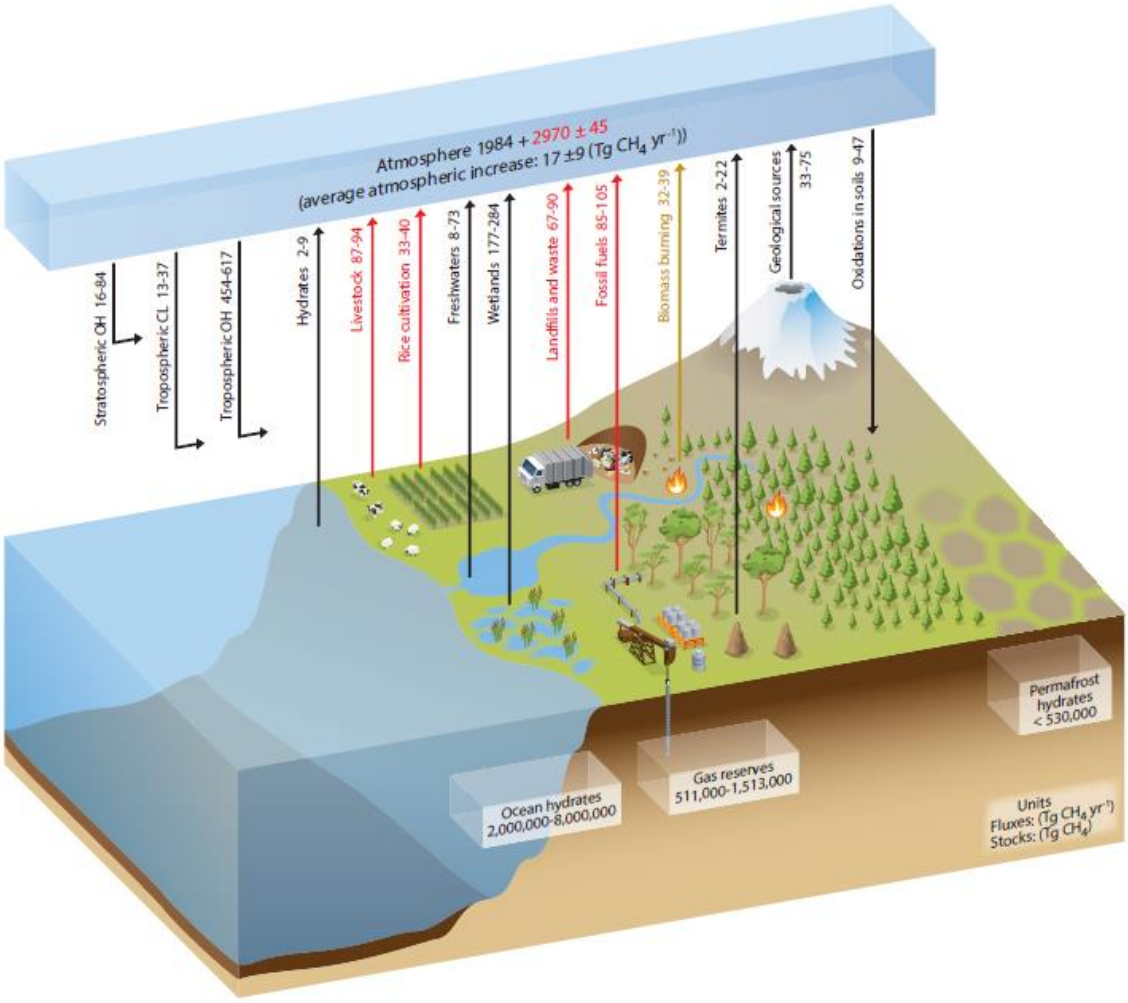

Figure 2.6: *Schematic diagram of the global cycle of CH_4 [IPCC AR5 (2013)]. Numbers represent annual fluxes in Tg(CH_4) yr^{-1} estimated for the time 2000–2009 and CH_4 reservoirs in Tg (CH_4): the atmosphere and three geological reservoirs (hydrates on land and in the ocean floor and gas reserves). Black arrows denote 'natural' fluxes, that is, fluxes that are not directly caused by human activities since 1750, red arrows anthropogenic fluxes, and the light brown arrow denotes a combined natural and anthropogenic flux [IPCC, AR5, 2013].*

2.3.1. Sources of Methane

The methane growth rate results from the balance between emissions and sinks. Methane is emitted by various sources both from natural occurrences and anthropogenic influences

(Figures 2.6 and 2.7) and released into the atmosphere. Evidence suggests that due to various forms of sources, methane emissions are changing over times which are affected by many factors such as energy use, distribution of human population, agricultural practices, waste management practices and climate. IPCC AR5 (2013) published that during the decade of the 2000s, natural sources of CH4 account for 35 to 50% of the decadal mean global emissions, whereas anthropogenic CH_4 sources are estimated to range between 50% (in bottom-up models and inventories) and 65% (in top-down inversions) of the global emissions for the 2000s.

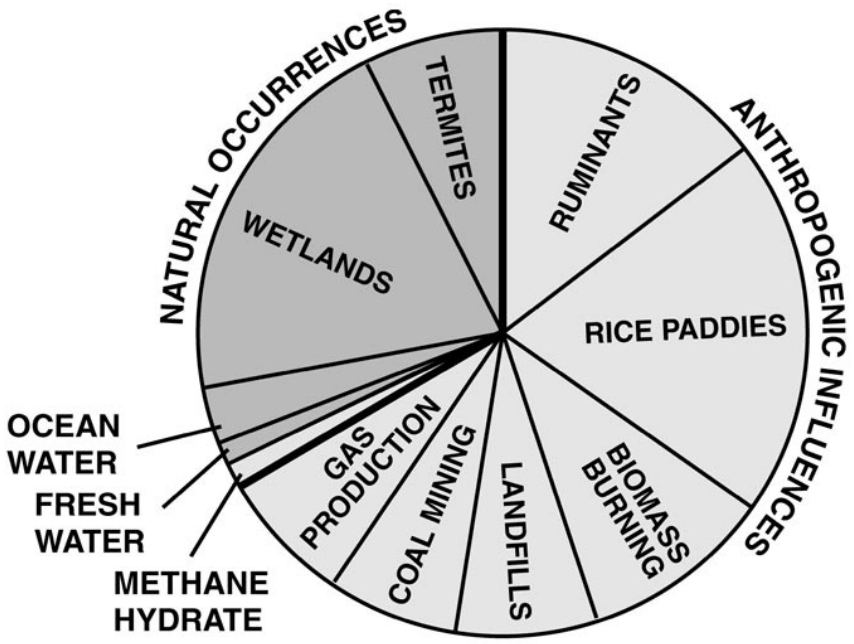

Figure 2.7: *Different sources of methane (Image: U.S. Dept. of Energy Technology Laboratory, National Methane Hydrate Program) [Methane: A Scientific Journey from Obscurity to Climate Super-Stardom by Gavin Schmidt, September 2004].*

Natural and anthropogenic methane emissions around the globe are further categorized based on the origin as either biogenic, thermogenic, or pyrogenic as discussed below:

Biogenic Emissions:

The major source of methane emissions in the atmosphere is of biogenic origin. Biogenic sources are identified as emission from natural wetlands, ruminants, waste, landfills, rice paddies, fresh waters, termites (Figures 2.6 and 2.7). Biogenic emission of methane occurs when methane producing microorganisms, methanogens, produce energy by decomposition of organic matter using an anaerobic process called methanogenesis which generates methane in warm, moist soils as well as in the digestive tracts of ruminant animals. Certain archaea cleave acetate produced during anaerobic fermentation and yield methane and carbon dioxide by the process called *Acetoclastic methanogenesis*.

$H_3C\text{-}COOH \rightarrow CH_4 + CO_2$

Archaea oxidize hydrogen with carbon dioxide to yield methane and water by the process called *Hydrogenotrophic methanogenesis.*

$4H_2 + CO_2 \rightarrow CH_4 + 2H_2O$

These microbial methanogenesis processes take place in anaerobic environments such as in natural wetlands and rice paddies, oxygen-poor freshwater reservoirs (such as dams),

digestive systems of ruminants and termites, and organic waste deposits (such as manure, sewage, and landfills).

Another natural source of methane generated by biological community but different from traditionally known biogenic pathways, has been identified by some studies which is from terrestrial plants in presence of oxygen. Keppler et al. (2006) reported that plants under aerobic conditions emit CH_4, and thus potentially could involve a large additional methane emission and may have important implications for the global methane budget. Later studies did not support plant emissions (Dueck et al., 2007; Wang et al., 2008; Nisbet et al., 2009) or showed small to negligible emissions in the context of the global CH_4 budget (Butenhoff and Khalil, 2007; Vigano et al., 2008; Nisbet et al., 2009; Bloom et al., 2010). Rice et al. (2010) reported results from a greenhouse mesocosm study that indicate significant emissions of anaerobically produced CH_4 transmitted to the atmosphere through broadleaf riparian tree species grown under flooded conditions and The carbon isotopic composition of CH_4 emitted was found to be significantly enriched compared with expectations ($\delta^{13}C \sim -54‰$) and provided an important isotopic constraint on the global source which coincides with the mean of the globally scaled greenhouse-based estimate. IPCC AR5 (2013) mentioned about an apparent aerobic CH_4 production, which involve (1) adsorption and desorption (Kirschbaum and Walcroft, 2008; Nisbet et al., 2009), (2) degradation of organic matter under strong ultraviolet (UV) light (Dueck et al., 2007; Nisbet et al., 2009) and (3) methane in the groundwater emitted through internal air spaces in tree bodies (Terazawa et al., 2007). This source of methane has been largely discredited by researchers due to lack of appropriate evidence of the substantial aerobic methane emission by

terrestrial vegetation regionally or globally. IPCC AR5 (2013) did not report this source in the methane budget table since a significant emission of CH_4 by plants under aerobic conditions is very unlikely. However, recently it has been discovered that leaf surface wax exposed to UV radiation in the presence of oxygen is an aerobic source of methane (Bruhn et al., 2014).

According to the methane budget published in the most recent report of IPCC in AR5 (2013), the single most dominant CH_4 source of the global flux and interannual variability is CH_4 emissions from wetlands (177 to 284 $Tg(CH_4)\ yr^{-1}$). Rice paddies emit between 33 to 40 $Tg(CH_4)\ yr^{-1}$, ruminant livestock such as cattle, sheep, goats, etc. produce CH_4 by food fermentation with a total estimate of between 87 and 94 $Tg(CH_4)\ yr^{-1}$, termites produce 2 to 22 $Tg(CH_4)\ yr^{-1}$, oxygen-deficient freshwater reservoirs emit 8 to 73 $Tg(CH_4)\ yr^{-1}$ and methanogenesis in landfills, livestock manure and waste waters together produces a total between 67 and 90 $Tg(CH_4)\ yr^{-1}$ due to anoxic conditions and a high availability of acetate, CO_2 and H_2 as reported in IPCC AR5 (2013).

Thermogenic Emissions:

Thermogenic sources emerge from the slow transformation of organic matter into fossil fuels on geological time scales (natural gas, coal, oil). Methane is vented from the earth's subsurface into the atmosphere through natural features (such as terrestrial seeps, marine seeps, and mud volcanoes), and through anthropogenic activities by the exploitation of fossil fuels such as coal, oil, and natural gas. Fossil fuel sources of methane are from coal

extraction, crushing and processing, and abandoned mines; oil extraction and gas flaring; and especially from natural gas extraction, storage, processing, transmission, distribution, and usage.

As the coal is mined, the methane gas that has been trapped between layers of coal during its formation is released. Global and even regional estimates of CH_4 emissions from coal mines depend on many assumptions regarding the type of coal, the depth of the mine, mining practices, the methane content of the coal seam, and whether methane is flared or released (Beck et al., 1993; Kirchgessner, 2000; Wuebbles et al., 2002; and references therein).

The primary component of natural gas is methane (over 90%). Methane emitted in the atmosphere during different stages such as extraction, processing, storage, transmission and distribution of natural gases and other different activities such as production, processing, transportation and distribution of crude oil since natural gas is often found alongside with petroleum, crude oil. Regional leakage percentages were estimated to range from 1% to 15% of total natural gas production, depending on the quality of the pipelines, the extraction process, leakage control, the method used to estimate gas losses, and other factors (e.g., Mitchell, 1993; Matthews, 1994; Bazhin, 1994; Beck et al., 1993; Wuebbles et al., 2002). It has been suggested that trapping of this methane emission from these sources (agriculture, energy sectors and landfills) and using it as an energy source may provide additional benefits (Wuebbles et al., 2002; Dlugokencky et al., 2011).

According to AR5 (2013), using bottom-up approaches, global fossil fuel related fugitive methane emission is estimated between 85 and 105 Tg(CH_4) yr^{-1} for the decade of 2000-2009 (Dentener et al., 2005; EDGAR4 database, 2009; EPA, 2011) and using top-down inversions, it is estimated to be 77 to 123 Tg(CH_4) yr^{-1} (Curry, 2007; Pison et al., 2009; Bergamaschi et al., 2009; Bousquet et al., 2011; Spahni et al., 2011; Ito and Inatomi, 2012). In IPCC AR5 (2013), natural geological sources were estimated between 33 and 75 Tg(CH_4) yr^{-1}. Etiope et al. (2008) provided improved emission estimates from terrestrial (13 to 29 Tg(CH_4) yr^{-1}) and marine (~20 Tg(CH_4) yr^{-1}) seepages, mud volcanoes (6 to 9 Tg(CH_4) yr^{-1}), hydrates (5 to 10 Tg(CH_4) yr^{-1}) and geothermal and volcanic areas (3 to 6 Tg(CH_4) yr^{-1}), which represent altogether between 42 and 64 Tg(CH_4) yr^{-1} (IPCC, AR5, 2013). The warmer Arctic Ocean is leading to rapid loss of sea ice and melting permafrost resulting in increased wetland areas, combined with warmer temperatures further increasing methane emission, in addition, it also slowly increases methane emission from hydrates on shallow Arctic continental shelves where pools of free gas are released when overlying layer of impermeable clathrate decays (Dlugokencky et al., 2011). IPCC AR5 (2013) mentioned potential importance of the natural sources of CH_4 emissions from thawing permafrost and CH_4 hydrates in the northern circumpolar region in the 21st century, since they could increase dramatically due to the rapid climate warming of the Arctic and the large carbon pools stored there (Tarnocai et al., 2009; Dlugokencky et al., 2011; Walter Anthony et al., 2012). However, hydrates are estimated to represent only an exceedingly small emission, between 2 and 9 Tg(CH_4) yr^{-1} during the decade of 2000-2009 as mentioned by IPCC AR5 (2013). The supersaturation of dissolved methane at the bottom and surface waters in the East Siberian Arctic Shelf with a net sea-air flux of 10.5

$Tg(CH_4)yr^{-1}$, similar in magnitude for the entire ocean (Shakhova et al., 2010) and ebullition of CH_4 from decomposition and thawing of lake sediments in north Siberia with an estimated flux of ~4 $Tg(CH_4)\ yr^{-1}$ demonstrated importance of potential methane release in the future (Walter et al., 2006; van Huissteden et al., 2011; IPCC, AR5, 2013).

Pyrogenic Emissions:

Pyrogenic CH_4 is produced by the incomplete combustion of both living and dead organic matter in biomass and soil carbon during wildfires, and of biofuels and fossil fuels. When combustion is incomplete, large amounts of CH_4, and other higher-order hydrocarbons can be produced. Methane emissions from biomass burning depend on the stage of combustion reached, the carbon content of the biomass, and the amount of biomass burned (Levine et al., 2000). Methane emissions from these sources can be either human induced, primarily for agricultural purposes and biofuel combustion, or natural occurrence like forest fires. Most biomass burning is initiated by humans for agricultural land clearing such as seasonal grassland fires that spread from crop waste burning, especially in savannah Africa and for land-use change e.g., burning after logging to clear land for eventual agricultural use (Dlugokencky et al., 2011).

Pyrogenic sources of CH_4 are assessed to have a small contribution in the global flux for the 2000s (32 to 39 $Tg(CH_4)\ yr^{-1}$) as published in the IPCC AR5 (2013). Similar as the emission from wetlands, emission from biomass burning such as from tropical and boreal forests (17 to 21 $Tg(CH_4)\ yr^{-1}$) is also meteorologically driven, but plays smaller role in

interannual variability of CH_4 growth rate except during intensive fire periods (Langenfelds et al., 2002; Simpson et al., 2006). Burning of forests and peatland in Indonesia and Malaysia, during the 1997–1998 record strong El Nino, released ~12 Tg(CH_4) which contributed to the observed growth rate anomaly (Langenfelds et al., 2002; van der Werf et al., 2004). IPCC AR5 (2013) also discussed about some smaller fire CH_4 emissions positive anomalies suggested over the northern mid-latitudes in 2002–2003, over Eastern Siberia in 2003 (van der Werf et al., 2010) and Russia in 2010. Moreover, traditional biofuel burning is estimated to emit 14 to 17 Tg(CH_4) yr^{-1} (Andreae and Merlet, 2001; Yevich and Logan, 2003).

2.3.2. Sinks of Methane

The processes that consume methane from the atmosphere are considered "sinks" of atmospheric methane. The most prominent of these processes occur because of methane either being destroyed in the atmosphere or broken down in soil. Figure 2.8 shows a pie-chart demonstrating relative effects of sinks of atmospheric methane. There is a small imbalance of about 3 Tg(CH_4)yr^{-1} between rate of atmospheric methane emission from sources and loss due to sinks observed for the decade of 2000s (IPCC, AR5, 2013). The major sink of atmospheric methane is oxidation by OH radicals (7 to 11 years lifetime) and two more minor sinks are soil sinks (160-year lifetime) and stratospheric loss by reaction with ·OH, ·Cl and $\cdot O^1D$ in the stratosphere (120 year lifetime), giving a net lifetime of

atmospheric CH_4 of 8.4 years. A recent estimate of the CH_4 lifetime is 9.1 ± 0.9 years (Prather et al., 2012).

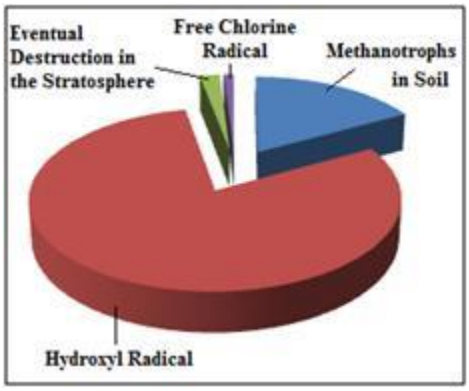

Figure 2.8: *Pie-chart showing relative effects of atmospheric methane sinks (Reference website: https://commons.wikimedia.org/wiki/File:MethaneSinkPieChart.jpg).*

Reaction with Hydroxyl Radicals:

The main primary sink of atmospheric CH_4 is its oxidation initiated by OH radicals, a chemical reaction that takes place mostly in the troposphere and stratosphere (Ehhalt and Heidt, 1973). In the troposphere, this oxidation reaction gets triggered especially in the presence of strong sunlight in the tropics and is highly influenced by meteorological variation (Dlugokencky et al., 2011). Methane in the atmosphere reacts with hydroxyl (OH) radicals to produce $\cdot CH_3$ radical and water vapor as shown in the chemical reaction:

$$CH_4 + \cdot OH \rightarrow \cdot CH_3 + H_2O$$

This reaction is the first step of an oxidation chain reaction further producing CO and CO_2, as described previously in the section 2.2.3 in this chapter. The reaction with hydroxyl radical is responsible for removal of CH_4 equivalent to about 90% of all surface emissions each year and 9% of the total burden of CH_4 in the atmosphere, which defines a partial atmospheric lifetime with respect to OH for an atmospheric burden of 4800 Tg(CH_4) (4700 to 4900 TgCH_4) as computed by Atmospheric Chemistry and Climate Model Intercomparison Project (ACCMIP) atmospheric chemistry models in Voulgarakis et al. (2013) (IPCC, AR5, 2013).

The photolysis of ozone, produces excited atomic oxygen which reacts with water vapor to produce hydroxyl (OH) radicals as shown in the reactions below:

$$O_3 \xrightarrow{h\nu} O_2 + O(^1D)$$

$$O(^1D) + H_2O \rightarrow 2OH$$

OH, thus formed from the photodissociation of tropospheric ozone and water vapor, is the primary oxidant for most tropospheric pollutants, including carbon monoxide, NOx species, and organic compounds (e.g, Crutzen, 1995; Wuebbles et al., 2002). Methane being the most abundant organic species in the atmosphere, plays an influential role in determining the tropospheric oxidizing capacity, initiating an important series of chemical reactions (Wuebbles et al., 2002). The indirect effect of this methane oxidation influences the increase of other pollutants. Large amount of methane in the atmosphere means fewer

amount of hydroxyl (OH) radicals which create all over low oxidizing power of the atmosphere.

Over the past decade, many publications estimated global OH concentrations and variations (Prinn et al., 2001; Dentener et al., 2003; Bousquet et al., 2005; Prinn et al., 2005; Rigby et al., 2008; Montzka et al., 2011). It is almost impossible to measure directly global OH concentrations in the atmosphere, because of its noticeably short lifetime and low concentration in the atmosphere. To obtain a global mean OH value and time variations, Chemical Transport Models (CTMs), Chemistry Climate Models (CCMs) or proxy methods must be used. However, most estimates of OH concentration have been made through measuring the concentration of a tracer molecule such as methyl chloroform [MCF (CH_3CCl_3)]. MCF emissions are exclusively industrial, relatively well known, and main sink is OH radicals, thus can be used to infer the OH concentration with chemical transport model. Using CH_3CCl_3 data from 1978 to 1994 obtained at five ALE/GAGE stations around the globe, modeling studies deduced the average globally integrated concentration of OH to be 9.7×10^5 molecules/cm^3 (Prinn et al., 1995) and 1.07×10^6 molecules/cm^3 (Krol et al., 1998). When measurements of MCF tracer are used to reconstruct OH, due to oversensitivity to uncertainties on their emissions, atmospheric inversion results showed much larger inter-annual variations of OH (5 to 10%) for the 1980s and the 1990s (Montzka et al., 2011), although reduced variations are inferred after 1998 by Prinn et al. (2005). The Montreal protocol (1987) and its further amendments led to limitations in the MCF emissions and thus reduction of MCF in the atmosphere and allowed a consistent estimate of small OH variations between atmospheric inversions

(<±5%) and CCMs/CTMs (<±3%) by the decade of 2000s (Voulgarakis et al., 2013; Young et al., 2013; IPCC, AR5, 2013). However, IPCC AR5 (2013) mentioned the need to find another tracer to reconstruct global OH in the upcoming years, as is imposed by the extremely low atmospheric values of MCF (few ppt in 2010).

As published in the IPCC AR5 (2013), a recent extensive analysis by Prather et al. (2012) inferred a global chemical loss of 554 ± 56 Tg(CH4)yr^{-1} due to OH, whereas other CTMs and CCMs (Young et al., 2013) estimated a global chemical loss of methane of 604 Tg(CH_4) yr^{-1} [509 to 764 Tg(CH_4) yr^{-1}] for the decade of 2000s. According to IPCC AR5 (2013), top-down inversions using MCF measurements to infer OH provided a smaller chemical loss of 518 Tg(CH_4) yr^{-1} with a narrower range of 510 to 538 Tg(CH_4) yr^{-1} in the 2000s, without accounting for all sources of uncertainties (Prather et al., 2012).

Removal of CH_4 in Stratosphere

Other processes that contribute minor CH_4 removal from the troposphere are upward loss to the stratosphere. If CH_4 is not destroyed in the troposphere, then it moves to the next atmospheric layer, will last for approximately 120 years, and eventually gets destroyed. The reaction of CH_4 occurs with Cl radicals and O(^{1}D) in the stratosphere (Shallcross et al., 2007; Neef et al., 2010). This reaction in the stratosphere accounts for about ~3% of global CH_4 sink (Kirschke et al., 2013). Destruction of CH_4 in the stratosphere occurs the

same way that it does in the troposphere, methane is oxidized to produce carbon dioxide and water vapor.

Reaction with Cl

A small sink of atmospheric CH_4 is suspected, but still debated, in the marine boundary layer due to a chemical reaction with chlorine (Allan et al., 2007; IPCC, AR5, 2013). Reaction with chlorine radicals from sea salt in the marine boundary layer accounts for about ~3% of the global CH_4 sink (Kirschke et al., 2013). Methane reacts with natural chlorine gas in the atmosphere to produce chloromethane and hydrochloric acid (HCl), the process is known as free radical halogenations.

$$CH_4 + Cl_2 \rightarrow CH_3Cl + HCl$$

The HCl produced in this reaction leads to catalytic ozone destruction in the stratosphere.

Removal by Methanotrophs in soil

Methanotrophic bacteria that reside within soil use methane as a source of carbon and energy in methane oxidation. Reaction of methane with oxygen produces carbon dioxide and water.

$CH_4 + 2O_2 \rightarrow CO_2 + 2H_2O$

Methanotrophic bacteria in aerated soils account for about ~4% of global CH4 sink (Kirschke et al., 2013). As published in IPCC AR5 (2013), oxidation in upland soils (with oxygen) by methanotrophic bacteria removes about 9 to 47 Tg(CH4) yr^{-1} (Curry, 2007; Dutaur and Verchot, 2007; Spahni et al., 2011; Ito and Inatomi, 2012).

Methanotrophs are also important in the oceans where they can oxidize a significant fraction of CH_4 emitted from seeps on the seabed into CO_2, before methane reaches the atmosphere. According to Dlugokencky et al. (2011), in future this may be a major uptake of widely dispersed emissions from seabed hydrates, which store methane in the seabed both by anaerobic biological methanogenesis in shallow sediment and by geological heating at deeper levels.

2.4. Isotopes

The isotopic composition of atmospheric CH_4 is determined by chemical and physical processes. The rates of the chemical reactions of methane production and removal depends on isotopes; hence all sources and sinks exhibit a characteristic fractionation of the methane isotopes and thus, valuable information concerning the strength of methane sources and sinks, and their contribution to changes in atmospheric methane abundance can be obtained from its isotopic composition. Mass spectroscopy is used to measure different isotopes of

methane (Stable isotopes $^{13}CH_4$, CH_3D and radioisotope $^{14}CH_4$). Routine monitoring of $^{13}CH_4$ in CH_4 in ambient air is presently limited, mainly carried out by the University of Colorado, Institute of Arctic and Alpine Research (INSTAAR), for the US NOAA network of sites, by the National Institute of Water and Atmospheric Research in New Zealand, by the University of Heidelberg in Germany and by Royal Holloway University London (RHUL) in the UK. Stable isotope $^{13}CH_4$ helps separate biogenic emissions from other sources. Measurements of the δD stable isotope (CH_3D) provide constraints on the uncertain OH CH_4 sink. Radiocarbon CH_4 data ($^{14}CH_4$) helps constrain the uncertain fossil part of CH_4 emissions, if $^{14}CH_4$ emissions from nuclear installations can be accurately estimated. In the next following section, only $^{13}CH_4$ isotope of atmospheric methane is discussed, since other isotopes of methane are not included in this work.

^{13}C-CH_4:

^{13}C-CH_4, the most measured isotope of atmospheric methane, which is generally expression of the ratio of ^{13}C to ^{12}C relative to a reference standard. Isotopic ratios are conventionally expressed as per mil deviations from a certain standard to emphasize the small changes due to source and sink processes. In this thesis, the most prominent isotope $^{13}CH_4$ formulated the definition of the carbon isotope signature as:

$$\delta^{13}C - CH_4 = \left[\frac{\left[\frac{^{13}CH_4}{^{12}CH_4}\right]_{Measured\ \ Ratio}}{\left[\frac{^{13}C}{^{12}C}\right]_{PDB}} - 1 \right] \times 1000$$

where $[^{13}C/^{12}C]_{PDB}$ = 0.0112372 is the Chicago PeeDee Belemnite (PDB) standard. The global average atmospheric $\delta^{13}C$ ranges from -47.3‰ to -46.2‰ (Stevens and Rust, 1982; Stevens, 1993; Quay et al., 1991, 1999; Tyler et al., 1999). Recently, Levin et al. (2012) found the atmospheric mean $\delta^{13}C{-}CH_4$ is close to -47‰ with less depleted values in the Southern Hemisphere and an inter-hemispheric difference of approximately 0.3‰ and has changed less than 0.05‰ since 1990.

The $^{13}CH_4$ ratios are used to differentiate between methane from bacterial sources such as agriculture and ruminant animals, which are ^{13}C-depleted relative to atmospheric methane, and the ^{13}C-enriched methane emitted from non-bacterial sources such as natural gas and biomass burning, which is generally 20–30 ‰ higher (Tyler, 1986; Tyler et al., 1987; Cicerone and Oremland, 1988; Quay et al., 1988; Stevens and Engelkemeir, 1988; Conny and Currie, 1996; and references therein). CH_4 formed at high temperatures (combustion) is enriched in the heavier isotope and CH_4 from biogenic origin is depleted, which means thermogenic emission of methane has a larger ratio of $^{13}C/^{12}C$ sample than that of methane produced biogenically. IPCC AR5 (2013) published emissions characterized by ranges in its isotopic composition in ^{13}C-CH_4 typically as –55 to –70‰ for biogenic, –25 to –45‰ for thermogenic, and –13 to –25‰ for pyrogenic. Different photosynthetic pathways in C3

and C4 plants lead to quite different organic carbon isotope signatures, so, when these are either burned or digested, the CH_4 released has different isotopic signatures. Pyrogenic emissions of methane are least depleted depending on the ratio of C3 to C4 plants with a range of isotopic signature as $\delta^{13}C\text{-}CH_4$ = -7 to -27 ‰ (Yamada et al., 2006). Isotopic signatures of different categoric sources as published in Dlugokencky et al. (2011) are: Wetlands have signatures between −70 and −60‰ at high northern latitudes and between −60 and −50‰ in tropical climates. Savannah grassland burning (C4) have $\delta^{13}C\text{-}CH_4$ of −20 to −15‰, whereas boreal forest burning releases CH_4 at −30 to −25‰. Similarly, ruminants digesting C4 plants give off CH_4 at −55 to −50‰, whereas those eating C3 plants give off −65 to −60‰ CH_4. The natural gas industry produces CH_4 of variable isotopic signature of -50 to -25‰ depending on the formation temperature of the gas reservoir (biogenic or thermogenic).

CHAPTER 3

Physical and Mathematical Concepts

In this chapter, the physical and mathematical concepts of inverse modeling are explained with its application on understanding the recent trends of global budget of atmospheric methane emissions.

Firstly, to understand the inverse problem, it is stated, discussed and its general solution is obtained based on the approach of Bayesian probability theory. Secondly, the uncertainties associated with the solution are derived and estimated. Thirdly, reduction of computational demands by implementation of Kalman smoothing technique with sequential stepping through observational data is discussed. Fourthly, discussion on incorporating isotopic measurements is done. Finally, interval constraints are enforced to ensure results which are physically sensible.

Most of the derivations in this chapter have been taken and modified from the published literatures such as Houweling et al. (1999), Kasibhatla et al. (2000), Mikaloff Fletcher et al. (2004a), Bruhwiler et al. (2005), Tang and Zhuang (2011), and Röger (2013).

3.1. Inverse Modeling

3.1.1. Inverse Problem and its Solution

Solving, by definition, a 'direct (or forward) problem' is to obtain information on the values of some measurable quantities using a theoretical relationship, when given some information on the values of the set of parameters. Whereas, when given some information

on the values of some measured quantities, using a theoretical relationship to obtain information on the values of the set of parameters, then it is solving an '**inverse problem**.' For a direct problem, the values of the parameters are 'data,' and the values of some observable quantities are 'unknowns.' For an inverse problem, the data are the results of some measurements, and the unknowns are the values of parameters. Inverse problem is an expanding branch of Mathematics that has found numerous applications. Inverse problem theory was essentially developed in geophysics, to deal with largely underdetermined problems such as to localize the earthquake centers (Tarantola and Valette, 1982a; Hein et al., 1997). The inverse modeling approach was first used in atmospheric science by Enting (1993) and Enting et al. (1993) to study atmospheric CO_2 cycle.

Tarantola and Valette (1982a) mentioned about the minimal constraints necessary for the formulation of an inverse problem as:

1. The formulation must be valid for linear as well as for strongly nonlinear problems.
2. The formulation must be valid for overdetermined as well as for underdetermined problems.
3. The formulation of the problem must be consistent with respect to a change of variables.
4. The formulation must be general enough to allow for general error distributions in the data (which may be not gaussian, asymmetric, multimodal, etc.).
5. The formulation must be general enough to allow for the formal incorporation of any a priori assumption (positivity constraints, smoothness, etc.).

6. The formulation must be general enough to incorporate theoretical errors in a natural way.

Two problems are called inverse to each other if the formulation of each of them requires full or partial knowledge of the other. Inverse problems deal with determining, for a given input-output system, an input that produces an observed output, or determining an input that produces a desired output (or comes as close to it as possible), often in the presence of noise.

Inverse Modeling Approach

Inverse modeling often called the top-down approach, plays an important role in quantifying the sources and sinks of various trace gases (Enting, 2002). It compares forward model simulations from atmospheric transport models using prior sources and sinks with the spatiotemporally discrete observations (Tang and Zhuang, 2011). The prior sources and sinks are optimized by minimizing a cost function defined by the distances between the forward model simulation and observations (Gurney et al., 2002; Tang and Zhuang, 2011). Like upscaling techniques, inverse modeling can be used to estimate sources. This method translates measurements of trace gas concentrations to constrain the sources by means of an atmospheric transport model. Generally, the number of available measurements is a limiting factor in this approach (Houweling et al., 1999). For such an inverse problem to have a single solution either the number of emission parameters to be estimated must be adjusted according to the available measurements, or different

constraints must be introduced (Houweling et al., 1999). It is often required that by introducing first guess or a priori information of the sources, the solution gets close to existing knowledge (Houweling et al., 1999). The inverse techniques involve comparing predictions from atmospheric transport models and measurements of atmospheric carbon abundances at observation sites distributed over the regions of interest. The spatial pattern of the observed and predicted differences is used to infer the spatial distribution of sources and sinks of trace gases by seeking a distribution of fluxes that in a least squares sense minimizes the difference between the model predictions and observations, as well as any prior information used to constrain the problem (Bruhwiler et al., 2005).

A consistent way of doing this is by adopting a so-called **Bayesian approach**, in which all parameters are expressed as statistical probability distributions. A solution in the form of a superposition of all statistical distributions involved can be computed, from which means and covariances can be derived.

Until now, several studies have quantified global-scale sources of different trace gases using inverse methods, such as CO_2 (Keeling et al. 1989b; Enting and Mansbridge, 1989; Tans et al., 1990a; Enting, 1993; Enting et al., 1993, 1995; Rayner et al., 1996; Law and Simmonds, 1996; Kaminski et al., 1999b; Gurney et al., 2002), CFCs (Brown, 1993; Hartley and Prinn, 1993; Plumb and Zheng, 1996; Mulquiney and Norton, 1998; Mulquiney et al., 1998), CO (Bergamaschi et al., 2000b; Kasibhatla et al., 2002), CH_4 (Brown, 1993, 1995; Hein and Heimann, 1994; Hein et al., 1997; Houweling et al., 1999; Mikaloff Fletcher et al., 2004a, b; Bergamaschi et al., 2005; Chen and Prinn, 2006;

Bousquet et al., 2006; Meirink et al., 2008b; Wecht et al., 2012; Rice et al., 2016). Some of the previous modeling studies on quantifying different atmospheric trace gases are discussed in section 1.3.1 of chapter 1 in this thesis and previous studies with inverse modeling approach to quantify atmospheric methane are also discussed in section 1.3.2 of Chapter 1 in this thesis. The present work is done implementing an inverse modeling technique and some improvements (discussed in section 1.3.3 of chapter 1 in this thesis), investigating the extent to which the global magnitude of the various methane sources can be constrained by prior emission information, atmospheric observations, and isotopic measurements. The mathematical methods adopted in this study for inverse modeling of atmospheric methane are being discussed in the following sections.

3.1.2. Inverse Modeling Technique used to quantify Atmospheric Methane

Inverse modeling is a formal approach for estimating the values of the variables driving the evolution of a system by taking measurements of the observable manifestations of that system and using our physical understanding to relate these observations to the driving variables. We call the variables that we wish to estimate the state variables, and assemble them into a state vector **x**. We similarly assemble the observations into an observation vector **y**. Our understanding of the relationship between **x** and **y** is described by a physical model **F**, called the forward model:

$$\mathbf{y} = \mathbf{F}(\mathbf{x}, \mathbf{p}) + \boldsymbol{\varepsilon} \tag{3.1}$$

where **p** is a parameter vector including all model variables that we do not seek to optimize (we call them model parameters), and **ε** is an error vector including contributions from errors in the observations, in the forward model, and in the model parameters. From inversion of equation (3.1), we can obtain x given y. In the presence of error ($\boldsymbol{\varepsilon} \neq 0$), the best that we can achieve is a statistical estimate. The optimal solution of **x** reflecting this ensemble of constraints is called a posteriori. The choice of state vector (i.e., which variables to include in **x** vs. in **p**) is up to us. It depends on what variables we wish to optimize, what information is contained in the observations, and what computational costs are associated with the inversion.

The inversion method adopted in the present study includes information on the observed atmospheric methane mixing ratios and isotope ratios at the monitoring sites in conjunction with a priori estimates on the spatial and temporal patterns of fluxes of individual methane sources globally and their uncertainties. The prior estimates are only used for the elements we wish to optimize i.e., the state vector, not for the observational data. The results of solving the inverse problem are a posteriori estimates of methane source magnitudes and their a posteriori uncertainties (Tarantola and Valette, 1982a, 1982b; Tarantola, 1987). The surface emissions and concentrations are related by a global atmospheric chemical transport model (CTM). Mathematically, CTM defines mapping (or function) between parameter space which is surface emission fluxes and data space which is concentration. The dimensions of these vector spaces depend on the number of fluxes needed to be

estimated '**n**' and the number of available observations '**m**'. For any given CTM, the inverse model problem can be represented as:

$$\boldsymbol{H}\mathbf{x} = \mathbf{y}_{\mathbf{obs}} - \mathbf{y}_{\mathbf{ref}} + \boldsymbol{\varepsilon} \qquad (3.2)$$

$$= \mathbf{y}_{\mathbf{diff}} + \boldsymbol{\varepsilon}$$

Equation (3.2) assumes that the spatial distributions of all sources are well known. Here, **x** is a **n**-element state vector which is to be estimated. $\mathbf{y}_{\mathbf{obs}}$ is the **m**-element observation vector used to constrain the inversion. $\mathbf{y}_{\mathbf{ref}}$ is the modeled mixing ratios at the times and locations of the observations which is obtained by a reference run of CTM using a priori emission estimates. The adjustments to the emissions specified in the reference run are interpreted as the scaling factors in **x**. For a set of a priori estimates, **x** contains the difference between estimated emissions and that prior estimates. $\mathbf{y}_{\mathbf{diff}}$ represents the difference between the observation vector and the modeled mixing ratio vector from the reference run. $\boldsymbol{\varepsilon}$ describes the model-data uncertainty vector in this estimation. This uncertainty may arise firstly from errors in $\mathbf{y}_{\mathbf{obs}}$ measurement including instrument calibration error, sampling errors, statistical errors, and secondly from not precisely simulating near-field influences on the observations as well as long-range transport errors referred to as model-data mismatch error produced by this simplified model with coarse spatial resolution. For example, model-data mismatch errors occur when the transport model calculates transport for grid boxes several hundred kilometers in extent for comparison to what is essentially a point measurement, and small-scale processes that dominate the observed signal are not likely to be represented well by the transport model

(Bruhwiler et al., 2005). The elements of **m** x **n** matrix of response functions **H** are calculated using the atmospheric transport model and quantify the response at each measurement site for each time due to emissions originating from each source region at each time. In a formal way, the impulse response or Green's function **H** is the Jacobian matrix which represents the first derivative of the modeled concentrations at the observational sites and dates with respect to the elements of **x** i.e., the coefficients of the source components.

Bayesian inverse formalism can be used for non-linear systems only if the equations are linearized (Tarantola, 1987) and an iterative procedure is employed. In case of chemical sinks of methane, the assumption of linear relation does not hold, since the loss rate of CH_4 is directly proportional to its atmospheric abundance. For OH sink, the loss rate of CH_4 is calculated as follows:

$$\frac{d}{dt}[CH_4] = k_{OH}[OH][CH_4] \tag{3.3}$$

where k_{OH}, the reaction rate constant between the hydroxyl radical and methane is a function of temperature. The methane loss rate depends on [OH] concentration and [CH_4] concentration, while in turn the dependance of [OH] concentration on methane flux made [CH_4] concentration to cause a nonlinear response to the fluxes at the observational sites. A non-linear feedback mechanism is set as the tropospheric methane oxidation influences OH mixing ratio. Similar non-linear relations are also associated with Chlorine and $O(^1D)$

sinks. When the sink strengths are to be estimated as well, then all these non-linear responses must be accounted for in the inversion. Since this work is limited to the estimation of the sources, we are not concerned about details regarding sink strengths. Bayesian inverse formalism can be applied to the non-linear systems if the equations are linearized (Tarantola, 1987) and an iterative procedure is employed (Bousquet et al., 2005). An iterative scheme is introduced by Bousquet et al. (2005) to incorporate this issue and can be referred for further use. In our setup, we assume a linear relation between methane flux and [CH_4] concentration, as the feedback of methane concentration on methane oxidation due to reaction with OH and other sinks is neglected, thus eliminating non-linearity.

The process of atmospheric inverse problem represented by equation (3.2) is severely hampered by a mathematical characteristic known as ill-conditioning. In the real world, loss of details in the information on emissions occur due to dissipative processes during atmospheric transport. The estimation process acting in the opposite direction to the real-world chain of causality, requires an amplification of small-scale details to counter-act this attenuation of information. However, this will also amplify errors in the observational process and errors in the transport model which can destabilize the inverse problem solution due to sensitivity of the estimates on these small errors. This loss of information can be quantified in terms of how rapid are the variations which makes the attenuation to become severe as the length-scale decreases. Bayesian estimation technique based on an independent a priori estimates of the emissions along with the optimal use of available information from measurements can stabilize the ill-conditioned inversion solution.

In the context of Bayesian estimation, the emission estimates should be as close as possible to the a priori information, while also leading to the closest possible agreement between modeled and measured concentrations which is the goal of any inversion. The classical Bayesian formalism performs optimization by minimizing a quadratic cost function between modeled and observed concentrations on one side and prior estimates and optimized estimates on other side, each term weighted by variance or covariance matrices.

According to Gaussian statistics, the probability density function (PDF), ***p***, of a vector, $\mathbf{y_{diff}}$, given state vector, **x**, is

$$p(\mathrm{y}_{\mathrm{diff}}|\mathrm{x}) = \frac{1}{\sqrt{2\pi\,|R|}} \exp\left(-\frac{1}{2}\left(H\mathrm{x}\text{-}\mathrm{y}_{\mathrm{diff}}\right)^{T} R^{-1}\left(H\mathrm{x}\text{-}\mathrm{y}_{\mathrm{diff}}\right)\right) \tag{3.4}$$

where, **R** is **m** x **m** error covariance matrix of observations corresponding to the difference vector $\mathbf{y_{diff}}$. Considering the expectation values $\langle \mathbf{y_{diff}} - \mathbf{Hx} \rangle = \langle \boldsymbol{\varepsilon} \rangle = 0$ so that, **R**, the error covariance matrix, is related to **ε** by

$$\begin{aligned} R &= \langle \left(\mathrm{y}_{\mathrm{diff}} - H\mathrm{x}\text{-}\,\langle \mathrm{y}_{\mathrm{diff}} - H\mathrm{x}\rangle\right)\left(\mathrm{y}_{\mathrm{diff}} - H\mathrm{x}\text{-}\,\langle \mathrm{y}_{\mathrm{diff}} - H\mathrm{x}\rangle\right)^{T} \rangle \\ &= \langle (\mathrm{y}_{\mathrm{diff}} - H\mathrm{x})(\mathrm{y}_{\mathrm{diff}} - H\mathrm{x})^{T} \rangle = \langle \varepsilon\varepsilon^{\mathrm{T}} \rangle \end{aligned} \tag{3.5}$$

It is commonly assumed that all measurements are uncorrelated. Likewise, with the assumption that **x** is normally distributed about the vector of a priori values, $\mathbf{x_{apr}}$, its prior Probability Density Function (PDF) is given by

$$p(\mathrm{x}) = \frac{1}{\sqrt{2\pi\,|Q|}} \exp\left(-\frac{1}{2} \left(\mathrm{x}\text{-}\mathrm{x}_{\mathrm{apr}}\right)^{T} Q^{-1} \left(\mathrm{x}\text{-}\mathrm{x}_{\mathrm{apr}}\right) \right) \tag{3.6}$$

where **Q** is **n** x **n** error covariance matrix of deviations of x from $\mathrm{x}_{\mathrm{apr}}$. **R** and **Q** are prescribed as diagonal matrices, the values of which specify the relative confidence in observations and information about set of prior fluxes.

It is important to note that the assumption $< (\mathbf{y_{diff}} - \mathbf{Hx}) > = 0$ and $< (\mathbf{x}\text{-}\mathbf{x_{apr}}) > = 0$ means there is no bias imposed by the model-data error or the a priori estimates. In either case, this assumption may not be strictly correct always.

According to Bayes theorem, the probability of state vector **x** given $\mathbf{y_{diff}}$ is given by

$$p(\mathrm{x}|\mathrm{y}_{\mathrm{diff}}) = \frac{p(\mathrm{y}_{\mathrm{diff}}|\mathrm{x})\,p(\mathrm{x})}{\int p(\mathrm{y}_{\mathrm{diff}}|\mathrm{x})\,p(\mathrm{x})\,d\mathrm{x}} \tag{3.7}$$

Equation (3.7) states that the probability of a vector **x** given the data $\mathbf{y_{diff}}$ equals the probability of $\mathbf{y_{diff}}$ given **x** times the prior probability of the state vector normalized by the total probability of the data for all sources.

If the probability density function describing a priori information is Gaussian, then the a posteriori density function will also be Gaussian (Tarantola and Valette, 1982).

Incorporating pdfs (3.4) and (3.6) in equation (3.7), the a posteriori density function is given by:

$$p(\mathrm{x}|\mathrm{y}_{\mathrm{diff}}) = \exp\left(-\frac{1}{2}\left[(H\mathrm{x}\text{-}\mathrm{y}_{\mathrm{diff}})^T R^{-1}(H\mathrm{x}\text{-}\mathrm{y}_{\mathrm{diff}}) + (\mathrm{x}\text{-}\mathrm{x}_{\mathrm{apr}})^T Q^{-1}(\mathrm{x}\text{-}\mathrm{x}_{\mathrm{apr}})\right]\right) \tag{3.8}$$

In case of large number of parameters, solving non-linear inverse problem depends on solving of forward problem a large enough number of times (Tarantola and Valette, 1982b). For forward problems with costlier solution where either the computation of probability density in the parameter space or calculation of mean values and covariances cannot be performed in a reasonable computer time, Tarantola and Valette (1982b) suggested to restrict the problem to the search of maximum likelihood point in the parameter space (the point at which the density of probability is maximum). This computation becomes easy to perform with use of classical methods for particular assumptions about the form of probability densities of experimental data and a priori assumptions on parameters, for example, with Gaussian assumptions, the search for the maximum likelihood point simply becomes a classical least squares problem (Tarantola and Valette, 1982b). By using step functions, the a posteriori probability density in the parameter space becomes constant

inside a given bounded domain, while by using linear programming techniques, the maximum point of this domain can be reached (Tarantola and Valette, 1982b). The a posteriori probability density functions have discontinuities in slope, algorithms searching for maximum likelihood point will oscillate around the point of slope discontinuity (Tarantola and Valette, 1982b).

To find the maximum likelihood point in the Gaussian distribution in the parameter space, the a posteriori probability density function $p(\mathrm{x}|\mathrm{y}_{\mathrm{diff}})$ can be maximized by minimizing the objective function J(x) which is defined as

$$J(\mathrm{x}) = \left(\mathrm{x}\text{-}\mathrm{x}_{\mathrm{apr}}\right)^{T} Q^{-1} \left(\mathrm{x}\text{-}\mathrm{x}_{\mathrm{apr}}\right) + \left(H\mathrm{x}\text{-}\mathrm{y}_{\mathrm{diff}}\right)^{T} R^{-1} \left(H\mathrm{x}\text{-}\mathrm{y}_{\mathrm{diff}}\right) \tag{3.9}$$

To get the optimal agreement of the model solution, inversion procedure needs to minimize the weighted sum of squared deviations. The mathematical solution of this minimization problem is given by Tarantola and Valette (1982b). As shown in equation (3.9), now, we will try to minimize the squared deviations of the emission estimates and the modeled concentrations from the a priori values and the observations in units of squared standard deviations. Therefore, the matrices Q and R act as weighting factors for the constraints imposed by the priors and the measurements.

J(x) can be minimized by equating its derivative with respect to x to zero:

$$\left.\frac{\partial J}{\partial \mathrm{x}}\right|_{\mathrm{x}'} = \left(\mathrm{x}'\text{-}\mathrm{x}_{\mathrm{apr}}\right)^{T} Q^{-1} + \left(H\mathrm{x}'\text{-}\mathrm{y}_{\mathrm{diff}}\right)^{T} R^{-1} H = 0 \tag{3.10}$$

where the x′ indicates the "a posteriori" state vector to be solved which is the aim of this inversion model.

From equation (3.10), solving by means of singular vector decomposition, x′ can be expressed as

$$\mathrm{x}' = \mathrm{x}_{\mathrm{apr}} + \left[H^{T} R^{-1} H + Q^{-1}\right]^{-1} H^{T} R^{-1} \left(\mathrm{y}_{\mathrm{diff}} - H\mathrm{x}_{\mathrm{apr}}\right) \tag{3.11}$$

or

$$\mathrm{x}' = \mathrm{x}_{\mathrm{apr}} + QH^{T}(QH^{T})^{-1}[H^{T}R^{-1}H + Q^{-1}]^{-1}H^{T}R^{-1}\left(\mathrm{y}_{\mathrm{diff}} - H\mathrm{x}_{\mathrm{apr}}\right)$$

or

$$\mathrm{x}' = \mathrm{x}_{\mathrm{apr}} + QH^{T}[H^{T}R^{-1}HQH^{T} + Q^{-1}QH^{T}]^{-1}H^{T}R^{-1}\left(\mathrm{y}_{\mathrm{diff}} - H\mathrm{x}_{\mathrm{apr}}\right)$$

or

$$\mathrm{x}' = \mathrm{x}_{\mathrm{apr}} + QH^{T}[H^{T}(R^{-1}HQH^{T} + I)]^{-1}H^{T}R^{-1}\left(\mathrm{y}_{\mathrm{diff}} - H\mathrm{x}_{\mathrm{apr}}\right)$$

or

$$\mathrm{x}' = \mathrm{x}_{\mathrm{apr}} + QH^{T}(R^{-1}HQH^{T} + I)^{-1}(H^{T})^{-1}H^{T}R^{-1}\left(\mathrm{y}_{\mathrm{diff}} - H\mathrm{x}_{\mathrm{apr}}\right)$$

or

$$x' = x_{apr} + QH^T(R^{-1}HQH^T + I)^{-1}R^{-1}(y_{diff} - Hx_{apr})$$

or

$$x' = x_{apr} + QH^T(RR^{-1}HQH^T + R)^{-1}(y_{diff} - Hx_{apr})$$

or

$$x' = x_{apr} + QH^T\left(R + HQH^T\right)^{-1}\left(y_{diff} - Hx_{apr}\right) \quad (3.12)$$

The optimal solution of the inverse problem (3.2) is given by equations (3.11) and (3.12).

Note that (3.12) requires the calculation of the inverse of a m × m matrix, while in (3.11) a n × n matrix needs to be inverted, where 'm' is the number of available observations and 'n' is the number of fluxes to be estimated. For example, if the number of fluxes to be estimated is significantly smaller than the number of observations, it is more computationally efficient to use the equation (3.11) even though $\mathbf{R}^{-1}$ and $\mathbf{Q}^{-1}$ must be calculated. **R** is generally assumed to be diagonal, and **Q** is relatively small in dimension if the number of source regions is not large. But in our inverse modeling algorithm, we have used equation (3.12), since the number of source regions in our study is large with a spatial resolution of $2^{o}\times2.5^{o}$ or 13104 surface grid cells, considering each cell as a source region, and the number of fluxes to be estimated (n) is larger compared to the number of

available observations (m), thus calculation of inverse of m × m matrix is more computationally efficient.

3.1.3. Uncertainties associated with the solution

It is essential to quantify the uncertainty associated with the state vector x'. The uncertainties associated with the model-data error and the a priori values are given by R and Q, respectively. Since the objective function is quadratic in x (Equation 3.9), the a posteriori probability density is also Gaussian and thus can be written as

$$p(\mathrm{x}) = \frac{1}{\sqrt{2\pi|Q'|}} \exp\left(-\frac{1}{2}(\mathrm{x}-\mathrm{x}')^T Q'^{-1}(\mathrm{x}-\mathrm{x}')\right) \tag{3.13}$$

with mean value of x' and posterior covariance Q'.

The corresponding objective function J(x) can be written as

$$J(\mathrm{x}) = \left(\mathrm{x}\text{-}\mathrm{x}'\right)^T Q'^{-1} \left(\mathrm{x}\text{-}\mathrm{x}'\right) \tag{3.14}$$

Taking the second derivative of (3.14) yields

$$\frac{\partial^2 J(\mathrm{x})}{\partial \mathrm{x}^2} = Q'^{-1} \tag{3.15}$$

Finally, we can see that all these calculations lead to the derived result of Q' which basically shows that the posterior covariance estimate can be found from the inverse of the Hessian of the objective function. Applying (3.15) to (3.9) gives

$$Q' = \left(H^T R^{-1} H + Q^{-1}\right)^{-1} \tag{3.16}$$

By rearranging,

$$Q' = Q - QH^T \left(R + HQH^T\right)^{-1} HQ \tag{3.17}$$

Here, we have again found two equivalent forms of the solution that require the inversion of a n × n or a m × m matrix, respectively. It is clear from equation (3.16) that the diagonal elements of Q′ (i.e., the squared standard deviations of the emission estimates), are always smaller than those of Q (i.e., the squared standard deviations of the priors), since elements of diagonal matrix Q have been weighted by uncertainties in observations i.e., by $(R+HQH^T)R^{-1}$. The prior uncertainties are reduced by the inversion using information from the observations. The amount of reduction of the uncertainties depends on the modeled chemistry and transport information represented by H, and on the uncertainties of priors and observations, Q and R.

3.2. Kalman Smoother Technique

3.2.1. Basic Principle

In this section, we discuss the development of the Fixed-Lag Kalman Smoother starting with basic consideration of Bayesian estimation.

Let us assume that *l* months of observations are available from *p* observation sites, and we want to estimate monthly emissions from *k* different sources, then equation (3.1) becomes

$$\begin{pmatrix} H_{l,l} & H_{l,l-1} & . & . & . & H_{l.1} \\ 0 & H_{l-1,l-1} & H_{l-1,l-2} & . & , & H_{l-1,1} \\ 0 & 0 & H_{l-2,l-2} & H_{l-2,l-3} & . & H_{l-2,1} \\ . & . & . & . & . & . \\ . & . & . & . & . & . \\ 0 & 0 & 0 & . & . & H_{1,1} \end{pmatrix} \begin{pmatrix} x_l \\ x_{l-1} \\ . \\ . \\ . \\ x_1 \end{pmatrix} = \begin{pmatrix} y_l^{diff} \\ y_{l-1}^{diff} \\ . \\ . \\ . \\ y_1^{diff} \end{pmatrix} \quad (3.18)$$

where we neglect ε.

Each element of the vectors and matrix is itself a vector or matrix. Each x_i is a vector of length *k*, each y_i^{diff} is a vector of length *p* and each $H_{i,j}$ is a matrix of dimension $p \times k$. The vectors x_l and y_l^{diff} refer to month '*l*'. The fact that emissions from a month do not impact concentrations before that month is reflected, as all elements of the matrix of response

functions below the diagonal are zero. The optimal solution of equation (3.18) could be obtained in one step by using equations (3.11) and (3.16) or alternatively (3.12) and (3.17).

This approach has been most employed to estimate carbon fluxes in several studies and is referred to as the **Bayesian synthesis inversion** (e.g., Enting et al., 1995; Hein et al., 1997; Houweling et al., 1999; Bergamaschi et al., 2005, 2007). For this method, a cost function is formulated with two terms; one involves the observations and other involves a prior estimate of the fluxes. Hence, the resulting flux estimates are constrained both by the observations and a prior guess of the solution. For the case of atmospheric inversions prior information is needed since the observational network is generally too sparse to allow estimation of fluxes on the scales of interest. More specifically, the problem tends to be underdetermined in regions where observations are sparse, and possibly overdetermined in regions where there are many observations, depending on the spatial scale of the fluxes to be estimated. However, Bayesian synthesis grows very computationally demanding since the size of the matrices in the estimation equation gets very large, and since the amount of computation involved in generating basis functions becomes prohibitive, even if an adjoint transport model is used (Bruhwiler et al., 2005). The size of the large matrix of basis functions in Eq. (3.18) grows rapidly as the number of observations and source regions increases. For example, 35 years of data from 105 sites and 10 source processes yield a total H matrix dimensioned 44100 by 4200, but when considering the model with spatial grid resolution of $2^{o} \times 2.5^{o}$ or 13104 surface grid cells, each grid cell becomes a source region, the same example will have a total H matrix dimensioned 44,100 by 5503680. Thus, as size of the matrices grows, the computational costs become expensive. Using an adjoint

model, the basis functions are calculated by transporting pulses forward from each source region or backwards in time from each observation site. The atmospheric inversion problem becomes more efficient by using a stepping technique that relies on the observational fact that these basis functions get well mixed throughout the troposphere until constant values are reached (Bruhwiler et al., 2005). At a particular time in the inversion process, the current measurements do not constrain the fluxes very well from sufficiently far past years, because the atmospheric mixing leads to smoothing out of the spatial gradients over time (Bruhwiler et al., 2005). This is caused by dissipative processes in the real world just similar as the ill-conditioning of the inverse problem, and lead to the continuous loss of information over time inherent to atmospheric mixing. This fact is clearly reflected in the response functions where most of the signal used to distinguish the sources from each other occurs within the first 12 months.

These computational demands can be reduced by filtering techniques using sequential stepping through observations while remembering only relevant parts of the matrices. In this study, the **fixed-lag Kalman smoother** is used for sequential estimation of the atmospheric methane fluxes. This technique is built upon the **Kalman Filter**, the optimal filtering technique originally developed by Kalman (1960) for estimating the state of a system given imperfect prior information and observations adapted by Bruhwiler et al. (2005) for estimation of atmospheric CO_2 fluxes. This technique relies on the fact that most of the information about the spatial distribution of sources and sinks is observable within a few months to half of a year of emission, after which the spatial structure of sources is diluted by transport and cannot significantly constrain flux estimates. Bruhwiler et al.

(2005) described this estimation technique that steps through the observations sequentially, using only the subset of observations and modeled transport fields that most strongly constrain the fluxes at a given time step. The time over which transport information is retained is the "**fixed-lag**". Estimates of each set of fluxes are sequentially updated multiple times, using measurements taken at different times, and the estimates and their uncertainties are shown to quickly converge. Final flux estimates are incorporated into the background state of trace gas and transported forward in time, and the final flux uncertainties and covariances are considered when estimating the covariances of the fluxes still being estimated. This technique is referred to as a **Kalman smoother** because it produces estimates of fluxes at a time using observations from that time step as well as observations from subsequent times (Bruhwiler et al., 2005). An approach based on the Kalman filter was first applied by Chen and Prinn (2006) in estimation of global methane emissions.

3.2.2. Time Stepping

At a given timestep j, only a subset of transport information is kept, and the equation (3.18) is effectively reduced to the form:

$$\begin{pmatrix} H_{j,j} & H_{j,j-1} & . & . & . & H_{j,j-q} \end{pmatrix} \begin{pmatrix} x_j \\ x_{j-1} \\ . \\ . \\ . \\ x_{j-q} \end{pmatrix} = \begin{pmatrix} y_j^{diff} \end{pmatrix} \tag{3.19}$$

where j denotes the current time step and q is the number of months of transport information kept at each time step, called as the fixed-lag. As seen in Eq. (3.19), the source vector at each time step x_j will be estimated q times, each time by a different set of observation data vector. The **H** matrix gives the response to pulses emitted a time step at each of the observation sites, where **H**j,j are pulses emitted from the most recent month, and **H**j,j-q are responses due to pulses emitted q months in the past. At each subsequent time step from j to j+1, a source vector is shifted downward, while the basis functions for each month are shifted to the right. A source vector and basis function matrix for a new month are added to the right-hand side of Eq. (3.19). Once a source vector has been estimated q times it is dropped from the part of the state still being estimated. The last element x_{j-q} exits out of the state vector and becomes fully optimized with best estimate x'_{j-q} , and a new element x_{j+1} is added at the top. The partly optimized estimates x'_j , x'_{j-1} , ..., x'_{j-q+1}, obtained by using equation (3.12), serve as new priors $x_{apr,j}$, $x_{apr,j-1}$, ..., $x_{apr,j-q+1}$ for the next time step. The prior for x_{j+1} can sensibly be chosen based on estimates from previous time steps, independent information, or a combination of both. The shifting of the elements of x is referred to as the state-space or forecast equation as used in the Kalman filter terminology and is formally represented by

$$\mathrm{x}_{\mathrm{apr}} = M\mathrm{x}' + \mathrm{n}_{\mathrm{j+1}} \tag{3.20}$$

where the matrix M makes the elements of x′ move down and for all sources' new priors for the month j+1 are contained in $\mathrm{n}_{\mathrm{j+1}}$ as explicitly mentioned below,

$$M = \begin{pmatrix} 0 & . & . & . & 0 \\ 1 & 0 & . & . & 0 \\ 0 & 1 & 0 & . & 0 \\ . & . & . & . & . \\ . & . & . & . & . \\ 0 & . & 0 & 1 & 0 \end{pmatrix} \quad \text{and} \quad \mathrm{n}_{\mathrm{j+1}} = \begin{pmatrix} x_{apr,\,j+1} \\ 0 \\ . \\ . \\ . \\ 0 \end{pmatrix}.$$

The covariance matrix is shifted by

$$Q = MQ'M^T + N_{j+1} \tag{3.21}$$

And then gets updated to equation (3.17). N_{j+1} contains the covariance matrix Q_{j+1} of $x_{apr,j+1}$ in the top left corner and is zero everywhere else.

The equations (3.12) and (3.17) are known as the state and the covariance update equations of the discrete Kalman filter. The Kalman gain matrix may be identified as

$$K = QH^T \left(R + HQH^T \right)^{-1} \tag{3.22}$$

The Kalman gain matrix functions as a weighting factor between the a priori values $\mathbf{x_{apr}}$ and their error covariance matrix $\boldsymbol{Q}$ on one side and new information from the observations contained in $\mathbf{y_{diff}}$ on the other. Let us consider the following illustrations:

$\mathbf{R \rightarrow 0}$: As the error covariance matrix of the measurements R becomes much smaller than the matrix HQH^{T}, i.e., R→0, then the Kalman gain matrix approaches its "maximum" value $K \rightarrow H^{-1}$ (the pseudo-inverse of H, since H is not a square matrix). In this limiting case, the state update equation (3.12) yields $\mathbf{x' \rightarrow H^{-1}\, y_{diff}}$ and the estimated state vector depends only on the difference vector and the response functions representing the chemistry and available transport information.

$\mathbf{R \rightarrow \infty}$: On the other hand, if the measurements are noisy with much larger model-data mismatch error and therefore associated with larger uncertainties, i.e., R>>Q then the Kalman gain matrix approaches its "minimum" value $K \rightarrow 0$. Consequently, $\mathbf{x' \rightarrow x_{apr}}$ and $\mathbf{Q' \rightarrow Q}$. The prior estimates are retained, and the observations are de-emphasized in the inversion not providing useful constraints on the fluxes being estimated.

The method described up to this point assumed that the inversion is done 'on-line' that means the transport model is run forward in time with prior flux estimates to produce predictions of CH_4 abundances which are then compared with observed CH_4 at each site, the final flux estimates are then incorporated into the background state of CH_4 using transport information in the form of basis functions and the transport model is run to the

next inversion time step. The fixed lag Kalman smoother can also be used 'off-line' without running the transport model that means the pre-calculated basis functions are used to reproduce transport fields over the entire time period and are used to propagate the optimized fluxes forward in time, thus updating the background state (Bruhwiler et al., 2005). In the next section, the method implemented in our study using off-line fixed lag Kalman smoother will be discussed based on the technique mentioned by Bruhwiler et al. (2005).

3.2.3. Propagation of Covariance

The Kalman smoother uses only a subset of the available observations to constrain fluxes, hence, it is reasonably expected to decrease computing cost only by generating larger uncertainties since each estimate is constrained by less data, than the Bayesian synthesis inversion, which constrains estimates by measurements from all subsequent times. But this was not always the same in the comparison study by Bruhwiler et al. (2005). It was noteworthy in Bruhwiler et al. (2005) study that the estimated uncertainty for the Kalman smoother was sometimes smaller than that for the Bayesian synthesis inversion, which was contradictory since Bayesian synthesis uses all the available data rather than a subset, it should have given the lowest uncertainties. In addition, they also found that the Kalman smoother uncertainty estimates were often lowest for cases where the basis functions had been transported for the least amount of time. Uncertainties estimated using only one month of transport were the most questionable, since these estimates falsely appeared to

be much less uncertain than the Bayesian estimates. They mentioned the fact that recent emissions produced the largest signals at measurement sites and the largest spatial gradients may have caused the generally acceptable small increases in estimated uncertainty provided that at least several months of transport are used. The length of time needed for the basis functions to be transported depends on two opposing factors: one is the time taken by the emission pulse from the source region to transport to the observation site that constrain the fluxes and other is the time taken for diffusion of pulses by atmospheric mixing that flattens the spatial gradient (Bruhwiler et al., 2005).

However, this case was modified by Bruhwiler et al. (2005) as demonstrated in an inversion of CO_2 fluxes. Bruhwiler et al. explained this unexpected behavior by the fact that the Kalman smoother does not consider the covariance between monthly fluxes that are no longer being estimated and those are still being estimated. Additionally, once a final estimate is made of a set of monthly fluxes, these fluxes are incorporated into the background state that is propagated forward in time by using the calculated transport fields (Bruhwiler et al., 2005). Kalman smoother treats fluxes that have been fully optimized as perfectly well-known quantities, neglecting their associated uncertainties. Bruhwiler et al. mentioned that as the time-dependent flux estimates tend to over and undershoot the solution at successive time steps, these temporal correlations may lead to a smaller total uncertainty aggregated over time, on the other hand, the incorporation of estimated fluxes into the background state without accounting for estimated uncertainty implies a certain level of uncertainty underestimation for subsequent time steps. Correlations between

online (not yet fully optimized) and offline (fully optimized) state variables are also ignored. Bruhwiler et al. (2005) required the propagation of these correlations forward in time and thus proposed a technique as the solution to correct these shortcomings. They found that with at least six months of basis functions used to recreate the background state, the difference in model predicted concentrations and estimated fluxes are considerably small, although, using Kalman smoother in off-line mode causes increased uncertainty, but also leads to great savings in computational costs. Thus, inverse problem can be solved off-line with a subset of basis functions without further use of transport model (Bruhwiler et al., 2005).

The offline variables are introduced to the reduced inverse problem, with equation (3.19) taking the form as;

$$\begin{pmatrix} H_u & H_v \end{pmatrix} \begin{pmatrix} \mathrm{x_u} \\ \mathrm{x_v} \end{pmatrix} = \mathrm{y_{diff}} \tag{3.23}$$

where the subscript ‘u’ refers to the part of the state vector still being estimated, and ‘v’ refers to the part of the state vector no longer being estimated. More specifically source vectors and response function vectors become as follows:

$$x_u = \begin{pmatrix} x_j \\ x_{j-1} \\ . \\ . \\ . \\ x_{j-q} \end{pmatrix}, \quad \mathrm{x_v} = \begin{pmatrix} x_{j-q-1} \\ x_{j-q-2} \\ . \\ . \\ . \\ x_{j-q-r} \end{pmatrix}$$

and

$$\mathrm{H_u} = \begin{pmatrix} H_{j,j} & H_{j,j-1} & . & . & . & H_{j,j-q} \end{pmatrix}, \quad \mathrm{H_v} = \begin{pmatrix} H_{j,j-q-1} & H_{j,j-q-2} & . & . & . & H_{j,j-q-r} \end{pmatrix}$$

where r is the number of months for propagating correlations, $\mathbf{H}_u$ is dimensioned the number of measurement sites, m, by the number of fluxes to be estimated, n. $\mathbf{H}_v$ is transport information from some number of time steps further back, for which estimates are no longer being made. It is dimensioned as m, by the number of months for which we intend to consider correlations times the number of source regions.

Now, the objective function is rewritten as;

$$J\left(\mathrm{x_u}, \mathrm{x_v}\right) = \left(\begin{pmatrix} \mathrm{x_u} \\ \mathrm{x_v} \end{pmatrix} - \begin{pmatrix} \mathrm{x_{apr,u}} \\ \mathrm{x_{apr,v}} \end{pmatrix} \right)^T \begin{pmatrix} Q_{uu} & Q_{uv} \\ Q_{vu} & Q_{vv} \end{pmatrix}^{-1} \left(\begin{pmatrix} \mathrm{x_u} \\ \mathrm{x_v} \end{pmatrix} - \begin{pmatrix} \mathrm{x_{apr,u}} \\ \mathrm{x_{apr,v}} \end{pmatrix} \right)$$
$$+ \left(\begin{pmatrix} H_u & H_v \end{pmatrix} \begin{pmatrix} \mathrm{x_u} \\ \mathrm{x_v} \end{pmatrix} - \mathrm{y_{diff}} \right)^T R^{-1} \left(\begin{pmatrix} H_u & H_v \end{pmatrix} \begin{pmatrix} \mathrm{x_u} \\ \mathrm{x_v} \end{pmatrix} - \mathrm{y_{diff}} \right) \tag{3.24}$$

where, $x_{apr,u}$ and $x_{apr,v}$ are defined in similar way as x_u and x_v. Q_{uu} and Q_{vv} are the covariance matrices of online and offline state variables, respectively and Q_{uv} and $Q_{vu} = Q_{uv}^T$ represent the covariances between the states still being estimated and those no longer being estimated. Now, introducing the matrices Q_{aa} , Q_{bb} , Q_{ab} , and Q_{ba} defined by

$$Q^{-1} = \begin{pmatrix} Q_{uu} & Q_{uv} \\ Q_{vu} & Q_{vv} \end{pmatrix}^{-1} = \begin{pmatrix} Q_{aa}^{-1} & Q_{ab}^{-1} \\ Q_{ba}^{-1} & Q_{bb}^{-1} \end{pmatrix} \tag{3.25}$$

Using a matrix partitioning identity, the following equivalent expressions can be found:

$$Q_{aa}^{-1} = \left(Q_{uu} - Q_{uv} Q_{vv}^{-1} Q_{vu} \right)^{-1} \tag{3.26}$$

$$Q_{ab}^{-1} = \left(Q_{ba}^{-1} \right)^T = -\left(Q_{uu} - Q_{uu} Q_{vv}^{-1} Q_{vu} \right)^{-1} Q_{uu} Q_{vv}^{-1} \tag{3.27}$$

$$Q_{bb}^{-1} = \left(Q_{vv} - Q_{vu} Q_{uu}^{-1} Q_{uv} \right)^{-1} \tag{3.28}$$

Taking the derivative of $J(x_u , x_v)$ with respect to x_u and setting it equal to zero gives

$$\left. \frac{\partial J(\mathrm{x_u}, \mathrm{x_v})}{\partial \mathrm{x_u}} \right|_{x_u^{/}} = \left(\mathrm{x_u^{/}} - \mathrm{x_{apr,u}} \right)^T Q_{aa}^{-1} + \left(\mathrm{x_v} - \mathrm{x_{apr,v}} \right)^T Q_{ba}^{-1} + \left(H_u \mathrm{x_u^{/}} + H_v \mathrm{x_v} - \mathrm{y_{diff}} \right)^T R^{-1} H_u = 0 \tag{3.29}$$

where, the prime term represents the updated a posteriori state vector, given that x_v is no longer being updated, we set $x_v = x_{apr,v}$ and the second term drops out.

The new state update equation is yielded by reorganizing equation (3.29) as:

$$\mathrm{x}_{\mathrm{u}}^{/} = \mathrm{x}_{\mathrm{apr,u}} + Q_{aa} H_u^T \left[R + H_u Q_{aa} H_u^T \right]^{-1} \left(\mathrm{y}_{\mathrm{diff}} - H_u \mathrm{x}_{\mathrm{apr,u}} - H_v \mathrm{x}_{\mathrm{v}} \right) \tag{3.30}$$

Equation (3.30) looks remarkably similar to the original Kalman filter update equation (3.12) with the exception that Q_{aa} replaces Q and $H_v x_v$ is subtracted from y_{diff}. Q_{aa} considers any correlations of x_v with states still to be estimated (x_u). As in equation (3.26), Q_{aa} is the correction to the covariance matrix of the states still being estimated (Q_{uu}). This correction takes the form of correlations between online and offline state variables and is normalized by the covariance matrix of the final estimates. The correction is small when the correlations are small and the uncertainty of x_v is large and it is large when the correlations are large and the uncertainty of x_v is small. Since the correlation between emission estimates is largest for successive time steps and is reduced quickly with the distance in time between the estimates, it is to be expected that the benefit of adding additional months, i.e., increasing the number of months for which we propagate correlations, decreases. It is possible to apply the correction for up to one less than the number of months of states which are still being estimated. However, Bruhwiler et al. found a significant impact on their results with only the first month of covariance propagation.

An expression for the covariance is found by calculating the inverse of the Hessian of the revised objective function by applying equation (3.15) to (3.24) leading to

$$\left(\frac{\partial^2 J(\mathrm{x})}{\partial \mathrm{x}^2}\right)^{-1} = \begin{pmatrix} H_u^T R^{-1} H_u + Q_{aa}^{-1} & H_u^T R^{-1} H_v + Q_{ab}^{-1} \\ H_v^T R^{-1} H_u + Q_{ba}^{-1} & H_v^T R^{-1} H_v + Q_{bb}^{-1} \end{pmatrix}^{-1} = \begin{pmatrix} Q'_{uu} & Q'_{uv} \\ Q'_{vu} & Q'_{vv} \end{pmatrix} \tag{3.31}$$

The top left term is the covariance of the part of the state that is still being estimated; the cross terms relate to the covariance of the part of the state that is no longer being estimated with the part of the state that is still being estimated. These are incorporated into the new expression for the covariance. However, we are only interested in Q'_{uu} i.e., a posteriori covariance matrix of states still being updated, using the same matrix partitioning identity as in equation (3.26), the following is obtained:

$$Q'_{uu} = \left[\left(H_u^T R^{-1} H_u + Q_{aa}^{-1}\right) - \left(H_u^T R^{-1} H_v + Q_{ab}^{-1}\right)\left(H_v^T R^{-1} H_v + Q_{bb}^{-1}\right)^{-1}\left(H_v^T R^{-1} H_u + Q_{ba}^{-1}\right)\right]^{-1} \tag{3.32}$$

As equation (3.32) is compared to equation (3.16), it is found that again Q_{aa} replaces Q and a new term describing the correlations between online and offline state variables is subtracted. Bruhwiler et al. (2005) have shown that the differences between including 1 month of correlations and not propagating the covariance is large but including additional months has generally a small effect. Although, uncertainties obtained from equation (3.32) are always higher than those calculated in a Bayesian synthesis inversion, in agreement with the expectation that estimates constrained by less information had larger associated uncertainties. Thus, using the revised state update equation (3.30) of the Kalman smoother

improved calculations for estimated fluxes significantly and had superior results compared to the original update equation (3.12) as described by Bruhwiler et al. (2005). Therefore, as recommended by Bruhwiler et al. that the Fixed-Lag Kalman Smoother should also include the covariance propagation scheme.

3.3. Isotope Data

As in the original formulation of the inverse problem, any row of equation (3.2) corresponding to a specific observation, can be written as

$$\sum_{i=1}^{n} H_{ij} x_i = y_j^{obs} - y_j^{ref} \tag{3.33}$$

where ε is neglected. In this section, it is to be noted that H_{ij}, x_i, y_j^{obs}, and y_j^{ref} are not matrices and vectors, but only single elements. Using the measurements of the isotopic composition of methane at the same location and time, equation (3.33) is rewritten in terms of isotopic concentrations such as

$$\sum_{i=1}^{n} H_{ij} R_i^{src} x_i = R_j^{obs} y_j^{obs} - R_j^{ref} y_j^{ref} \tag{3.34}$$

where y_j^{obs} and y_j^{ref} are CH_4 mixing ratios and R_j^{obs} and R_j^{ref} are the corresponding observed and modeled isotopic ratios (e.g., $^{13}CH_4/^{12}CH_4$). The characteristic isotopic ratio for each source process is denoted by R_i^{src}. To match records of isotopic signatures, equation (3.34) is divided by an arbitrary constant R_j^{const}, subtracted equation (3.33), multiplied by 1000 and then rearranged to yield

$$\sum_{i=1}^{n} H_{ij}\delta_i^{src}x_i = \delta_j^{obs}y_j^{obs} - \delta_j^{ref}y_j^{ref} \tag{3.35}$$

where δ_i^{src}, δ_j^{obs} , and δ_j^{ref} are defined by

$$\delta_j^{src} = \left(\frac{R_j^{src}}{R_j^{const}} - 1\right) \times 1000 \tag{3.36}$$

$$\delta_j^{obs} = \left(\frac{R_j^{obs}}{R_j^{const}} - 1\right) \times 1000 \tag{3.37}$$

$$\delta_j^{ref} = \left(\frac{R_j^{ref}}{R_j^{const}} - 1\right) \times 1000 \tag{3.38}$$

The definition of the delta notation is referred in Section 2.4. R_j^{const} is chosen to be equal to $[^{13}C/^{12}C]_{PDB}$ or $[^{2}H/^{1}H]_{VSMOW,}$ reported values of δ_j^{obs} and δ_i^{src} are directly inserted and thus, the obtained equations are added to the inversion. Since equation (3.35) only implies a linear relationship between the emissions and the product of the CH_4 concentrations with the isotopic signatures, therefore, an inversion based on equation (3.35) tries to compensate

for an underestimate of the concentration by an overestimate of the isotopic signature and vice versa. Thus, R_j^{const} the isotopic ratio calculated in the reference run serves as a better choice. Hence, we set $R_j^{const} = R_j^{ref}$, therefore, from equation (3.38), $\delta_j^{ref} = 0$ and the last term in equation (3.35) vanishes.

$$\sum_{i=1}^{n} H_{ij}\delta_i^{*src}x_i = \delta_j^{*obs}y_j^{obs} \tag{3.39}$$

where $\delta_i{*}^{src}$ and $\delta_j{*}^{obs}$ are isotopic signatures for each source process and observation defined in terms of the reference ratio at the sampling location. δ_j^{*obs} is a linear function of each x_i when equation (3.39) is divided by the constant y_j^{obs}. Thus, isotope observational data can be used in the form of equation (3.39) to constrain the inversion.

As an example, when we have measurements of the CH_4 mixing ratio (y_j^{obs}) and its isotopic signature $\delta^{13}C - CH_4$ (δ_j^{obs}, relative to $[^{13}C/^{12}C]_{PDB}$) for a specific time and location (identified by j), with estimates of the model-data error (ε_j^{y} and ε_j^{δ}) and the mixing ratio data has already been reflected in $\boldsymbol{H}$, $\boldsymbol{R}$ and $\mathbf{y_{diff}}$. Then, the isotope data can be used by following these steps:

1. The isotopic ratio R_j^{ref} at the measurement time and location is obtained from the CTM reference run.

2. δ_j^{obs} is converted to δ_j^{*obs} by using

$$\delta_j^{*obs} = \left(\delta_j^{obs} + 1000\right)\frac{\left[\frac{^{13}C}{^{12}C}\right]_{PDB}}{R_j^{ref}} - 1000$$

This conversion equation is obtained by solving (3.37) for R_j^{obs} and inserting it into itself using $R_j^{const} = [^{13}C/^{12}C]_{PDB}$ and $R_j^{const} = R_j^{ref}$, respectively.

3. $\delta_j^{*obs} y_j^{obs}$ is written into a new entry at the end of $\mathbf{y_{diff}}$.

4. All source signatures δ_i^{src} are converted to δ_i^{*src} by using

$$\delta_j^{*src} = \left(\delta_j^{src} + 1000\right)\frac{\left[\frac{^{13}C}{^{12}C}\right]_{PDB}}{R_j^{ref}} - 1000$$

This equation is retrieved from equation (3.36) in the same way as in step 2.

5. $H_{1j}\delta_1^{*src}$, $H_{2j}\delta_2^{*src}$, ..., $H_{nj}\delta_n^{*src}$ are written into a new row at the end of H.

6. The error $\varepsilon_j^{*\delta}$ on δ_j^{*obs} is found by using error propagation:

$$\varepsilon_j^{*\delta} = \varepsilon_j^{\delta} \frac{\left[\frac{^{13}C}{^{12}C}\right]_{PDB}}{R_j^{ref}}$$

7. The error $\varepsilon_j^{*\delta y}$ on $\delta_j^{*obs} y_j^{obs}$ is found by using

$$\varepsilon_j^{*\delta y} = \sqrt{\left(\delta_j^{*obs} \varepsilon_j^{y}\right)^2 + \left(y_j^{obs} \varepsilon_j^{*\delta}\right)^2}$$

8. The model-data covariance matrix **R** is extended by a row and a column. $(\varepsilon_j^{*\delta y})^2$ is written into the bottom right corner of the matrix. It is assumed that the isotope measurements are not correlated to any other observation.

Thus, we solve the inverse problem with larger matrices and vectors as described before after repeating steps 1-8 for every available isotopic measurement.

3.4. Interval Constraints

The inverse flux estimates are found to have unreasonable values due to the ill-posedness of the inverse problem. An exclusively known source process might turn into a sink with the estimates of the total source strength becoming negative. Sometimes, estimates for an aseasonal process might strongly fluctuate from month-to-month which should not be varying much. The estimates are made to lie within a certain range considered as feasible

to overcome the problem of such unphysical results. Since the Kalman Smoother only deals with linear operators, the method used here to impose interval constraint is based on the projection operator method described by Simon and Chia (2002) and Simon (2010) applied in an iterative two-step approach described by Tang and Zhuang (2011).

Inequality constraints are dealt as in the mathematical form

$$\mathbf{Dx} \leq \mathbf{d} \tag{3.40}$$

where x is the state vector, D is a known matrix and d is a known vector.

Choosing D and d in equation (3.40) as negative values incorporates inequalities of the form $Dx \geq d$. In the first step, x, and Q (subscript u is dropped in this section) are obtained for the unconstrained inverse problem. In the second step, it is checked whether x lies in the feasible region then no further action is required, and if x does not satisfy equation (3.40), then a solution is found by minimizing a cost function defined as

$$J(\mathrm{x}) = \left(\mathrm{x}\text{-}\mathrm{x}'\right)^T Q'^{-1} \left(\mathrm{x}\text{-}\mathrm{x}'\right) \tag{3.41}$$

with the condition that x satisfies (3.40). First, the elements of x that violate their respective constraints are identified and referred them as the active set. Then, D and d are reduced to only those rows representing the violated constraints. The unconstrained solution was

projected onto the surface of the feasible region where the violated inequality constraints become equality constraints, i.e.

$$D^*x = d^* \tag{3.42}$$

where D* and d* are the reduced versions of D and d, respectively. Equation (3.42) is of similar form as the inverse problem (3.2) without the error term, therefore the optimal estimates x and Q are found using the Kalman state and covariance update equations (3.12) and (3.17) which yields

$$x'' = x' + Q'D^{*T}(D^*Q'D^{*T})^{-1}(d^* - D^*x') \tag{3.43}$$

and

$$Q'' = Q' - Q'D^{*T}(D^*Q'D^{*T})^{-1}D^*Q' \tag{3.44}$$

Since the elements of x are being fixed that are in the active set on the surface of the feasible region, therefore, their posterior variance obtained in this way would be zero. To avoid this, noise is added to the inverse matrix in equation (3.44). Adding a covariance matrix to the inverse matrix as suggested in equation (3.17), equation (3.44) becomes

$$Q''= Q' - Q'D^{*T}(C + D^*Q'D^{*T})^{-1}D^*Q' \tag{3.45}$$

where C is a diagonal matrix containing the new posterior variances for the state variables violating their constraints after the first step. The elements of C are assigned rationally by truncating the original Gaussian probability density functions (pdf) of the variables in the active set at their boundaries and calculating the covariance of the part of the pdf that lies within that viable region. This is illustrated for a state variable x_i and considering probability density function of the unconstrained flux estimates with mean x'_i and two-sided truncated pdf with feasible region lying between a_i and b_i.

The covariance C_{ii} of the truncated pdf enclosed is given by the following equation (3.46) which has been derived by Johnson et al. (1994).

$$C_{ii} = \sigma'^{2}_{i}\left[1+\frac{\frac{a_i-x'_i}{\sigma'_i}\phi\left(\frac{a_i-x'_i}{\sigma'_i}\right)-\frac{b_i-x'_i}{\sigma'_i}\phi\left(\frac{b_i-x'_i}{\sigma'_i}\right)}{\Phi\left(\frac{b_i-x'_i}{\sigma'_i}\right)-\Phi\left(\frac{a_i-x'_i}{\sigma'_i}\right)}-\left(\frac{\phi\left(\frac{a_i-x'_i}{\sigma'_i}\right)-\phi\left(\frac{b_i-x'_i}{\sigma'_i}\right)}{\Phi\left(\frac{b_i-x'_i}{\sigma'_i}\right)-\Phi\left(\frac{a_i-x'_i}{\sigma'_i}\right)}\right)^2\right] \tag{3.46}$$

where the variables in the equation (3.46) are defined as

$$\sigma'_i = \sqrt{Q'_{ii}} \tag{3.47}$$

$$\phi(z) = \frac{1}{\sqrt{2\pi}}\exp\left(-\frac{1}{2}z^2\right) \tag{3.48}$$

$$\Phi(z) = \frac{1}{2} + \frac{1}{2} erf\left(\frac{z}{\sqrt{2}}\right) \tag{3.49}$$

$$erf(z) = \frac{2}{\sqrt{\pi}} \int_0^z \exp\left(-t^2\right) dt \tag{3.50}$$

From the above equations, the uncertainty of the estimate can be clearly seen to be reduced by the update, i.e., $C_{ii} < Q'_{ii}$. The pdfs of the state variables not included in the active set can also be truncated for an additional uncertainty reduction. However, this may not be needed since the Kalman filter assumes untruncated Gaussian pdfs. After updating the estimates with one iteration using equations (3.43) and (3.45) it is needed to be checked if all variables are within their feasible regions to accommodate the active set, otherwise, the above iteration is repeated until all constraints are satisfied.

CHAPTER 4

Methods

This chapter includes the methodology involved in the setup and the implementation of inverse modeling process in this study. The chapter is organized in the following sequence: in the beginning the working methodology flow diagram is presented, then each part of the flowchart is described in the sections followed. Sections 4.1 describes input data with methane emission sources in sub-section 4.1.1 and sink processes in 4.1.2, and section 4.1.3 discusses about the observations of methane mixing ratio and isotopic composition, also included the procedure of processing of raw measurement data and calculation of their uncertainties. Section 4.2 describes the Chemical Transport Model GEOS-Chem. Next, methods involved in inversion process are discussed in section 4.3 describing each of the structure of the computer programs developed and their implementation procedures to perform the inversion process and finally the overview of the sensitivity tests done is given in section 4.4.

Inversion Setup and Implementation

In this work the inverse modeling is performed to estimate the trends of methane budget over the last 35 years. Observed and interpolated methane mixing ratios from 106 sites and $\delta^{13}C\text{-}CH_4$ data from 21 sites are used to estimate the monthly source strengths of 10 source processes for the time of 1984-2015. Kalman smoother with a fixed lag of 11 months and covariance propagation of 1 month are also implemented in this study. The estimates of aseasonal source processes is further constrained to vary slowly in time so that all estimates are confirmed within a physically realistic range. The robustness of the results is determined by sensitivity tests done by varying network densities with availability of data

over the span of years. The steps involved in setup and implementation of the inverse modeling process are organized in the flow diagram as seen in Figure 4.1.

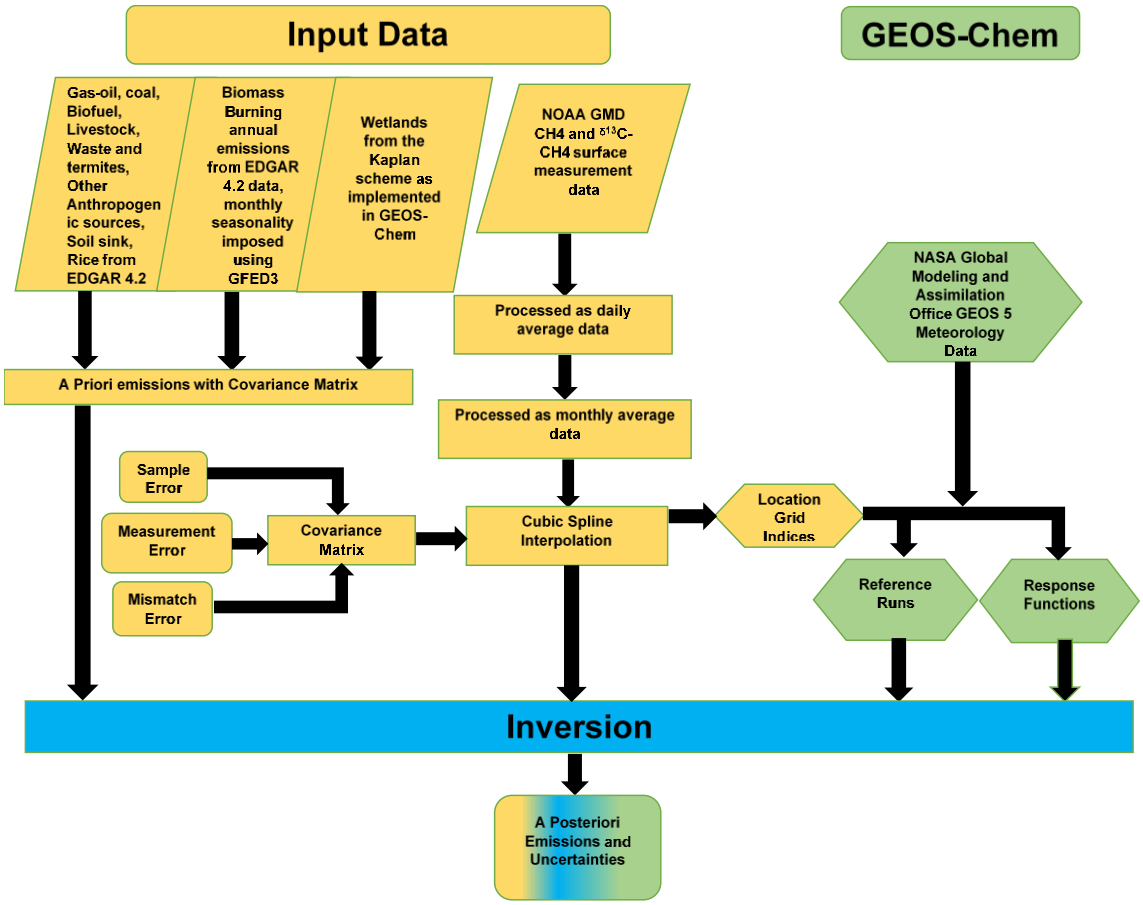

Figure 4.1: Working Methodology Flow Diagram

4.1. Input Data

4.1.1. Emission Sources

The flux fields in synthesis inversion are represented by a linear combination of a set of spatio-temporal patterns (Kaminski et al., 2001). In our work using Goddard Earth Observation System - Chemical Transport Model (GEOS-Chem) discussed in section 4.2, at every time step, the amount of methane emitted from each surface grid cell is constructed by the linear combination of all such patterns. As mentioned by Kaminski et al. (2001), the patterns may be contiguous regions because of the source processes (Rayner et al., 1999) or regions reflecting some underlying similarity such as the biome classifications (Enting et al., 1995) or patterns also may have some prescribed internal structure, reflecting external knowledge of fluxes e.g. Fan et al., 1998 used net primary productivity shape the terrestrial flux patterns or the patterns also contain temporal structure such as a prescribed seasonal cycle or monthly pulse. The solution of the inverse problem involves finding the coefficient multiplying each of the patterns (Kaminski et al., 2001) i.e., scaling factors, so that the resulting emissions match the observations. Each of these spacetime flux patterns are referred to as basis functions. The concentration arising from a given basis function subjected to atmospheric transport is referred to as the corresponding response function. Response functions are calculated by using a basis function as an input to an atmospheric transport model and by sampling the output of the transport model at chosen observation locations. The matrix of response functions for the full set of basis functions is represented by the Jacobian matrix for the problem and contains all necessary information about

atmospheric transport relevant to a particular setup. The structure chosen for the basis functions will determine the magnitudes returned by the inversion procedure. Atmospheric information about the sources alone cannot distinguish between net source and net sink, additional information is provided by choosing the pattern. Thus the a priori choice of basis functions plays an important role in inversion procedure. If there is any error within the internal structure of the patterns that cannot be resolved by the inversion, then that will cause bias in the estimates. The errors from wrongly shaped pattern structures causing difference in response functions in regions and inhomogeneous sampling causing bias in inversion of larger region towards strongly observed sub-region led to a type of error named as 'aggregation error' (Kaminski et. al., 2001).

Non-homogeneous sampling by the sparse network leads to biased emission estimates (Trampert and Snieder, 1996) and an approach to deal with this was described by Trampert and Snieder (1996) which required higher resolution model as they proposed an algorithm to compute for extra data error resulted from the uncertainty in the inhomogeneity of fluxes within resolved regions, by adjusting weights of the respective data. In this situation, the Bayesian approach is preferable as it solves fluxes separately for regions and prevents from an over-interpretation of the concentrations collected at sparse networks and stabilizes the inversion, mainly by decreasing the size of the regions or by defining the regions such that the uncertainty in the flux distribution over each region is minimal. Using an adjoint method, Kaminski et al. (1999a) have demonstrated the efficient calculation of a set of basis functions at the resolution of their transport model. The Jacobian matrix contained concentration responses to the surface fluxes at the measurement sites because of

atmospheric transport only. This matrix is efficiently computed using the adjoint version of the CTM since the number of measurement stations is small compared with the number of surface flux parameters (Kaminski et al., 1999a) with the atmospheric transport acted linearly on the concentration and the sources are assumed to be independent of the atmospheric methane mixing ratio. The adjoint of the GEOS-Chem model is constructed from a combination of manually and automatically derived discrete adjoint algorithms and numerical solutions to continuous adjoint equations (Henze et al., 2007). The adjoint model is used to calculate the gradient of cost function with respect to a set of model parameters and thus optimization of estimates is acquired by minimizing the cost function iteratively.

According to Kaminski et al. (2001), due to the lack of information about the true source shape, they used the shape of the a priori source to construct the patterns. Kaminski et al. (2001) have carried out a set of atmospheric transport inversions for CO_2 using the Jacobian matrix of a three-dimensional transport model to solve for the unknown magnitudes of low-resolution or high-resolution prescribed surface flux patterns, aggregating the fluxes over larger regions. By comparing the fluxes to the ones inferred by an inversion on the grid of the underlying transport model, they were able to quantify errors due to such aggregation. For computational reasons, however, for many potential inversion studies aggregations will be unavoidable. Kaminski et al. (2001) reduced the degree of aggregation by moving from low to high resolution regions which about halved the error and suggested using a resolution as high as computationally feasible. The use of a high-resolution inversion is expected to improve the uncertainty estimates and a posteriori estimates are expected to be more realistic. Röger (2013) and Rice et al. (2016) optimized methane fluxes over larger

regions and to minimize computational demands, they opted for a low-resolution ($4^0 \times 5^0$ horizontal grid resolution) inversion. However, in this work, a computationally feasible higher resolution ($2^0 \times 2.5^0$ horizontal grid resolution) inversion is opted to optimize the scaling factors for 10 source processes monthly. The higher resolution grid allowed us to extract more information from the observations due to the improved ability of the model to simulate CH_4 at each station and the decreased need to aggregate neighboring stations. This in turn increased the error reduction between the a priori and posterior emissions leading to more accurate estimates of the retrieved fluxes.

Atmospheric observations of $^{12}CH_4$ give information on only spatial distribution of total amount of CH_4 emitted from a geographical region, it is difficult to distinguish between different source processes represented by similar patterns and spatial overlap. Previous works such as Hein et al. (1997), Bergamaschi et al. (2000a), Miller et al. (2002), Mikaloff Fletcher (2004a, b), Rice et al. (2016), investigating the trends in atmospheric methane have generally used observations of stable carbon isotope ratios in atmospheric methane ($\delta^{13}CH_4$), in conjunction with methane observations, to provide additional constraints on the sources of methane. $\delta^{13}CH_4$ has been used to determine the sources governing atmospheric methane concentrations since it not only provides unique constraint to the underdetermined inverse problem, but also improves partitioning between flux estimates from different methane sources and sinks with similar spatial patterns but distinct isotopic signatures (Mikaloff Fletcher et al., 2004a). In this inversion study, the emission patterns are categorized based on their source processes instead of their geographical location

except for wetlands and $^{13}C/^{12}C$ isotopic ratios of atmospheric CH_4 from 21 measurement sites were used as additional constraint to the methane budget.

In this study, the spatially-gridded monthly-varying prior emissions fields are constructed from several sources. In this study, we have used similar emission fields obtained from the similar sources as in the work of Röger (2013) and Rice et al. (2016). For natural emission sources of methane including biomass burning emission, the GEOS-Chem base inventories have been used and for anthropogenic sources of methane, Emissions Database for Global Atmospheric Research release version 4.2. (EDGAR v. 4.2) provided annual emission maps from 1970 to 2008 for 16 sectors on a $0.1^{o} \times 0.1^{o}$ grid. Röger (2013) and Rice et al. (2016) reprocessed these maps and re-gridded them using 4^{o} x 5^{o} GEOS-Chem horizontal grids using an IDL routine provided by Kevin Wecht (former: Atmospheric Chemistry Modeling Group at Harvard University) and combined closely related sectors to form patterns for the inversion. Similarly, in this work those annual maps are re-gridded using 2^{0} x 2.5^{0} GEOS-Chem horizontal grids and same combined patterns are used for this inversion. Emissions of isotopic tracers $^{13}CH_4$ are obtained by multiplying the emissions by the characteristic isotope ratios of the underlying process. Overall, we represented emissions and optimization based on ten large-scale time-dependent spatial patterns, based on source category and region. The methane emission source patterns and sinks used in this work are also described in detail by Röger (2013) and Rice et al. (2016) and references therein. Here, a priori sources and sinks are briefly discussed as used by Röger (2013), Rice et al. (2016) and this current study and then the procedures followed in this study to process

the emission sources maps (including contributions by 2015 summer REU student late David Bryon Lofdahl of Eastern Oregon University) are discussed as follows:

Fossil Fuels: Emissions from fossil fuels are represented by two patterns. First one is the combination of EDGAR sectors 'Gas production and distribution' and 'Oil production and refineries', which is referred to as **'Gas and Oil'** in Röger (2013), Rice et al. (2016) and this work. The second pattern is the combination of emissions from coal mining found in the sector 'Fugitive from solid' with the other energy related sectors 'Energy manufacturing transformation', 'Industrial process and product use', 'Road transportation', 'Non-road transportation', and 'Fossil fuel fires'. This pattern is referred to as **'Coal'**. Spatial distributions of fossil fuel emissions remained almost constant throughout the whole year, thus, we used same monthly maps for all 12 months for any year. In this work, we converted each year's annual EDGAR $0.1^{o} \times 0.1^{o}$ ascii files containing gas and oil emissions data and coal emissions data into $2^{o} \times 2.5^{o}$ bpch files using IDL routine.

Rice: 'Agricultural soils' sector of EDGAR v. 4.2 provides the annual rice emission maps. Röger (2013) and Rice et al. (2016) accounted seasonal variations of rice in their model by considering average seasonal cycles of every grid cell from the data set provided by Matthews and Fung (1987) and by applying in the annual EDGAR emission maps. Likewise, we created the maps of monthly fractions of rice emissions in $2^{o} \times 2.5^{o}$ grid resolution by modifying the routine and splitting the obtained file into separate monthly files and converting the annual EDGAR $0.1^{o} \times 0.1^{0}$ ascii emission data into $2^{0} \times 2.5^{0}$ bpch

files of monthly rice emission data. Thus, a monthly varying pattern **'Rice'** is obtained since emissions mainly occur during growing season.

Wetlands: Methane released from wetlands strongly respond to the fluctuations in surface temperature and rainfall trends, thus, are calculated at every emission timestep. For interannual variations in wetland emissions, the sensitivity of emission rates to warming at high northern latitudes and to rainfall changes in the tropics need to be more consistently quantified in wetland models (Kirschke et al., 2013). Röger (2013) and Rice et al. (2016) applied a scheme in their wok based on Kaplan (2002) and described by Pickett-Heaps et al. (2011), for calculating wetland methane emissions E from every grid cell at every time step according to,

$$E = \delta W F \beta A \exp\left(\frac{-E_o}{T - T_o}\right)\left(\frac{C_S}{\tau_S} + \frac{C_L}{\tau_L}\right) \tag{4.1}$$

where, δ=1, if the presence of wetlands is indicated by GEOS-5 soil moisture and δ=0, if not. 'W' represents the maximum potential wetland fraction of the grid box by excluding lakes, oceans, and frozen areas. 'F' is a scaling factor to match estimates for tropical and boreal wetlands simultaneously. A = 1.0 exp (3), $\beta = 3 \times 10^{-2}$ mol CH_4/mol C, E_0 = 309K, T_0 = 227K are parameters specifying the dependence on the soil temperature 'T' and the amount of available respired carbon. The soil temperature is approximated by the GEOS-5 skin temperature. 'C_S' and 'C_L' are soil and litter carbon pools with residence times τ_S = 32 year and τ_L = 2.8 year, obtained from the Lund-Potsdam-Jena (LPJ) global vegetation

model. Like the work by Röger (2013) and Rice et al. (2016), we also sampled the monthly averaged wetland emission maps for all 6 years of available met-fields (January 2004 to January 2010) from GEOS-Chem run and reused them for entire time of inversion but at $2^{o} \times 2.5^{o}$ grid resolution, since the monthly time step of inversion required fixed patterns for every month. We splitted the $2^{0} \times 2.5^{0}$ files of monthly wetland emission into three geographical regions to reduce aggregation error and to include the isotopic measurements which may account the fact indicating that northern high latitude wetlands are isotopically lighter than tropical wetlands. The wetland distribution pattern is divided into three latitudinal bands as **'Wetlands 90N-30N'**, **'Wetlands 30N-0N'**, and **'Wetlands 0S-90S'**.

Biomass Burning: Röger (2013) and Rice et al. (2016) mentioned that the monthly maps of methane emission from biomass burning based on satellite observations of burned area from the Global Fire Emissions Database version 3 (GFED3) described by Giglio et al. (2010), are provided by GEOS-Chem since 1997 to 2008. The EDGAR sectors 'Large scale biomass burning', 'Residential', containing emissions from biofuels, and 'Agricultural waste burning' with the average monthly seasonality obtained from the GFED3 data were combined for earlier years in their studies. In our work, we used same data sources and same procedure to create $2^{0} \times 2.5^{0}$ grid resolution biomass burning emission maps. We converted EDGAR $0.1^{0} \times 0.1^{0}$ ascii data files of annual biomass burning emission maps into $2^{0} \times 2.5^{0}$ bpch files of annual biomass burning emission maps by modifying the IDL routines and similarly created C4 plant distribution map at $2^{0} \times 2.5^{0}$ resolution. We created the monthly averaged fractions of emission maps from GFED3 data

by running GEOS-Chem at $2^0 \times 2.5^0$ grid resolution from 1997 to 2008. We recompiled GEOS-Chem by recycling met data for years 1997 to 2003 since GEOS5 met data was available 2004 onwards and by making appropriate modifications to the source codes. We have modified another IDL routine to read the GEOS-Chem output emissions file and used it to split them into monthly emission maps of biomass burning. The isotopic signature of biomass burning emissions depends on whether vegetation burned had C3 or C4 carbon cycle, hence, the biomass burning pattern was split accordingly, using a vegetation map generated by Still et al. (2003), called the two resulting patterns as **'Biomass Burning C3'** and **'Biomass Burning C4'**, like the work by Röger (2013) and Rice et al. (2016).

Livestock: Röger (2013) and Rice et al. (2016) combined the EDGAR sectors 'Enteric Fermentation' and 'Manure Management' into a pattern named **'Livestock'** in their work. Likewise, in this study also, we used the same name for the pattern and created the $2^0 \times 2.5^0$ resolution annual livestock emission maps from EDGAR $0.1^0 \times 0.1^0$ ascii files of annual livestock emission maps.

Waste: In addition, the EDGAR sectors 'Solid waste disposal', including emissions from landfills, and 'Wastewater' are combined with natural emissions from termites (termites data set by Fung et al., 1991) to form a **'Waste and Termites'** pattern, sometimes referred to as **'Waste'** for short by Röger (2013) and Rice et al. (2016). We did the same likewise by converting the EDGAR $0.1^0 \times 0.1^0$ ascii files of annual waste emission maps into $2^0 \times$

2.5^0 resolution bpch files of annual waste emission maps. Both patterns are assumed as aseasonal with annual variations.

Biofuel: We converted annual EDGAR $0.1^o \times 0.1^o$ ascii files of biofuel emissions data into $2^o \times 2.5^o$ resolution bpch files of annual biofuel emissions by using IDL routine.

Other Anthropogenic: We converted annual EDGAR $0.1^0 \times 0.1^0$ ascii files of other anthropogenic emissions data into $2^0 \times 2.5^0$ resolution bpch files of annual other anthropogenic emissions by using IDL routine.

All the above major sources of methane are accounted in the process. Emissions from biofuel were later added to the biomass burning emissions category and other anthropogenic emissions were added to coal category and thus final ten patterns were formed for output.

In the inversion, a priori estimates include the global emissions from each of these patterns at every time step. The independence of inversion source fluxes was evaluated through source covariance by Rice et al. (2016). Results of their analysis indicate that correlations were weak for all paired sources ($|r|<0.15$), implying that inversion sources are largely independent. Strongest covariance occurred between the two biomass burning source categories (C3 and C4, $r= –0.14$) and northern and southern hemispheric tropical wetland emissions ($r= –0.12$), with all other correlations lower ($|r|<0.1$).

4.1.2. Sinks

Tropospheric OH Sink: One year of monthly varying 3-Dimensional OH fields used in the methane simulation is provided by the GEOS-Chem, generated in a full chemistry run of the model (Röger, 2013 and Rice et al., 2016). The photochemical sink of CH_4 is large and difficult to quantify, as the lifetime of OH is noticeably short (~1 sec). Direct measurements of atmospheric OH radicals do not have the required accuracy and coverage to derive global OH concentrations and consequently the magnitude of the CH_4 sink. The OH concentration as calculated by inversions based on measurements of tracers such as methyl chloroform with known emissions and whose dominant sink is oxidation by OH. Methyl Chloroform (1,1,1 trichloroethane, called CH_3CCl_3 hereafter) can be used to constrain OH, because its sources are relatively accurately known, and the hydroxyl radical reaction constitutes the most important sink. With full chemistry run of GEOS Chem, Röger (2013) and Rice et al. (2016) found that the tropospheric lifetimes of methyl chloroform and CH_4 are 5 years and 8.5 years, respectively which match well with recent estimates and the global mean OH concentration is 10.8×10^5 molec cm^{-3}, which is close to the value of 10.9×10^5 molec cm^{-3} as calculated by Prinn et al. (2005). Similarly, we have determined one year of monthly varying 3D tropospheric OH fields for our inversion from the GEOS-Chem full chemistry run with given known chemical reactions. CH_4 is oxidized by OH in the reaction as follows:

$$CH_4 + OH \rightarrow CH_3 + H_2O \qquad (4.2)$$

GEOS-Chem model calculated a CH_4 loss due to above reaction (Δ^{CH4}_{OH}) in every grid cell at every chemistry time step such as:

$$\Delta_{OH}^{CH_4} = -k_{OH}\left[CH_4\right]\left[OH\right]\Delta t \tag{4.3}$$

where, Δt = 30 minutes i.e., time duration of the chemistry time-step.

$k_{OH} = 2.45 \times 10^{-12} \exp(-1775/T)$ in units cm^3 $molec^{-1}$ s^{-1} [DeMore et al., 1997], i.e., the temperature dependent reaction rate constant calculated from GEOS-5 temperature T.

Similarly, GEOS-Chem calculated a loss for $^{13}CH_4$ using equation such as:

$$\Delta_{OH}^{^{13}CH_4} = -k_{OH}\left[^{13}CH_4\right]\left[OH\right]\Delta t \tag{4.4}$$

with the reaction rate constant as, $k_{OH} = k_{OH} / KIE_{OH}\left(^{13}C\right)$, where the kinetic isotope effect (KIE) is given by Cantrell et al. (1990) from laboratory measurements with a value of 1.0054. We have reused the same OH fields for every year of the simulations, as controversies remain in the literatures with the inter-annual variability of OH. To check the effect of interannual variability of OH, Röger (2013) and Rice et al. (2016) did a sensitivity test where they globally scaled OH fields and matched with annually varying mean OH concentrations derived by Prinn et al. (2005) with fixed mean OH concentrations for years

after 2003. They found increase in the interannual variability of emissions from wetlands in tropics with more negative trend and no significant impact on emissions from wetlands in northern high latitudes.

Stratospheric Sink: In addition to approximately 88% of total CH_4 loss by tropospheric OH (Mikaloff Fletcher et al., 2004a), CH_4 is also destroyed by OH, chlorine, and $O(^1D)$ in the stratosphere. Like the work by Röger (2013) and Rice et al. (2016), loss frequency fields derived from a full chemistry simulation of NASA's Global Modeling Initiative (GMI) Stratospheric Model (Schneider et al., 2000 and Wang JS et al., 2004) are used in our work to calculate stratospheric sink, which accounts for reactions of methane with OH, chlorine, and $O(^1D)$. The stratospheric loss ($\Delta^{CH4}{}_{Strat}$) is computed by using the equation as:

$$\Delta_{Strat}^{CH_4} = -\left[CH_4\right] LF \Delta t \tag{4.5}$$

where *LF* is the term of loss frequency in s^{-1}. For isotope equation, *LF* is replaced by LF/KIE_{Strat} where KIE_{Strat} is the kinetic isotope effect with a value of 1.0154 given by Rice et al. (2003).

Soil Sink: As mentioned by Röger (2013) and Rice et al. (2016), GEOS-Chem considers the soil absorption sink as a negative source and at every time step, the spatial distribution gridded by Fung et al. (1991) had been used. Similarly, we have used the same spatial

distribution in our work with $2^{o} \times 2.5^{o}$ resolution and the soil sink magnitude is varied monthly by scaling the sink strength from this distribution (18 Tg yr^{-1}) by the ratio of the monthly global surface CH_4 burden to January 1990, which was taken as the reference month of the distribution. Since the soil sink strength of 18 Tg yr^{-1} is low compared to recent estimates of ~30 Tg yr^{-1} (IPCC, 2013), so Röger (2013) and Rice et al. (2016) conducted a sensitivity test to determine the impact of a larger soil sink which resulted in no significant difference. The loss of the isotope tracer, $^{13}CH_4$ due to soil sink is calculated as follows:

$$\Delta_{Soil}^{^{13}CH_4} = \frac{\left[{}^{13}CH_4\right]}{\left[CH_4\right] KIE_{Soil}\left({}^{13}C\right)} \Delta_{Soil}^{CH_4} \tag{4.6}$$

where KIE_{Soil} is the kinetic isotope effect with a value of 1.0220 given by Tyler et al. (1994).

Marine Chlorine Sink: Marine Chlorine sink has not yet been included in GEOS-Chem model due to controversy remaining on the magnitude of the atomic chlorine sink in the marine boundary layer (MBL) (Mikaloff Fletcher et al., 2004; Röger, 2013; Rice et al., 2016). Röger (2013) and Rice et al. (2016) implemented a sensitivity test in their work for simple MBL chlorine sink following the parameter choices proposed by Allan et al. (2007) which reported the total strength of MBL Cl sink of about 25 Tg/year, but with smaller sink strength of 19 Tg/year, which might have caused from differences in definition of

open ocean grid cells between CTMs or by larger prescription of total source of 580 Tg/year by Allan et al. (2007). The test resulted in decrease in biomass burning emissions by 20 Tg/year and increase in isotopically lighter biogenic emissions by 40 Tg/year mainly from southern hemisphere wetlands, to balance the isotopic budget (Röger, 2013; Rice et al., 2016). In their sensitivity test, the total sink of 503 Tg/year exceeding the total prior source of 480 Tg/year, constituted a bias in their a priori estimation. Thus, with exclusion of MBL Cl sink from GEOS Chem model, similar to the work of Röger (2013) and Rice et al. (2016), in this inversion work also, all the emission patterns are scaled by a factor of 1.08 to obtain a better optimization of the estimates and improve the agreement between modeled and observed concentrations. This avoids the spoiling of inversion results from the bias which may have constituted in the priors without the MBL chlorine sink.

4.1.3. Observations

Methane Mixing Ratios

Atmospheric Methane Dry Air Mole Fractions are obtained from the National Oceanic and Atmospheric Administration, Earth System Research Laboratory (NOAA, ESRL) Global Monitoring Laboratory (GML) Carbon Cycle Cooperative Global Air Sampling Network, for 1983-2015. The Global Monitoring Division of NOAA's Earth System Research Laboratory has measured methane since 1983 at a globally distributed network of air sampling sites (Dlugokencky et al., 1994). Methane is reported as a "dry air mole fraction",

defined as the number of molecules of methane divided by the total number of molecules in the sample, after water vapor has been removed. The mole fraction is expressed as nmol mol^{-1}, abbreviated "ppb" for parts per billion; 1 ppb indicates that one out of every billion molecules in an air sample is CH_4.

NOAA released the updated measurements of the surface concentrations of methane from 110 locations including 24 records from moving ship sites over eastern Pacific Ocean and South China Sea and 13 ocean-transect measurements over western Pacific Ocean. A map of all these measurement sites is shown in Figure 4.2. There are two different surface flask data files for each site. One file contains the monthly averaged CH_4 measurements, while the other file labeled as "event" contains the original measurements. The monthly averaged data are smoothed, interpolated, and extrapolated and do not contain estimates of measurement uncertainties which are required for the Bayesian inversion. For these reasons we did not use the monthly averaged data.

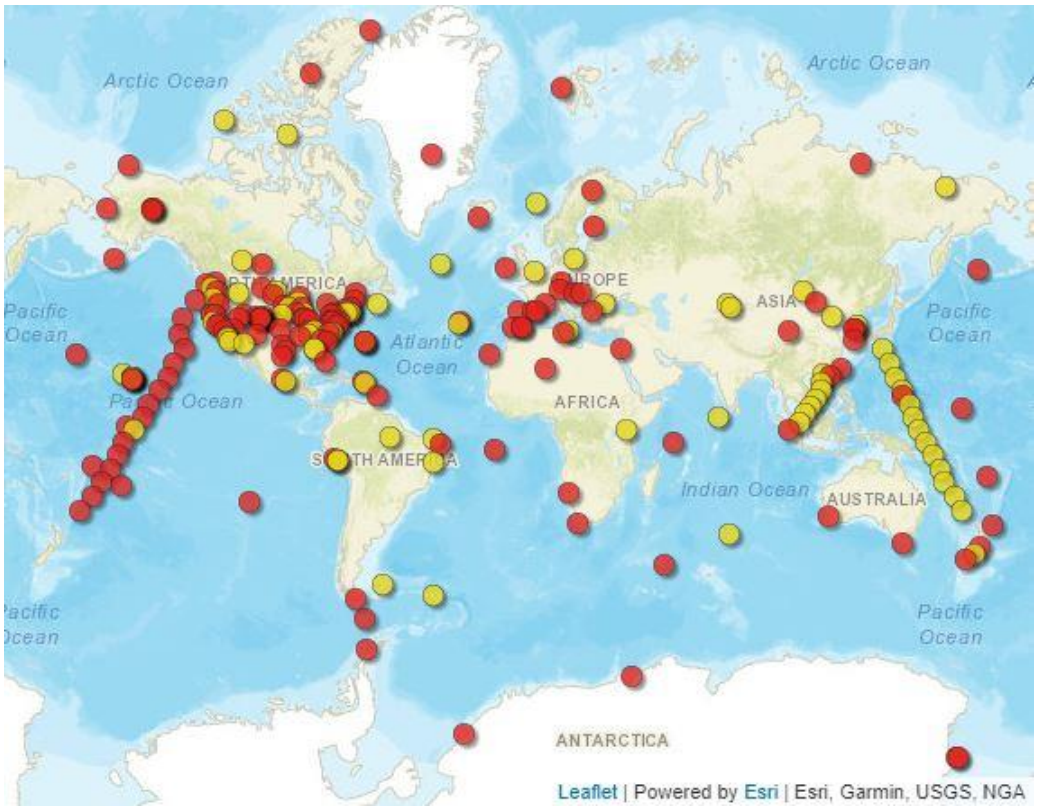

Figure 4.2: A map of atmospheric methane surface flask measurement sites as provided by NOAA ESRL GML. Red circles indicate active measurement sites and yellow circles indicate discontinued sites.

The event data files can be found in the following web page ftp://aftp.cmdl.noaa.gov/data/trace_gases/ch4/flask/surface/. The "event" files contain all measurements made at all sites. Measurements were made roughly weekly at each site. Beginning dates varied by site. There was unequal data coverage at many sites with no data at all for some sites. It is needed to fill in all missing data in the final data set by interpolating and extrapolating data. But for these months an exceedingly high uncertainty was assigned which effectively removed the data from the inversion.

For every measurement, NOAA collects two flasks of air. All samples were analyzed for methane at NOAA ESRL in Boulder, Colorado, by Gas Chromatography with Flame Ionization Detection (GC-FID). Prior to 1991 two samples from the same flask were analyzed by the GC-FID to determine the repeatability and instrumental uncertainties. From 1991 onwards, NOAA took one sample from each flask to determine instrumental uncertainties. Therefore, we see that for each day of data, there are two measurements provided. First it is needed to average these two daily measurements before calculating the monthly averages.

There are also some data that are flagged for various reasons. These data were filtered out and not used in the analysis. Flagged data are marked in the QC-Flag column of the data files where a three-character field indicates the results of NOAA's data selection and rejection process.

Calculation of Monthly-Average Mixing Ratios and Total Uncertainties Associated:

A better way to calculate the monthly-average mixing ratios and associated total uncertainties for each month throughout the observation period, requires knowing the daily measurements of mixing ratio (for one sample per day) or weighted average of daily measurements (for more than one sample per day) and uncertainties for each daily measurement to be used as weights. The equation for the weighted average assumes that each measurement is drawn from parent distributions with the same population mean. For

a specified month, the day to day measurements do not sample the same air mass due to random variations in the meteorology. So, even if there were no instrumental uncertainties, we still would not expect the measured mixing ratio to be constant throughout the month. This makes us think that each daily measurement as being drawn from a different population than on another day. However, if the total uncertainties related to the weekly measurements in each month are used as weights which include instrumental uncertainties from measurement error given in NOAA data files as well as other sources of uncertainties such as from calibration error, then the weighted monthly average mixing ratios can be calculated. Daily averaged mixing ratio were weighted using the uncertainties on individual measurements provided with each mixing ratio data considered as measurement errors which can be caused by imperfections in instrumentation, sampling or intercalibration. The daily observational uncertainty is given by,

$$\sigma_{daily} = \sigma_{measurement} \tag{4.6}$$

where, $\sigma_{measurement}$ is the uncertainty from individual measurement error which is provided in the NOAA event data files columned as analysis_uncertainty.

We assume that each daily measurement as being an estimator of the monthly average and these daily measurements are sampled from a normal distribution with mean equated to the monthly average and the statistical uncertainty equaled to standard deviation. Along with the monthly averages, it is needed to calculate the total observational uncertainties of the

monthly averages. The model-data uncertainties are calculated for every month and location which are needed to build the covariance matrix of the observations (called v and R in Chapter 3), which determines the relative weighting of the observations in the inversion. The total monthly observational uncertainty $\sigma_{total\_monthly}$ is given by,

$$\sigma_{total\_monthly} = \sqrt{\sigma_{sampling}^2 + \sigma_{statistical}^2 + \sigma_{mismatch}^2} \quad (4.7)$$

where, $\sigma_{sampling}$ is the uncertainty from the monthly sampling or standard error which represents the error in the monthly mean due to limited sampling frequency. It is calculated by,

$$\sigma_{sampling} = \frac{\sigma_{month}}{\sqrt{N}} \quad (4.8)$$

with N is the number of measurements per month that has been used to calculate the monthly mean and σ_{month} is the standard deviation of the measurements per month.

$\sigma_{mismatch}$ is the uncertainty from mismatch error that depends on the resolution of the model. As mentioned by Chen and Prinn (2006) and Rice et al. (2016), the mismatch error or the representation error describes the difference between an observation made at a single point in space and a model-simulated observation representing a large volume of air for an entire grid cell. The size of the mismatch error dictates the degree of the point measurement

failing to represent the volume of air in the entire grid cell. This difference depends on the resolution of the model, and the observational method and location. Most of the methane observing sites are chosen to be situated such as to sample large, well-mixed marine boundary layer air representing atmospheric methane background mixing ratio, which can be more accurately modeled (Chen and Prinn, 2006). Moreover, the mismatch error increases significantly due to local influences over continental sites near strong emitting regions compared to that near the remote ocean locations, which are not resolved at the model resolution (Chen and Prinn, 2006). The model systematically overestimates or underestimates the observed mole fractions and thus the mismatch error is difficult to quantify and may include bias error. Röger (2013) and Rice et al. (2016) calculated mismatch errors for all sites in their work based on the assumption of Chen and Prinn (2006) that the variability within a single grid cell is related to the variability among the surrounding grid cells and the mismatch error at each site can be estimated by using the standard deviation of the CH_4 mole fraction as follows:

$$\sigma_{mismatch} = \sqrt{\frac{1}{9}\sum_{i=1}^{9}\left(y_i - \bar{y}\right)^2} \tag{4.9}$$

where the y_i s are modeled methane concentrations in the 9 model grid cells contained and surrounded each observation site with mean $\bar{y}$, which were obtained from a GEOS-Chem run over the entire period of inversion. In this work also, the mismatch errors are calculated according to equation 4.9 with GEOS Chem run using $2^{o} \times 2.5^{o}$ grid resolution, where the

calculated mismatch error at each site varies monthly, consistent with seasonal changes in emissions and transport, and is usually largest near emitting grid cells.

The monthly total observational errors or uncertainties of the observational data have formed the diagonal elements of initial covariance matrix used in the inversion process.

I wrote a program named 'monthly_avg_CH42016_SK.pro' which processes the raw NOAA observation data to a form taking uncertainties into account which is input to the inversion. Thus, the steps involved in processing the observational data for calculating the daily-averaged and consecutively monthly-averaged methane mixing ratios and associated total uncertainties and consequently creating concentration data-set to be used in the inversion are summarized as follows:

1. All the flagged data were filtered out.
2. The estimated uncertainties associated with daily measurements σ_{daily} were provided in the analysis_uncertainty column of the data files which were used as weights *w* for the daily measurements. If there were two good daily measurements of CH_4 mixing ratios x_i, then weighted daily average of mixing ratios $\overline{x}_{daily}$ with *i* varies from *1* to *n*, where *n* is the number of measurements per day, were calculated as below:

$$\overline{x}_{daily} = \frac{\sum_{i=1}^{n} x_i w_i}{\sum_{i=1}^{n} w_i} \tag{4.10}$$

where the weight is given by,

$$w_i = \frac{1}{\sigma^2_{daily_i}} \tag{4.11}$$

The uncertainties of weighted daily averages were also calculated shown as:

$$\sigma_{\overline{x}_{daily}} = \frac{1}{\sqrt{\sum_{i=1}^{n} w_i}} \tag{4.12}$$

3. The weighted monthly-averaged CH_4 mixing ratios $\overline{x}_{month}$ were calculated using the weighted daily-averaged mixing ratios $\overline{x}_{daily,j}$ with *j* varies from *1* to *N*, where *N* is the number of measurements per month, such as follows:

$$\overline{x}_{month} = \frac{\sum_{j=1}^{N} \overline{x}_{daily,j} W_j}{\sum_{j=1}^{N} W_j} \tag{4.13}$$

where the weight is given by,

$$W_j = \frac{1}{\sigma_{\overline{x}_{daily}}{}^2_j} \tag{4.14}$$

4. The uncertainties of weighted monthly averages $\sigma_{\overline{x}_{month}}$ were calculated as below which represented $\sigma_{statistical}$ for each month in calculation of the total monthly observational uncertainty.

$$\sigma_{statistical} = \sigma_{\overline{x}_{month}} = \frac{1}{\sqrt{\Sigma_{j=1}^{N} W_j}} \quad (4.15)$$

5. The standard deviations of weighted daily averages for each month represented as σ_{month} were calculated which gave the $\sigma_{sampling}$ using equation 4.8, varying monthly. For the months having less than three daily averages, standard deviation could not be calculated and average annual standard deviations of daily average mixing ratios for that year were used instead.

6. There were some missing months with no available measurements. In the time domain, we performed cubic spline with the data set and interpolated values were fit to all records. But exceedingly high uncertainty values were assigned to indicate those as interpolated average and thus, contributed little information to the inversion.

7. The mismatch errors $\sigma_{mismatch}$ were calculated for $2^0 \times 2.5^0$ GEOS-Chem grid resolution and compared to those calculated for $4^0 \times 5^0$ grid resolution. The $2^0 \times 2.5^0$ resolution mismatch errors have smaller values on average than those of $4^0 \times$

5^0 resolution, which provided proof of more information been pertained on the monthly averages.

8. Then finally, the total monthly observational uncertainty $\sigma_{total\_monthly}$ was calculated as described above using equation 4.7 considering all the errors.

9. Further processing of the data was necessary to map the observational sites onto the $2^o \times 2.5^o$ GEOS-Chem grids. The sites that lie in the same grid cell, or those that are at elevation in the same grid cell as a surface site, were consolidated. If there were more than one observational site in a grid cell, then the corresponding measurement records were averaged. In addition, if multiple measurements were found at different varying altitudes but laid at the same latitude and longitude, all records were discarded except for the one closest to the surface, to avoid redundancy since data sampled from locations that are situated only at different elevations do not provide much additional information on the source configuration.

10. The available NOAA data was preceded by incorporating measurement data from 1980 to 1983 available from Oregon Graduate Institute (OGI) provided by Dr. Aslam Khalil and Dr. Christopher Butenhoff, described in Khalil et al. (2007) and thus extended the time span of the inversion to earlier years. This data set refers to some of the earliest continuous measurements of atmospheric methane which contains monthly mean concentrations from 7 locations situated between 70N to

90S. However, this small data set was used as part of a spin-up inversion to derive CH_4 concentration field for the first time-step of the main inversion but was excluded from main inversion because small number of sites do not provide good constraints on the fluxes.

Finally, the atmospheric methane concentration data set was created and was made ready for input to the inversion process.

Isotopic Composition of Atmospheric Methane

The atmospheric methane isotope data from specific locations can be incorporated into the inversion only if respective methane mixing ratio from those same locations are available. The measurements of the stable isotopic composition (^{13}C) of atmospheric methane were obtained from the NOAA GML Carbon Cycle Cooperative Global Air Sampling Network. The isotopic analysis was performed at the Stable Isotope Laboratory, CU-INSTAAR, using samples of air provided by the NOAA CMDL Carbon Cycle Cooperative Global Air Sampling Network. This release contained data for flask samples beginning in 1998 and extending through the end of 2015. Data were given for all sites where at least 18 months of data are available through the end of 2015. The subdirectory 'event' contained all measurements from flask samples collected at each site except for Montana de Oro, California. Monthly values are given only in those months where there are data, and no interpolation was made for missing months. The missing records of monthly mean

concentrations and sampling frequency errors based on measurements as described by Tyler et al. (2007) were provided by Professor Andrew Rice.

In the NOAA event files, isotope data are reported as 'delta' values: the ratio of minor to major isotopes relative to a standard, VPDB-CO_2. The 'delta' notation is represented as,

$$\text{delta} = [\ (^{13}C/^{12}C)\text{sample} / (^{13}C/^{12}C)\text{reference} - 1\ ] \times 1000 \qquad (4.16)$$

and is expressed in units of 'permil' (parts per thousand).

All the samples had been analyzed at the Stable Isotope Laboratory at CU-INSTAAR in Boulder, Colorado, using either a Micromass Optima or Micromass Isoprime isotope-ratio mass spectrometer coupled to methane custom-built trapping system, a gas chromatograph, and a combustion furnace. Measurement precision was approximately 0.1 permil for 13C (where 'precision' was taken as the standard deviation of three repeated measurements of standard air). The isotopic scale for $\delta^{13}C$ of CH_4 was tied to Stan Tyler's lab at the University of California Irvine.

Merging isotope data from different laboratories are necessary to improve spatial and temporal data representation for model inversion over the past three decades. Measuring stable isotopes in methane with high degree of precision is difficult and only performed by a few laboratories worldwide (Levin et al., 2012). Interlaboratory comparisons crucial for quality control, become particularly challenging with periods of sample analysis not

overlapping (Levin et al., 2012; Monteil et al., 2011). At Portland State University, Dr. Doaa Teama and Dr. Andrew Rice measured the carbon and hydrogen isotopic composition of methane from archived air sampled at Cape Meares, Oregon from 1978 to 1999 on a roughly monthly basis, by using a continuous flow isotope ratio mass spectrometer (Teama, 2013). These measurements are one of the longest continuous records of isotopic composition of methane with high temporal resolution dating back further than any available data set (Röger, 2013).

Much information might not be gained from including hydrogen isotope data in the inversion process with sparsely available δD-CH_4 measurements and wide range estimates of the source signatures found in other literatures (Röger, 2013). In this work, we did not include the δD-CH_4 data and limited our isotopic dataset to $\delta^{13}C$ of CH_4.

In this work, the records are obtained from 3 separate sources such as the NOAA ESRL database based on measurements by White et al. (2015) at the Stable Isotope Laboratory at the Institute of Arctic and Alpine Research (SIL INSTAAR), NOAA GMD Carbon Cycle Cooperative Global Air Sampling Network 'event' data files and Cape Meares data set and measurements by Tyler et al. (2007) and Quay et al. (1999) provided by Dr. Andrew Rice. $^{13}CH_4$ was introduced to the model as an independent tracer with source signatures drawn from previous work by Röger (2013) and Rice et al. (2016). The NOAA ESRL $\delta^{13}C$-CH_4 dataset contained individual measurements with corresponding monthly means for 17 sites from 1998 to 2011, 4 records were excluded as those started after 2007, as mentioned by Röger (2013) in the inversion work done with $4^{o} \times 5^{o}$ grid resolution. We included the

NOAA raw data from 'event' files in this work and Dr. Rice provided the records of monthly means and sampling frequency errors for the Cape Meares data set which contained 4 additional sites and extended back 5 of the NOAA records to earlier years (South Pole; Tutuila, American Samoa; Mauna Loa, HI; Cape Grim, Tasmania; Point Barrow, AK). Additional $\delta^{13}C$ measurements by Quay et al. (1999) at Cheeka Peak, WA, and Baring Head, New Zealand, and by Tyler et al. (2007) at Niwot Ridge, CO, and Montaña de Oro, CA, were also added. We avoided introducing artificial trends as the measurements are brought to same scale since the standards used to calibrate the measurements differ among laboratories. Dr. Rice compared overlapping segments of the records and did not find any statistically significant offset between data sets (Röger, 2013). There are total of 21 measurement sites with records of $\delta^{13}C\text{-}CH_4$ used in this inversion work. The total uncertainties for all available records were calculated using equation (4.6), with mismatch error using equation (4.8) where y_i s are model calculated $\delta^{13}C\text{-}CH_4$ signatures and $\bar{y}$ s are corresponding means. The measurement error was taken as 0.08‰ as mentioned in supplemental information provided in the NOAA data without any correlation.

The isotope data were processed as follows:

1. The program 'new_datafile.pro' was used to create 'gvmm.save' file which holds the $^{13}C/^{12}C$ model mismatch errors.

2. The program ‘prepare_dC13.pro’ was used to create ‘noaa.save’ file which holds the NOAA-SIL dC13 data.

3. The program ‘prepare_drew.pro’ was used to create ‘drew.save’ file which contains the OGI/Quay dC13 data.

4. ‘Concentration_data.txt’ file contains CH_4 mixing ratio data and new isotope data from NOAA event files.

5. All of the above files were then used as input to the program ‘Isotopes.pro’ which was then compiled and ran at $2^{0} \times 2.5^{0}$ grid resolution. Thus, created the output file named as ‘Isotope_data.txt’ which contains the monthly averaged total $^{13}CH_4$ data for 21 sites present in 2x25/ data/ observations directory.

Isotopic methane was included in this study as an independent tracer to constrain the inversion modeled source estimates to better distinguish between underlying processes. The isotopic $\delta^{13}C\text{-}CH_4$ ratios of different source categories drawn from previous works are shown in table 4.1. The emission estimates are multiplied with corresponding characteristic isotopic ratios of source categories to get isotopic emission estimates from respective source categories.

Table 4.1: Isotopic fractionation signatures of different source categories drawn from previous studies.

Source Process	$\delta^{13}C\text{-}CH_4$ ‰
Fossil Fuel	
Gas & Oil	-44.0[1]
Coal	-37.3[1]
Livestock	-62.0[2]
Waste and Termite	-55.3[1]
Rice	-63.0[1]
Biomass Burning	
C3 Vegetation	-26.5[3]
C4 Vegetation	-7.4[3]
Wetlands	
90N-30N	-63.4[4]
30N-0	-58.0[1]
0-90S	-58.0[1]
Total	

[1]Whiticar (1993); [2]Levin (1994); [3]Yamada et al. (2006); [4]Umezawa et al. (2011)

4.2. GEOS-Chem

Goddard Earth Observation System - Chemical Transport Model (GEOS-Chem) is a global 3-dimensional offline Chemical Transport Model (CTM) of atmospheric composition which originated in the atmospheric chemistry group at Harvard University. Bey et al. (2001) developed this second generation model by grafting Wang et al. (1998a) modules of photochemistry, emissions, and deposition onto the original GEOS CTM developed by Allen et al. (1996a, 1996b) and Lin and Rood (1996). Further, it is developed and used

by research groups worldwide as a versatile tool for application to a wide range of atmospheric composition problems. It utilizes assimilated meteorological observations solving for equations of continuity for a species of interest instead of solving all the primitive equations for the atmosphere. The model is driven by input meteorological data assimilated by the Goddard Earth Observing System (GEOS) at the NASA Global Modeling and Assimilation Office (GMAO) (Bey et al., 2001) which includes fields such as winds, surface pressures, temperatures, specific humidities, wet convective mass fluxes and detrainment rates, column cloud fractions, cloud optical depths, precipitation, surface albedos, roughness heights, friction velocities, and mixing depths, updated every 6 hours or 3 hours with either instantaneous or averaged values. This study uses the GEOS-Chem (Bey et al., 2001) as the atmospheric transport model for CH_4 transport simulations. The GEOS-Chem model version v9-01-02 (http://acmg.seas.harvard.edu/geos/doc/archive/man.v9-02/index.html) has been employed in the work presented here for simulating transport of CH_4. An evolution of different versions of GEOS assimilated meteorology data from GEOS-1 to most recent GEOS-FP are used in GEOS-Chem simulations. In this study, GMAO data product GEOS-5 is used in GEOS-Chem simulations which contains meteorological variables for years 2004 - 2010. For earlier and later years, the available 6 years meteorology data are recycled. A sensitivity test performed by Röger (2013) showed no significant impact on inversion results by recycling the meteorology data for one year repeatedly.

A CTM numerically solves the continuity equations for mass conservation of chemicals in the atmosphere to compute the concentration of some chemical species of interest referred

to as tracers and their variability in space and time, using meteorological information as input. Generally, CTMs are of two forms – Eulerian CTM with air parcel in fixed frame of reference and Lagrangian CTM with air parcel in moving frame of reference. An Eulerian CTM, GEOS Chem simulates the concentration of tracers in an array of fixed computational cells. It divides the atmosphere into latitude-longitude horizontal grid boxes extended in vertical direction and solves continuity equations for each box separately involving fluxes, chemical production/loss and deposition occur over time using a global/fixed frame of reference. The horizontal grid resolutions and the vertical sigma (σ) levels of a model are represented by the total number of grid boxes. The work done by Röger (2013), and Rice et al. (2016) used relatively coarser grid of 4^0 latitude by 5^0 longitude to reduce the computational demands. In this current work, we increased the horizontal resolution of the simulation to 2^0 latitude by 2.5^0 longitude increasing computational demands and accuracy. The vertical dimension is divided into 47 hybrid σ-levels spanning 80km vertically that extends from 1000 hPa at surface level to 0.01 hPa at top level. In this computation, the total number of grid cells involved are 91 x 144 x 47 = 615888.

The GEOS-Chem accurately represents the fluxes (e.g. advection), chemical production/loss, and deposition of every tracer caused due to emissions, transport and chemical sinks in each grid box. Advective is computed every 15 minutes based on the flux-form semi-Lagrangian method as described by Lin and Rood (1996) and moist convective transport is computed using the GEOS convective, entrainment and detrainment

mass fluxes as described by Allen et al. (1996a, 1996b) (Bey et al., 2001). In this computation, the time-step used is 15 minutes for both emissions and chemistry. Full mixing is assumed within the GEOS-diagnosed atmospheric mixing layer generated by surface instability (Bey et al., 2001). The atmospheric CH_4 simulation using GEOS-Chem was first described by Wang et. al. (2004) which was further developed by Wecht et. al. (2012). The CH_4 sources and sinks for GEOS-Chem are described with more details in Röger (2013), Rice et al. (2016) and references therewithin. In addition to total CH_4 emission, the tagged tracers which are [CH_4] emitted from different source processes or regions are also included in our computation. Thus, response functions for all source categories are computed simultaneously. As reaction with OH constitutes the main sink for CH_4, calculation of concentrations of other tracers is not required. We prescribed the OH concentration fields instead of calculating them which decreased the computational demands drastically in this computation. The tracer for $^{13}CH_4$ is also included as an additional constraint in this computation. However, CH_3D was also included in the previous computation of CH_4 fluxes with 4^0 x 5^0 resolution, but not included in this study.

This work extensively used the Global Atmospheric Modeling Analysis Package (GAMAP) which is the standard software package used for visualization of output generated by the GEOS-Chem model. GAMAP program contains a user-friendly, menu-driven interface also called as GAMAP subroutines independent of the main program written in Interactive Data Language (IDL). GAMAP takes advantage of IDL's facilities for reading different types of file formats, including netCDF, HDF, and HDF–EOS and

makes extensive use of IDL's powerful plotting features to aid the visualization of the GEOS-Chem model output data results.

4.3. Methods involved in Inversion Process

An overview of the methods involving various programs been developed and used to perform the inversion process, are discussed in this section. As GEOS-Chem model uses FORTRAN 90 programming language, all our program codes are also written in FORTRAN 90 to make compatible with GEOS-Chem. The Fortran program inverse.F is the main program that runs the inversion process to optimize CH_4 emissions over the specified run time using NOAA CH_4 observational data and $^{13}CH_4$ data. This program calls a number of routines that read in input files needed for the inversion process which includes response functions (H-matrix), CH_4 concentrations and isotope observations, prior emissions and reference run. All these input files are created using some other Fortran programs at the grid resolution of $2^0 \times 2.5^0$. The routines call various versions of GEOS-Chem executables which we created by compiling corresponding versions of GEOS-Chem codes at resolution of $2^0 \times 2.5^0$. Array-sizes, paths, filenames, extended time period, and other resolution dependent parameters were updated for all programs and procedures for inversion were followed. The inputs of inverse.F program include:

- Reference model concentrations (y_{ref}): Created using ***reference.F***.

- NOAA CH_4 and isotope observations which were aggregated to grid resolution of $2^0 \times 2.5^0$ as mentioned earlier in section 4.1.3.
- Total uncertainties associated to the observations calculated as mentioned earlier in section 4.1.3.
- Response functions (H-matrix): Created using ***response.F*.**
- Adjusted response functions (H^{adj} – matrix): Created using ***response_adj.F***.
- Adjusted response functions for isotopes(H^{13adj}–matrix): Created using ***response_adjIso.F***.

The above mentioned programs involved in model runs calculate the matrix of response functions $\boldsymbol{H}$ and the reference vector $\boldsymbol{y_{ref}}$.

4.3.1. Response Functions

The response functions used in this inversion work are briefly described in this section which were detailed by Röger (2013). We calculated response functions for the inversion using the chemical-transport model GEOS-Chem run at a horizontal grid resolution of $2^0 \times 2.5^0$. The elements of H matrix are expressed as the ratio of methane concentrations (y) to emissions (x) from sources in the state vector as follows:

$$H_{ijtt'} = \frac{\partial y_{it'}}{\partial x_{jt}} \simeq \frac{y_{it'} - \tilde{y}_{it'}}{x_{jt} - \tilde{x}_{jt}} \tag{4.17}$$

where *i* represents observational site, *j* represents methane source region, *t* and *t′* represent timesteps with $t' \geq t$. $y_{it'}$ and $\widetilde{y_{it'}}$ respectively denotes the concentration (in ppb) at site *i* at time *t′* caused by emissions (in Tg/year) x_{jt} and $\widetilde{x_{jt}}$ from source *j* at time *t*. The elements of H matrix are generated from multiple GEOS-Chem runs for each source of interest starting at time *t* and ending at *t′*. We get $H_{ijtt'} = y_{it'}$ in ppb/(Tg/yr), where no initial background concentration field was used, i.e., $\widetilde{y_{jt'}}$ = 0 and the emissions from the pattern corresponding to source *j* was chosen to be 1 Tg/yr during month *t* i.e., x_{jt} =1 Tg/yr and 0 Tg/yr in every other month i.e., $\widetilde{x_{jt}}$ = 0 Tg/yr. Thus, within these runs, one month pulse of methane emission is considered and its dispersion for all subsequent months are calculated as the emitted pulse become well mixed in the atmosphere after certain time. This led us to run the emission pulses from every month only for up to 6 months and approximate the remaining 6 months by using response functions from a full set of computations for the same month of the year 1990, similar to the work done by Röger (2013) and Rice et al. (2016). This process including the runs distributed over multiple nodes helped us to improve efficiency by reducing the computation time significantly. The changes in methane concentration with feedback in the sink strength due to impact of hydroxyl radical and stratospheric sinks as chemical sinks destroying tracer concentration also got considered in the *H* matrix. With specific settings, appropriate version of GEOS-Chem model is run to create bpch output files which are then read in by routine response.F to extract response functions for CH_4 at all mixing ratio and isotope measurement sites i.e., H.bin and HIso.bin, by routine response_adj.F to extract the adjustment response functions for CH_4 at all mixing ratio and isotope measurement sites i.e., H_adj.bin and H_adjIso.bin,

and by routine response_adjIso.F to extract the adjustment response functions for $^{13}CH_4$ at all isotope measurement sites i.e., H_adjIso2_Strat.bin, thus reaction rates have to be corrected with respective KIEs for OH and stratospheric sinks in the corresponding GEOS-Chem run.

Calculation of response functions (H-matrix):

The response functions i.e., H matrix, are calculated offline by using the routine response.F with the help of GEOS-Chem model run, which are required later within the process of inversion. The code is based on an earlier version of inversion which contained some obsolete variables no longer been used and some comments may not be applied any longer. The command to compile the code and execute the routine is given in the beginning of the routine before 'implicit none' statement. The time frame needed for the process has to be set with the variables been initialized in the declaration part. The output file has to be stored in the directory mentioned in the subroutine 'write_to_output_file'. The routine is placed in the 2x25/routines directory, appropriate version of GEOS-Chem source codes are present in gc-code/Code.Response directory and the corresponding GEOS-Chem run directory including the script called 'response.script' required to execute the routine is placed in the gc/GEOS-Chem.Response directory. The following steps are undertaken to create the binary files:

1. For this version of work, global_ch4_mod.F present in the directory gc-code/Code.Response_CB2/GeosCore, was investigated and modified by including

lines of codes required for change in grid resolution, changing array sizes, allocations for model run time period, paths to the files and other resolution-dependent codes, saved and then compiled at $2^{o} \times 2.5^{o}$ resolution to create an executable named as 'geos' in the gc-code/Code.Response/bin directory.

2. As response.F calls geos with arguments '1 0 0', which tells geos to run with all emissions of CH_4 to be on, to use zero CH_4 concentration field in restart file, and to not create any new restart file for subsequent months. This set of arguments tells input_mod.F which is used to accept command line arguments to geos, to use 'input.geos.inversion.4'. So, this file needed to be updated to work with $2^{0} \times 2.5^{0}$ version of GEOS-Chem.Response.

3. Before updating 'input.geos.inversion.4', the restart file for $2^{0} \times 2.5^{0}$ version has to be created. In 2x25/gc/GEOS-Chem.Response_SK/restart directory, a zero CH_4 restart file was created to initialize the GEOS-Chem run using GAMAP routine 'MAKE_RESTART.pro'. This had only one tracer for TOT_CH_4.

4. All input data files for $2^{o} \times 2.5^{o}$ version of the work are put in data/geos-chem/GEOS_2x25/EDGAR directory. All emission and sink data files which are updated and modified for the current version of work as already mentioned in the sections 4.1.1 and 4.1.2 in this chapter, are put in the same directory.

5. All meteorological data available up to 2007 are put in data/geos-chem/GEOS_2x25 directory.

6. In 2x25/gc/GEOS-Chem.Response_SK directory, ‘input.geos.inversion.4’ was checked and updated with required changes according to the current version. The file was modified to specify the name of the output bpch file which will be created and also checked and corrected the options for restart file and specified the path to the restart file created in previous step.

7. Next, the routine response.F was investigated and updated with modifications required to work with current version.

8. In 2x25/routines directory, response.F should be compiled and executed to create ‘response’ executable. This executable should then be submitted to the job scheduler Sum-Grid Engine (SGE), using the job script ‘response.script’ located in GEOS-Chem run directory. This should be done because the response.F calls and uses ‘geos’ executable and creates binary punch file ‘Inversion.bpch’ in 2x25 /gc /GEOS-Chem.Response_SK /rundirs /response.script_YYMM /output directory generated using forward run of GEOS-Chem, which is then be called by response.F again to create H.bin and HIso.bin standard response function files for first 6 months of years from 1979 to 2016.

9. The calculation of response functions was spread out to multiple routines, so that multiple nodes can be used to reduce the time of computation, since every model run for response function is independent of each other. Thus, multiple response.F routine and GEOS-Chem.Response run directories were created as required for this work, named as response_2.F and GEOS-Chem.Response.2 respectively, and so on. Then in each of these routines, required changes for the names and paths were done such as correction of executable was done by replacing '.response' with '.response_2' and so on.

10. Next, to run all the response scripts simultaneously, 'responsesplit.pro' was used which created separate run scripts for each of response.F versions and 'response.pro' was used to submit all the run scripts to the job scheduler.

11. After the runs were completed, the outputs for each version called as 'Inversion.bpch' were extracted and found in 2x25/ gc/ GEOS-Chem.Response/ rundirs/ response_script_YYYYMM/ output directory. These binary punch files were then again read into different versions of response.F to create H.bin and HIso.bin files. All versions of response.F are present in 2x25/routines/splitresponse directory, and all executables are created in 2x25/routines/exec/SK_exec directory. All H.bin and HIso.bin files for first 6 months of all years were created in 2x25/data/response_functions/Standard directory as YYYYMM_YYYYMM2.bin files.

12. For last 6 months, responsetails_base.F was worked on similar to last step for 12 months run for the year of 1990. For creating the tails for bin files, multiple versions of responsetails_base.F were made named as reponsetails_19901.F and so on in 2x25/routines/splitresponsetails directory and each version was modified for different allocations accordingly.

13. Response tails for 19901-199012, 19902-199101, …, 199012-199112 runs were submitted in multiple nodes similar to response standard runs. Thus, responsetailsSplit.pro in 2x25/IDL/responseSplit directory was worked on and checked with all allocations and then compiled and run in the same directory to create separate executables such as responsetails_19901, ..., responsetails_199012 in 2x25/routines/exec directory. Then in the same directory, these executables were run to create separate Inversion.bpch files in each of the output directories in 2x25/ gc/ GEOS-Chem.Response/ rundirs/ responsetails.script_YYYYMM/ output and all 'yyyymm_yyyymm2.bin' files were created in 2x25/ data/ response_functions/ Tails directory.

14. While working on both standard and tail runs of response functions, it was checked that the correct files for input.geos.inversion.4, diaginfo.dat, tracerinfo.dat, etc. exist in the respective run directories.

15. Next, in 2x25/IDL directory, cp_tails.pro was worked on with required modifications, compiled and run to attach response tails to standard bin files and

create full sets of response functions named as 197901_197901.bin, 197901_197902.bin, and so on up to 201512_201611.bin files in 2x25/ data/ response_functions/ Standard directory.

Calculation of adjusted response functions (H^{adj} -matrix):

The adjusted response functions i.e., H^{adj} matrix, are calculated offline by using the routine response_adj.F, with the help of GEOS-Chem model run, which are required later within the process of inversion. H^{adj} matrix is used to adjust the reference run concentrations to emissions that occurred more than 12 months before the current timestep. The elements of H^{adj} matrix are calculated from GEOS-Chem model run that is initialized with zero CH_4 restart file and a 1 Tg pulse of emission from all sources in the first month and is run from 01/1979 to 01/2017. This model run essentially simulates how a 1 Tg spike of methane emission decays over the entire 38 years of model period and the output of this model run is then sampled to get H^{adj}. An earlier version of inversion code is the basis of this Fortran routine which contained some obsolete variables no longer been used and some comments may not be applied any longer. The command to compile the code and execute the routine are given in the beginning of the routine before 'implicit none' statement. The time frame needed for the process has to be set with the variables been initialized in the declaration part. The output file has to be stored in the directory mentioned near the end of the main program. The routine is placed in the 2x25/routines directory, appropriate version of GEOS-Chem source codes are present in gc-code/ Code.Response.Adj directory and the corresponding GEOS-Chem run directory including the script named 'geos.script' required

to execute the routine is placed in the gc/ GEOS-Chem.Response.Adj directory. The following steps are undertaken to create the binary files:

1. Similar to standard response functions, for adjusted response functions also, global_CH_4_mod.F present in 2x25/ gc-code/ Code.Response.Adj_SK/ GeosCore directory was investigated and modified by including lines of codes required for change in grid resolution, different allocations for model run time period, change in number of measurement sites, change in paths to the files, etc., saved and compiled at $2^{o} \times 2.5^{o}$ grid resolution and created a new executable named 'geos' in 2x25/ gc-code/ Code.Response.Adj_SK/ bin directory.

2. Next, in 2x25/ gc/ GEOS-Chem.Response.Adj_CB directory, 'input.geos.inversion.4' was investigated and changes were made required to work with this version of model run, including change in model run time, paths to the files, input and output file names, choice of restart file – initialized with zero CH_4 restart file, turning on all emissions from all sources with total of 1 Tg pulse emitted in the first month, and with making new restart files with each timestep for the entire model run.

3. Next in the same directory, 'geos.script' was checked and the correct path to the 'geos' executable was included as mentioned in step 1, saved and submitted to the job scheduler.

This forward run of GEOS Chem model created 'Response_Adj_197901-201701.bpch' file in 2x25/ gc/ GEOS-Chem.Response.Adj_CB/ output_SK directory.

4. Next, in 2x25/ routines directory, 'response_adj.F' was investigated and required modifications were made to work with current version of model run, including change in array sizes, model run time, names and paths for the input and output files, number of measurement sites and other resolution-dependent codes. Then codes for a subroutine Read_bpch3 were included to open the file outside the main do loop to avoid extra run times, saved and compiled. An executable named 'response_adj' was created in 2x25/ gc/ GEOS-Chem.Response.Adj_CB directory, which was then executed to create H_adj.bin and H_adjIso.bin files in 2x25/ data/ response_functions/ Adj_SK directory.

Calculation of adjusted response functions for isotopes (H^{13adj} -matrix):

The adjusted response functions for isotopes i.e., H^{13adj} matrix, are calculated offline by using the routine response_adjIso.F, with the help of GEOS-Chem model run, which are required later within the process of inversion. H^{13adj} matrix is also used to adjust the reference run concentrations to emissions that occurred more than 12 months before the current timestep. Similar to H^{adj} matrix, the elements of H^{13adj} matrix are also calculated from GEOS-Chem model run that is initialized with zero CH_4 restart file and a 1 Tg pulse of emission from all sources in the first month and is run from 01/1979 to 01/2017. This

model run essentially simulates how a 1 Tg spike of isotopic methane emission decays over the entire 38 years of model period and the output of this model run is then sampled to get H^{13adj}. The only difference with the version of GEOS-Chem generating response_adj functions, is that in this version of GEOS-Chem, kinetic isotope effect (KIE) of $^{13}CH_4$ are included for OH and stratospheric sinks. An earlier version of inversion code is the basis of this Fortran routine which contained some obsolete variables no longer been used and some comments may not be applied any longer. The command to compile the code and execute the routine are given in the beginning of the routine before 'implicit none' statement. The time frame needed for the process has to be set with the variables been initialized in the declaration part. The output file has to be stored in the directory mentioned near the end of the main program. The routine is placed in the 2x25/routines directory, appropriate version of GEOS-Chem source codes are present in gc-code/ Code.Response.AdjIso directory and the corresponding GEOS-Chem run directory including the script named 'geos.script' required to execute the routine is placed in the gc/ GEOS-Chem.Response.AdjIso directory. The following steps are undertaken to create the binary files:

1. Similar to adjusted response functions, in adjusted response functions for isotopes also, global_CH_4_mod.F present in 2x25/ gc-code/ Code.Response.AdjIso_SK/ GeosCore directory was investigated and modified by including lines of codes required for change in grid resolution, different allocations for model run time period, change in number of measurement sites, change in paths to the files, correction for KIE of $^{13}CH_4$ are included in the calculation of reaction rates for OH

and stratospheric sinks etc., saved and compiled at $2^{o} \times 2.5^{o}$ grid resolution and created a new executable named 'geos' in 2x25/ gc-code/ Code.Response.AdjIso_SK/ bin directory.

2. Next, in 2x25/ gc/ GEOS-Chem.Response.AdjIso_CB directory, 'input.geos.inversion.4' was investigated and changes were made required to work with this version of model run, including change in model run time, paths to the files, input and output file names, choice of restart file – initialized with zero CH_4 restart file, turning on all emissions from all sources with total of 1 Tg pulse emitted in the first month, and with making new restart files with each timestep for the entire model run.

3. Next in the same directory, 'geos.script' was checked and the correct path to the 'geos' executable was included as mentioned in step 1, saved and submitted to the job scheduler. This forward run of GEOS Chem model created 'Response_AdjIso_197901-201701.bpch' file in 2x25/ gc/ GEOS-Chem.Response.AdjIso_CB/ output_SK directory.

4. Next, in 2x25/ routines directory, 'response_adjIso.F' was investigated and required modifications were made to work with current version of model run, including change in array sizes, model run time, names and paths for the input and output files, number of measurement sites and other resolution-dependent codes. Then codes for a subroutine Read_bpch3 were included to open the file outside the

main do loop to avoid extra run times, saved and compiled. An executable named 'response_adjIso' was created in 2x25/ gc/ GEOS-Chem.Response.AdjIso_CB directory, which was then executed to create H_adjIso2_Strat.bin file in 2x25/ data/ response_functions/ Adj_SK directory.

Methods used for Comparison between response functions from $4^0 \times 5^0$ grid resolution model run and $2^0 \times 2.5^0$ grid resolution model run:

1. A program named 'plot_H.pro' was written in 2x25/ IDL directory, which compared response functions i.e., H.bin files created in $4^0 \times 5^0$ and $2^0 \times 2.5^0$ grid resolution for lag months 0 to 11, using constant observation month of 07/2006 and also of 12/1980 for each source, for 20 sites distributed around the world. The plots matched very well with red lines representing $4^0 \times 5^0$ H.bin data and blue lines representing $2^0 \times 2.5^0$ H.bin data.

2. Another program named 'plot_H_adj.pro' was written in 2x25/ IDL directory, which compared adjusted response functions i.e., H_adj.bin files created in $4^0 \times 5^0$ and $2^0 \times 2.5^0$ grid resolution for lag months, using constant observation month at the end of entire model run time for each source, for 20 sites distributed around the world. The plots matched very well with red lines representing $4^0 \times 5^0$ H_adj.bin data and blue lines representing $2^0 \times 2.5^0$ H_adj.bin data.

3. Another program named ‘plot_H_adjIso.pro’ was written in 2x25/ IDL directory, which compared adjusted response functions for isotopes i.e., H_adjIso2_Strat.bin files created in $4^0 \times 5^0$ and $2^0 \times 2.5^0$ grid resolution, using constant observation month at the end of entire model run time for each source, for 20 sites distributed around the world. The plots matched very well with red lines representing $4^0 \times 5^0$ H_adjIso2_Strat.bin data and blue lines representing $2^0 \times 2.5^0$ H_adjIso2_Strat.bin data.

4. Then, I wrote another program named ‘compare_INVERSION_bpch_timeseries.pro’ in the same directory, which compares the plots of INVERSION.bpch timeseries of 7 months, using observation month of 07/1980, 07/2006, 01/2013 and 01/2015 for each source, created from model run at $4^0 \times 5^0$ (red lines) and $2^0 \times 2.5^0$ (blue lines) grid resolution. The plots were consistent and correctly depicted the decay of the emissions for above mentioned year’s adjusted response function files.

5. Next, I wrote a program named ‘Total_CH4_ResponseAdjIso_bpch_SK.pro’ in the same directory, which plotted the decay of emission of 1 Tg of total CH_4 mass over the entire model run time in the adjusted response function file for isotopes. The plots looked consistent on the decay of methane mass with increasing months, starting at 0.8 Tg for CH_4_tot and 0.08 Tg for 10 different tracers.

4.3.2. Reference Run

The reference run provides us with model predictions of CH_4 and $^{13}CH_4$ i.e., $\mathbf{y_{ref}}$, sampled at the same sites and times as the corresponding observations formed $\mathbf{y_{obs}}$. The model predictions are then compared with the actual observations and the difference between the two is used to update and optimize emissions. These model reference predictions can be obtained in two different ways: one approach is online where the model is run parallel to the inversion and other is offline approach where the model is run once for the entire time period before the inversion. Both these approaches were discussed in detail by Röger (2013). In this section, a brief description of the offline approach of the reference run is discussed which we have used for our work being much less demanding. During one-time model run for entire time period, the mixing ratios and the isotopic signatures for all observations are sampled at every time step and we get reference values $\hat{y}_{\mathrm{ref}}$. To account for the difference in estimated and reference emission values, these reference values are adjusted during the inversion as expressed by the following equation:

$$\left(\mathrm{y}_{\mathrm{ref}}\right)_i = \left(\mathrm{y}_{\mathrm{ref}}\right)_i + \sum_{t,j} H_{it}^{adj} \left(\mathrm{x}_{\mathrm{opt}}\right)_{jt} \tag{4.18}$$

where *i* refers to specific observational site, *j* to specific methane source region and *t* to a specific time step. $\mathrm{y}_{\mathrm{ref}}$ represents the atmospheric abundance of observed methane calculated in the grid cells containing the observational sites and $\hat{y}_{\mathrm{ref}}$ refers to the modeled methane abundance, obtained from the entire time period reference run, $\mathrm{x}_{\mathrm{opt}}$ denotes the

fully optimized estimates of the source strength for specific source region for a time step and H^{adj} is the set of basis functions containing the responses specifying the impact of emissions which occurred more than 12 months prior to the observations with transport model acting on these emissions. H^{adj} matrices are obtained from conducting GEOS-Chem run over the entire inversion time period starting with zero concentration fields and a combined 1 Tg/yr emission pulse from all sources in the first month, as mentioned by Röger (2013) and Rice et al. (2016). The elements of H^{adj} comprises of the adjustments in the CH_4 concentrations to the reference emissions from each source region at each observational site for the first 12 months. In order to calculate the isotopic ratios from the reference run, the $\delta^{13}C\text{-}CH_4$ reference values are corrected by using similar equation obtained from formulation of Mikaloff Fletcher et al. (2004) as follows:

$$\left(\mathrm{y}_{\mathrm{ref}}^{13}\right)_i = \left(\mathrm{y}_{\mathrm{ref}}^{13}\right)_i + \sum_{t,j} H_{it}^{^{13}adj} \left(\mathrm{x}_{\mathrm{opt}}\right)_{jt} \left(R^{\mathrm{src}}\right)_j \tag{4.19}$$

where the vector R^{src} contains the isotopic ratios corresponding to the source signatures calculated using following equation:

$$\mathrm{R}^{\mathrm{src}} = \left(\delta^{src}/1000 + 1\right) \times \left[\frac{^{13}C}{^{12}C}\right]_{PDB} \tag{4.20}$$

where, δ^{src} is the isotopic signature of the specific source process. $H^{13_{adj}}$ comprises of the response functions calculated similar as H^{adj} with reaction rates of OH and stratospheric

sink using their respective KIEs as mentioned earlier. An error of size of elements in x_{opt} is introduced due to the approximation using equations (4.18) and (4.19) to avoid the model running along the inversion.

Creating Reference Runs:

Reference runs were created offline with GEOS-Chem model run using the a priori emissions data. Later throughout the inversion, the model predictions in the reference run were adjusted using fully optimized emissions. The following steps were considered to get $\mathbf{y_{ref}}$:

1. In 2x25/ gc-code/ Code.Reference.SK/ GeosCore directory, Geos Chem source codes such as global_CH4_mod.F, a3_read_mod.F, a6_read_mod.F, i6_read_mod.F, tracer_mod.F, input_mod.F, etc. were investigated and updated with modifications required to work for current version of model run. There were changes in array sizes, paths to different files, other resolution-dependent codes, model run time and lines of codes were included as required for adjustments, saved and then compiled to work at $2^0 \times 2.5^0$ grid resolution. A new executable 'geos' was created in 2x25/ gc-code/ Code.Reference.SK/ bin directory.

2. Next in 2x25/ gc/ GEOS-Chem.Reference_CB directory, checked with all the existing run directories and then 'input.geos.inversion.4' file was investigated and

modified according to the changes required to work with this version of model run, such as corrected the model run time, output file names and paths, options for restart files, emissions of tracers, etc. A new restart file was created for $2^{o} \times 2.5^{o}$ grid resolution. The reference run version of restart file for $4^{o} \times 5^{0}$ grid resolution was a simple restart file where both hemispheres had been initialized with constant CH_4 and isotopic composition. I wrote a program named 'Convert_restart_4x5to2x25.pro' which converted the restart file made in $4^{0} \times 5^{0}$ grid resolution to restart file in $2^{0} \times 2.5^{0}$ grid resolution.

3. Next in the same directory, 'geos.script' was modified to include the correct path to the 'geos' executable, saved and then submitted to the job scheduler to create 'Reference_021979-012017.bpch' file in 2x25/ gc/ GEOS-Chem.Reference_CB/ output_SK directory.

4. Reference version of GEOS-Chem is used to create both the reference runs for the inversion to calculate y_{diff} i.e., the difference between the a priori simulated CH_4 and the measured CH_4 and also to create a bpch output file that is used to calculate the mismatch error of the CH_4 observations. There are over 200 sites of CH_4 mixing ratio measurements worldwide and about 21 locations for isotope measurements. These data are input to the inversion process, so these data needed to be placed at $2^{o} \times 2.5^{o}$ model grid cells. In some cases, more than one observation site lies in the same model grid cell, so the observational data set needed to be aggregated in the

$2^{o} \times 2.5^{o}$ model grid cells and the correct model grid latitude and longitude index to be assigned. So, I wrote a program named 'Check_gridIndices.pro' which checked latitude and longitude coordinates of each observation site and also whether grid indices for each site were transformed from latitude and longitude coordinates correctly or not.

5. I wrote another program named 'gv_SK_2016.pro' present in 2x25/ IDL directory, which reads in input text file 'processed_NOAA_CH4_2016_reduced.txt' and considers aggregation, mismatch error calculation, uncertainty assignments, correcting data from ocean transects and then generates output text file named 'NOAA_2016_OceanCorrect.txt'.

6. Then, OGI data for some sites were manually added to the above mentioned output text file, removed POCS15 data since the site was situated in the same grid cell as SMO which had longer timeseries of data, thus created a text file named 'Concentration_data_2016_Correct.txt' which was then renamed as 'Concentration_data.txt' present in 2x25/ data/ observations directory.

7. The model predicted CH_4 concentrations in the grid cells where we have CH_4 observations, were saved to a binary data file. Thus, reference.F needed to know the grid cell indices of the CH_4 observation sites, which can be provided by Concentration text file created earlier in the above step. I wrote a program named 'Site_indices.pro' which reads in 'Concentration_data.txt' files for both $4^{o} \times 5^{o}$ and

$2^0 \times 2.5^0$ grid resolution and creates two output files named 'NOAA4x5Site_indices.txt' and 'NOAA2x25Site_indices.txt' printing names and corresponding grid indices of all observation sites.

8. The values of all data for a priori emissions were processed and printed in text file which was used for reference runs. The 'apriori_values.pro' program was used by modifying the codes to work for current version, to create the 'Apriori_SK.txt' file in the 2x25/ data/ priors directory.

9. Next in 2x25/ routines directory, reference.F was investigated and modified accordingly as required to work with the current version of work, to include resolution dependent codes for $2^o \times 2.5^o$ version, updated array sizes, paths and filenames. The timeframe for the model run was changed to start date as 01/1980 and end date as 12/2015, since in this work, we have data through 12/2016 and we need 12 months of additional data to constrain emissions of 12/2016, thus inversion will run until 12/2015. Reference bpch file had data from 02/1979 to 01/2017 and Concentration_data.txt had data from 01/1977 to 01/2016, hence timeframes for different variables were set accordingly. The codes for reference.F were saved and compiled in the same directory and then in the run directory 2x25/ gc/ GEOS-Chem.Reference_CB, the executable was run or reference.script was submitted to the job scheduler to create rRef.bin which wrote out $^{13}C/^{12}C$ ratio for GEOS-Chem to read for delta calculation, Reference_1.bin which wrote out y_ref,

Reference_2.1.bin which wrote out y_refIso1 and Reference_2.2.bin which wrote out y_refIso2 in the 2x25/ data/ reference_runs/ output_SK directory.

During inversion process, observations of CH_4 and $^{13}CH_4$ are compared with GEOS-Chem model simulated CH_4 and $^{13}CH_4$, i.e., y_{obs} and y_{ref} and the difference between these two at each timestep are used to update the prior 'best guess' estimates of CH_4 emissions in ten different source categories. The GEOS-Chem predictions are stored in reference run files which are created as mentioned in the above steps, outside the inversion. As the inversion process was run proceeding with each timestep through the model period, it optimizes the emissions month by month. The reference concentrations were calculated from offline GEOS-Chem model run, so those are not optimized with updated emissions and do not reflect the updated optimized emissions. These reference concentrations need to be updated or adjusted with the changes made to prior emissions by the inversion. These adjustments were made using H_adj and H_adjIso and H^{13adj} matrices which were obtained from response functions run within the inversion process.

4.3.3. Main Inversion Process Deriving a posteriori estimates and covariance matrix

Here in this section, the steps followed in the calculations in the main inversion program are being discussed which are identical to the inversion work done previously with $4^{o}x5^{o}$ resolution by Röger (2013). However, all the relevant equations and theoretical concepts

have already been discussed in Chapter 3. The main task of this program named 'inverse.F' was to derive a posteriori estimates of CH_4 emission and their covariance matrix from a priori emission values, the measurement values from observation sites and previously calculated model output. The codes for the main inverse program performed the following steps which involved the inversion process:

1. At first, the adjusted response functions H_adj, H_adjIso and H_adjIso2_Strat binary files were read in.

2. Then, observations of CH_4 were read into y_obs for all sites for entire time period.

3. Then, a priori emissions for all ten sources starting at 02/1979 were read into AprioriEmissions.

4. These a priori emissions were scaled by a factor of 1.08 to better match emissions required by OH fields.

5. If interval constraints were used, physically realistic lower and upper bounds were set.

6. Then, reference run for all sites i.e., y_ref was read in, if using isotopes, reference run of ^{12}C concentrations at isotopic sites i.e., y_refIso1 was read in and reference

run of ^{13}C concentrations at isotopic sites i.e., y_refIso2 was read in from reference run binary files.

7. Next, for last 11 months of year 1979, the state vector $\mathbf{x}'_{\mathbf{u}}$ and its covariance matrix $\boldsymbol{Q}'_{\boldsymbol{uu}}$ were initialized. Before the first time-step began, the state vector contained the adjustments to the priors with all values zero everywhere. During the first 11 months, the uncertainties of the priors form the diagonal elements of the initial covariance matrix which were calculated by multiplying assigned relative uncertainties 50% for aseasonal sources and 100% for seasonal sources, with the corresponding a priori values. The off-diagonal elements of the covariance matrix were zero. These partially optimized values for the first 11 months entered the inversion.

8. Time stepping began on 02/1979 as the inversion start date would be 01/1980 and end date 12/2015, so the loop would be over all months for which emissions to be optimized. The next steps were executed for every time-step and thus, would run in a loop in the program.

9. The available NOAA ^{13}C-CH_4 data and their uncertainties (SigISO) for current observation month were read in and got number of available constraints (NIso) with the indices of locations providing the constraints (indarr).

10. The a priori emission adjustments and its covariance matrix shift for the current time-step were calculated using state space equations (3.20) and (3.21) respectively from Chapter 3. The active set of state vector was updated by pushing the elements down one month and for the month included recently, the variables were set to zero initial adjustments and uncertainties were calculated by total a priori values of the month multiplied with the assigned relative uncertainties. The fully optimized elements were extracted out from $\mathbf{x}'_{\mathbf{u}}$ and $\boldsymbol{Q}'_{\boldsymbol{uu}}$ forming x_v, Q_{uv}, and Q_{vv}. Thus, the state vector was stored that fell out of the active set.

11. Using the equations (4.18) and (4.19) from the reference run, the adjustments were made for methane concentrations and isotopic signatures. Then, the vector $\mathbf{y_{diff}}$ for the current month was obtained by subtracting the reference concentrations from the observations as referred in equation (3.2). The reference $^{13}C/^{12}C$ ratio was calculated for current observation month at each of the isotopic sites.

12. As discussed in section 3.3, all 8 steps were performed for this time-step using all isotopic data available to constrain the inversion.

13. The response functions H and HIso were read in for all months constrained by the current observation month.

14. A first estimate of the flux for the current time-step was calculated using the state update and covariance update equations (3.30) and (3.32) respectively. The inverses were calculated by using singular value decomposition method. Then using equation (3.23), the estimate was used to check for predicting whether all observations matched well or not. However, when the model was unable to satisfy all the constraints at the same time with observations not matching within 3 standard deviations, then these observations were assigned a large weight in the cost function and thus ignored these unmatched measurements to get the best fit with matched ones. Therefore, the state and covariance updates were repeated without using these unmatched observations.

15. Moreover, an iterative method was used for consistency check as described in section 3.4 where interval constraints were imposed to the unphysical estimates and were projected to their feasible range. If an estimate suggested a negative source strength as lower bound, it was considered as unphysical, similarly as upper bound, a posteriori emissions more than 3 times larger than a priori emissions were not allowed. 12-months mean flux of every source were determined for four aseasonal sources from the 11 unconstrained estimates and $\mathbf{x_v}$. The feasible region for the fluxes of the sources were defined between 10% larger and 10% smaller than their respective annual mean flux.

16. The updated optimized emission estimate for all sources at each timestep and updated covariance values, along with other required variables were written out in

an output text file named ‘output_SK.txt’. Then the main loop ended. All different subroutines were written after the main program which were called within the main inversion process as needed for coding.

The estimates for 2016 are not fully optimized and therefore not evaluated. As mentioned by Röger (2013), similarly in this work also, we used singular value decomposition routine DGESVD to invert matrices in the inversion process, which is publicly available in packages of LAPACK from the Intel Math Kernel FORTRAN library.

Problems during Process runs and Finding their Solutions:

There appeared few problems while running the inverse program to get the final results which were addressed by using several intermediate steps and writing several subsidiary programs to check the consistency of the values. Some of the works included:

In the 2x25/ routines directory, the program ‘inverse_SK.F’ was investigated and modified to include correct allocations required to work for the current version, modified input and output paths and filenames, added lines of codes to check different intermediate values within the main program and different subroutines. After inverse_SK.F was run, got some error messages such as SVD error and got NaN values for noise, Deviations in upper and lower truncate boundary values, Covariance ‘C_new’ as NaN, there were larger than expected number of interval constraint violations. To fix these issues, I checked with the values of matrices multiplications and transposes in different intermediate steps. With

interval constraint set to false, ran the program, there were no NaN values, but with the constraint set as on, the problems appeared. So, I checked with the codes for subroutines 'truncate_u' and 'truncate_l' and calculated manually the covariance 'C_{ii}' for truncated probability density function (pdf) enclosed with upper and lower bound variables, found error in the codes of calculation of phi, written previously in earlier version. Then I modified the codes accordingly and added codes to print out the variances, the NaN issue was solved, but then next got C_new value as negative larger than -0.1, checked with C_new values with interval constraint on and off. To solve for this issue, checked with H.bin files, I wrote the program 'Plot_H.pro' to plot the values and compare between H.bin files with the response functions for both $2^{o} \times 2.5^{o}$ and $4^{o} \times 5^{o}$ versions, which varied more than expected. Then checked with the response function GEOS-Chem source codes, in global_CH4_mod.F, added print statements at different intermediate steps to check whether CH_4 emissions for all different sources at each site for first month is 1Tg/year or not, checked with 'CH_4_emis' and 'inv_factor' values. I wrote another program 'compare_INVERSION_bpch_timeseries.pro' to compare the bpch files plotting INVERSION.bpch timeseries of 7 months for both $2^0 \times 2.5^0$ and $4^0 \times 5^0$ versions. The plots for $4^0 \times 5^0$ version did not look good, problem was with the restart file, ran the codes with corrections, made all new bpch files, printed out 'CH_4_Tot' minimum and maximum values and 'CH_4_emis' values and compared the numeric values and the units for those same parameters for $2^0 \times 2.5^0$ version. Then also to check the CH_4 loss for both versions, I wrote another program 'Total_CH4_Inversion_bpch.pro' and compared the values of total CH_4, CH_4 mixing ratio for each source and some other variables. Next in response

source code of 'global_CH4_mod.F', I checked with values of CH_4 decay, CH_4_loss, loss rate, CH_4_strat, AD19 and temporal scaling of soil absorption, where found array error which was solved by changing TYPE to INTEGER from REAL8. Then turning CH_4_DECAY off, checked the CH_4 mass for each tracer without CH_4 loss due to OH, also checked values of different parameters with turning CH_4_DECAY on, found average tropospheric temperature too high in the routine CH_4_AVGTP. The comparison plots for Inversion.bpch files for both versions did not look correct. Next, I re-ran all response_adj functions after GEOS-Chem run, found NaN value in 'CHECK_STT (82, 4, 1, 13). Then, after doing some more investigations, made some changes such as in 'input.geos.inversion.4', excluded $\delta^{13}C$-CH_4 and CH_4-D from 'Tracer Menu' for making H_adj.bin files, set 'false' for 'make new restart file', ran the model and created new 'geos' executable. Similar changes were made for H_adjIso.bin files but included the isotopic tracers in 'Tracer Menu', checked 'global_CH4_mod.F' to include KIE values and KRate-13, 'Time for Decay' was made sure to set 'True' for later months, but 'False' for first month, ran the model and created new separate 'geos' executable. In both Response_adj.F and Response_adjIso.F, array sizes were modified as required for $2^0 \times 2.5^0$ version and also Filename is opened outside of Read_bpch3 subroutine to reduce runtime, ran the codes and checked with the plots, still plots did not look correct. After conversations with Prof. Butenhoff, he checked with the codes and created 'geos executable for Response_adjIso codes, T_avg values looked good within 300 loops, he mentioned not to use DEBUG option during GEOS-Chem run which was causing problems by turning off all the optimizations within the codes. Then, all the reference runs, standard response functions,

adjusted response functions were run with all above mentioned corrections. In GEOS-Chem source code directory, the codes for 'global_CH4_mod.F' were checked, in subroutine CH_4-DISTRIB (PREVCH_4), isotope tracers were included, the model was run and created Response_AdjIso_197901-201701.bpch file. Then, I wrote another program named 'Total_CH4_ResponseAdjIso_bpch_SK.pro' and plotted the decay of emission of 1 Tg of total CH_4 mass over the entire model run time of the adjusted response function bpch file for isotopes. The plots looked consistent on the decay of methane mass with increasing months, starting at 0.8 Tg for CH_4_tot and 0.08 Tg for 10 different tracers. After compiling and running 'Response_adjIso.F', H_adjIso2_Strat.bin was created, and finally checked the comparison plots of the binary files of both versions with 'Plot_H_adjIso.pro' which looked consistent for all tracers. Similarly, checked the comparison plots of H.bin and H_adj.bin files of both versions with 'Plot_H.pro' and 'Plot_H_adj.pro' respectively, which also looked consistent for all tracers.

Finally, in 2x25/ routines directory, checked the codes of 'inverse_SK.F', updated and modified as required to work with current version, compiled, 'inverse_SK' executable was run and created output file with optimized methane emissions from 01/1983 to 12/2015, named as 'output_SK.txt' in 2x25/ data/ inverse_output directory. Next, in 2x25/ IDL directory, checked the codes of 'inversion_read.pro', updated and modified as required, compiled and ran the program. This program read in the output text file and converted it to save file, thus, created 'S1_SK.save' file in 2x25/ data/ results_SK directory, containing the final results of the base inversion.

Next, program ‘compare_all_records_SK.pro’ was used to create all ‘.eps’ files which plotted the NOAA observation data, a priori emissions and inversion run records of optimized a posteriori emissions for all 105 CH_4 measurement sites and 21 isotopic measurement sites. Next ‘anomalies_eps_S1_SK.pro’ was used to create ‘Anomalies_S1.eps’ file which showed the plots of anomalies in a priori and a posteriori CH_4 emissions for standard base inversion and ‘anomalies_fancy.pro’ was used to create the plots of anomalies in a priori and a posteriori CH_4 emissions for all different sources combined in categories as ‘fossil fuels’, ‘Wetlands’, ‘Biomass Burning’, ‘Biogenic’, ‘Anthro Biogenic’ and ‘Total’. Next, ‘Avg_Seasonal_cycle_eps.pro’ program was used to create ‘avg_seasonal_cycle.eps’ file which plotted the a priori and a posteriori seasonal average CH_4 emissions from seasonally variable sources and also total CH_4 emission varying seasonally for all years.

4.4. Sensitivity Tests

Sensitivity tests are considered as important tool used to investigate the size of the systematic or external errors introduced by biases in the inversion settings and CTM. Calculation of the posterior covariance matrix characterizes errors caused by the uncertainties in the priors and observations which are referred as internal errors by Peylin et al. (2002), since they were calculated with inversion process. Sensitivity tests were conducted by repeating the base inversion process several times with one setting being altered within a reasonable range each time. The range of these results from this ensemble

of inversion scenarios quantify the systematic or external errors caused by different tested settings. Throughout the base inversion process, the observational network density and consequently network geometry changed with the inhomogeneous data records present in the NOAA raw data measurements which may cause bias in the inferred fluxes. In this work, sensitivity tests were conducted to assess the impact of this discontinuity of data coverage over the entire length of the time period of inversion for particular set of sites on the flux trends. Seven different tests were performed where observational network density was varied based on the number of years of continuous availability of data. In each test, a homogeneous network i.e., network of observation sites with continuous data coverage, was created for inversion by removing a particular set of sites having data for less than certain number of years each time, such as omitting sites having data less than 3 years, 5 years, 10 years, 15 years, 20 years, 25 years and 30 years respectively as mentioned below in Table 4.2. Thus, the final sensitivity test was performed with homogeneous network density by restricting the inversion to use only 18 observational sites with continuous data coverage spanning from 1983 to 2016.

At first, the text files were created having number and codenames of sites to be omitted. Then I created separate version of inverse program named as 'inverse_SK_reduced.F', included codes for the network density variation process, modified the paths for input and output files, compiled the codes and ran the program to create output text file named as 'output_SK_S2a.txt' which included the first scenario of optimized CH_4 emissions by excluding a certain number of sites having data for less than 3 years. Likewise, updated the codes in 'inverse_SK_reduced.F' to create other output text files for each scenario. Then,

modified the codes in ‘inversion_read.pro’ accordingly, compiled and ran the program each time for each separate scenario to create all separate save files. Next, ‘anomalies_fancy.pro’ was updated to include these save files and create the final plot of different sensitivity test scenarios included with the base inversion scenario. The plot showed the ensemble range of emission anomalies for different sources separately as well as for combined categories over the entire time period.

I included these 7 sensitivity tests based on network density variation in this thesis for completion of my master’s degree. However, we need to explore the sensitivity of these results to the choices of numerous model parameters in separate inversion set-ups. Thus, some more sensitivity tests need to be done to check the robustness of the inversion results.

Table 4.2: Sensitivity Tests done by variation in Observational Network Densities based on number of sites omitted from inversion with continuous data coverage available for more than above mentioned number of years.

Number of Sensitivity Tests	Sensitivity Test Scenarios	Continuous Data available for more than following number of years	Number of observation sites omitted
1	S2a	3	5
2	S2b	5	9
3	S2c	10	37
4	S2d	15	50
5	S2e	20	54
6	S2f	25	69
7	S2g	30	87

CHAPTER 5

Results and Discussion

In this chapter, the main results of the inversion of methane emissions over more than the last three decades are presented as in Section 5.1 and an interpretation of the analysis of the results is discussed in Section 5.2.

The results include the comparison of modeled a priori and a posteriori concentrations and isotopic signatures with observations in Section 5.1.1, and the interannual variability and average seasonal variations of the emission estimates discussed in Sections 5.1.2 and 5.1.3 respectively. In the Discussion section, 2^{o}x2.5^{o} and 4^{o}x5^{o} grid resolution model-data mismatch errors are compared in section 5.2.1, comparison of optimized methane emission anomalies from $2^{0} \times 2.5^{0}$ and $4^{0} \times 5^{0}$ horizontal grid resolution inversions until 2008-2009 are presented in section 5.2.2. Modeled estimates and trends of emissions from all source categories are compared with previous studies in Section 5.2.3 and finally, main possible reasons of post 2006 rise in global atmospheric methane levels are discussed in section 5.2.4.

5.1. Results

5.1.1. Model Inversion Results and their Comparison with Observations

The results reveal that the inversion process improved the fit of the model predictions with the observed CH_4 concentrations and $\delta^{13}C$ data at almost all sites as compared to predictions made using the prior flux data. The inversion model results for all 105 CH_4 and

all 21 $\delta^{13}C-CH_4$ observational sites sorted from south to north, are shown in Figure 5.1. The list of observed mixing ratios (in ppbv), modeled mixing ratios (in ppbv) averaged over entire modeled time period 01/1983 to 12/2015 and total uncertainties in observations for all 105 NOAA measurement sites with their corresponding site code, location name, latitude, longitude and elevation (in meters) is presented in Table 5.1.

The figure depicts the comparison of processed observations (blue) of CH_4 concentration from NOAA GML 'event CH_4 data file' and $\delta^{13}C$ of CH_4 from PSU, UCI, INSTAAR, and UW with modeled values at each observational site. Results are shown for emissions inventories source estimates scaled uniformly (as explained near the end of Section 4.3) *a priori* in red and for optimized base-case inversion estimates *a posteriori* in black over the modeled period 1984–2015. The blue shaded areas represent the ± 1σ range of the model-data error described in Section 4.4. The optimized emissions are the results taken from the standard base-case inversion. Without scaling the priors, model predictions using the prior emissions were biased high by approximately 60 to 70 ppb for all sites.

It is clearly seen from the figure that at most sites the inversion did a good job fitting both the long-term trend and seasonal cycle of the measurements. The inversion derived a posteriori estimates matched for both magnitude and trend of the observed concentrations and isotopic signatures much better than the prior source strengths. There remained few small discrepancies which might have been caused by aggregation error and could be solved in a higher resolution inversion and by optimizing for more source categories. The sites that were not well matched, e.g., South China Sea (SCS; 4^{o}N, 105^{o}E and SCS; 22^{o}N,

115°E), Shangdianzi, China (SDZ; 40.0°N, 117.5°E), Lac La Biche, Alberta, Canada (LLB; 54°N, 112.5°W), generally had large model-data errors (total uncertainties in Table 5.1) compared to other sites, therefore measurements from these sites were not weighted as significantly in the inversion. This may be caused in case when the site is close to a source region and is not well represented by the coarse model grid leading to errors (discussed in chapter 4). As seen in the figure, for some sites, the inversion could not perfectly match the seasonal cycle in the CH_4 emissions such as model estimates were lower than the observations at Southern Great Plains, Oklahoma, USA (SGP; 36^0N, 97.5^0W) and model estimates were higher than observations at Tae-ahn Peninsula, South Korea (TAP; 36°N, 125°E). The $\delta^{13}C$-CH_4 measurements were matched remarkably well by the inversion except some small overestimates in the higher latitudes of Northern Hemisphere, as seen in the figure for Barrow, Alaska (BRW; 71.3°N, 156.6°W) and Alert, Canada (ALT; 82.5°N, 62.5°W) and small underestimates in the Southern Hemisphere, for Baring Head, New Zealand (BHD; 41.4°S, 174.9°E). Rice et al. (2016) noticed Tae-ahn Peninsula site as unusual without a summer dip of CH_4 in comparison to many other northern mid-latitude sites and attributed this to the location of this site within a grid cell with combined influence of upwind isotopically depleted emissions from rice agriculture and natural wetlands as discussed by Dlugokencky et al. (1993). This site's influence on the inversion is reduced relative to other sites because of the large model-data mismatch error.

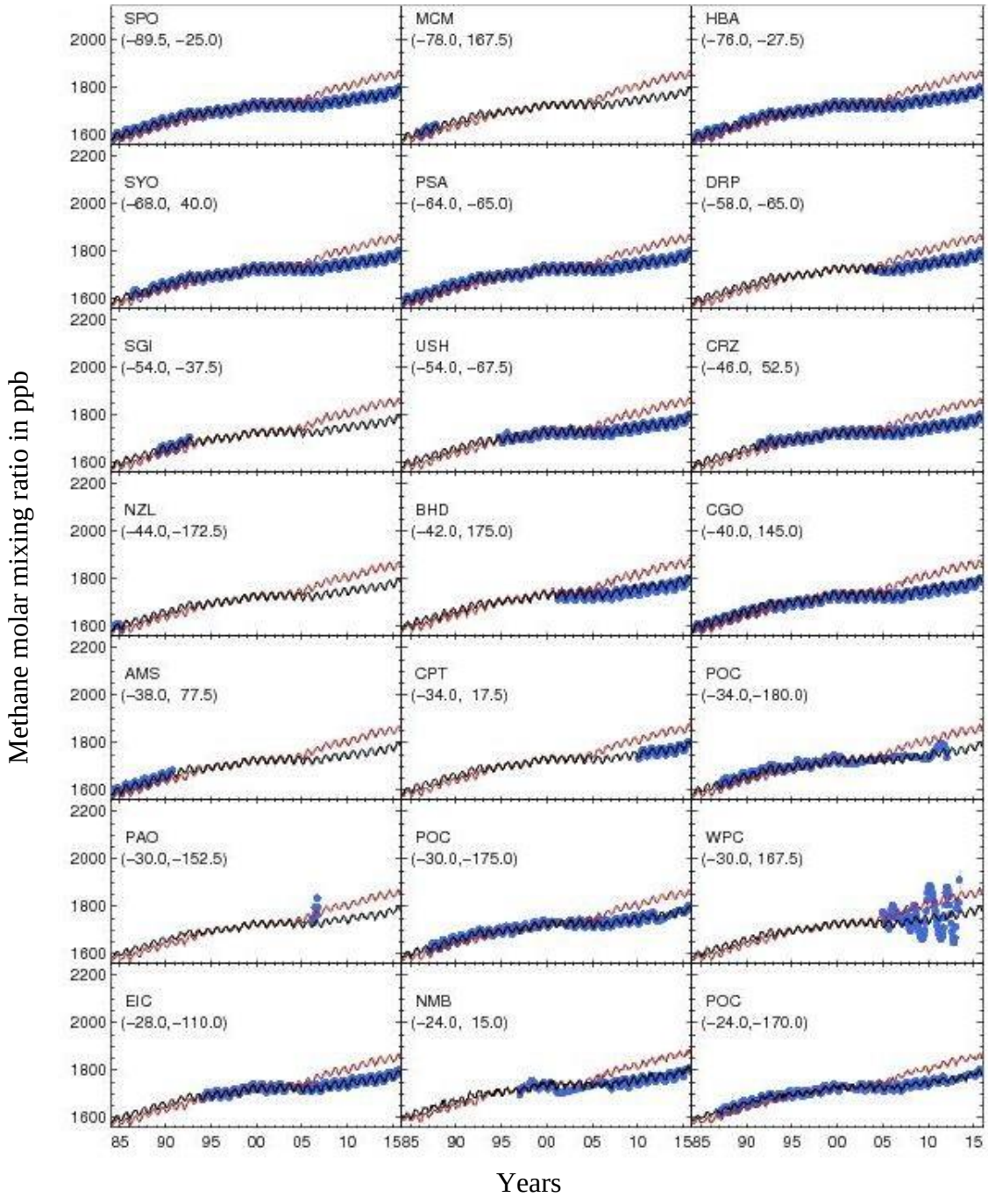

Figure 5.1: *The inversion model results for all 105 CH_4 and all 21 $\delta^{13}C-CH_4$ observational sites sorted from south to north. This depicts the comparison of processed observations (blue) of CH_4 concentration from NOAA GMD 'event CH_4 data file' and $\delta^{13}C$ of CH_4 from PSU, UCI, INSTAAR, and UW with modeled values at each observational site. Results are shown for emissions inventories source estimates scaled uniformly a priori in red and for optimized base-case inversion estimates a posteriori in black over the modeled period 1984–2015. The blue shaded areas represent the ± 1σ range of the model-data error.*

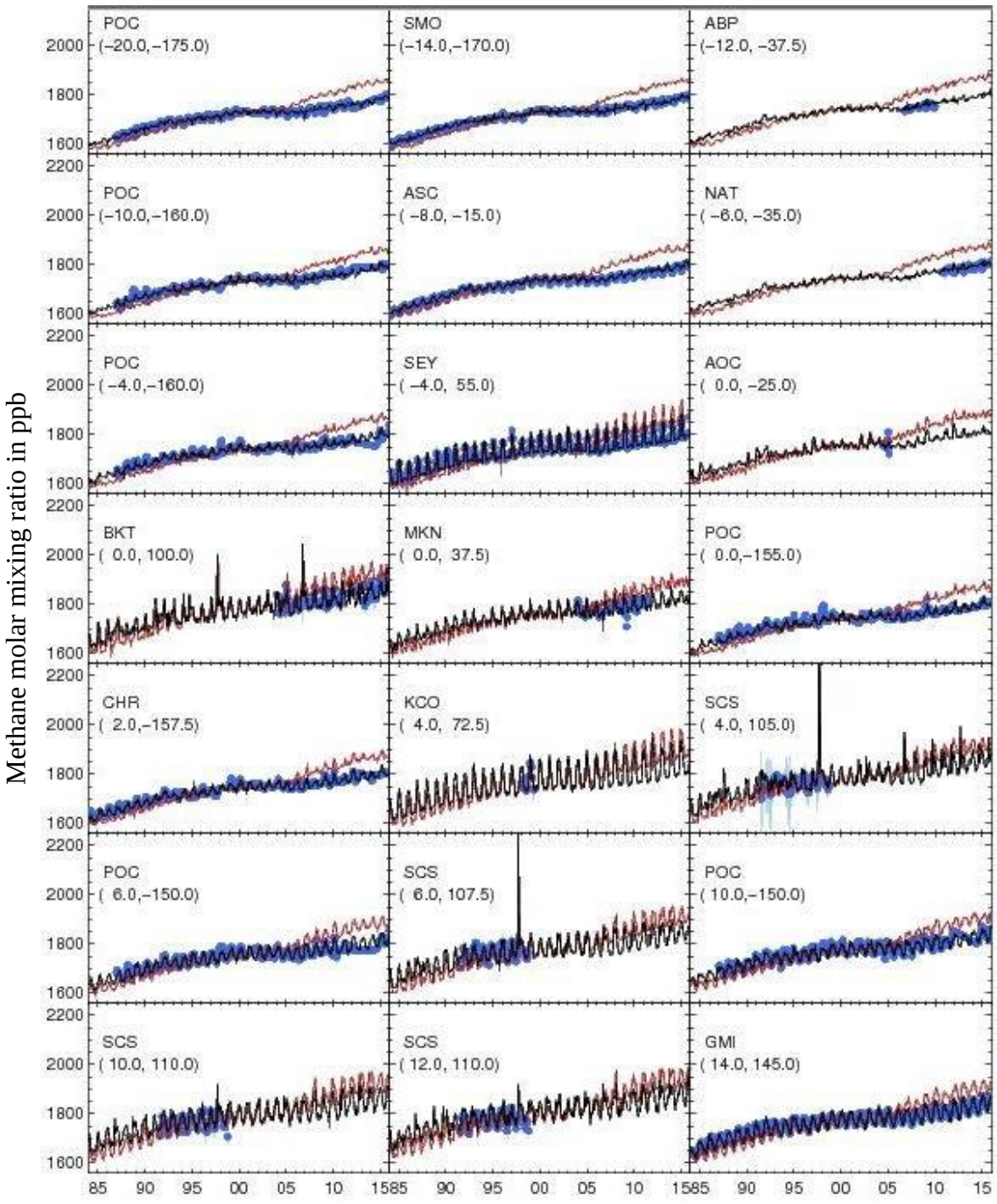
POC
(−20.0,−175.0)
SMO
(−14.0,−170.0)
ABP
(−12.0, −37.5)
POC
(−10.0,−160.0)
ASC
(−8.0, −15.0)
NAT
(−6.0, −35.0)
POC
(−4.0,−160.0)
SEY
(−4.0, 55.0)
AOC
(0.0, −25.0)
BKT
(0.0, 100.0)
MKN
(0.0, 37.5)
POC
(0.0,−155.0)
CHR
(2.0,−157.5)
KCO
(4.0, 72.5)
SCS
(4.0, 105.0)
POC
(6.0,−150.0)
SCS
(6.0, 107.5)
POC
(10.0,−150.0)
SCS
(10.0, 110.0)
SCS
(12.0, 110.0)
GMI
(14.0, 145.0)
2000
1800
1600
2200
85
90
95
00
05
10
15
Methane molar mixing ratio in ppb
Years

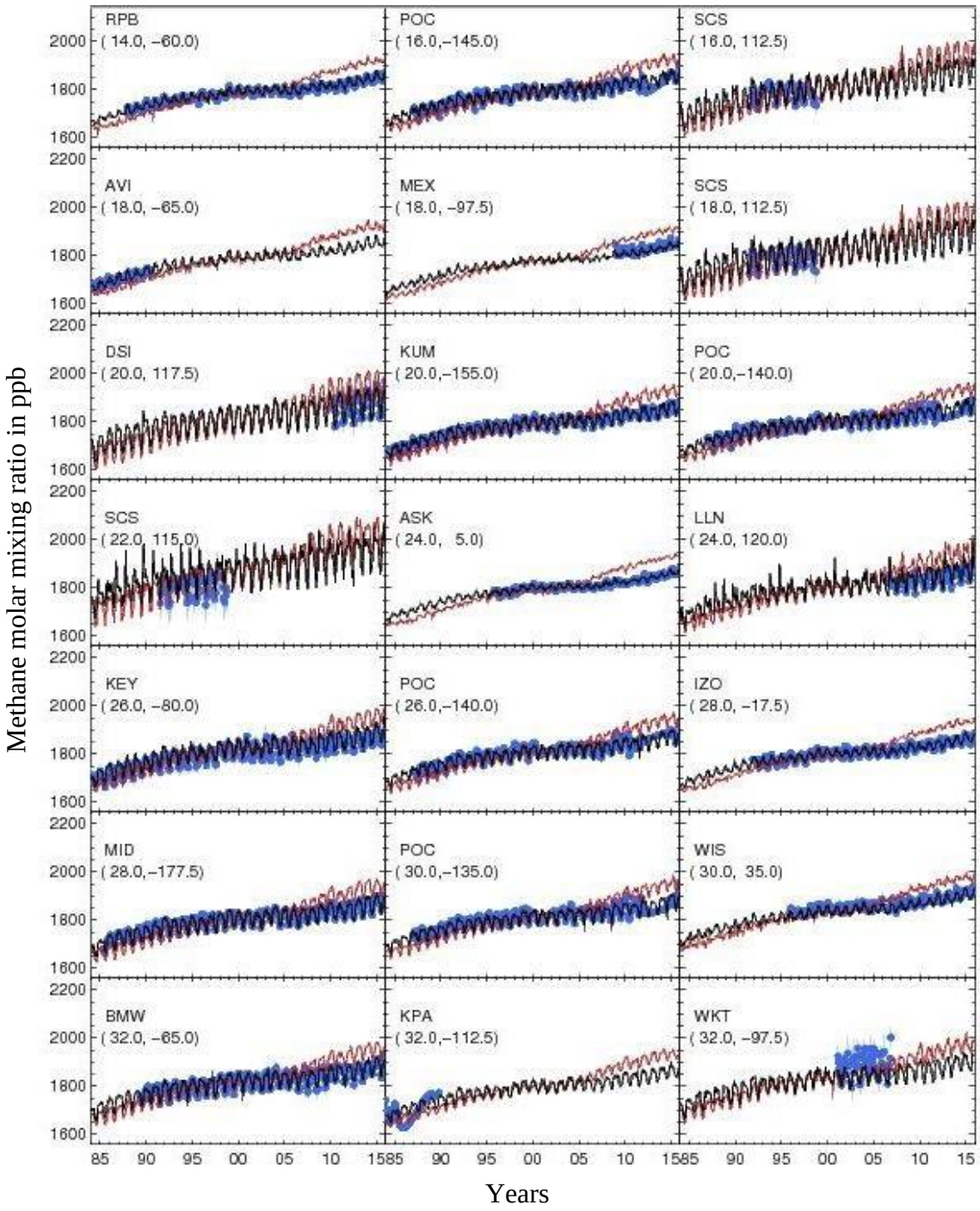
RPB
(14.0, −60.0)
POC
(16.0,−145.0)
SCS
(16.0, 112.5)
AVI
(18.0, −65.0)
MEX
(18.0, −97.5)
SCS
(18.0, 112.5)
DSI
(20.0, 117.5)
KUM
(20.0,−155.0)
POC
(20.0,−140.0)
SCS
(22.0, 115.0)
ASK
(24.0, 5.0)
LLN
(24.0, 120.0)
KEY
(26.0, −80.0)
POC
(26.0,−140.0)
IZO
(28.0, −17.5)
MID
(28.0,−177.5)
POC
(30.0,−135.0)
WIS
(30.0, 35.0)
BMW
(32.0, −65.0)
KPA
(32.0,−112.5)
WKT
(32.0, −97.5)
1600
1800
2000
2200
85 90 95 00 05 10 15
Methane molar mixing ratio in ppb
Years

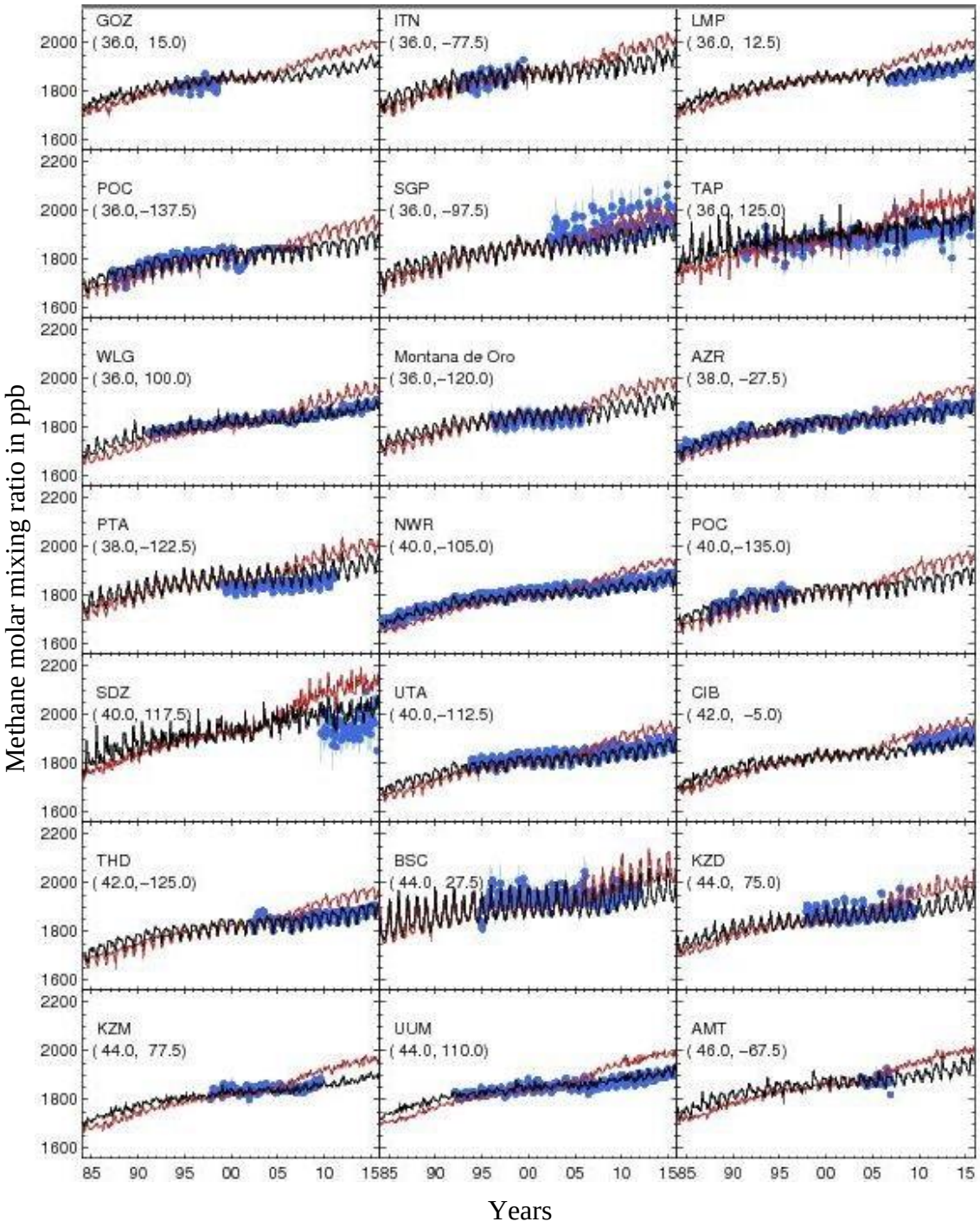
GOZ
(36.0, 15.0)
ITN
(36.0, −77.5)
LMP
(36.0, 12.5)
POC
(36.0,−137.5)
SGP
(36.0, −97.5)
TAP
(36.0, 125.0)
WLG
(36.0, 100.0)
Montana de Oro
(36.0,−120.0)
AZR
(38.0, −27.5)
PTA
(38.0,−122.5)
NWR
(40.0,−105.0)
POC
(40.0,−135.0)
SDZ
(40.0, 117.5)
UTA
(40.0,−112.5)
CIB
(42.0, −5.0)
THD
(42.0,−125.0)
BSC
(44.0, 27.5)
KZD
(44.0, 75.0)
KZM
(44.0, 77.5)
UUM
(44.0, 110.0)
AMT
(46.0, −67.5)
1600
1800
2000
2200
85 90 95 00 05 10 15
Methane molar mixing ratio in ppb
Years

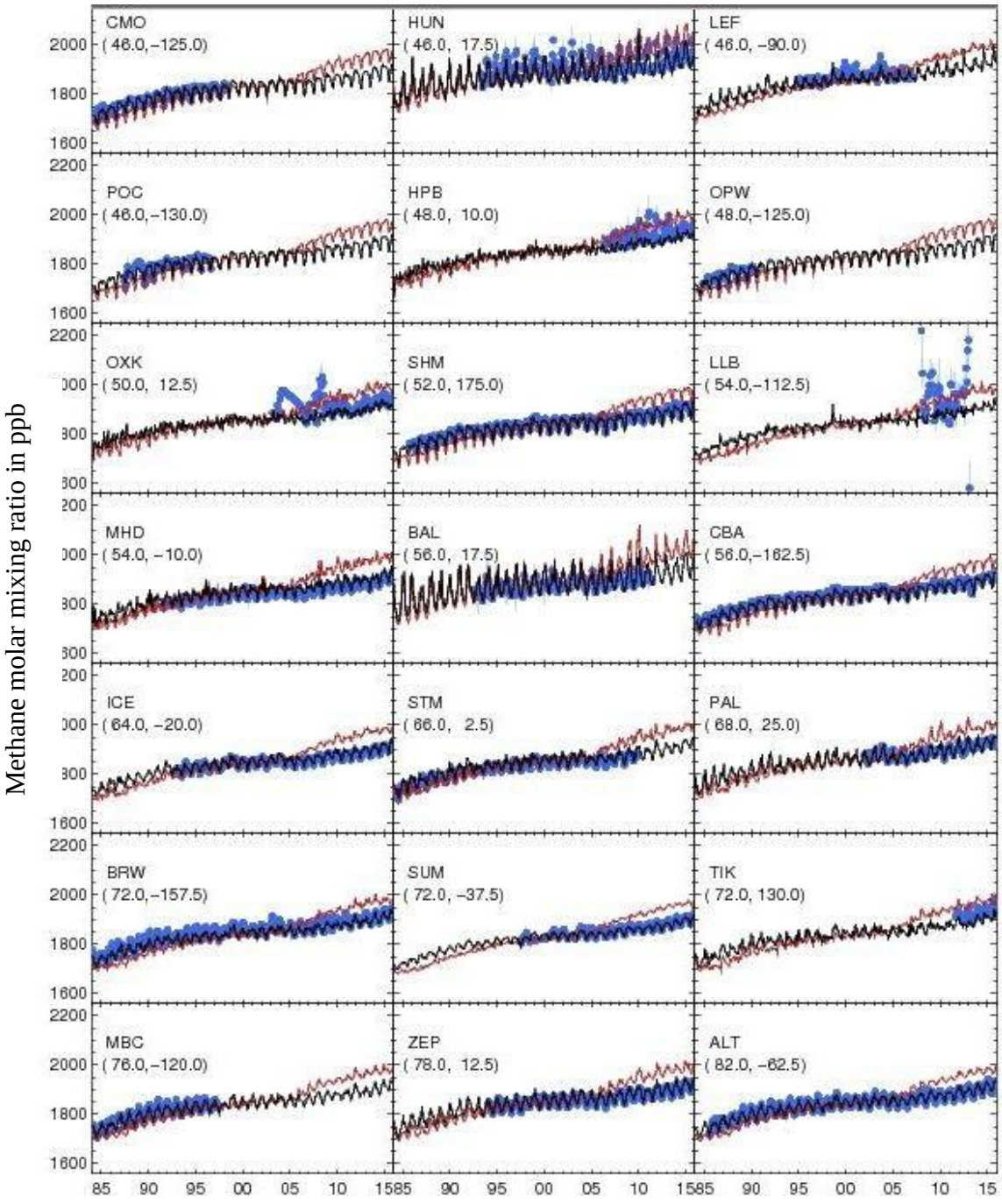

Methane molar mixing ratio in ppb

Years

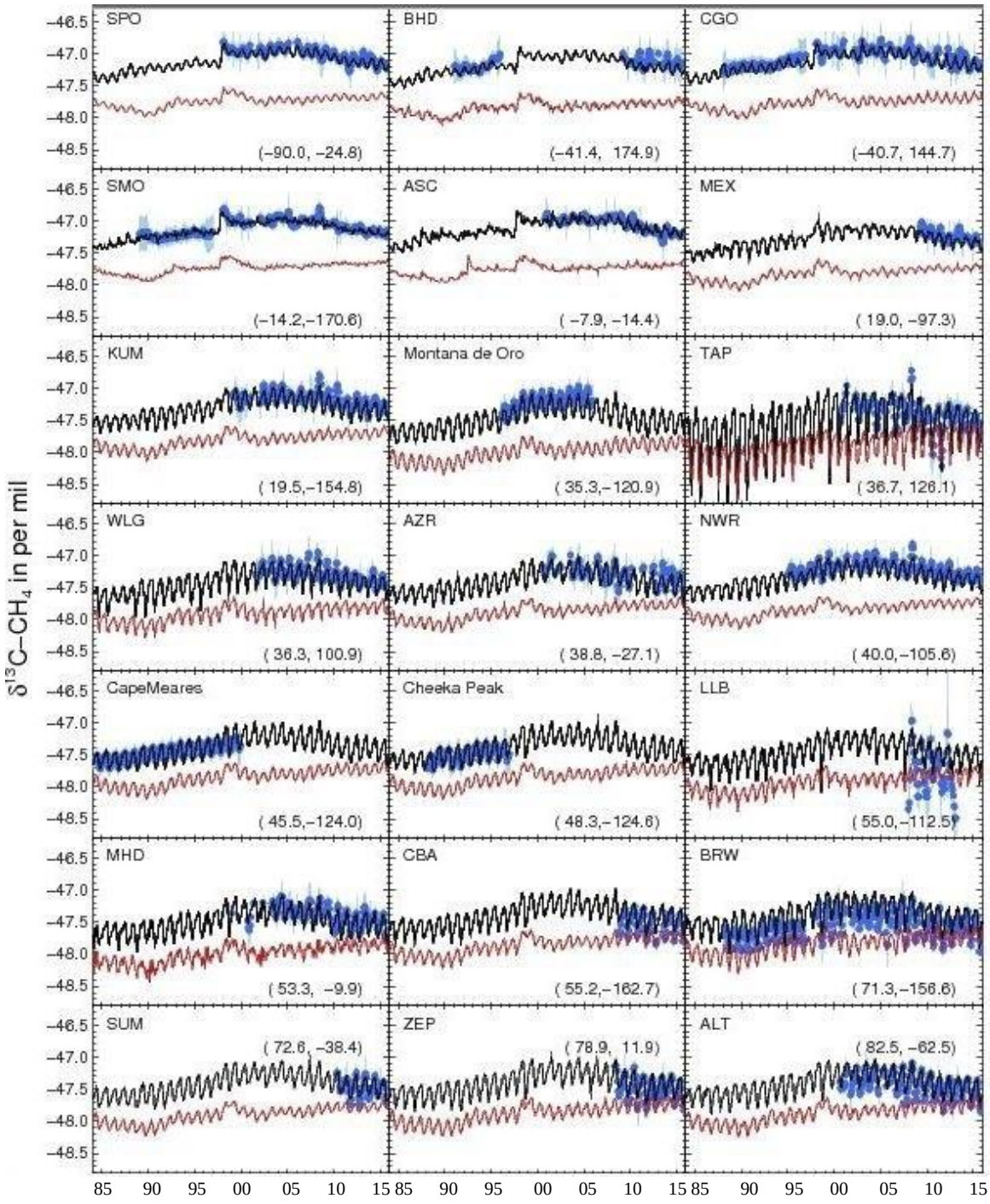
SPO
(–90.0, –24.8)
BHD
(–41.4, 174.9)
CGO
(–40.7, 144.7)
SMO
(–14.2,–170.6)
ASC
(–7.9, –14.4)
MEX
(19.0, –97.3)
KUM
(19.5,–154.8)
Montana de Oro
(35.3,–120.9)
TAP
(36.7, 126.1)
WLG
(36.3, 100.9)
AZR
(38.8, –27.1)
NWR
(40.0,–105.6)
CapeMeares
(45.5,–124.0)
Cheeka Peak
(48.3,–124.6)
LLB
(55.0,–112.5)
MHD
(53.3, –9.9)
CBA
(55.2,–162.7)
BRW
(71.3,–156.6)
SUM
(72.6, –38.4)
ZEP
(78.9, 11.9)
ALT
(82.5, –62.5)
–46.5
–47.0
–47.5
–48.0
–48.5
85 90 95 00 05 10 15
δ13C–CH4 in per mil
Years

Table 5.1: List of observed mixing ratios (in ppbv), modeled mixing ratios (in ppbv) and total uncertainties in observations for all 105 NOAA measurement sites with their corresponding site code, location name, latitude, longitude and elevation (in meters).

Site Code	Location Name	Latitude	Longitude	Elevation (meters)	Observed mix ratio (ppbv)	Modeled mix ratio (ppbv)	Total Uncertainties in Observations
ABP	Arembepe, Bahia, Brazil	-12.77	-38.17	1.0	1751.43	1720.47	12.0112
ALT	Alert, Nunavut, Canada	82.45	-62.50	185.0	1845.42	1834.29	7.93945
AMS	Amsterdam Island, France	-37.79	77.53	55.0	1624.99	1702.71	7.88537
AMT	Argyle, Maine, USA	45.03	-68.68	53.0	1876.51	1855.80	14.8516
AOC	Atlantic Ocean Cruise	0.00	-25.00	10.00	1760.88	1737.82	11.7218
ASC	Ascension Island, UK	-7.96	-14.40	85.0	1716.32	1718.09	4.07834
ASK	Assekrem, Algeria	23.26	5.63	2710.0	1813.68	1782.30	6.69782
AVI	St. Croix, Virgin Islands, USA	17.75	-64.75	3.0	1700.80	1776.79	7.90110
AZR	Terceira Island, Azores, Portugal	38.76	-27.37	19.0	1810.43	1810.09	12.0246

BAL	Baltic Sea, Poland	55.35	17.22	3.0	1881.46	1881.07	30.7385
BHD	Baring Head Station, New Zealand	-41.40	174.87	85.0	1748.45	1711.78	12.5436
BKT	Bukit Kototabang, Indonesia	-0.20	100.31	845.0	1829.84	1771.78	26.3394
BMW	Tudor Hill, Bermuda, UK	32.26	-64.87	30.0	1822.91	1807.36	17.2039
BRW	Barrow Atmospheric Baseline Observatory, USA	71.32	-156.61	11.0	1846.13	1834.65	10.7847
BSC	Black Sea, Constanta, Romania	44.17	28.66	0.0	1940.71	1901.26	34.7971
CBA	Cold Bay, Alaska, USA	55.21	-162.72	21.3	1833.17	1825.63	5.91210
CGO	Cape Grim, Tasmania, Australia	-40.68	144.69	94.0	1708.22	1708.52	9.96606
CHR	Christmas Island, Republic of Kiribati	1.70	-157.15	0.0	1732.75	1728.59	8.68016
CIB	Centro de Investigacion de la Baja Atmosfera (CIBA), Spain	41.81	-4.93	845.0	1899.48	1818.28	12.4270
CMO	Cape Meares, Oregon, USA	45.47	-123.96	30.0	1776.19	1816.14	16.9944

CPT	Cape Point, South Africa	-34.35	18.48	230.0	1769.02	1706.78	7.00439
CRZ	Crozet Island, France	-46.43	51.84	197.0	1728.36	1703.03	6.16016
DRP	Drake Passage	-59.00	-64.69	0.0	1745.93	1702.98	9.94414
DSI	Dongsha Island, Taiwan	20.69	116.73	3.0	1871.48	1807.66	33.4112
EIC	Easter Island, Chile	-27.16	-109.42	47.0	1734.42	1701.25	4.26751
GMI	Mariana Islands, Guam	13.38	144.65	0.0	1762.84	1759.34	9.43753
GOZ	Dwejra Point, Gozo, Malta	36.04	14.88	1.0	1828.88	1839.86	15.2862
HBA	Halley Station, Antarctica, UK	-75.60	-26.21	30.0	1701.72	1702.85	6.27646
HPB	Hohenpeissenberg, Germany	47.80	11.02	936.0	1921.95	1841.27	20.9232
HUN	Hegyhatsal, Hungary	46.95	16.65	248.0	1917.99	1877.71	26.6978
ICE	Storhofdi, Vestmannaeyjar, Iceland	63.40	-20.28	118.0	1857.23	1835.88	6.59746

ITN	Grifton, North Carolina, USA	35.36	-77.39	8.0	1853.76	1861.69	26.1154
IZO	Izana, Tenerife, Canary Islands, Spain	28.30	-16.49	2372.9	1811.89	1785.58	8.93626
KCO	Kaashidhoo, Republic of Maldives	4.97	73.47	1.0	1772.23	1763.14	24.3575
KEY	Key Biscayne, Florida, USA	25.66	-80.15	1.0	1797.14	1809.69	24.6543
KPA	Kitt Peak, Arizona, USA	32.00	-112.00	2083.0	1700.12	1785.11	29.8287
KUM	Cape Kumukahi, Hawaii, USA	19.56	-154.88	8.0	1780.81	1781.63	8.43999
KZD	Sary Taukum, Kazakhstan	44.08	76.87	595.0	1877.34	1845.29	14.7908
KZM	Plateau Assy, Kazakhstan	43.25	77.88	2519.0	1842.65	1814.51	11.7095
LEF	Park Falls, Wisconsin, USA	45.94	-90.27	472.0	1873.20	1848.62	14.5368
LLB	Lac La Biche, Alberta, Canada	54.95	-112.46	540.0	1941.34	1832.19	57.4941
LLN	Lulin, Taiwan	23.47	120.87	2862.0	1840.94	1797.39	19.6813

LMP	Lampedusa, Italy	35.51	12.63	45.0	1877.81	1840.90	11.2236
MBC	Mould Bay, Northwest Territories, Canada	76.24	-119.35	30.0	1798.84	1835.32	6.02818
MCM	McMurdo Station, Antarctica, USA	-77.83	166.60	11.0	1621.32	1702.86	12.1148
MEX	High Altitude Global Climate Observation Center, Mexico	18.98	-97.31	4464.0	1830.33	1762.12	9.54460
MHD	Mace Head, County Galway, Ireland	53.32	-9.89	5.0	1847.74	1840.98	17.4193
MID	Sand Island, Midway, USA	28.21	-177.36	4.6	1804.00	1792.95	9.95521
MKN	Mt. Kenya, Kenya	-0.06	37.29	3644.0	1786.47	1748.93	13.2518
NAT	Farol De Mae Luiza Lighthouse, Brazil	-5.79	-35.18	50.0	1787.03	1725.03	16.4415
NMB	Gobabeb, Namibia	-23.58	15.03	456.0	1747.24	1715.60	12.7202
NWR	Niwot Ridge, Colorado, USA	40.05	-105.58	3523.0	1800.67	1790.51	9.80435
NZL	Kaitorete Spit, New Zealand	-43.83	172.63	3.0	1599.91	1703.83	2.71497

OPW	Olympic Peninsula, Washington, USA	48.30	-124.62	486.0	1756.00	1815.30	14.8446
OXK	Ochsenkopf, Germany	50.03	11.80	1022.0	1920.87	1844.49	20.2667
PAL	Pallas-Sammaltunturi, GAW Station, Finland	67.97	24.11	565.0	1891.44	1851.53	11.7673
PAO	Pacific- Atlantic Ocean	-30.00	-152.5	10.0	1773.53	1703.52	11.7266
POC	Pacific Ocean Cruise (0N)	0.00	-155.0	0.0	1740.65	1725.24	10.6114
POC	Pacific Ocean Cruise (5N)	5.00	-150.0	0.0	1750.17	1739.76	16.4426
POC	Pacific Ocean Cruise (10N)	10.0	-150.0	0.0	1775.36	1758.86	17.6733
POC	Pacific Ocean Cruise (15N)	15.0	-145.0	0.0	1786.79	1778.39	15.5298
POC	Pacific Ocean Cruise (20N)	20.0	-142.0	0.0	1796.90	1788.76	16.9453
POC	Pacific Ocean Cruise (25N)	25.0	-140.0	0.0	1811.38	1796.33	15.4847
POC	Pacific Ocean Cruise (30N)	30.0	-135.0	0.0	1814.66	1801.68	17.7973

POC	Pacific Ocean Cruise (35N)	35.0	-137.5	0.0	1803.71	1804.73	18.9575
POC	Pacific Ocean Cruise (40N)	40.0	-135.0	0.0	1784.42	1808.76	17.2250
POC	Pacific Ocean Cruise (45N)	45.0	-130.0	0.0	1794.38	1814.56	17.6244
POC	Pacific Ocean Cruise (5S)	-5.0	-160.0	0.0	1734.60	1721.92	9.76386
POC	Pacific Ocean Cruise (10S)	-10.0	-160.0	0.0	1730.20	1714.58	8.58279
POC	Pacific Ocean Cruise (20S)	-20.0	-175.0	0.0	1719.53	1706.68	8.53313
POC	Pacific Ocean Cruise (25S)	-25.0	-170.0	0.0	1718.42	1705.06	9.13451
POC	Pacific Ocean Cruise (30S)	-30.0	-175.0	0.0	1718.27	1703.99	9.96132
POC	Pacific Ocean Cruise (35S)	-35.0	-180.0	0.0	1710.92	1704.44	9.99928
PSA	Palmer Station, Antarctica, USA	-64.77	-64.05	10.0	1702.61	1702.72	4.12632
PTA	Point Arena, California, USA	38.95	-123.74	17.0	1846.77	1858.54	18.3974

RPB	Ragged Point, Barbados	13.16	-59.43	15.0	1786.51	1774.00	6.46079
SCS	South China Sea (3N)	3.00	105.00	15.0	1759.01	1780.28	64.9477
SCS	South China Sea (6N)	6.00	107.00	15.0	1762.18	1769.47	19.5373
SCS	South China Sea (9N)	9.00	109.00	15.0	1763.52	1784.19	23.6392
SCS	South China Sea (12N)	12.00	111.00	15.0	1774.87	1800.70	22.3732
SCS	South China Sea (15N)	15.00	113.00	15.0	1782.42	1800.67	21.6552
SCS	South China Sea (18N)	18.00	113.50	15.0	1788.47	1814.90	30.8362
SCS	South China Sea (21N)	21.00	114.00	15.0	1802.67	1872.42	65.3227
SDZ	Shangdianzi, China	40.65	117.11	293.0	1951.58	1931.28	58.7823
SEY	Mahe Island, Seychelles	-4.68	55.53	2.0	1729.37	1729.56	14.4184
SGI	Bird Island, South Georgia, UK	-54.00	-38.05	30.0	1670.02	1703.68	12.7959

SGP	Southern Great Plains, Oklahoma, USA	36.60	-97.48	314.0	1933.73	1834.79	34.6426
SHM	Shemya Island, Alaska, USA	52.71	174.12	23.0	1841.96	1827.55	7.39247
SMO	Tutuila, American Samoa	-14.24	-170.56	42.0	1709.85	1710.54	4.92672
SPO	South Pole, Antarctica, USA	-89.98	-24.80	2810.0	1702.17	1703.40	3.37086
STM	Ocean Station M, Norway	66.00	2.00	0.0	1820.66	1844.51	7.58497
SUM	Summit, Greenland	72.59	-38.42	3209.5	1856.38	1818.26	4.53202
SYO	Syowa Station, Antarctica, Japan	-69.01	39.59	14.0	1714.07	1702.83	9.30828
TAP	Tae-ahn Peninsula, Republic of Korea	36.73	126.13	16.0	1888.73	1893.78	34.2578
THD	Trinidad Head, California, USA	41.05	-124.15	107.0	1862.27	1813.01	8.06771
TIK	Hydrometeorological Observatory of Tiksi, Russia	71.59	128.88	19.0	1926.85	1832.29	10.6897
USH	Ushuaia, Argentina	-54.84	-68.31	12.0	1735.57	1704.57	8.45644

UTA	Wendover, Utah, USA	39.90	-113.71	1327.0	1836.51	1798.60	11.1868
UUM	Ulaan Uul, Mongolia	44.45	111.09	1007.0	1858.06	1836.76	11.5237
WIS	Weizmann Institute of Science at the Arava Institute, Ketura, Israel	29.96	35.06	151.0	1867.06	1822.09	16.4558
WKT	Moody, Texas, USA	31.31	-97.32	251.0	1887.73	1822.91	39.2672
WLG	Mt. Waliguan, Peoples Republic of China	36.28	100.89	3810.0	1834.60	1806.19	11.5788
WPC	Western Pacific Cruise (30S)	-30.0	167.5	0.00	1758.33	1704.41	19.2124
ZEP	Ny-Alesund, Svalbard, Norway and Sweden	78.90	11.88	474.0	1866.15	1842.69	6.55654
Montana de Oro	Montana de Oro, California, USA	35.3	-120.9	281.0	1839.20	1834.26	26.4605

5.1.2. Interannual Variability in CH_4 Emissions from Different Sources

For all 10 basic source categories namely gas and oil, coal, livestock, waste, biomass burning from C3 vegetation and C4 vegetation, rice and wetlands (90N-30N, 30N-0 and 0-90S), the interannual changes of the optimized methane emissions for time period of 01/1983 to 12/2015 are shown in Figure 5.2.

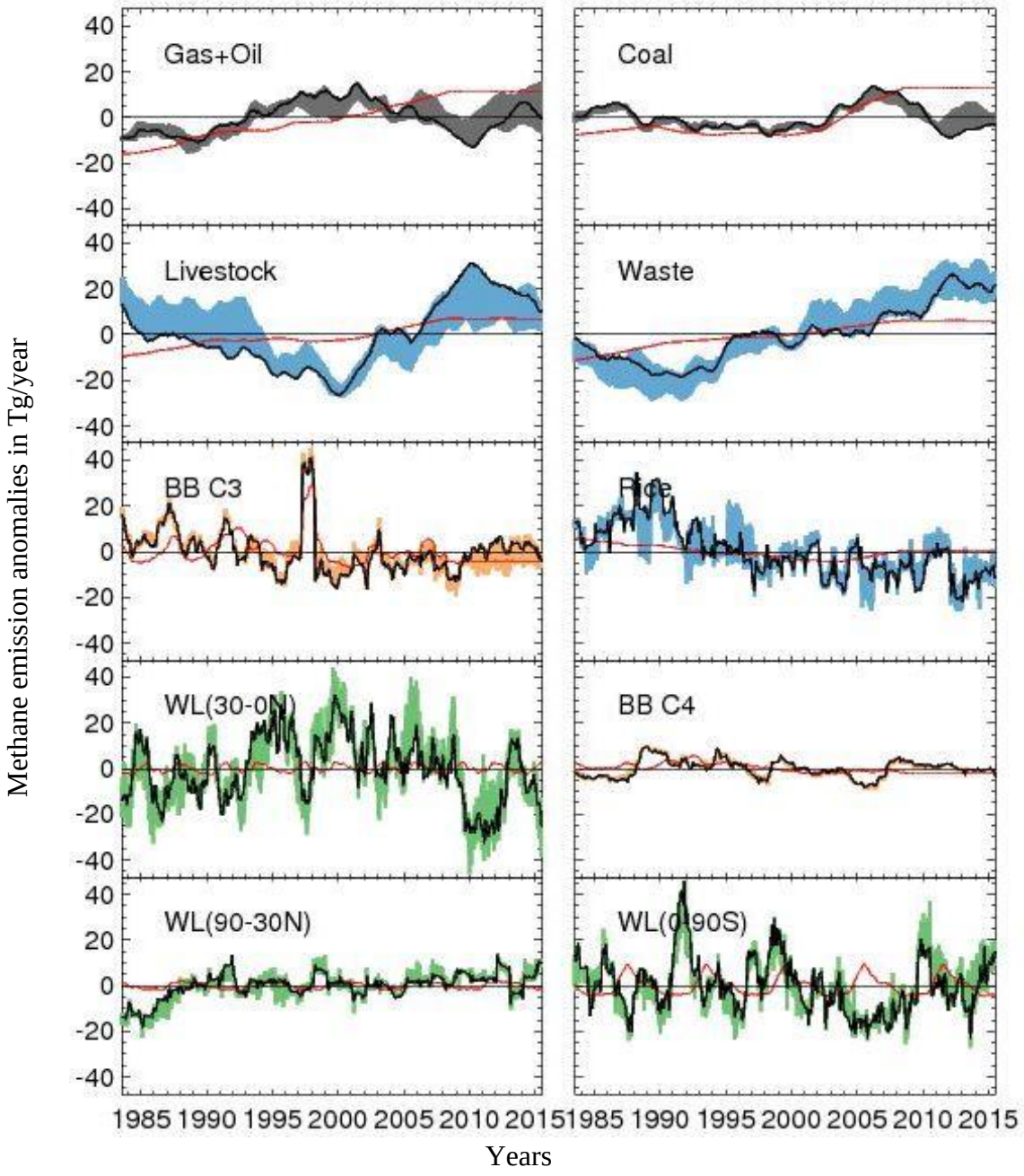

Figure 5.2: *Deseasonalized CH_4 emission anomalies from 10 separate source categories.* ***Black lines*** *indicate the base inversion results.* ***Red lines*** *indicate anomalies in the prior emissions. Shaded* ***colored areas*** *represent the variations in the inversion scenarios using different observational network densities. Note: 2007 onwards recent upward trends are observed in the Wetlands (0-90S) emissions, Livestock and Wastes; and downward trends in Biomass Burning, Wetlands (30-0N) and Rice agriculture categories.*

The interannual changes in optimized emissions from aggregated source categories for

fossil fuel, wetlands, biomass burning, biogenic, anthro-biogenic and total emissions for time period of 01/1983 to 12/2015 are depicted in Figure 5.3.

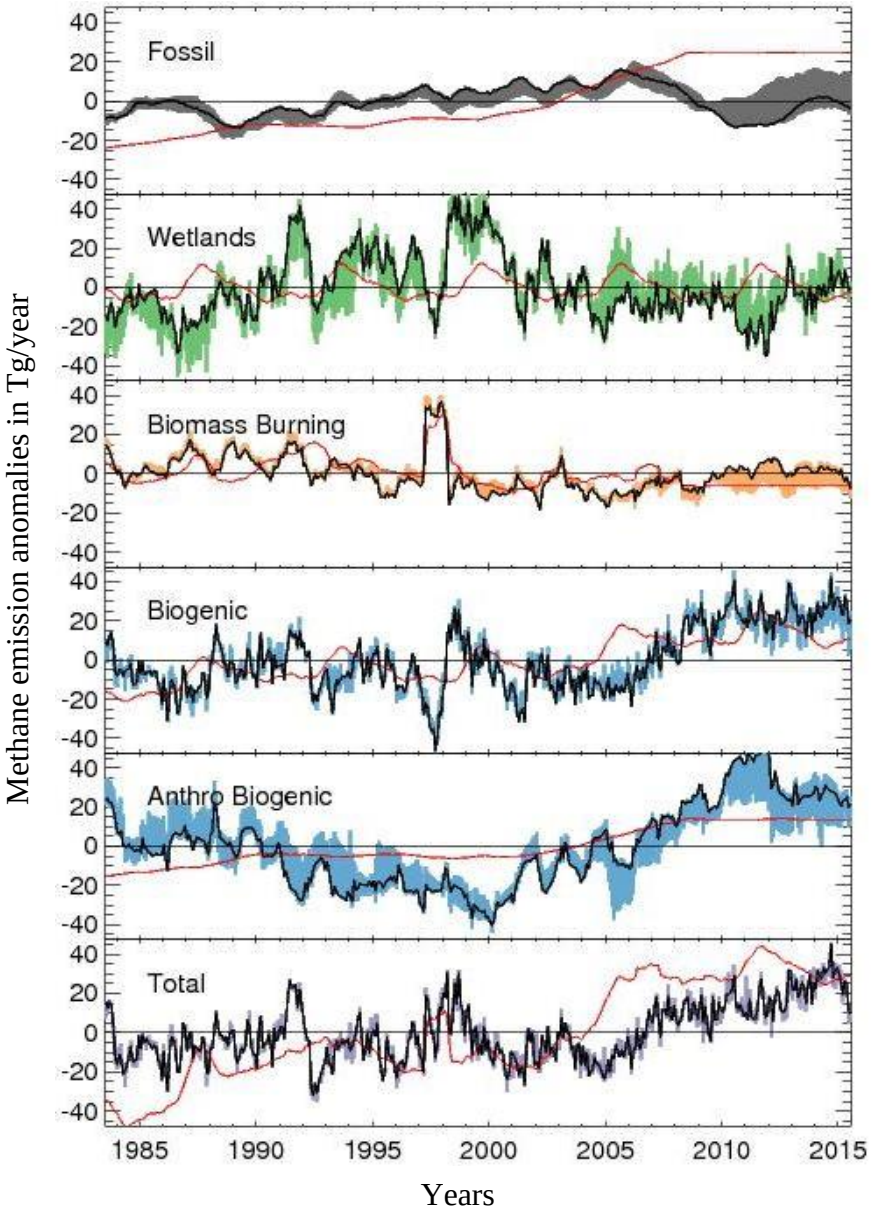

Figure 5.3: *Deseasonalized CH_4 emission anomalies from aggregated fossil fuels, biomass burning, wetlands, biogenic (including wetlands), anthro-biogenic (rice, livestock and waste) and total emissions.* ***Black lines*** *indicate the standard inversion results.* ***Red lines*** *indicate anomalies in the prior emissions. Shaded* ***colored areas*** *represent the variation in the observational network density of the inversion scenarios. Note: 2007 onwards, recent upward trends in the total methane emissions are dominated by increase in all biogenic emissions both from natural and anthropogenic sources.*

The shaded areas in the plots illustrate the robustness of the anomalies across the sensitivity tests. The anomalies are calculated by subtracting the long-term means over the full time period of simulation from the deseasonalized i.e., 12 months running mean estimates of the emissions. As already mentioned in Section 4.2 that the prior emissions from wetlands used a six-year cycle with the limited amount of meteorological data, however, the figures demonstrate that this behavior does not seem to influence the final estimates, with the inversion results mostly driven by the observations and almost independent of the a priori values.

As seen in Figure 5.2, the results from the inversion analysis indicate that the emission rate of all anthropogenic sources (biomass burning not included) increased over the entire study period with significant rise of emissions from fugitive fossil fuel i.e., gas and oil until 2001 and again 2010 onwards and coal until 2006 and again 2011 onwards, ruminant livestock from 2000 to 2010 and waste management emissions from 1994 onwards. In Figure 5.3 the time-dependent relative contributions of aggregated categories to the total deseasonalized emission anomalies are shown. In Figure 5.3, category 'Fossil' contains the combined emission anomalies from sources 'gas and oil' and 'coal'; category 'Wetlands' contains the same from sources 'Wetlands (90N-30N, 30N-0, 0-90S)'; category 'Biomass Burning' contains the same from 'Biomass Burning C3 and C4' sources; category 'Biogenic' contains the same from sources 'Livestock', 'Waste', 'Rice' and all three zones of 'Wetlands'; category 'Anthro Biogenic' contains the same from sources 'Livestock', 'Waste' and 'Rice'; and category 'Total' contains the same from all sources. It can be inferred from Figures 5.2 and 5.3 that the wetlands are the largest contributor to the inter-

annual variability and growth rate of methane emissions over the inversion time period because of the similarities found on the phase patterns of the plots of aggregated wetland, all biogenic, and total emissions. Within this variability, the wetland source emissions had increased during 1984–2000, but the following decade 2000–2010 experienced a significant decrease in emissions from wetland sources (30-0N, 0-90S) and during this current decade after 2011 onwards, again an increase is found in wetland CH_4 emissions from all three zones. The wetland emissions appeared to be the primary cause of 1991-1993 anomaly in the total aggregated category of emissions, large biomass burning emission in 1997 also with elevated wetland emissions in 1998 may have contributed to the 1997-1998 anomaly in the total emission category. Although highly variable, rice emissions decrease significantly over the entire modeled period 1984–2015. The biomass-burning emissions show smaller contribution toward interannual variability except the large emission during the 1997–1998 anomaly. However, a negative emission trend is found from biomass burning over most of the period 1991–2005 and during current decade, a little rise can be detected in the figures. However, the derived anomalies from all source categories are noted to depend on the assumption of constant OH. Overall increases in biomass burning, wetland emissions, biogenic emissions due to rising livestock and waste emissions, and the enhanced emissions from fossil fuels cause total methane emissions to rise markedly after 2005.

5.1.3. Results of Sensitivity Tests

In this work, sensitivity tests were conducted to assess the impact of discontinuity in the

data coverage over the entire time of inversion for different observation sites on the methane flux trends. Seven different sensitivity tests were performed where the number of observational sites was varied based on the number of years with continuous availability of data. The sensitivity test inversion scenarios for all of the source categories maintained same trends of methane emissions throughout the study period as base case inversion scenarios discussed above but, in some cases, with significantly wider range in the mean values of the emissions. It can be observed from Figure 5.3 that aggregated fossil fuels and anthro-biogenic sources and from Figure 5.2 that sources of gas and oil, coal, livestock and wastes categories are more sensitive to the variation of network densities of observation sites with continuous data coverage. Combined fossil fuel (Figure 5.3) and gas and oil (Figure 5.2) showed significantly higher range in the mean values of the emission anomalies from 2005 onwards, while coal (Figure 5.2) emissions had higher values from 2010 onwards. The methane emissions from sensitivity tests for livestock showed significantly wider range in the mean values with ensemble spread much higher than the mean anomaly trendline from beginning of study period until 2000 and much lower from 2000 until the end of the study period, whereas wastes emissions showed contrasting ensemble spread of much lower than the anomaly mean trendline from start year until 2000 and much higher from 2000 to end year (Figure 5.2). The sensitivity tests for rice showed significantly wider range in the mean values of the emissions during few time spans such as 1988-1989, 1992-1993, 1994-1996, 2005-2006, 2009-2011 and 2013-2014 (Figure 5.2). The sensitivity test emissions from livestock, landfilled wastes and rice cultivation aggregated together as anthro-biogenic category showed significantly wider range in the mean values of the emissions with higher ensemble spread from the beginning of the study

period until 2000 and then trending lower ensemble spread from 2000 until the end of the study period (Figure 5.3). Significant wider range in the mean values of the emissions were also observed for combined Wetlands since start year until 1994 and then again since 2004 onwards until end year (Figure 5.3) and also for different geographically separated wetland regions (Figure 5.2) such as throughout the study period for Wetlands (30^0N-0^0) and since 2009 onwards for Wetlands (0^0-90^0S). Lastly, the sensitivity test scenarios for biomass burning showed significant wider range in the mean values of the emissions after 2010 as seen in total biomass-burning (Figure 5.3) and biomass-burning from C3 vegetation (Figure 5.2).

5.1.4. Global Methane Emission estimates per source category

The inversion modeled estimates of emissions from ten different source categories and aggregated categories averaged over the entire time period of 01/1983 to 12/2015 are presented in Table 5.2. The *a priori* and *a posteriori* emission estimates in Tg/Year are obtained from the base standard inversion with errors on optimized estimates from the calculated standard deviations and isotopic signatures are presented in per mil for all source categories. The ensemble spread shows the range of minimum and maximum estimates of emissions in Tg/Year obtained from the results of different sensitivity inversions with extrema sensitivity test scenarios presented in parenthesis.

The results of this work reveal that the total averaged global methane emission over years of 1983 to 2015 is estimated to be 530±50 Tg/year. The global methane emissions over

these years from all biogenic sources of both natural and anthropogenic origin account for ~73% of the total global CH_4 emissions. Anthro-biogenic sources contribute about 39% of the total CH_4 emissions, whereas natural wetlands contribute about 34.5% of the total CH_4 emissions. Moreover, emissions from combined natural wetlands account for ~47% of the total all-biogenic emissions, whereas emissions from anthro-biogenic sources account for ~53% of the total all-biogenic emissions. The emissions from livestock accounts for ~37%, wastes accounts for ~30% and rice accounts for ~33% of the total anthro-biogenic emissions. Further, the relative contribution of combined natural wetlands can be attributed to the partitioned contributions of emissions from wetlands (90N-30N) of ~22%, from wetlands (30N-0) of ~46% and from wetlands (0-90S) of ~32% of the total emissions from combined wetlands. Fossil fuels sector contributes about 18.5% of the total global CH_4 emissions, within which ~60% of the contribution is accounted from gas and oil sources and ~40% from coal mining. Biomass burning contributes about 8.3% of the total global CH_4 emissions. However, biomass burning of C3 vegetation contributes ~64% and of C4 vegetation contributes ~34% of the total biomass burning emissions.

Table 5.2: Modeled Global Methane budget and isotopic signatures averaged over time period of 01/1983 to 12/2015 with a priori and a posteriori emission estimates by source category. The a priori and a posteriori values are obtained from the base standard inversion with errors on optimized estimates from the calculated standard deviations. The ensemble spread shows the range of minimum and maximum estimates of emissions obtained from the results of different sensitivity inversions with extrema sensitivity test scenarios (as in Table 4.2) presented in parenthesis.

Source Category	*a prioiri* (Tg/year)	*a posteriori* (Tg/year)	$\delta^{13}C\text{-}CH_4$ (‰)	Ensemble Spread (Tg/year)	
				Min	Max
Fossil Fuels	98±38	98±5		95±6 (S2d)	103±7 (S2g)
Gas and Oil	57±31	59±4	-44.00	56±4 (S2e)	63±6 (S2g)
Coal	41±23	39±4	-37.30	39±4 (S2a)	41±4 (S2f)
Anthro-Biogenic	207±82	205±23		194±24 (S2f)	207±24 (S2d)
Livestock	104±56	75±6	-62.00	62±5 (S2f)	76±5 (S2a)
Waste and Termites	66±36	62±7	-55.30	62±7 (S2a)	72±7 (S2d)
Rice	37±48	67±22	-63.00	59±24 (S2g)	70±22 (S2e)
Biomass Burning	32±30	44±17		40±18 (S2g)	44±17 (S2b)
Biomass Burning C3	23±29	28±16	-26.50	24±17 (S2g)	29±17 (S2b)
Biomass Burning C4	9±10	15±9	-7.40	15±9 (S2f)	15±9 (S2b)
Wetlands	160±112	183±46		183±46 (S2a)	194±47 (S2f)
Wetlands (90N-30N)	27±41	40±9	-63.40	39±11 (S2d)	42±12 (S2f)
Wetlands (30N-0)	53±57	84±35	-58.00	83±35 (S2c)	90±36 (S2f)
Wetlands (0-90S)	81±87	58±33	-58.00	58±34 (S2g)	62±33 (S2f)
All Biogenic	368±139	388±51		387±55 (S2g)	391±52 (S2d)
Total	498±148	530±50		529±52 (S2f)	530±50 (S2b)

5.1.5. Global Methane Budget for over Three Decades

The global budget of methane emissions from different source categories for over three decades is presented in Table 5.3. The modeled methane emission estimates per source category in Tg/year are averaged over entire time period of 01/1983 to 12/2015, then separately averaged over time period of 01/1983 to 12/1993, next over time period of 01/1994 to 12/2005 and then over decade of 01/2006 to 12/2015. For the last decade, the global budget of methane emissions per source category are also obtained separately averaged over years of 01/2006 to 12/2010 and of 01/2011 to 12/2015. The emission estimates in Tg/year are obtained from base standard inversion case with errors obtained from the calculated standard deviations. The results in this table reveal the changes in the contribution of methane emissions from each source category in decadal scale. The source attributions for over three separate decades help us in better understanding the causes behind the long-term slowdown of methane growth rate during 1990s to early 2000s, as well as the sudden increase in methane growth rate after 2006 onwards. The total averaged global methane emission in the decade of 2006-2015 is estimated to be 543±44 Tg/year which is ~20 Tg/year more than that during previous decade, during 2006-2010 it is estimated to be 539±44 Tg/year, whereas during 2011-2015, the estimated emission reached 547±45 Tg/year. The averaged emission estimate of all biogenic sources (both natural and anthropogenic) shows an increase of about ~25 Tg/year during 2006-2015 than that during 1994-2005, whereas the anthro-biogenic sources show highest increase in averaged emission estimate of about ~43 Tg/year during 2006-2015 than that during 1994-2005.

Table 5.3: Global budget of methane emissions per source category for over entire time period (01/1983-12/2015), over three separate decades (01/1983-12/1993, 01/1994-12/2005, 01/2006-12/2015) and then over separate time periods of 01/2006-12/2010 and 01/2011-12/2015. The averaged emission estimates in Tg/year are obtained from base standard inversion with errors obtained from the calculated standard deviations.

Source Category	Emission Estimates (Tg/year)					
	01/1983-12/2015	01/1983-12/1993	01/1994-12/2005	01/2006-12/2015	01/2006-12/2010	01/2011-12/2015
Fossil Fuels	98±5	92±6	104±5	96±5	99±5	93±5
Gas and Oil	59±4	53±5	66±3	56±3	53±3	60±4
Coal	39±4	39±4	38±3	40±4	46±4	34±3
Anthro-Biogenic	205±23	203±29	187±19	230±20	225±19	234±20
Livestock	75±6	73±7	63±5	94±5	95±6	94±5
Waste and Termites	62±7	49±7	60±6	78±7	71±7	84±7
Rice	67±22	80±28	63±18	58±19	59±18	57±19
Biomass Burning	44±17	50±21	40±16	42±14	40±13	45±14
Biomass Burning C3	28±16	34±20	26±15	27±13	24±13	30±13
Biomass Burning C4	15±9	16±10	15±8	15±6	16±6	15±6
Wetlands	183±46	180±53	192±42	174±41	174±41	175±41
Wetlands (90N-30N)	40±9	36±11	40±8	43±8	43±7	44±8
Wetlands (30N-0)	84±35	81±41	95±32	75±31	78±32	72±30
Wetlands (0-90S)	58±33	63±38	58±30	56±28	54±28	59±29
All Biogenic	388±51	383±61	379±46	404±46	400±45	409±46
Total	530±50	525±60	523±45	543±44	539±44	547±45

It can be observed in the table that mainly the source categories of coal, livestock, wastes, biomass burning of C3 vegetation and northern high latitude wetlands show increase in their averaged emission estimates of ~2 Tg/year, ~31 Tg/year, ~18 Tg/year, ~1 Tg/year and ~3 Tg/year respectively, during the decade of 2006-2015 than that during previous decade. Some changes in the contribution from different source categories have been observed in the table when we consider last decade been divided in separate time periods each spanning for 5 years. For fossil fuel sector, averaged emission estimate from source of gas and oil increases by ~7 Tg/year during 2011-2015 than during 2006-2010, whereas estimate from coal mining decreases by ~12 Tg/year. For anthro-biogenic sector, averaged emission estimate from livestock decreases by ~1 Tg/year, rice decreases by ~2 Tg/year whereas, estimate from waste increases by ~13 Tg/year during 2011-2015 than during 2006-2010. For biomass burning sector, averaged CH_4 emission estimate from burning of C3 vegetation increases by ~6 Tg/year, whereas that of C4 vegetation decreases by ~1 Tg/year during 2011-2015 than during previous 5 years. For source of natural wetlands, averaged emission estimate from wetlands (90N-30N) increases by ~1 Tg/year, from wetlands (0-90S) increases by ~5 Tg/year, whereas from northern tropical wetlands decreases by ~6 Tg/year during 2011-2015 than during 2006-2010. For aggregated categories, the increase in averaged emission estimates during 2011-2015 compared to that during previous 5 years, are mainly from sources of all biogenic (~9 Tg/year), anthro-biogenic (~9 Tg/year), natural wetlands (~1 Tg/year) and biomass burning (~5 Tg/year), whereas fossil fuel source shows a decrease of ~6 Tg/year during the same time period.

5.1.6. Average Seasonal Cycle

The average seasonal cycles of the seasonally varying sources such as rice cultivation, biomass burning from C3 and C4 vegetation, wetlands (90N-30N, 30N-0, 0-90S) and total aggregated sources are shown in Figure 5.4. The seasonality of these sources can be explained better with consideration of weather patterns existed worldwide, as compared to the a priori emissions, depicting that the model simulated a posteriori emissions are overall best representation of the withheld observational data. The optimized emissions show larger peaks for sources of rice cultivation, boreal wetlands and Southern Hemispheric wetlands in comparison to the priors. However, the error bars indicate substantial year-to-year variability. It can be noted that the a priori total emissions peak in August whereas a posteriori total emissions peak in July and September, driven by combined effects of emissions from boreal wetlands, rice cultivation and biomass burning of C3 vegetation. A smaller maximum in April is displayed in the a posteriori total emissions, corresponded to the driving effect of emissions from Southern Hemispheric wetlands. In contrast to priors, Wetlands (30-0N) a posteriori emissions showed two peaks in April and November following the highest rainfall seasons in the tropics during March and September due to interaction between Inter Tropical Convergence Zone (ITCZ) and Monsoons. Our result is consistent with a study by Nisbet et al. (2016) mentioning that wetlands in northern tropics get flooded from runoff in the late rainy season from August-September onwards and later in river-fed swamps. Wetlands (90N-30N) a posteriori emissions corresponded with priors showing larger peak in July consistent with report by Nisbet et al. (2016) that isotopically depleted methane emissions occurring from Arctic and boreal wetlands increased during

late summer (Fisher et al., 2011; Sriskantharajah et al., 2012). Wetlands (0-90S) emissions peaked during March-April just after hot and humid seasons in Southern Hemisphere such as Australia, and Southern Amazon basin. This result is consistent with the fact that wetlands in southern tropics fill up during February-March onward (Nisbet et al., 2016). It also displayed two more secondary smaller peaks during September and November mainly driven by north-south migration of tropical rains occurring in Australia, in the Amazon basin of northern South America, West Africa, Mexico and the U.S. Southwest. In Figure 5.4, tropical seasonal wetland emissions occurring few months later (October-November), are observed to be distinguishable from dry season biomass burning emissions (August-September) from same general regions around equatorial belt and tropics which is also mentioned by Nisbet et al. (2016). Methane emitted from fires in tropical C4 grasslands with $\delta^{13}C\text{-}CH_4$ values around -20‰ to -10‰ occur in Northern Hemisphere during winter (November–February) and in Southern Hemisphere during winter (May–August) (unpublished RHUL results, Dlugokencky et al., 2011 and Nisbet et al., 2016). Similar conclusions can be drawn from our result in Figure 5.4 that biomass burning emissions from C4 vegetation maximized during December-January and from C3 vegetation showed a small peak in June and a larger peak in September. The contribution of biomass-burning emissions toward interannual variability is minor except during the 1997–1998 anomaly and has little impact on meridional distribution of methane (Rice et al., 2016) which is consistent in Figure 5.4. The a posteriori methane emission from rice cultivation in the figure is observed to drastically increase from May onwards but with longer time period spanning until November with larger amplitude than priors maximizing in August which corresponds to the highest rainfall monsoonal season in the tropics. This result is also

supported by Nisbet et al. (2016) mentioning emissions from rice agriculture and fodder growth for ruminants respond to high rainfall, but the impact of year-to-year fluctuations in recent years had been smoothed out due to widespread water storage and improved irrigation facilities in the seasonal tropics.

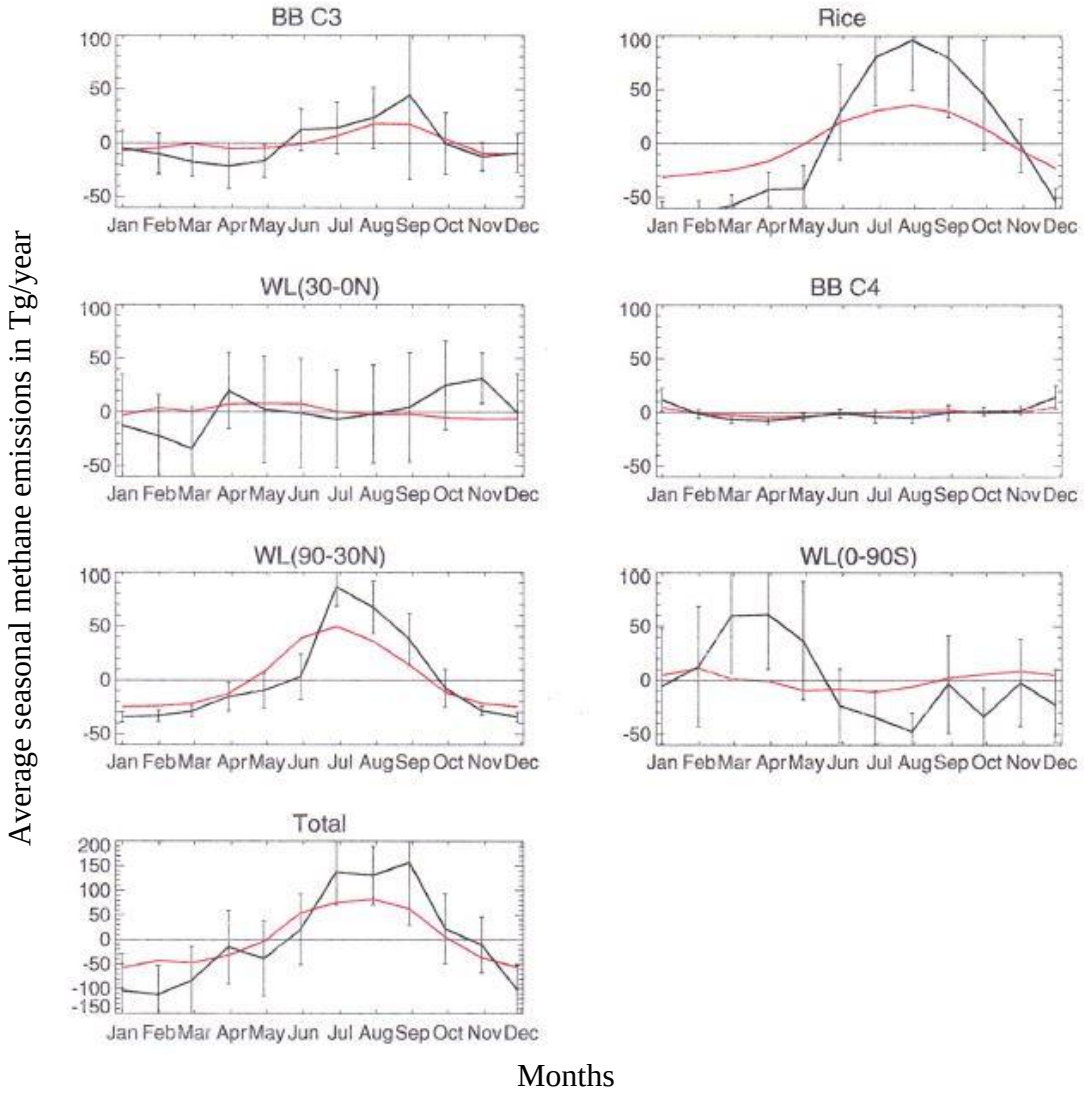

Figure 5.4: *Average seasonal cycles of the inversion modeled emission estimates of seasonally varying sources. The time series of the estimates were detrended by subtracting 12-month running means and then separately averaged for every month of the year. The red line indicates a priori emissions. The black line represents the a posteriori emissions from standard base inversion with error bars indicating the standard deviation of the detrended estimates.*

5.2. Discussion

5.2.1. Comparison of Model-Data Mismatch Errors Between $2^0 \times 2.5^0$ and $4^0 \times 5^0$ Horizontal Grid Resolution

Optimized emissions are sensitive to model-data mismatch errors (described in Section 4.4) as seen in the upper left plot of Figure 5.5. In this plot, the optimized C3 vegetation biomass burning emissions from $4^0 \times 5^0$ horizontal grid resolution base inversion (represented in black) are compared to the emissions from an inversion with reduced model-data mismatch errors (represented in green). The large anomaly in emission during 1997-1998 is significantly smaller for green line which shows the sensitivity of optimized emissions to reducing model-data mismatch errors. One of the motivations to do the current inversion process in higher resolution is to reduce the model-data mismatch errors and increase the weight of the information from the observations. The inversion work presented here based on a horizontal $2^0 \times 2.5^0$ grid resolution was conducted in part to reduce model data mismatch errors. The comparison of the model-data mismatch errors from all sites between $2^o \times 2.5^o$ and $4^o \times 5^o$ horizontal grid resolution are shown in upper right plot of Figure 5.5. In this plot, each red dot represents the ratio of model-data mismatch error (in ppbv) from each of the measurement sites for $2^0 \times 2.5^0$ horizontal grid resolution to that for $4^0 \times 5^0$ horizontal grid resolution. It is noted that $2^o \times 2.5^o$ grid reduces error significantly relative to $4^o \times 5^o$ grid, since almost all of these red dots lie below the 45^o black line. Horizontal grid resolution of $2^0 \times 2.5^0$ is also preferred as it increases information content of observations since model is better able to simulate mixing ratios at

monitoring sites (red dots represent NOAA measurement sites) as shown in bottom panels of Figure 5.5. The background maps in these two bottom plots show the same region of south-east Asia and the colors indicate the range of total methane mixing ratio (in ppbv) as simulated by GEOS-Chem model in two different grid resolutions based on the same observations on November 1997 at surface level L=1. This higher resolution grid allowed us to extract more information from the observations due to improved ability of the model to simulate CH_4 at each station and decreased need to aggregate neighboring stations, leading to more accurate estimates of the retrieved fluxes and improved understanding of the driving sources underlying the current variations in the global methane budget.

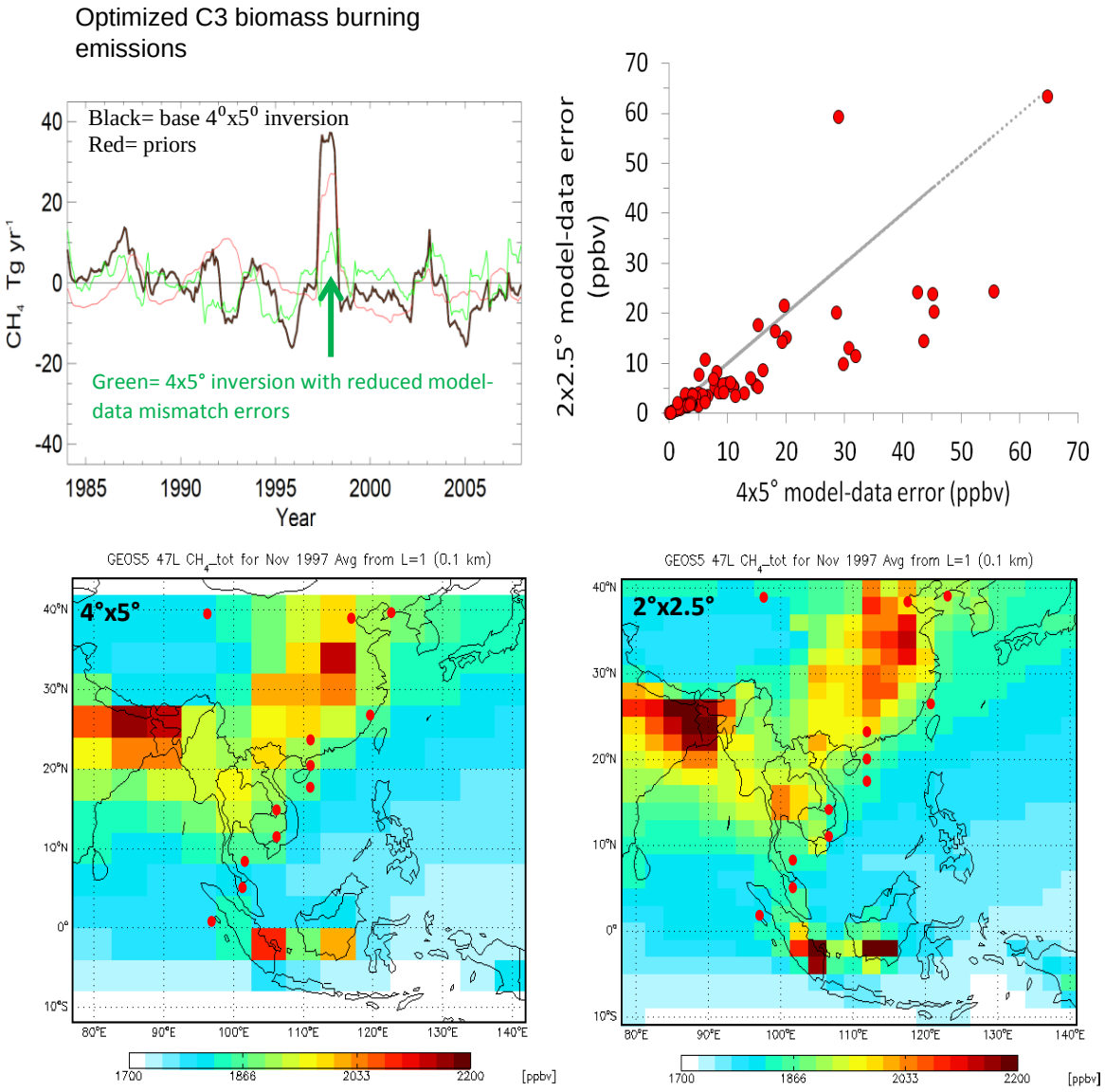

Figure 5.5: *Optimized emissions are sensitive to model-data mismatch errors (upper left). $2^{0} \times 2.5^{0}$ grid reduces error significantly relative to $4^{0} \times 5^{0}$ (upper right) where each red dot represents the ratio of model-data mismatch error (in ppbv) from each of the measurement sites for $2^{0} \times 2.5^{0}$ horizontal grid resolution to that for $4^{0} \times 5^{0}$ horizontal grid resolution. $2^{0} \times 2.5^{0}$ grid resolution increases information content of observations since model is better able to simulate mixing ratios at monitoring sites (bottom panels, red dots are NOAA measurement sites). The background maps in these two bottom plots show the same region of south-east Asia and the colors indicate the range of total methane mixing ratio (in ppbv) as simulated by GEOS-Chem model in two different grid resolutions based on the same observations on November 1997 at surface level L=1. (Reference: Karmakar et al., 2015 at AGU Fall Meeting, 2015, San Francisco CA, 14-18 December 2015, https://agu.confex.com/agu/fm15/meetingapp.cgi/Paper/85278).*

5.2.2. Comparison of Optimized Methane Emission Anomalies from Inversions at $2^0 \times 2.5^0$ and $4^0 \times 5^0$ Horizontal Grid Resolution

One of the main goals of this study was to test how the results of optimized methane emissions would change when using the raw measurement data of CH_4 from NOAA event files in the process of inversion at a higher horizontal grid resolution of $2^o \times 2.5^o$ rather than using much processed GLOBALVIEW data of CH_4 at a coarser horizontal grid resolution of $4^o \times 5^o$. The comparison between the results of optimized methane emissions from this current inversion work ($2^0 \times 2.5^0$) and previously done inversion work ($4^0 \times 5^0$) up through the end of 2008 is presented in this section. Deseasonalized methane emission anomalies of all 10 source categories from $4^0 \times 5^0$ inversion work are shown (upper) and same from $2^0 \times 2.5^0$ inversion work are shown (lower) in Figure 5.6. Deseasonalized methane emission anomalies of aggregated source categories from both inversion works are shown in Figure 5.7. The most prominent differences in the emission anomalies plots between the previous and the current inversions until the end of 2008 can be found in the individual source categories of gas and oil, coal, livestock and waste (Figure 5.6) and in the aggregated source categories of fossil fuels, wetlands and all biogenic (Figure 5.7). These differences are discussed as follows:

Fossil Fuels : The $4^0 \times 5^0$ plots of gas and oil emissions are observed to increase throughout their entire study period from 1984 to 2008 (Rice et al., 2016), whereas the current $2^0 \times 2.5^0$ plots of same indicate a little decrease in late 1980s, followed by increase from 1990 until 2000, then after 2001, again a decrease was observed throughout the

decade (Figure 5.6). In contrast, $4^0 \times 5^0$ plots of emissions from coal sector are observed to decrease in 1980s followed a leveling off in 1990s until 2000, and then a small increase in 2000s (Rice et al., 2016), whereas $2^0 \times 2.5^0$ plots of same show an increase until 1986, followed by a decrease in late 1980s, followed by a leveling off in 1990s until early 2000s, then an increase followed until 2006, and then again, a decrease is observed later in the decade (Figure 5.6). The combined category of fugitive fossil fuel CH_4 emissions as seen in $4^0 \times 5^0$ plots are flat during the period 1984-2000, then increased over next subsequent 9 years (Rice et al., 2016), whereas the same category emissions as seen in $2^0 \times 2.5^0$ plots show some different result with an increase during few years at the beginning of the study period, then a small decrease during late 1980s, followed by a long increase during 1989-2005, then a drop over next subsequent years of the decade (Figure 5.7). The possible reasons behind the recent rise of emissions in this sector for $4^0 \times 5^0$ work, suggested by Rice et al. (2016) were the increased coal mining in China and increased natural gas extraction from the onset of hydraulic fracturing of shale gas as substantiated by other studies (Dlugokencky et al., 2011; Howarth et al., 2011) and emission inventories (EDGAR 4.2, 2011). The possible reasons behind the observed trends for $2^0 \times 2.5^0$ work are detailed in section 5.2.3, when compared with other previous studies. The decrease in emission during late 2000s in the current $2^0 \times 2.5^0$ study may be caused mainly due to the rising economic value of natural gas, emissions linked specifically to the growing natural gas industry and the development of cleaner technologies which may have led to sharp reductions in the release of light hydrocarbons into the atmosphere, including methane and ethane, associated with production and processing of petroleum (Aydin et al., 2011; Simpson et al., 2012; Schaefer et al., 2016).

Livestock and Waste : The $4^0 \times 5^0$ plots of both livestock and waste CH_4 emissions are generally considered to have increased over the entire study period of 1984-2009 (Rice et al., 2016), whereas the current $2^0 \times 2.5^0$ plot of the livestock emissions are observed to decrease from the start of the study period until 2000, followed by an increase throughout the next decade with a small dip during 2003-2005 (Figure 5.6) and plot of the waste emissions indicates a decrease from beginning of the study period until 1991-1992, and then followed a long two decades of increase (Figure 5.6). The possible reasons behind these observed trends for $2^0 \times 2.5^0$ work are detailed in section 5.2.3, when compared with other previous studies. The main difference is the decrease of emissions from both sectors during the beginning of our study period to 2000 for livestock and early 1990s for waste which can be attributed to the slowing of increase in livestock numbers during the 1990s particularly in developed countries (Tubiello et al., 2013; Dangal et al., 2017) and observed high oxidation rates of CH_4 in landfill cover soils (Whalen et al., 1990), and also decline in waste generation in North America during 1980s due to economic downturn and in Europe during early 1990s attributable to the economic situation in the former USSR (Bogner et al., 2003).

Wetlands : The plots of CH_4 emission anomalies from wetlands (30ºN-0º and 0º-90ºS) for both $4^0 \times 5^0$ and $2^0 \times 2.5^0$ inversion studies show similar trends for the entire study period until 2008-2009 except with much larger range in the values for anomalies in Tg/year for $2^0 \times 2.5^0$ plots such as during 1984-1986, the fluctuation in emission anomalies observed from wetlands (30^0N-0^0) for $2^0 \times 2.5^0$ plots ranged from +20 Tg/year to -20 Tg/year, and

again during 2002-2008, the fluctuation in same for $2^0 \times 2.5^0$ plots ranged from +30 Tg/year to -5 Tg/year which are clearly higher than that observed for $4^0 \times 5^0$ plots, during 1990-1992, the fluctuation in emission anomalies observed from wetlands (0^0-90^0S) for $2^0 \times 2.5^0$ plots also varied with much higher values from +45 Tg/year to -10Tg/year as compared to the same observed for $4^0 \times 5^0$ plots (Figure 5.6). The plots of CH_4 emission anomalies from wetlands (30ºN-90ºN) for $2^0 \times 2.5^0$ study started with a lower value of -20 Tg/year approximately during 1984-1985 and increased over next few years to a value of +15 Tg/year during 1991-1992, and then leveled off with a similar trend as compared to that of $4^0 \times 5^0$ plots for the rest of the study period until 2008 (Figure 5.6). The combined wetland category for $4^0 \times 5^0$ study (Figure 5.7) inferred a little increase in the trend of interannual variations in CH_4 emissions during 1984-2000, then the following decade during 2000-2009 experienced a decrease in the trend of the emission anomalies (Rice et al., 2016). In comparison, the same for this current $2^0 \times 2.5^0$ study (Figure 5.7) showed a small increase in the trend at the beginning of the study period, followed by a small decrease until 1987 and then a decade long increase including a large drop in 1997 (also observed in emission from wetlands in northern hemisphere) followed by a sharp rise in 1998 (also observed in emission from wetlands in southern hemisphere) and then the trend experienced a decrease over next subsequent years from 2000 to 2005 and again followed a small increase from 2005 onwards. The possible reasons behind these observed trends for $2^0 \times 2.5^0$ work are detailed in section 5.2.3, when compared with other previous studies. The sharp dip in emissions in 1997 from northern hemisphere wetlands and increase in emissions in 1998 from southern hemisphere wetlands due to successive regional dryer and wetter climate conditions (Uppala et al., 2005) have also been reported by Bousquet et al.

(2006). The main reason of increasing CH_4 levels from 2005 onwards was a surge in emissions from natural wetlands in response to abnormally high temperatures in northern high latitudes in summer and autumn of 2007, and increased rainfall during wet seasons over Southern Hemisphere tropics under the ITCZ in 2008–2009 (Bousquet et al., 2011; Kirschke et al., 2013; Nisbet et al., 2016).

All Biogenic : The plots of CH_4 emission anomalies from aggregated category of all biogenic which includes sources rice, livestock, waste and wetlands from all zones, for both $4^0 \times 5^0$ and $2^0 \times 2.5^0$ inversion studies show similar trends for the entire study period until 2008-2009 except with much larger range in the values for anomalies in Tg/year for $2^0 \times 2.5^0$ plots such as during 1986-1988, the fluctuation in emission anomalies ranged from -30 Tg/year to +20 Tg/year for $2^0 \times 2.5^0$ plots and again during 1997-1998, the same ranged from -45 Tg/year to +25 Tg/year, which are much higher compared to that for $4^0 \times 5^0$ plots (Figure 5.7). The trend in the emissions from this category is the result of combined effects of emission trends from all natural and anthropogenic biogenic sources. The possible reasons behind the observed trends from all separate sources for $2^0 \times 2.5^0$ work are detailed in section 5.2.3, when compared with other previous studies. The large fluctuation during 1997-1998 is caused due to fluctuations in emissions contributed from wetlands as well as from rice which had been affected by climatic conditions prevailed in northern and southern hemispheres. In both $4^0 \times 5^0$ plots and $2^0 \times 2.5^0$ plots, the emission trend of biogenic category can be noted to be increasing after 2006 until 2008-2009 (Figure 5.7) which are discussed in detail in section 5.2.3 and 5.2.4.

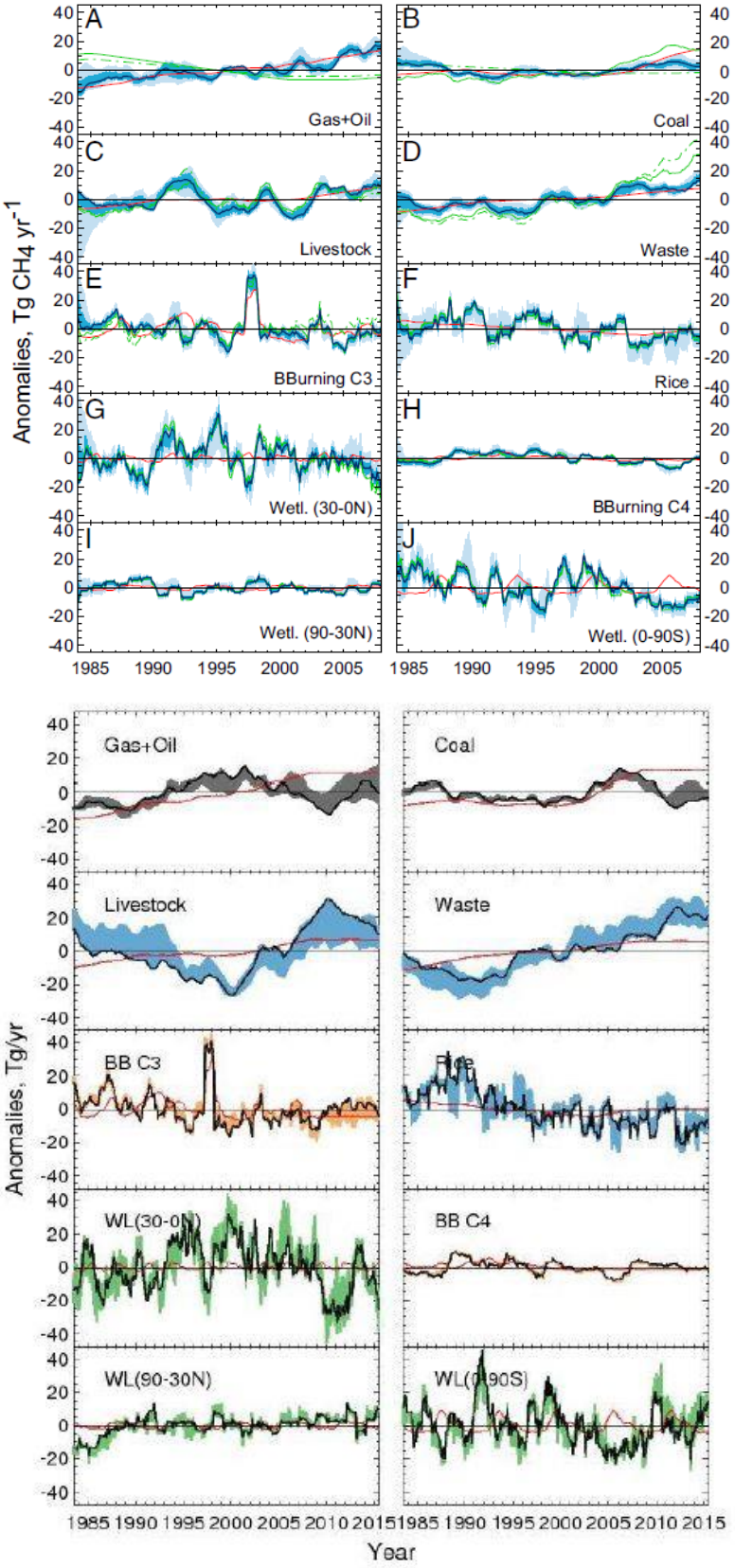

Figure 5.6: *Upper figure shows deseasonalized methane emission anomalies for all 10 source categories from inversion at $4^{o} \times 5^{o}$ grid resolution. The base inversion results are shown with the heavy dark blue line, and the red line indicates the prior emissions. The light blue shading shows the entire range of all 53 sensitivity runs in the ensemble. The green lines are inversions where the fossil fuel emissions were fixed according to a scenario by Simpson et al. (2012) based on measurements of atmospheric ethane. The solid green line shows the inversion where all fossil fuel emissions were assigned to the gas + oil category and coal emissions and all other sources were optimized, and in the dashed green line inversion, both gas + oil and coal emissions were fixed based on a 65/35 split of the fossil fuel emissions (Ref: Rice et al., 2016).*

Lower figure (same as figure 5.2) shows deseasonalized CH_4 emission anomalies for all 10 separate source categories from inversion at $2^{o} \times 2.5^{o}$ grid resolution. Black lines indicate the base inversion results. Red lines indicate anomalies in the prior emissions. Shaded colored areas represent the variations in the inversion scenarios using different observational network densities.

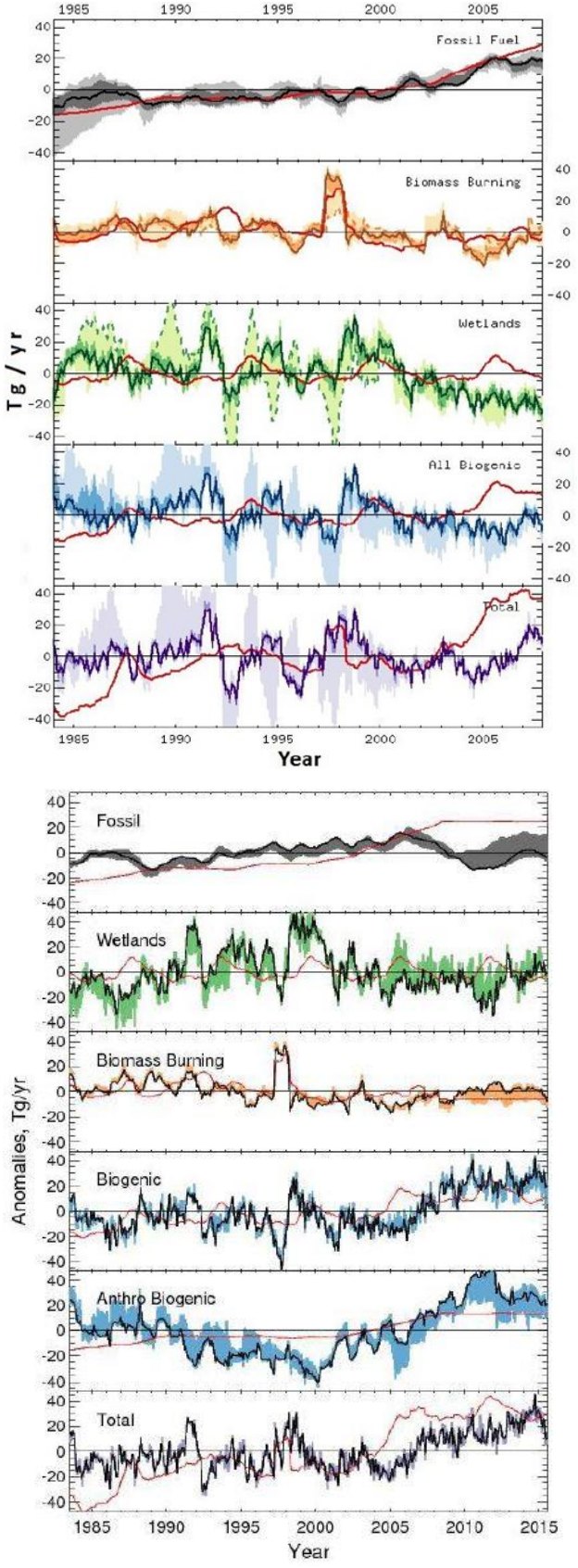

Figure 5.7: *Upper figure shows deseasonalized CH_4 emission anomalies from aggregated fossil fuels, biomass burning, wetlands, all biogenic (including wetlands) and total emissions from inversion done at $4^0 \times 5^0$ grid resolution. The base inversion results are shown with the heavy darker colored lines, and the red line indicates the prior emissions. The light colored shading shows the entire range of all 53 sensitivity runs in the ensemble (Ref: Röger, 2013).*

Lower figure (same as figure 5.3) shows deseasonalized CH_4 emission anomalies from aggregated fossil fuels, biomass burning, wetlands, all biogenic (including wetlands), anthro-biogenic (rice, livestock and waste) and total emissions from inversion done at $2^0 \times 2.5^0$ grid resolution. Black lines indicate the standard inversion results. Red lines indicate anomalies in the prior emissions. Shaded colored areas represent the variation in the observational network density of the inversion scenarios.

5.2.3. Comparison of Inversion Results with Previous Studies

Fossil Fuels: The fugitive fossil fuel methane emission anomalies in Tg/year show four distinct regimes in the Figure 5.3 such as: a decrease before 1990, oscillations with a slight increasing slope during 1990-2005, then a decrease until 2010, and then again, an increase after 2011. At the beginning of the time series in 1980s, combined fugitive fossil fuel CH_4 emission anomalies are observed to increase, followed by a drop during late 1980s to early 1990s possibly due to collapse in the production at the beginning of the Former Soviet Union breakup (Dlugokencky et al., 2003; Röger, 2013; Schaefer et al., 2016). After little stabilizing, fossil fuel emissions started increasing again during mid-1990s to until mid-2000s with higher trend than Emissions Database for Global Atmospheric Research (EDGAR) emission inventories as seen in Figure 5.3. The fugitive fossil fuel emissions decreased subsequently from 2005 to 2010, then leveled off over 2 years and again showed an increase over next subsequent years. The inversion results in Figure 5.2, attribute this trend to growth in natural gas and oil sector emissions over the period 1992 to 2000, followed by a decrease from 2001 to 2010 and then a slight increase over next following years. This trend is contrasted by coal emissions which experienced a decrease during 1980s, then remained flat during 1990s, then followed a subsequent increase in 2000s until 2006, then a decrease until 2012 and again with slight increase thereafter. The increase in emissions from coal are substantiated by previous studies such as by Ohara et al. (2007), Dlugokencky et al. (2011), Kirschke et al. (2013), Rice et al. (2016) and Nisbet et al. (2016) that after 2000, coal mining in China had doubled which may have led to the increase in methane emissions. However, two studies by Aydin et al. (2011) and Simpson et al. (2012)

based on ethane derived from firn air and atmospheric measurements of ethane indicated that CH_4 emissions from the fossil fuel sector decreased between 1985 and 2000 at a rate of −0.4 to −0.8 Tg CH_4 yr^{-1}, and attributed such a decline to decreasing fugitive emissions (leaks during extraction, treatment and use of fossil fuels) from oil and gas industries, which contradicted our results. Alternatively, our results of continued increase in emissions from combined fossil fuel sector until 2005 as well as gas and oil sector until early 2000s are supported by the studies of Kirschke et al. (2013), Rice et al. (2016) and Nisbet et al. (2016) which referred that over decades of 1980s, 1990s and 2000s, with the potential intensive exploitation of natural gas from large-scale hydraulic fracturing of shale formations performed in the United States and other thermogenic fossil fuel sources in the world including South Africa's coal industry, subequatorial gas fields in South America, and widespread large gas fields and coal fields in Asia and Australia, may have led to additional CH_4 emissions into the atmosphere. As the geographical distributions of shale basins and conventional gas and oil fields in the United States overlap, there was evidence of yielding significantly larger methane emissions with this production practice than conventional gas production as presented in the study by Howarth et al. (2011) based on measurements from five wells across the United States, which was arguable without more extensive measurements. Considering all these scenarios after 2000, a slower decline or stabilization of fossil fuel emissions may have resulted, also referred by Kirschke et al. (2013). Although, our results (Figure 5.3) showed the drop of fugitive fossil fuel emissions started after 2005 and gas and oil emissions began to decrease after 2000, but these results can be speculated in similar manner as Aydin et al. (2011). Their result displayed persistent decline in fossil fuel based methane emission during 1980 to 2000 but increase in emissions

using EDGAR 4.1 data after 2000, caused mainly due to the rising economic value of natural gas, emissions linked specifically to the growing natural gas industry and the development of cleaner technologies which may have led to sharp reductions in the release of light hydrocarbons into the atmosphere, including methane and ethane, associated with production and processing of petroleum (Aydin et al., 2011). Moreover, Simpson et al. (2012) argued that the gas and oil methane emissions decreased since 1990s which is not supported by our results (Figure 5.2) which showed emissions increased from 1990 to 2000. But the decreasing estimates of ethane and methane concentrations and emissions until 2010 by Simpson et al. (2012) and findings of Schaefer et al. (2016) of decreasing-to-stable fossil fuel sources until same time period also indicate reduction in annual thermogenic CH_4 emissions which are corroborated by our result showing decreased fossil fuel CH_4 emissions during 2005 to 2011 (Figure 5.3). However, the recent increase in extraction of natural gas and coal mining worldwide as mentioned earlier may provide evidence for the increase in our result from 2011 onwards (Figure 5.2). CH_4 with variable isotopic signatures produced during natural gas extraction depending on the temperature of gas reservoir such as -50‰ for Siberian gas (Dlugokencky et al., 2011) and isotopically lighter methane produced from coal fields such as -66.4‰ to -60.8‰ for bituminous coal mines in Australia (Zazzeri et al., 2016) caused mitigation efforts to be diminished by additional emission of secondary biogenic CH_4 from combustion of more depleted $^{13}\delta C$-CH_4 fossil fuel sources (Kirschke et al., 2013; Nisbet et al., 2016). These give a plausible explanation of recent increase of isotopically depleted methane emissions from fossil fuels consistent with our result. In figures 5.2 and 5.3, the ensemble of sensitivity tests inversion scenarios with variation in number of available measurement data sites are shown as shaded

area, the fugitive fossil fuel emissions show similar trend as discussed above but with significantly wider range in the mean values of the emissions 2005 onwards.

Wetlands: In Figure 5.3, four regimes can be distinguished in combined wetland emissions: a decrease in wetland emissions during 1985 to 1987, followed by an increase in the trend in the late 1980s with few large fluctuations in 1990s until 2000, then a strong decrease was observed in the early 2000s with fluctuations until 2005 and then again followed by a small increase during 2005-2010 with more increase 2012 onwards. This decrease during 2000s was also mentioned in the findings of Bousquet et al. (2006), Kirschke et al. (2013) and Rice et al. (2016) and also agreed well with bottom-up studies such as Prigent et al. (2001) that attributed the decrease to the worldwide reduction in flooded area, as suggested by satellite observations, causing the decrease in global wetland emissions. Hayman et al. (2014) evaluated wetland emission estimates derived using the UK community land surface model (JULES) against atmospheric observations of methane, including, total methane columns derived from the SCIAMACHY instrument on board the ENVISAT satellite for the period of 1999 to 2007. They found that the annual cycles observed in the SCIAMACHY measurements and at many of the surface sites influenced by non-wetland sources could not be reproduced in their HadGEM2 runs which suggested that the emissions over certain regions were possibly too high and/or emission patterns for specific sectors were incorrect. After 2005, the increase in wetland CH_4 emissions had also been concluded by several other studies such as Bousquet et al. (2011), Kirshcke et al. (2013) and Nisbet et al. (2016) that one of the main reason of increasing CH_4 levels was a surge in natural wetlands in response to abnormally high temperatures in northern high

latitudes in summer and autumn of 2007, and increased rainfall during wet seasons over Southern Hemisphere tropics under the ITCZ in 2008–2009 and late 2010–2011 and subsequent years, including the warmer year of 2014. Some bottom-up studies such as Spahni et al. (2011) showed result consistent with this work, indicating upward decadal-scale trends in global wetland emissions, whereas some top-down estimates such as Rice et al. (2016) using ground-based observations favored constant or declining wetland emissions over the past few decades.

Methane emissions from wetlands can be clearly distinguished between three separate latitudinal zones as shown in Figure 5.2. The spike in the wetland emission in the southern hemisphere (0^0-90^0S) around 2009-2010 as seen in the Figure 5.2, can be explained as a result of remarkably high Amazon flood levels in 2009 also been mentioned in the study of Nisbet et al. (2016). The upticks in 2011 and 2012 and the increase after 2013 in CH_4 emissions from southern hemisphere wetlands (Figure 5.2) are also supported by the events such as during the La Niña of early 2011 (Boening et al., 2012), many southern tropical regions were unusually wet and equatorial Amazon flood levels were high again, Amazon flooding also took place in 2012–2014 (Nisbet et al., 2016) and before the onset of the 2014 El Niño, extreme flood events occurred in the Amazon wetlands of Bolivia (Ovando et al., 2015). In Figure 5.2, 0°–30°N Northern Hemisphere tropical wetlands showed upward emission trend till 2000, then a decade of downward trend and during 2009-2011, a rapid decrease in emission was observed. Figure 5.2 reveals the methane growth during 2011-2014 due to the monsoonal effects on 0°–30°N Northern Hemisphere wetlands, in South and East Asia (Nisbet et al., 2014; Patra et al., 2016), also contributed to post-2011

combined wetlands methane emission growth seen in Figure 5.3. As seen in the Figure 5.2, there is a rise in emission from 30^0-90^0N wetlands as well after 2011, also supported by several recent studies. In Figure 5.2, the ensemble of our sensitivity tests reveal increase in emissions from wetlands in higher latitudes of northern hemisphere in 2007 mainly caused due to warmer temperature and higher than normal precipitation (Dlugokencky et al., 2009), which supported the studies of Bergamaschi et al. (2013) that estimated increase of 1.2-3.2 Tg CH_4 in 2007 and Bruhwiler et al. (2014) that estimated 4.4 Tg CH_4 emissions higher than 2000-2010 decadal average in 2007. The atmospheric sampling and Keeling plot studies (Fisher et al., 2011; Sriskantharajah et al., 2012) showed much depleted $\delta^{13}C$-CH_4 values from Alert, Canada and in Fennoscandia, in autumn 2007 which confirmed the presence of methane-rich boreal and Arctic wetland air. Figure 5.2 shows arctic region methane emissions decreased in 2008, 2010-2012, which can be related to the study by Nisbet et al. (2016) where they mentioned that although Arctic emissions contributed to the Arctic methane shift in 2007, they do not seem to have been major contributors since then. The 30^0-90^0N wetland emission spikes in 2012-2013 and 2014-2015 shown in Figure 5.2 might be contradictory to the findings of Nisbet et al. (2016) where they mentioned that from 2008 to 2013 no major sustained methane growth (no growth in concentration does not necessarily imply no growth in emission anomalies were observed) occurred due to fast horizontal mixing at high latitudes efficient on the emission zones, but might had agreed well with 2014 strong growth of methane (this does not necessarily imply strong growth in emission anomalies) and isotopic shifts in the Arctic that occurred at a similar rate in comparison to the global increase record. In Figures 5.2 and 5.3, the ensemble of sensitivity test inversion scenarios with variation in number of available measurement data sites are

shown as shaded area, the wetland emissions show similar trend as discussed above but with significantly wider range in the mean values of the emissions after 2005.

Biomass Burning: Figure 5.3 shows four distinct regions in the combined biomass burning emission trend as follows: a slight increasing trend in late 1980s until 1991, then a prolonged decrease until 2005 with a large sharp anomaly peak during 1997-1998 and a small peak in 2003, then a slight increase until 2012 and over next subsequent years the emissions exhibit roughly constant trend. Other recent studies such as Kirschke et al. (2013), Nisbet et al. (2016), Rice et al. (2016) also agreed well with the long-term decrease of biomass burning emissions over past decades. There is independent evidence in studies by Yang et al. (2014) and in spatial pattern for trends in source isotopic signatures by Le Quéré et al. (2014) for declines in CH_4 emissions from global biomass-burning over the past few decades which are consistent with the result of this work, however, Mieville et al. (2010) disagreed and inferred increasing trends in this source.

Methane emission trends over the inversion period from biomass-burning of C3 and C4 vegetations are separately shown in Figure 5.2. For C3 vegetation burning seen in Figure 5.2 methane emission shows same trend as the total biomass-burning methane emission trend as seen in Figure 5.3. For C4 vegetation burning as seen in Figure 5.2, methane emission trend shows increase during 1987-88, then shows a decrease until 2005 with fluctuations and after 2006 shows an increase later with little decrease and then remaining constant over next subsequent years. Similar to the trend as presented in this inversion work, global-scale model inversion results presented by Röger (2013) also favored a

decrease in fire CH_4 emissions until 2005 based on the isotopic budget of CH_4 resulting from enriched $\delta^{13}C$ signature. A global decrease in biomass-burning emissions mostly located in the tropics also has minimum effect on the meridional distribution of CH_4 (Rice et al., 2016). When optimized emissions are aggregated over large regions on global scale, emissions from biomass burning are the largest in Africa and in tropical South America, also been reported by Kirschke et al. (2013) where they compared the bottom-up estimates to the top-down estimates and mentioned simulated biomass burning emission areas were almost consistent between models over the period 1997–2000, revealing robust large emission zones around the thermal equator (It is the belt encircling the earth, defined by a set of locations with highest mean annual temperature at each longitude around the earth) in Africa, central South America (Brazil and Bolivia), Indonesia, and to a lesser extent in eastern Russia, Laos, and Mexico and in northern Australia and in boreal regions (Canada and Siberia) and also mentioned that small fires are often undetected by satellite retrieval algorithms used in bottom up estimates. Post 2006 rise in biomass burning emission is also supported by study of Bousquet et al. (2011) which mentioned that other sources than natural wetlands contributing to the 2007 flux anomaly are biomass burning (+3±5 Tg, mostly in South America) and anthropogenic sources (+2±6 Tg) and Worden et al. (2013) mentioned that during moderate El Niño event in 2006, methane emissions from Indonesian fires could have compensated for an expected decrease in tropical wetland methane emissions from reduced rainfall. The pronounced anomaly peak in the 1997-1998 may have caused by the massive emissions from Indonesian forest fires due to the changing land use which made the tropical forest vulnerable to fire during a drought associated with that year's El Niño (Nisbet et al., 2016). This major increase is also supported in our

inversion result plots in record of South China Sea observation site representing a closer location to Indonesia. Biomass burning priors obtained from the GFED3 data product, which is based on satellite observations of burned area worldwide, also contain a distinctive peak in 1997. In 2010, our results (Figure 5.2) show rise in biomass-burning methane which was consistent with the findings of Nisbet et al. (2016) where they mentioned in 2010 Amazonia experienced a major drought and biomass burning and the early 2010 rise in methane at Ascension (ASC; 8ºS, 15ºW) possibly been driven by biomass burning (Crevoisier et al., 2013), were consistent with their observed enrichment of isotopic methane during early to mid-2010, both resulted from C4 savanna grassland fires. In the years 2012 onwards, we find biomass emission with no further change. Rice et al. (2016) mentioned lack of much data from bottom-up fire inventories on the long-term trends in CH_4 emissions from biomass burning in recent years (Granier et al., 2011) but noted evidence of decreasing burned area from fires in recent decades (Giglio, Randerson, van der Werf, 2013; Yang et al., 2014) supporting the result from this work. In Figures 5.2 and 5.3, the ensemble of sensitivity test inversion scenarios with variation in number of available measurement data sites are shown as shaded area, the biomass burning emissions show almost similar trend as discussed above but after 2010 with significantly wider range in the mean values of the emissions seen in total biomass-burning emission and biomass-burning from C3 vegetation.

Livestock: Figure 5.2 shows three distinct regions in the trend of methane emissions from ruminant animals: more than a decade-long decrease from the beginning of our inversion study period until 2000, followed by a decade-long increase in the trend with a little dip

during 2003-2005 and then after 2010, a sharp decrease followed over next subsequent years. The decrease of livestock CH_4 emissions during the late 1980s and the decade of 1990s followed by an increase over the next subsequent decade of 2000s (Figure 5.2) are supported by few recent studies such as Tubiello et al., (2013) and Dangal et al., (2017), which mentioned slowing of methane emissions from global livestock sector are caused due to slowing of increase in livestock numbers during the 1990s particularly in developed countries. Thereafter, the prolonged rise in emissions from ruminant animals are also generally recognized over the past few decades due to increased populations of livestock by inventories such as EDGAR (2011) and United Nations Food and Agriculture Organization Statistics Division (U.N. FAOSTAT database, 2016). Increase in livestock emissions during last decade 2000-2010, are also supported by inversion results of Rice et al. (2016). Methane generating microbes such as methanogens present in the anaerobic environments in the digestive tracts of ruminant animals and termites emit methane to the atmosphere. Depending on different photosynthetic pathways of C3 and C4 vegetations, ruminants digesting C4 plants give off CH_4 at −55 to −50‰, whereas those eating C3 plants give off −65 to −60‰ CH_4 (Dlugokencky et al., 2011). In this current study, although livestock CH_4 emissions are not separately determined based on the isotopic signatures of C3 or C4 vegetation due to enteric fermentation inside digestive tract of ruminants, but to find reasons behind this inversion estimated livestock emission-trend over our study period and relate with other studies to get more specific information on the increase or decrease of livestock CH_4 emissions from different geographic regions of the world, we are considering the isotopic signatures of C3 and C4 vegetation available as fodder for ruminants. Some other studies such as Bousquet et al. (2011), Kirschke et al. (2013),

Schaefer et al. (2016), also mentioned the contribution of increased livestock industries from Asia and South America in methane emissions in last decade. Kirschke et al. (2013) reported about relatively strong contribution of methane emission by termites from Africa and tropical South America. Nisbet et al. (2016) argued that tropical agricultural emissions from ruminants had indeed increased in highly rainy seasons, but these increases were probably mainly in South America and Africa. Though there are very sparse tropical ruminant data and lack of studies on the isotopic values of tropical ruminant methane emissions in the field, Nisbet et al. (2016) pointed out that grasslands and ruminant fodder crops in the tropics are mostly C4 dominated instead of C3 dominated as assumed by Schaefer et al. (2016) that ruminants are C3-fed. Nisbet et al. (2016) noted that a large number of free-grazing tropical ruminants in savanna grasslands survive on all $\delta^{13}CCH_4$-enriched C4 supplemental fodder such as maize, millet, sorghum crop waste, or sugarcane tops and thus, methane emitted from these ruminants is substantially more enriched than -60‰ C3 value and more likely to have $\delta^{13}C$-CH_4 values around -50‰ or less (Dlugokencky et al., 2011). After 2010, the decrease in methane emissions from ruminants in our result as seen in Figure 5.2 may have occurred due to animal based mitigation strategies taken such as reduction in the number of CH_4-producing microbes during enteric fermentation in ruminants by improving feed quality, feed additives, improving animal productivity and their reproductive efficiency (Dlugokencky et al., 2011; Gerber et al., 2013). This decrease after 2010 in our result is also consistent with the report presented by Nisbet et al. (2016) where they mentioned due to mostly average to poor monsoons in recent years over India, the nation with the world's largest ruminant animal population, cattle populations had declined. Figure 5.2 shows the ensemble of sensitivity test inversion scenarios with

variation in number of available measurement data sites as shaded area, the methane emissions from livestock show almost similar trend as discussed above but with significantly wider range in the mean values of the emissions.

Waste: The trend of methane emissions from wastes can be distinguished in three zones as observed in Figure 5.2 such as: a long decreasing trend from beginning of our study period until 1991-1992, then followed by two decades of increase until 2012 and finally a decreasing trend in next subsequent years. The decrease in CH_4 emissions from landfilled waste during late 1980s and early 1990s (Figure 5.2) can be related to the findings in IPCC (1992), where they mentioned slight reduction in the emissions because of observed high oxidation rates of CH_4 in landfill cover soils (Whalen et al., 1990). In comparison, another study by Bogner et al. (2003) where two of their modeled scenarios indicated global CH_4 emission from landfilled solid waste declined in 1980s, then increased until 1991, then a drop during 1992-1993 and again increased from 1994 to 1996 which they linked to the modeled decline in waste generation in North America during 1980s due to economic downturn and a decline in Europe during early 1990s attributable to the economic situation in the former USSR. The increase in the global CH_4 emissions from solid waste over the next decades from mid 1990s to 2012 (Figure 5.2) had also been reported by studies of Kirschke et al. (2013), Rice et al. (2016), Schaefer et al. (2016). According to Bogner et al. (2003) and EDGAR (2011), there was increase in landfilled solid waste over past decades, even as CH_4 recovery increased. The decrease of the emission after 2012 as seen in Figure 5.2, may be due to measures taken to recover and utilize CH_4 from anaerobic digestion of cattle waste as mentioned by Dlugokencky et al. (2011). Other viable opportunities for CH_4

emission reductions suggested by Dlugokencky et al. (2011) might have been taken into consideration, such as landfill gas with approximately 50% CH_4 may have been collected, processed and distributed to end-users to produce bioelectricity or heat. Organic matter from landfills might have been diverted to composting which further reduced CH_4 emissions and had other environmental benefits including end-product use as a soil amendment that improved moisture retention and carbon storage, and reduced use of inorganic fertilizer, potentially reduced N_2O emissions as suggested by Dlugokencky et al., 2011. All these measures might have been considered at different locations which may have resulted in the decrease of landfill and waste CH_4 emissions from 2012 onwards. Figure 5.2 shows that the ensemble of sensitivity test inversion scenarios with variation in number of available measurement data sites as shaded area, the methane emissions from wastes show almost similar trend as discussed above but with significantly wider range in the mean values of the emissions.

Rice: In Figure 5.2, the trend of methane emissions from rice agriculture shows two distinct regimes such as: an increase from beginning of study period until 1990 and then followed by a long-term decrease throughout the rest of the inversion period with large interannual fluctuations. These findings may agree with the theories of reduced rice emissions due to changes in agricultural and irrigational practices (Li et al., 2002). Several bottom-up emission inventories also indicated significant decrease in rice CH_4 emissions over the past few decades (Khalil et al., 2006; Kai et al., 2010). A decrease in microbial sources in the northern hemisphere which attributed to a decrease in rice emission was proposed by Kai et al. (2011) as an evidence to the decrease in Inter-Hemispheric Difference (IHD)

observed in the isotopic signatures of methane. This was opposed by Levin et al. (2012) with no significant change in IHD and proposed constant fossil fuel and microbial emissions. According to the EDGAR 4.2 inventory (2011), the rice paddy emissions have decreased during the 1980-2000 period and remained stable between 2000 and 2005 (Kirschke et al., 2013). The anthro-biogenic emissions from aggregated categories of agriculture, livestock and waste shown in Figure 5.3, contradicts the comparison study of bottom-up and top-down estimates of methane budget listed by Kirschke et al. (2013) which showed an increase in agricultural and waste emissions over three decades for bottom-up estimates and an increase in the same emissions during 1980s and 1990s, followed by more than a decade long decrease until 2009 as observed for top-down estimates. According to Rice et al. (2016), inversion analysis for the period of 1984-2009 also confirmed the decrease in rice emissions, but with no IHD in isotopic signatures which made agreement to the fact that either decrease in rice emission was surpassed by the increase in emissions from other microbial sources (waste, landfills and livestock) or the IHD in $\delta^{13}C$ is insensitive to the changes in rice emissions mainly occurring at the tropics (EDGAR 4.2 inventory, 2011). In contrary, Schaefer et al. (2016) used a one-box model based on remote sensing data, postulated the hypothesis that the growth in $[CH_4]$ after 2006 had been driven by agricultural emissions in the northern hemisphere, but then commented on uncertainty of the evidence. However, Nisbet et al. (2016) argued that the abrupt change of growth trend in 2007 matched with the hypothesis of change in natural emissions due to meteorological driving factors rather than that from anthropogenic sources such as ruminants population and rice cultivated area which would have been slower and more gradual. Furthermore, Nisbet et al. (2016) found no evidence of any sharp increase in rice

emissions in 2007 and mentioned about fluctuating rice-harvested area in Asia with no evidence of any step change in cultivated rice fields in China, world's largest rice producing country and also mentioned that harvested paddy field area was relatively stable and had declined from 2006 to 2007 (http://faostat.fao.org). Results from this work concur with the findings of most of the above-mentioned studies such as Khalil et al. (2006), Kai et al. (2010, 2011), Nisbet et al. (2016) and Rice et al. (2016). The ensemble of sensitivity test inversion scenarios with variation in number of available measurement data sites are shown as shaded area in Figure 5.2 and 5.3, the methane emissions from rice agriculture are shown in Figure 5.2 and emissions from livestock, waste landfills and rice cultivation aggregated together as anthro-biogenic category are shown in Figure 5.3. The sensitivity tests for rice emissions show almost similar trend as discussed above but with significantly wider range in the mean values of the emissions during few time spans such as 1988-1989, 1992-1993, 1994-1996 and 2005-2006.

5.2.4. Possible Reasons for the Increase of Global Methane Levels in the Atmosphere from 2006 onwards

This study was conducted by extending the timeseries until 2016 with the motivation to determine the main causes of the sudden rise of atmospheric methane concentrations since 2006. After multidecadal decline in methane growth rate, the increase in global methane levels post 2006 is the result of imbalance of methane in the atmosphere caused due to addition of methane as emitted from different sources and removal of methane by different sinks. Thus, to know the reasons behind this recent increase and to understand the methane

budget of various sources and sinks, this study helped us to quantify the emission estimates from different sources of methane and their variability for over almost last four decades. The results of this study for all separate source categories throughout the study period are already discussed and compared with other recent studies in section 5.2.3, the main driving factors of the increase post 2006 as revealed from this study are emphasized in this section as follows:

1. The results of this study suggest that the major contribution of emissions from all biogenic sources both natural and anthropogenic as well as minor contribution from biomass burning may have caused the increase in global methane levels since post-2006. It is revealed that the emissions from individual source categories of livestock, wastes, coal, northern high latitude wetlands and biomass burning of C3 vegetations had increased during 2006-2015 (Table 5.3). Although a persistent increase in total methane levels can be observed until the end of the study period, but there may be a shift in contributions from the emissions of individual source categories since 2011 onwards. With the decline in emissions from anthro-biogenic sources of livestock and rice, from northern tropical wetlands, from fossil fuel source of coal and from biomass burning of C4 vegetations since 2011-2012, the increase in global methane levels since 2011 until the end of the study period may possibly be due to the contribution of increased emissions from sources of wastes, natural wetlands (southern hemisphere and northern high latitudes), fossil fuel source of gas and oil and biomass burning of C3 vegetations globally (Table 5.3).

2. The emissions from all biogenic category showed a positive trend (Figure 5.3) from 2006 onwards until the end of the study period with the combined effects of emissions from all zones of wetlands and from all anthro-biogenic sources. The average estimate of emissions from all biogenic sources had increased by ~25 Tg/year, from anthro-biogenic sources by ~43 Tg/year and from wetlands (90N-30N) by ~3 Tg/year during 2006-2015 than that during 1994-2005 (Table 5.3). Thus, it can be inferred that the increase of global methane emissions during late 2000s was caused due to increase of emissions from biogenic sources of both natural and anthropogenic origin, which is supported by the findings of other studies such as Bousquet et al. (2011), Kirschke et al. (2013), Nisbet et al. (2016), Schaefer et al. (2016).

3. The livestock and landfilled solid waste categories both showed a continued positive emission trends before and after 2006 and then a decrease in livestock emission from 2010 onwards and waste emission from 2012 onwards were observed (Figure 5.2). The rise in emissions from ruminant animals are also generally recognized over the past few decades due to increased populations of livestock by inventories such as EDGAR (2011) and United Nations Food and Agriculture Organization Statistics Division (U.N. FAOSTAT database, 2016). The increase in livestock methane emission until 2010 is also supported by other studies by Bousquet et al. (2011), Kirschke et al. (2013), Rice et al. (2016), Schaefer et al. (2016), Nisbet et al. (2016). After 2010, the decrease in methane emissions from ruminants in our result (Figure 5.2 and Table 5.3) may have occurred due to animal

based mitigation strategies taken such as reduction in the number of CH_4-producing microbes during enteric fermentation in ruminants by improving feed quality, feed additives, improving animal productivity and their reproductive efficiency (Dlugokencky et al., 2011; Gerber et al., 2013). This recent decrease after 2010 is also consistent with the report presented by Nisbet et al. (2016) where they mentioned due to mostly average to poor monsoons in recent years over India, cattle populations had declined. Furthermore, the increase in the global CH_4 emissions from solid wastes over two decades until 2012 (Figure 5.2) had also been reported by studies of Kirschke et al. (2013), Rice et al. (2016), Schaefer et al. (2016). According to Bogner et al. (2003) and EDGAR (2011), there was increase in landfilled solid waste over past decades, even as CH_4 recovery increased. The trend of emissions from wastes after 2012 can be observed slightly negative (Figure 5.2), as the averaged emission estimate during 2006-2015 was ~18 Tg/year increase than that during 1994-2005 and it was ~13 Tg/year increase during 2011-2015 than that during 2006-2010 (Table 5.3). This little difference in averaged estimates may have occurred due to mitigation measures taken at various locations throughout the world to recover and utilize CH_4 from anaerobic digestion of cattle waste and manure management, landfill gas with approximately 50% CH_4 may have been collected, processed and distributed to end-users to produce bioelectricity or heat, organic matter from landfills might have been diverted to composting which further reduced CH_4 emissions and had other environmental benefits including end-product use as a soil amendment that improved moisture retention and carbon storage, and reduced use of inorganic fertilizer, as mentioned by Dlugokencky et al. (2011).

4. The methane emissions from rice agriculture showed a continuous negative trend (Figure 5.2) before and after 2006 until end of the study period and also averaged estimate decreased by ~5 Tg/year during 2006-2015 than that during 1994-2005 (Table 5.3). This decrease is also consistent with other previous studies by Khalil et al. (2006), Kai et al. (2010, 2011), Nisbet et al. (2016) and Rice et al. (2016). Thus, the emission trend of anthro-biogenic category (Figure 5.3) showed the combined effects of emission trends of sources of livestock, waste and rice, which continued to be positive before and after 2006 but became slightly negative from 2011 onwards.

5. The combined category of wetlands in Figure 5.3 showed a positive trend in emissions during 2005-2006, continued to remain in that same level until 2010, then a dip was observed during 2010-2011, and thereafter, again a positive trend was observed in the emissions. Wetlands (90^{o}N-30^{o}N) showed an increase of ~3 Tg/year from 2006 onwards (Table 5.3), and with a negative trend during 2012-2013, it continued to rise again 2013 onwards (Figure 5.2) with average emission estimate to increase by ~1 Tg/year during 2011-2015 (Table 5.3). These changes mainly caused due to warmer temperature and higher than normal precipitation (Dlugokencky et al., 2009), which are supported by the studies of $\delta^{13}C\text{-}CH_4$ values by Fisher et al. (2011), Sriskantharajah et al. (2012) and also confirmed by studies of Bergamaschi et al. (2013), Bruhwiler et al. (2014), Kirschke et al. (2013) and Nisbet et al. (2016). Wetlands (30^{o}N-0^{o}) showed a slight negative trend from 2006

onwards and greater negative trend during 2009-2011 and thereafter a sharp positive trend was observed during 2011-2013 (Figure 5.2) and average emission estimate had decreased by ~20 Tg/year during 2006-2015 as compared to previous decade, but showed a decrease of ~6 Tg/year during 2011-2015 than that during 2006-2010 (Table 5.3). These changes were due to the monsoonal effects on Northern Hemisphere tropical wetlands, in South and East Asia (Nisbet et al., 2014; Patra et al., 2016). Wetlands (0º-90ºS) showed a positive trend in methane emissions 2006 onwards until 2010, then a negative trend during 2010-2013 with small upticks in 2011 and 2012 and again a positive trend was observed from 2014 onwards (Figure 5.2). The average emission estimate had increased by ~5 Tg/year during 2011-2015 than that during 2006-2010 (Table 5.3). The spike in the emission around 2009-2010, can be explained as a result of remarkably high Amazon flood levels in 2009 also been mentioned in the study of Nisbet et al. (2016). The upticks in 2011 and 2012 and the increase thereafter in CH_4 emissions from southern hemisphere wetlands are also supported by the events such as during the La Niña of early 2011 (Boening et al., 2012), many southern tropical regions were unusually wet and equatorial Amazon flood levels were high again, Amazon flooding also took place in 2012–2014 (Nisbet et al., 2016) and before the onset of the 2014 El Niño, extreme flood events occurred in the Amazon wetlands of Bolivia (Ovando et al., 2015).

6. The emission trend from aggregated category of fossil fuels (Figure 5.3) became negative since 2006 until 2010-2011 and then became slightly positive during next

subsequent years until the end of the study period. The averaged emission estimate had decreased by ~8 Tg/year during 2006-2015 as compared to previous decade, with a decrease of ~6 Tg/year during 2011-2015 than that during 2006-2010 (Table 5.3). The decrease from 2006 onwards might have caused mainly due to the rising economic value of natural gas, emissions linked specifically to the growing natural gas industry and the development of cleaner technologies which may have led to sharp reductions in the release of light hydrocarbons into the atmosphere, including methane and ethane, associated with production and processing of petroleum (Aydin et al., 2011). The decreasing estimates of ethane and methane concentrations and emissions until 2010 by Simpson et al. (2012) and findings of Schaefer et al. (2016) of decreasing-to-stable fossil fuel sources until same time period also indicate reduction in annual thermogenic CH_4 emissions which are corroborated by our result showing decreased fossil fuel CH_4 emissions during 2006 onwards (Figure 5.3 and Table 5.3). However, the increase in extraction and processing of natural gas worldwide from the onset of large-scale hydraulic fracturing of shale gas, also substantiated by recent studies and emissions inventories (EDGAR, 2011; Dlugokencky et al., 2011; Howarth et al., 2011; Nisbet et al., 2016, Rice et al., 2016) may provide evidence for the increase of ~7 Tg/year in averaged emission estimate during 2011-2015 than that during 2006-2010 in our result (Table 5.3). In contrast, averaged emission estimate from coal mining showed an increase of ~2 Tg/year during 2006-2015 as compared to previous decade, but followed a decrease of ~12 Tg/year during 2011-2015 than during 2006-2010 (Table 5.3). CH_4 with variable isotopic signatures produced during natural gas

extraction depending on the temperature of gas reservoir such as -50‰ for Siberian gas (Dlugokencky et al., 2011) and isotopically lighter methane produced from coal fields such as -66.4‰ to -60.8‰ for bituminous coal mines in Australia (Zazzeri et al., 2016) caused mitigation efforts to be diminished by additional emission of secondary biogenic CH_4 from combustion of more depleted $^{13}\delta C\text{-}CH_4$ fossil fuel sources (Kirschke et al., 2013; Nisbet et al., 2016).

7. The emission trend from aggregated biomass burning category (Figure 5.3) became a slight positive since 2006 until 2012 with a little dip during 2008-2009 and then leveled off thereafter. The average emission estimate of aggregated biomass burning was observed to increase by ~2 Tg/year during 2006-2015 than that during previous decade and increase by ~5 Tg/year during 2011-2015 than that during 2006-2010 (Table 5.3). These increases are simultaneous with the estimated emissions from burning of C3 vegetation with averaged emission showed an increase of ~1 Tg/year during 2006-2015 than that during 1994-2005 and an increase of ~6 Tg/year during 2011-2015 than that during 2006-2010 (Table 5.3). Post 2006 rise in emission is also supported by study of Bousquet et al. (2011) which mentioned that other sources than natural wetlands contributing to the 2007 flux anomaly are biomass burning (+3±5 Tg, mostly in South America) and anthropogenic sources (+2±6 Tg) and Worden et al. (2013) which mentioned that during moderate El Niño event in 2006, methane emissions occurred from Indonesian fires. Our results (Figure 5.2) show positive trend in biomass-burning methane from C4 vegetation from 2006 which was consistent with the findings of

Nisbet et al. (2016) where they mentioned in 2010 Amazonia experienced a major drought and biomass burning and the early 2010 rise in methane at Ascension (ASC; 8^0S, 15^0W) possibly been driven by biomass burning (Crevoisier et al., 2013), were consistent with their observed enrichment of isotopic methane during early to mid-2010, both resulted from C4 savanna grassland fires. In the subsequent years 2012 onwards, we find biomass emission with no further change. Rice et al. (2016) mentioned lack of much data from bottom-up fire inventories on the long-term trends in CH_4 emissions from biomass burning in recent years (Granier et al., 2011) but noted evidence of decreasing burned area from fires in recent decades (Giglio, Randerson, van der Werf, 2013; Yang et al., 2014) supporting the results of this work.

CHAPTER 6

Summary and Conclusions

In this chapter, the overall summary of this study is presented in section 6.1, the conclusions are presented in section 6.2 and some further improvements needed to better understand the methane budget in future are discussed in section 6.3.

6.1. Summary

The behavior of atmospheric methane is considerably more complex than other greenhouse gases and is much less understood on account of the spatiotemporal variability of its emissions which include biogenic (e.g., wetlands, rice agriculture, ruminants), thermogenic (fossil fuels) and pyrogenic (biomass burning) sources. After a sustained growth throughout most of the 20th century, the methane growth rate declined from ~15 ppb/yr during 1980s to ~6 ppb/yr in the 1990s falling to near zero and even negative values in the early 2000s. However, with some surprise, the growth rate rebounded in 2007 and annual increase in globally-averaged atmospheric methane abundance has been 7.86 ppb/year on average during the past 14 years from 2007 to 2020 [*Ed Dlugokencky, NOAA/GML (gml.noaa.gov/ccgg/trends_ch4/)*]. The driving factors of the slowdown in methane growth rate until 2006 are still debated and the post 2006 increase in the growth rate due to imbalance of CH_4 sources and sinks are not yet understood clearly. Thus, this rise since 2007 needed assessment of global methane budget for recent years. There are few studies which addressed multidecadal variability in atmospheric methane levels, but the relative contributions of different sources over decadal timescale are highly uncertain. To understand and quantify these spatio-temporal changes in source categories over last three

decades, global observations of spatial distribution of CH_4 concentrations and isotopic composition act as top-down constraint in our atmospheric methane modeling work. Therefore, in this thesis, the decadal variations before 2006 and the recent changes post 2006 in the global methane budget are estimated by atmospheric inverse modeling of global methane emissions over a time of more than three decades spanning from 1983 to 2015. The global methane optimized source strengths are calculated by inverse modeling of atmospheric observations and a priori information on temporal and spatial distribution of emissions, with the help of the chemical transport model GEOS-Chem at a horizontal grid resolution of $2^{o} \times 2.5^{o}$ for atmospheric transport and exchange processes. The Kalman smoothing technique was used to derive time-dependent global methane emissions from various source processes with measurements of the atmospheric mixing ratios and carbon isotopic composition of methane over past three decades. In addition, inverse model sensitivity tests are performed to test the robustness of our results with respect to variation in number of measurement sites with different time spans of availability of data. The results of this work are found to be consistent with other recent studies and the summary of the analysis are pointed out as follows:

- The Bayesian inversion using GEOS-Chem produced optimized emission estimates, constrained by long-term measurements of methane concentrations at all 105 observational sites and carbon isotopic signatures at all 21 $\delta^{13}C-CH_4$ observational sites obtained from NOAA Global Monitoring Laboratory (GML) "event-level" CH_4 measurements. The model simulated concentrations using optimized emissions demonstrated much better fit with the NOAA measurements

compared to the model simulated concentrations using prior emissions. The a priori values are obtained from the EDGAR inventory for anthropogenic emissions, GFED3 inventory for biomass burning emissions and from the GEOS-Chem base inventories for natural emissions, and uniformly scaled to match the prescribed OH sink. The model simulated concentrations using the a posteriori emission estimates matched remarkably well for both the long-term trend and magnitude of the observed NOAA concentrations as well as the seasonal cycle of the measurements. However, a few small discrepancies remain between model and observations already discussed in detail in chapter 5 of this thesis. The interannual difference in the CH_4 mixing ratios for some sites did not match perfectly. There are some overestimates and underestimates in carbon isotopic composition estimates along with their seasonal cycle at very few sites.

- The inversion analysis indicated as seen in Figure5.3 that the emission rate from the anthro-thermogenic sources i.e., combined fossil fuels increased over most of the study period from 1990s to 2006 and again after 2012 until end of the study period, while anthro-biogenic sources increased rapidly from 2000 until 2011 and all biogenic sources increased rapidly from 2005 onwards until the end of the study period, whereas pyrogenic source of biomass burning showed a small increase since 2005 until 2012 and remained almost constant thereafter. The results of this work as observed in Table 5.2 revealed that the total averaged global methane emission over years 1983 to 2015 is estimated to be 530±50 Tg/year. The global methane emissions over years of 1983 to 2015 from all biogenic sources of both natural and

anthropogenic origin account for ~73% of the total global CH_4 emissions. Anthro biogenic sources attribute about 39% of the total CH_4 emissions, whereas natural wetlands attribute about 34.5% of the total CH_4 emissions. Emissions from fossil fuels sector constitutes about 18.5% of the total global CH_4 emissions and from biomass burning about 8.3% of the total global CH_4 emissions.

- As seen in Figure 5.2, the inversion analysis indicated that there was a significant rise in emissions from gas and oil since late 1980s until 2001 and again 2010 onwards and from coal since 2000s until 2006 and again 2011 onwards (seen in sensitivity tests ensemble), from ruminant livestock since 2000 until 2010 and from waste management since 1994 onwards, while emissions decreased from rice agriculture since 1990 until the end of the study period with much interannual variability and biomass burning over most of the period from 1991 to 2005 with little increase until 2012 and then remaining almost constant in recent years. Furthermore, the emissions from combined wetlands (Figure 5.3) from all over the world decreased during early 1980s, followed by an increase from late 1980s to 2000, then again, a strong decrease until 2005, followed by a small increase with remaining almost constant until 2010 and then rapid increase from 2011 onwards until the end of the study period.

- Global budget of methane emissions per source category for over entire time period (01/1983-12/2015), over three separate decades (01/1983-12/1993, 01/1994-12/2005, 01/2006-12/2015) and then over separate time periods of 01/2006-

12/2010 and 01/2011-12/2015 are tabulated (Table 5.3). The total averaged global methane emission in the decade of 2006-2015 is estimated to be 543±44 Tg/year which is ~20 Tg/year more than that during previous decade, during 2006-2010 it is estimated to be 539±44 Tg/year, whereas during 2011-2015, the estimated emission reached 547±45 Tg/year. The averaged emission estimate of all biogenic sources (both natural and anthropogenic) shows an increase of about ~25 Tg/year during 2006-2015 than that during 1994-2005, whereas the anthro-biogenic sources show highest increase in averaged emission estimate of about ~43 Tg/year during 2006-2015 than that during 1994-2005. It was observed in the table that mainly the source categories of coal, livestock, wastes, biomass burning of C3 vegetation and northern high latitude wetlands show increase in their averaged emission estimates of ~2 Tg/year, ~31 Tg/year, ~18 Tg/year, ~1 Tg/year and ~3 Tg/year respectively, during the decade of 2006-2015 than that during previous decade.

- Methane emissions estimated from three geographically separated wetland zones based on latitude ranges 90ºN-30ºN, 30ºN-0º and 0º-90ºS give us more detailed information about the spatial and temporal distribution of the natural methane emissions from wetlands from around the globe. The results from this work showed that the emission from southern hemispheric wetlands (0^0-90^0S) had no significant trend from the beginning of our study period until 2000 with a sudden spike in the emissions during 1991-1992, followed by a long-term decrease in emissions until 2006, then again, an increase until 2010 with a decrease in emissions until 2013 and then again, a rapid increase in emissions over next subsequent years from 2013

onwards. Our result is supported by wetland models comparison study of Melton et al. (2013) which suggested the tropical wetland emissions are higher in the southern hemisphere. Southern hemisphere wetland methane emissions are considered important as Nisbet et al. (2016) mentioned that the National Oceanic and Atmospheric Administration (NOAA, USA) Cooperative Global Air Sampling Network and Royal Holloway, University of London (RHUL, UK) measurements of methane mole fraction and $\delta^{13}C\text{-}CH_4$ from southern hemisphere polar, tropical and equatorial regions record trends of strong and sustained methane growth from natural biogenic sources since 2007 onwards with higher yearly rise in 2014 which is also corroborated by our results. The northern hemispheric tropical (0^0-30^0N) wetland emission showed a positive trend until 2000, then a decade of negative trend, with a rapid decrease in emissions during 2009-2010 and then significant increase in emission during 2011-2014 due to monsoonal effects in South and East Asia, and then after 2014 again a negative trend is observed. There is rise in emissions from northern higher latitude (30^o-90^oN) wetlands from start of the study period until 1991, which then showed no significant trend until 2006, a positive trend since 2007 onwards exceeding the decadal average, with a rising spike in emissions in 2012 followed by a dip in 2013 and again a positive trend since 2014 onwards until the end of the study period was observed. Our result is consistent with several other studies such as Kirschke et al. (2013), Nisbet et al. (2016) which also revealed similar trends in methane emissions from boreal and Arctic wetlands in response to abnormal high temperatures in 2007.

- Methane emissions from biomass burning of C3 and C4 vegetations estimated separately show different trends. For C3 vegetation burning, methane emissions show same trend as that from the total biomass burning emission trend, with a slightly positive trend in late 1980s until 1991, then a prolonged decrease in emissions until 2005 with a large sharp anomaly peak during 1997-1998 and a small peak in 2003, then a slight increase until 2012 with a small dip during 2008-2009 and during recent years the emissions exhibit roughly constant emissions. Some studies suggested that the pronounced anomaly peak in the 1997-1998 may have caused by the massive emissions from Indonesian forest fires due to the changing land use which made the tropical forest vulnerable to fire during a drought associated with that year's El Niño. For C4 vegetation burning, methane emissions show a positive trend during 1988-1989, then show a decrease in emissions until 2005 with fluctuations and again an increase during 2006-2007, later a slight negative trend and then remaining almost constant over next subsequent years. Within this variability, the emission anomalies for C3 vegetation show more long-term fluctuations until 2009 than that for C4 vegetation and after that fluctuations show significant decrease during years thereafter. Other recent studies also agreed well on the long-term decrease of biomass-burning emissions over past decades and in most recent years.

- It can be inferred from the plots that the wetlands are the largest contributor to the interannual variability and growth rate of methane emissions over the entire inversion time period as the plot patterns of aggregated wetlands and total

emissions are found to be in phase to each other. Within this variability, the emissions from wetlands show few long-term changes in anomalies until 2005 and after that these decrease through the end of the study period except during 2010-2012. The biomass burning emissions show smaller contribution towards interannual variability except the large emission peak during 1997-1998 anomaly. The wetland emissions appear to be the primary cause of 1991-1993 anomaly in the total aggregated category of emissions, large biomass burning emission in 1997 also with elevated wetland emissions in 1998 may have contributed to the 1997-1998 anomaly in the total emission category. However, the derived emission anomalies from all sources depend on the assumption of constant OH.

- The average seasonal cycles of seasonally varying sources are also estimated in this study. The seasonality of these sources can be explained better with consideration of weather patterns existed worldwide, as compared to the a priori emissions, depicting that the model simulated a posteriori emissions are overall best representation of the withheld observational data of methane concentrations. The inversion showed larger maxima peaks for sources of rice cultivation, boreal wetlands, and Southern Hemispheric wetlands in comparison to the priors. It can be noted in the plots that the a priori total emissions peak in August whereas a posteriori total emissions peak in July and September, driven by combined effects of emissions from wetlands (90N-30N), rice cultivation and biomass burning of C3 vegetation. A smaller maximum in April displayed in the a posteriori total

emissions, corresponded to the driving effect of emissions from Southern Hemispheric wetlands.

- This work was motivated to do the inversion process with higher horizontal grid resolution of $2^{o} \times 2.5^{o}$ in order to reduce the model data mismatch errors and increase the weights of the information content from the measurements relative to the a priori fluxes in the inversion producing stronger observational constraints on the optimized fluxes. This higher resolution grid allowed us to extract more information from the observations due to improved ability of the model to simulate CH_4 at each monitoring station and decreased need to aggregate neighboring stations within model grid cells, leading to more accurate estimates of the retrieved time-dependent CH_4 fluxes and therefore, improved our understanding of the driving sources underlying the current variations in the global methane budget.

- As one of the main goals of this study was to test how the results of optimized methane emissions would change when using the raw measurement data of CH_4 from NOAA event files in the process of inversion at a higher horizontal grid resolution of $2^{0} \times 2.5^{0}$ rather than using much processed GLOBALVIEW data of CH_4 at a coarser horizontal grid resolution of $4^{0} \times 5^{0}$, the comparison between the results of optimized methane emissions from this current inversion work ($2^{0} \times 2.5^{0}$) and previously done inversion work ($4^{0} \times 5^{0}$) up through the end of 2008 was done. The most prominent differences in the emission anomalies plots between the two until the end of 2008 were found in the individual source categories of gas and oil,

coal, livestock and waste (Figure 5.6) and in the aggregated source categories of fossil fuels, wetlands and all biogenic (Figure 5.7).

- In this work, sensitivity tests were conducted to assess the impact of discontinuity in the data coverage over the entire time of inversion for different observation sites on the methane flux trends. Seven different sensitivity tests were performed where the number of observational sites was varied based on the number of years with continuous availability of data. The sensitivity test inversion scenarios for all of the source categories maintained same trends of methane emissions throughout the study period as base case inversion scenarios discussed above but, in some cases, with significantly wider range in the mean values of the emissions. It was observed that aggregated sources of fossil fuels and anthro-biogenic sources (Figure 5.3) and individual sources of gas and oil, coal, livestock and wastes categories (Figure 5.2) are more sensitive to the variation of network densities of observation sites with continuous data coverage.

6.2. Inferences

The analysis in this study revealed the spatial and temporal changes in the distribution of atmospheric methane emitted from all around the world for more than three decades and explained the recent variations in the relative contributions of the emissions from 10 different source categories vital in the global methane budget. This work with the sensitivity tests assessed the contribution of these ten source categories to the spatial

heterogeneities in the observed CH_4 record and provided a new look into the causes of the recent growth in atmospheric methane. The rise of methane since 2007 and the decrease of the $^{13}CH_4/^{12}CH_4$ ratio of atmospheric methane suggests that the post 2006 methane growth was caused by an increase in $^{13}CH_4$-depleted biogenic emissions. Recent published studies have attributed this growth to increasing emissions from wetlands, rice agriculture, and ruminants. We find that the total averaged global methane emission over years 1983 to 2015 is estimated to be 530±50 Tg/year, over the decade of 2006-2015 is 543±44 Tg/year which is ~20 Tg/year more than that during previous decade, over years 2006 to 2010 it is estimated to be 539±44 Tg/year, whereas over years 2011 to 2015, it is estimated to be 547±45 Tg/year. The global methane emissions over years of 1983 to 2015 from all biogenic sources of both natural and anthropogenic origin account for ~73% of the total global CH_4 emissions. Anthro-biogenic sources contribute about 39% of the total CH_4 emissions, whereas natural wetlands contribute about 34.5% of the total CH_4 emissions. Emissions from fossil fuels sector constitutes about 18.5% of the total global CH_4 emissions and from biomass burning about 8.3% of the total global CH_4 emissions.

The averaged emission estimate of all biogenic sources (both natural and anthropogenic) showed an increase of about ~25 Tg/year during 2006-2015 than that during 1994-2005, whereas the anthro-biogenic sources showed highest increase in averaged emission estimate of about ~43 Tg/year during 2006-2015 than that during 1994-2005. Mainly the source categories of coal, livestock, wastes, biomass burning of C3 vegetation and northern high latitude wetlands showed increase in their averaged emission estimates of ~2 Tg/year, ~31 Tg/year, ~18 Tg/year, ~1 Tg/year and ~3 Tg/year respectively, during the decade of

2006-2015 than that during previous decade. The averaged CH_4 emission estimate from source of gas and oil increases by ~7 Tg/year, estimate from waste increases by ~13 Tg/year, estimate from burning of C3 vegetation increases by ~6 Tg/year, from wetlands (90N-30N) increases by ~1 Tg/year, from wetlands (0-90S) increases by ~5 Tg/year, whereas from northern tropical wetlands decreases by ~6 Tg/year and coal mining decreases by ~12 Tg/year during 2011-2015 than during 2006-2010. For aggregated categories, the increase in averaged emission estimates during 2011-2015 compared to that during previous 5 years, are mainly from sources of all biogenic (~9 Tg/year), anthro-biogenic (~9 Tg/year), natural wetlands (~1 Tg/year) and biomass burning (~5 Tg/year), whereas fossil fuel source shows a decrease of ~6 Tg/year. The dominant contributions for the interannual variability in the flux anomalies are from wetlands.

Finally, it can be concluded from the results of this study that the major contribution of emissions from all biogenic sources both natural and anthropogenic as well as minor contribution from biomass burning may have caused the increase in global methane levels since post-2006. It is revealed that the emissions from individual source categories of livestock, wastes, coal, northern high latitude wetlands and biomass burning of C3 vegetations had increased during 2006-2015. Although a persistent increase in total methane levels was observed until the end of the study period, but a shift in relative contributions from the emissions of individual source categories might have occurred since 2011 onwards. With the decline in emissions from anthro-biogenic sources of livestock and rice, from northern tropical wetlands, from fossil fuel source of coal and from biomass burning of C4 vegetations since 2011-2012, the increase in global methane levels since

2011 until the end of the study period might possibly be due to the contribution of increased emissions from sources of wastes, natural wetlands (southern hemisphere and northern high latitudes), fossil fuel source of gas and oil and biomass burning of C3 vegetations globally.

With a radiative forcing of 0.97 W/m^2 including both direct and indirect effects and a global warming potential of 28 over a 100-year time horizon, methane (CH_4) is considered as the second most important greenhouse gas after CO_2. The current globally averaged atmospheric methane monthly mean mole fraction value in March 2021 is 1888.5 ppb as reported by NOAA ESRL GML data [*Ed Dlugokencky, NOAA/GML (gml.noaa.gov/ccgg/trends_ch4/)*] which is already ~110 ppb higher since 2007. As CH_4 is the first indicator and first responder (Severinghaus and Brook, 1999; Möller et al., 2013; Etheridge et al., 1998; Nisbet et al., 2016) to the climate change, this recent unprecedented increase of methane might be showing us just the tip of an iceberg, as a forthcoming sign of much severe changes in climatic conditions in the near future. The reconfiguration of CH_4 budget since 2006 with dominated microbial emissions from climate-sensitive natural biogenic sources and human induced anthro-biogenic sources of livestock and wastes, implies that methane emission is responding to the changes in global temperature and precipitation as well as the changes in demand and supply for food and other resources for ever-increasing human population around the globe. During last decade since 2011, CH_4 budget might have undergone reconfiguration with dominated emissions from both biogenic sources and thermogenic sources. Wetland emissions play a significant role in the global methane budget with largest contribution in the global methane flux trend and

variability. Thus, wetland CH_4 emissions influence climate to change, whereas in turn, wetland emissions themselves are sensitive enough to respond to the changes in climate and are accounted for past changes in global atmospheric CH_4 concentration followed by abrupt (Chappellaz et al., 1997; Brook et al., 2000; Huber et al., 2006) and glacial-interglacial (Loulergue et al., 2008) climate changes (Melton et al., 2013). This positive climatic feedback apparently highlighted global wetlands to be considered as a subject of great concern to have impact on climate for their potentiality of causing large scale methane emissions in future global warming scenarios by the US Climate Change Science Program (CCSP, 2008) (Melton et al., 2013). In addition, due to increase in demands of energy production, the emissions from fossil fuel sources such as potential intensive exploitation of natural gas from shale formations and coal mining from around the world might reduce the effects of mitigation efforts and accelerate climate change (Kirschke et al., 2013).

6.3. Future Improvements

Our analysis as well as other studies suggest that improvements in the wetland models are needed by implementing better representation of wetlands areal extent, wetland CH_4 emissions in space and time, correlation between wetland area and response of CH_4 emissions with CO_2 concentration, global temperatures, and global precipitations, better availability of high spatial resolution wetland methane observation datasets and remotely sensed inundation datasets, reduction in parameter and structural uncertainties involved in all above processes. Improvements in better understanding of wetland hydrology,

biogeochemistry, and permafrost dynamics (Melton et al., 2013) and including their updated information in earth system and global climate models will be of much help in quantifying global wetland CH_4 emissions. Knowledge of global, regional, and local methane emission estimates (Dlugokencky et al., 2011) along with regular updates are required. More evenly distributed surface network measurements of methane concentrations and isotopic composition should be integrated with satellite data and ship track records with regular updates. Anthropogenic and biogenic emission estimates need to be improved in inventories (Kirschke et al., 2013) to deal with renewed increase in emissions from new fossil fuel sources such as extraction of natural gases from shale formations and wetland emission variations due to fluctuating temperatures in higher latitudes and precipitation in tropics. Better uncertainty reduction in all steps from data collection to chemistry and transport in bottom-up as well as top-down atmospheric models will be helpful. Better knowledge of some tracer gases can help in source attribution such as global ethane abundance in atmosphere and methane-to-ethane ratios can resolve to distinguish between the sources as in fugitive fossil fuel emissions and biomass burning emissions (Simpson et al., 2012; Rice et al., 2016). Comparison of abundance of ammonia as a co-emitter along with CH_4 can help quantify the impact of livestock and waste management CH_4 emissions on the recent rise of global methane (Peischl et al., 2018). Trends of global OH concentration and methyl chloroform mole fractions present in the atmosphere along with hemispheric differences should be regularly monitored and updated. Estimated OH interannual variations over time synergized as sink with the calculation of methane estimates coupled in the models will provide more accurate and promising results with GEOS-Chem running parallel to the inverse model which may

increase the computational demands (Röger, 2013). More accurate meteorological data over the entire time of modeling with higher spatial grid resolution (Röger, 2013) can improve the regional estimates with better precision. Furthermore, we need to explore the sensitivity of our results to a number of choices of numerous model parameters in separate inversion setups.

In perspective of making global climate change mitigation policies, methane with approximately 10 years of atmospheric lifetime which is shorter as compared to that of other greenhouse gases, reduction in its emission can serve as immediate effective measure against global warming. Moreover, further mitigation efforts in global level should address the methane source attribution of fossil fuel emissions, waste and landfill emissions, global wetland emissions including emissions from thawing of permafrost and hydrates due to Arctic warming. Atmospheric methane already known for its potentiality to exaggerate the global climate warming with large positive feedback, poses a threat to future climate change and better quantification of global methane budget and its changes with regular updates seems to be a challenge; whereas its ability to get destroyed in relative shorter time gives the opportunity towards possible mitigation step with reduction in its emissions (Kirschke et al., 2013).

Thus, the significance of this modeling work lies with its contribution in meeting the challenges of quantifying more than three decades of global methane budget and its variations more accurately in both spatial and temporal scale and helping policy makers to

accept the opportunity to utilize shorter lifetime of methane in the atmosphere for developing effective climate change mitigation policies which are required soon.

REFERENCES

Allan, W., Struthers, H. and Lowe, D. C., 2007. Methane carbon isotope effects caused by atomic chlorine in the marine boundary layer: Global model results compared with Southern Hemisphere measurements. J. Geophys. Res. Atmos., 112, D04306.

Allen, D. J., et al., 1996b. Transport induced interannual variability of carbon monoxide using a chemistry and transport model. J. Geophys. Res., 101, 28,655-28,670.

Allen, D. J., Rood, R. B., Thompson, A. M. and Hidson, R. D., 1996a. Three-dimensional ^{222}Rn calculations using assimilated data and a convective mixing algorithm. J. Geophys. Res., 101, 6871-6881.

Andreae, M. O. and Merlet, P., 2001. Emission of trace gases and aerosols from biomass burning. Global Biogeochem. Cycles, 15, 955–966.

Aydin, M., et al. 2011. Recent decreases in fossil-fuel emissions of ethane and methane derived from firn air. Nature, 476(7359), 198–201.

Barnola, J. M., Raynaud, D., Korotkevich, Y. S. & Lorius, C., 1987. Vostok ice core provides 160,000-year record of atmospheric CO_2. Nature 329, 408–414.

Bastviken, D., Tranvik, L. J., Downing, J. A., Crill, P. M. and EnrichPrast, A., 2011. Freshwater methane emissions offset the continental carbon sink. Science, 331, 50.

Bazhin, N., 1994. Sources and sinks of methane on the territory of the former USSR. Pure Appl. Chem. 66, 188–191.

Beck, L.L., Piccot, S.D., Kirchgessner, D.A., 1993. Industrial sources. In: Khalil, M. (Ed.), Atmospheric Methane: Sources, Sinks and Role in Global Change. Springer-Verlag, New York, NY, pp. 341– 399.

Bekki, S., Law, K.S., Pyle, J.A., 1994. Effects of ozone depletion on atmospheric CH_4 and CO concentrations. Nature 371, 595–599.

Bergamaschi, P., Bräunlich, M., Marik, T. and Brenninkmeijer, C. A. M., 2000a. Measurements of the carbon and hydrogen isotopes of atmospheric methane at Izaña, Tenerife, Seasonal cycles and synoptic-scale variations, J. Geophys. Res., 105, 14,531–14,546.

Bergamaschi, P., et al., 2009. Inverse modeling of global and regional CH4 emissions using SCIAMACHY satellite retrievals. J. Geophys. Res., 114, D22301.

Bergamaschi, P., et al., 2013. Atmospheric CH4 in the first decade of the 21st century: Inverse modeling analysis using SCIAMCHY satellite retrievals and NOAA surface measurements, J. Geophys. Res. Atmos., 118, 7350–7369.

Bergamaschi, P., Frankenberg, C., Meirink, J. F., Krol, M., Dentener, F., Wagner, T., Platt, U., Kaplan, J. O., K¨orner, S., Heimann, M., Dlugokencky, E. J., and Goede, A., 2007.

Satellite chartography of atmospheric methane from SCIAMACHY onboard ENVISAT: 2. Evaluation based on inverse model simulations, J. Geophys. Res., 112, D02304.

Bergamaschi, P., Hein, R., Heimann, M. and Crutzen, P.J., 2000b. Inverse modeling of the global CO cycle: 1. Inversion of CO mixing ratios, J. Geophys. Res., 105, 1909–1927.

Bergamaschi, P., Krol, M., Dentener, F., Vermeulen, A., Meinhardt, F., Graul, R., Ramonet, M., Peters, W., and Dlugokencky, E. J., 2005. Inverse modelling of national and European CH_4 emissions using the atmospheric zoom model TM5, Atmos. Chem. Phys., 5, 2431–2460.

Bergamaschi, P., Lowe, D. C., Manning, M. R., Moss, R., Bromley, T. and Clarkson, T. S., 2001. Transects of atmospheric CO, CH4, and their isotopic composition across the Pacific: Shipboard measurements and validation of inverse models, J. Geophys. Res., 106, 7993– 8011.

Bey, I., et al., 2001. Global modeling of tropospheric chemistry with assimilated meteorology: Model description and evaluation. J. Geophys. Res., 106(D19), 23,073-23,095.

Blake, D.R. and Rowland, F.S., 1988. Continuing worldwide increase in tropospheric methane, 1978 to 1987. Science 239, 1129 – 1131.

Blake, D.R., Meyer, E.W., Tyler, S.C., Makide, Y., Montague, D.C. and Rowland, F.S., 1982. Global increase in atmospheric methane between 1978-1980. Geophys. Res. Lett. 9, 477-480.

Bloom, A. A., Lee-Taylor, J., Madronich, S., Messenger, D. J., Palmer, P. I., Reay, D. S. and McLeod, A. R., 2010. Global methane emission estimates from ultraviolet irradiation of terrestrial plant foliage. New Phytologist, 187, 417-425.

Blunier, T., Chapellaz, J., Schwander, J., Stauffer, B., Raynaud, D., 1995. Variations in atmospheric methane concentration during the Holocene Epoch. Nature 374, 46 – 49.

Blunier, T., Chappellaz, J., Schwander, J., Dällenbach, A., Stauffer, B., Stocker, T.F., Raynaud, D., Jouzel, J., Clausen, H.B., Hammer, C.U., Johnsen, S.J., 1998. Asynchrony of Antarctic and Greenland climate change during the last glacial period. Nature 394, 739 – 743.

Boening, C., Willis, J. K., Landerer, F. W., Nerem, R. S. and Fasullo, J., 2012. The 2011 La Niña: So strong the oceans fell, Geophys. Res. Lett., 39, L19602.

Bogner, J. and Matthews, E., 2003. Global methane emissions from landfills: New methodology and annual estimates 1980–1996, Global Biogeochem. Cycles, 17(2), 1065.

Bousquet, P., et al., 2006: Contribution of anthropogenic and natural sources to atmospheric methane variability. Nature, 443, 439–443.

Bousquet, P., et al., 2011. Source attribution of the changes in atmospheric methane for 2006–2008. Atmos. Chem. Phys., 11, 3689–3700.

Bousquet, P., Hauglustaine, D. A., Peylin, P., Carouge, C. and Ciais, P., 2005: Two decades of OH variability as inferred by an inversion of atmospheric transport and chemistry of methyl chloroform. Atmos. Chem. Phys., 5, 2635–2656.

Brasseur, G., Kiehl, J., Muller, J.-F., Schneider, T., Granier, C., Tie, X., Hauglustaine, D., 1998. Past and future changes in global tropospheric ozone: impact on radiative forcing. Geophys. Res. Lett. 25, 3807–3810.

Britannica, The Editors of Encyclopaedia. "Methane". Encyclopedia Britannica, 29 May. 2020, https://www.britannica.com/science/methane. Accessed 21 July 2021.

Brook, E. J., Harder, S., Severinghaus, J. P., Steig, E. J., and Sucher, C. M., 2000. On the origin and timing of rapid changes in atmospheric methane during the last glacial period, Global Biogeochem. Cy., 14, 559–572.

Brook, E., Sowers, T., Orchardo, J., 1996. Rapid variations in atmospheric methane concentration during the past 110,000 years. Science 273, 1087–1091.

Brown, M., 1993. Deduction of fluxes of source gases using an objective inversion algorithm and a chemical transport model, J. Geophys. Res., 98, 12,639–12,660.

Brown, M., 1995. The singular value decomposition method applied to the deduction of the emissions and the isotopic composition of atmospheric methane, J. Geophys. Res., 100, 11,425–11,446.

Bruhn, D., Mikkelsen, T. N., Rolsted, M. M. M., Egsgaard, H. and Ambus, P., 2014. Leaf surface wax is a source of plant methane formation under UV radiation and in the presence of oxygen. Plant Biology (Stuttg.), Vol. 16, Issue 2, 512-516.

Bruhwiler, L. M. P., Michalak, A. M., Peters, W., Baker, D. F., and Tans, P., 2005. An improved Kalman Smoother for atmospheric inversions, Atmos. Chem. Phys., 5, 2691–2702.

Bruhwiler, L. M., Dlugokencky, E., Masarie, K., Ishizawa, M., Andrews, A., Miller, J., Sweeney, C., Tans, P. and Worthy, D., 2014. CarbonTracker-CH4: An assimilation system for estimating emissions of atmospheric methane, Atmos. Chem. Phys., 14, 8269–8293.

Bruhwiler, L., Tans, P. and Ramonet, M., 2000. A time-dependent assimilation and source retrieval technique for atmospheric tracers, in Inverse Methods in Global Biogeochemical Cycles, Geophys. Monogr. Ser., vol. 114, edited by P. Kasibhatla et al., pp. 265– 277, AGU, Washington, D. C.

Butenhoff, C. L., and Khalil, M. A. K., 2007. Global methane emissions from terrestrial plants, Environ. Sci. Technol., 41(11), 4032-4037.

Butler, T. M., Rayner, P. J., Simmonds, I. & Lawrence, M. G., 2005. Simultaneous mass balance inverse modeling of methane and carbon monoxide. J. Geophys. Res. 110, D21310.

Cantrell, C. A., Shetter, R. E., McDaniel, A. H., Calvert, J. G., Davidson, J. A., Lowe, D. C., Tyler, S. C., Cicerone, R. J. and Greenberg J. P., 1990. Carbon kinetic isotope effect in the oxidation of methane by the hydroxyl radical, J. Geophys. Res., 95, 22,455– 22,462.

Cao, M. K., Gregson, K., Marshall, S., Dent, J.B. and Heal, O. W., 1996a. Global methane emissions from rice paddies, Chemosphere, 33(5), 879–897.

Chappellaz, J., Barnola, J., Raynaud, D., Korotkevich, Y., Lorius, C., 1990. Ice-core record of atmospheric methane over the past 160,000 years. Nature 345, 127 – 131.

Chappellaz, J., Blunier, T., Kints, S., Dallenbach, A., Barnola, J., Schwander, J., Raynaud, D., Stauffer, B., 1997. Changes in the atmospheric CH_4 gradient between Greenland and Antarctica during the Holocene. J. Geophys. Res. 102, 15987 – 15997.

Chappellaz, J., Blunier, T., Raynaud, D., Barnola, J., Schwander, J., Stauffer, B., 1993a. Synchronous changes in atmospheric CH_4 and Greenland climate between 40-kyr and 8-kyr BP. Nature 366, 443– 445.

Chappellaz, J., Fung, I.Y., Thompson, A.M., 1993b. The atmospheric CH_4 increase since the Last Glacial Maximum. Tellus 45B, 228– 241.

Chen, Y. H. and Prinn, R. G., 2006. Estimation of atmospheric methane emissions between 1996 and 2001 using a three-dimensional global chemical transport model, J. Geophys. Res. atmos., 111, D10307.

Chen, Y. H., 2004. Estimation of methane and carbon dioxide surface fluxes using a 3-D global atmospheric chemical transport model, Ph.D. thesis, Mass. Inst. of Technol., Cambridge, Mass.

Ciais, P., et al., 2013. Carbon and Other Biogeochemical Cycles. In: Climate Change 2013: The Physical Science Basis. Contribution of Working Group I to the Fifth Assessment Report of the Intergovernmental Panel on Climate Change [Stocker, T.F., D. Qin, G.-K. Plattner, M. Tignor, S.K. Allen, J. Boschung, A. Nauels, Y. Xia, V. Bex and P.M. Midgley (eds.)]. Cambridge University Press, Cambridge, United Kingdom and New York, NY, USA.

Cicerone, R.J. and Oremland, R.S., 1988. Biogeochemical aspects of atmospheric methane. Global Biogeochem. Cycles 2, 299–327.

Conny, J.M. and Currie, L.A., 1996. The isotopic characterization of methane, non-methane hydrocarbons and formaldehyde in the troposphere. Atmos. Environ. 30, 621–638.

Craig, H., Chou, C.C., 1982. Methane: the record in polar ice cores. Geophys. Res. Lett. 9, 1221– 1224.

Crevoisier, C., et al., 2013. The 2007–2011 evolution of tropical methane in the mid-troposphere as seen from space by MetOp-A/IASI, Atmos. Chem. Phys., 13, 4279–4289.

Crutzen, P. and Bruhl, C., 1993. A model study of the atmospheric temperatures and concentrations of ozone, hydroxyl, and some other photochemically active gases during the glacial, the preindustrial Holocene and the present. Geophys. Res. Lett. 20, 1047–1050.

Crutzen, P. and Zimmermann, P., 1991. The changing photochemistry of the troposphere. Tellus 43AB, 136– 151.

Crutzen, P., 1995. Overview of tropospheric chemistry: developments during the past quarter century and a look ahead. Faraday Discuss. 100, 1 –21.

Curry, C. L., 2007. Modeling the soil consumption of methane at the global scale. Global Biogeochem. Cycles, 21, GB4012.

Curtis, J. B., 2002. Fractured shale-gas systems. American Association of Petroleum Geologists Bulletin, 86, 1921–1938.

Dangal, S. R. S., et al., 2017. Methane emission from global livestock sector during 1890–2014: Magnitude, trends and spatiotemporal patterns. Global Change Biology, 23(10), 4147-4161.

DeMore, W. B., Sander, S. P., Golden, D. M., Hampson, R. F., Kurylo, M. J., Howard, C. J., Ravishankara, A. R., Kolb, C. E. and Molina, M. J., 1997. Chemical kinetics and photochemical data for use in stratospheric modeling, Publ. 97-4, Jet Propulsion Lab., Pasadena, Calif.

Denman, K. L., et al., 2007. Couplings between changes in the climate system and biogeochemistry. In: Climate Change 2007: The Physical Science Basis. Contribution of Working Group I to the Fourth Assessment Report of the Intergovernmental Panel on Climate Change [Solomon, S., D. Qin, M. Manning, Z. Chen, M. Marquis, K. B. Averyt, M. Tignor and H. L. Miller (eds.)] Cambridge University Press, Cambridge, United Kingdom and New York, NY, USA, 499-587.

Dentener, F., et al., 2005. The impact of air pollutant and methane emission controls on tropospheric ozone and radiative forcing: CTM calculations for the period 1990–2030. Atmos. Chem. Phys., 5, 1731–1755.

Dentener, F., Peters, W., Krol, M., van Weele, M., Bergamaschi, P. and Lelieveld, J., 2003. Interannual variability and trend of CH4 lifetime as a measure for OH changes in the 1979–1993 time period. J. Geophys. Res. Atmos., 108, 4442.

Dickens, G., Castillo, M., Walker, J., 1997. A blast of gas in the latest Paleocene: simulating first-order effects of massive dissociation of oceanic methane hydrate. Geology 25, 259– 262.

Dlugokencky, E. J., et al., 2009. Observational constraints on recent increases in the atmospheric CH_4 burden, Geophys. Res. Lett., 36, L18803.

Dlugokencky, E. J., Harris, J. M., Chung, Y. S., Tans, P. P. and Fung, I., 1993. The relationship between the methane seasonal cycle and regional sources and sinks at Tae-ahn Peninsula, Korea. Atmos. Environ., 27(14), 2115-2120.

Dlugokencky, E. J., Houweling, S., Bruhwiler, L., Masarie, K. A., Lang, P. M., Miller, J. B. & Tans, P. P., 2003. Atmospheric methane levels off: temporary pause or a new steady-state? Geophys. Res. Lett. 30, 1992.

Dlugokencky, E. J., Nisbet, E. G., Fisher, R. and Lowry, D., 2011. Global atmospheric methane: Budget, changes and dangers. Philos. Trans. R. Soc. London Ser. A, 369, 2058–2072.

Dlugokencky, E., Dutton, E., Novelli, P., Tans, P., Masarie, K., Lantz, K., Madronich, S., 1996. Changes in CH_4 and CO growth rates after the eruption of Mt. Pinatubo and their link with changes in tropical tropospheric UV flux. Geophys. Res. Lett. 23, 2761– 2764.

Dlugokencky, E., Masaire, K., Lang, P., Tans, P., Steele, L., Nisbet, E., 1994b. A dramatic decrease in the growth rate of atmospheric methane in the northern hemisphere during 1992. Geophys. Res. Lett. 21, 45– 48.

Dlugokencky, E., Masarie, K., Lang, P., Tans, P., 1998. Continuing decline in the growth rate of the atmospheric methane burden. Nature 393, 447–450.

Dlugokencky, E., Masarie, K., Tans, P., Conway, T., Xiong, X., 1997. Is the amplitude of the methane seasonal cycle changing? Atmos. Environ. 31, 21– 26.

Dlugokencky, E., Steele, L., Lang, P., Masarie, K., 1994a. The growth rate and distribution of atmospheric methane. J. Geophys. Res. 99, 17021–17043.

Dlugokencky, E.J., Crotwell, A. M., Mund, J. W., Crotwell, M. J. and Thoning, K. W., 2017. Atmospheric Methane Dry Air Mole Fractions from the National Oceanic and Atmospheric Administration, Earth System Research Laboratories, Global Monitoring Laboratory (NOAA ESRL GML), Carbon Cycle Cooperative Global Air Sampling Network, 1983-2017, Version: 2017-07.

Dlugokencky, E.J., Walter, B.P., Masarie, K.A., Lang, P.M. and Kasischke, E.S., 2001: Measurements of an anomalous global methane increase during 1998. Geophys. Res. Lett., 28, 499-502.

Dueck, T. A., et al., 2007. No evidence for substantial aerobic methane emission by terrestrial plants: A 13C-labelling approach. New Phytologist, 175, 29–35.

Dutaur, L. and Verchot, L. V., 2007. A global inventory of the soil CH4 sink. Global Biogeochem. Cycles, 21, GB4013.

Ed Dlugokencky, NOAA/ ESRL/GML (www.esrl.noaa.gov/gmd/ccgg/trends_ch4/).

EDGAR4–database, 2009: Emission Database for Global Atmospheric Research (EDGAR), release version 4.0. http://edgar.jrc.ec.europa.eu, 2009. European Commission. Joint Research Centre (JRC) / Netherlands Environmental Assessment Agency (PBL).

Ehhalt, D. H. and Heidt, L. E., 1973. Vertical profiles of CH4 in troposphere and stratosphere. J. Geophys. Res., 78, 5265–5271.

Enting I.G. and Pearman, G.I., 1987. Description of a one-dimensional carbon cycle model calibrated using techniques of constrained inversion. Tellus, 39B, 459-476.

Enting, I. G., 2002. Inverse problems in atmospheric constituent transport, atmospheric and space science series, Cambridge University Press, Cambridge.

Enting, I. G., Trudinger, C. M., and Francey, R. J., 1995. A Synthesis Inversion of the Concentration and $\delta^{13}C$ of Atmospheric CO_2, Tellus Series B - Chemical and Physical Meteorology, 47B, 35–52.

Enting, I.G. and Mansbridge, J.V., 1989. Seasonal sources and sinks of atmospheric CO_2 Direct inversion of filtered data. Tellus B, Vol. 41B, Issue 2, 111-126.

Enting, I.G., 1993. Inverse problems in atmospheric constituent studies, III, Estimating errors in surface sources, Inverse Probl., 9, 649-665.

Enting, I.G., Trudinger, C.M., Francey, R.J. and Granek, H., 1993. Synthesis inversion of atmospheric CO_2 using the GISS tracer transport model, Div. of Atmos. Res. Tech. Pap. 29, Connnonw. Sci. and Ind. Res. Organ., Melbourne, Australia.

EPA, 2011a. Global anthropogenic non-CO2 greenhouse gas emissions: 1990–2030, United States Environmental Protection Agency (US EPA) Report. Washington, DC. http://www.epa.gov/climatechange/Downloads/EPAactivities/EPA_Global_NonCO2_Projections_Dec2012.pdf.

EPA, 2011b. Reactive nitrogen in the United States: An analysis of inputs, flows, consequences, and management options. Report EPA-SAB-11-013, Washington, DC, 140 pp.
http://yosemite.epa.gov/sab/sabproduct.nsf/WebBOARD/INCFullReport/$File/Final%20INC%20Report_8_19_11%28without%20signatures%29.pdf.

Etheridge, D., Pearman, G., Fraser, P., 1992. Changes in tropospheric methane between 1841 and 1978 from a high accumulation-rate Antarctic ice core. Tellus 44B, 282–294.

Etheridge, D., Steele, L., Francey, R., Langenfelds, R., 1998. Atmospheric methane between 1000 A.D. and present: evidence of anthropogenic emissions and climatic variability. J. Geophys. Res. 103, 15979 – 15993.

Etheridge, D.M., Steele, L.P., Langenfelds, R.L., Francey, R.J., Barnola J.M., and Morgan, V.I., 1996. Natural and anthropogenic changes in atmospheric CO_2 over the last 1000 years from air in Antarctic ice and firn, J. Geophys. Res., 101, 4115-4128.

Etiope, G., Lassey, K. R., Klusman, R. W. and Boschi, E., 2008. Reappraisal of the fossil methane budget and related emission from geologic sources. Geophys. Res. Lett., 35, L09307.

European Commission Joint Research Centre, Netherlands Environmental Assessment Agency, 2010. Emission Database for Global Atmospheric Research (EDGAR), Release Version 4.2. Available at http://edgar.jrc.ec.europa.eu. Accessed November 4, 2013.

Fan, S., Gloor, M., Mahlman, J., Pacala, S., Sarmiento, J., Takahashi, T. and Tans, P., 1998. A large terrestrial carbon sink in north america implied by atmospheric and oceanic carbon dioxide data and models, Science, 282, 442-446.

FAOSTAT, 2016. Food and Agriculture Organization of the United Nations Statistics Division (United Nations, Rome). Available at faostat.fao.org. Accessed August 29, 2016.

Fisher, R. E., et al., 2011. Arctic methane sources: Isotopic evidence for atmospheric inputs, Geophys. Res. Lett., 38, L21803.

Fraser, P.J., Khalil, M.A.K., Rasmussen, R.A. and Crawford, A.J., 1981. Trends of atmospheric methane in the southern hemisphere. Geophys. Res. Lett. 8, 1063-1066.

Freckleton, R., Highwood, E., Shine, K., Wild, O., Law, K. and Sanderson, M., 1998. Greenhouse gas radiative forcing: Effects of averaging and inhomogeneities in trace gas distribution. Q. J. R. Meteorol. Soc., 124, 2099–2127.

Freckleton, R., Highwood, E., Shine, K., Wild, O., Law, K. and Sanderson, M., 1998. Greenhouse gas radiative forcing: Effects of averaging and inhomogeneities in trace gas distribution. Q. J. R. Meteorol. Soc., 124, 2099–2127.

Fung, I., John, J., Lerner, J., Matthews, E., Prather, M., Steele L.P. and Fraser P.J., 1991: Three-dimensional model synthesis of the global methane cycle. J. Geophys. Res., 96D, 13033–13065.

Gauci, V., Dise, N. and Fowler, D., 2002. Controls on suppression of methane flux from a peat bog subjected to simulated acid rain sulfate deposition, *Global Biogeochem. Cycles*, 16(1), 1004.

Gerber, P. J., et al., 2013. Tackling climate change through livestock: a global assessment of emissions and mitigation opportunities, Food and Agriculture Organization of the United Nations (FAO).

Giglio, L., et al., 2010. Assessing variability and long-term trends in burned area by merging multiple satellite fire products. Biogeosciences, 7, 1171-1186.

Giglio, L., Randerson, J. T. and van der Werf, G. R., 2013. Analysis of daily, monthly, and annual burned area using the fourth-generation global fire emissions database (GFED4), J. Geophys. Res. Biogeosci., 118, 317–328.

GLOBALVIEW-CH_4, 2009. Cooperative Atmospheric Data Integration Project - Methane. (NOAA ESRL, Boulder, Colorado).

Granier C, et al., 2011. Evolution of anthropogenic and biomass burning emissions of air pollutants at global and regional scales during the 1980–2010 period. Clim Change 109(1-2), 163–190.

Gupta, M., Tyler, S., Cicerone, R., 1996. Modeling atmospheric $\delta^{13}CH_4$ and the causes of recent changes in atmospheric CH_4 amounts. J. Geophys. Res. 101, 22923–22932.

Gurney, K. R., Law, R. M., Denning, A. S., Rayner, P. J., Baker, D., Bousquet, P., Bruhwiler, L., Chen, Y. H., Ciais, P., Fan, S., Fung, I. Y., Gloor, M., Heimann, M., Higuchi, K., John, J., Maki, T., Maksyutov, S., Masarie, K., Peylin, P., Prather, M., Pak, B. C., Randerson, J., Sarmiento, J., Taguchi, S., Takahashi, T., and Yuen, C. W., 2002. Towards robust regional estimates of CO2 sources and sinks using atmospheric transport models, Nature, 415, 626–630.

Harriss, R., Bartlett, K., Frolking, S. and Crill P., 1993. Methane emissions from northern high-latitude wetlands, in Biogeochemistry of Global Change: Radiatively Active Gases, edited by R.S. Oremland, pp. 449-486, Chapman and Hall, New York.

Hartley, D., and Prinn, R.,1993. Feasability of determining surface emissions of trace gases using an inverse method in a three-dimensional chemical transport model, J. Geophys. Res., 98, 5183–5197.

Hayman, G. D., et al., 2014. Comparison of the HadGEM2 climate-chemistry model against in situ and SCIAMACHY atmospheric methane data. Atmos. Chem. Phys., 14, 13257–13280.

Hein, R. and Heimann, M, 1994. Determination of global scale emissions of atmospheric methane using an inverse modelling method, in Non-CO_2 Greenhouse Gases, edited by J. van Ham et al., pp. 271–281, Kluwer, Norwell, Mass.

Hein, R., Crutzen, P. J. and Heimann, M., 1997. An inverse modeling approach to investigate the global atmospheric methane cycle. Global Biogeochem. Cycles, 11, 43–76.

Henze, D. K., Hakami, A. and Seinfeld J. H., 2007. Development of the adjoint of GEOS-Chem, Atmos. Chem. Phys., 7, 2413–2433.

Hogan, K. and Harriss, R.C., 1994. Comments on ‘‘A dramatic decrease in the growth rate of atmospheric methane in the northern hemisphere during 1992’’ by E.J. Dlugokencky et al. Geophys. Res. Lett. 21, 2445– 2447.

Houweling, S., Kaminski, T., Dentener, F., Lelieveld, J. and Heimann, M., 1999. Inverse modeling of methane sources and sinks using the adjoint of a global transport model, J. Geophys. Res., 104, 26,137– 26,160.

Howarth, R., Santoro, R. and Ingraffea, A., 2011. Methane and the greenhouse-gas footprint of natural gas from shale formations. Clim. Change, 106, 679–690.

Huber, C., Leuenberger, M., Spahni, R., Flückiger, J., Schwander, J., Stocker, T. F., Johnsen, S., Landais, A., and Jouzel, J., 2006. Isotope calibrated Greenland temperature record over Marine Isotope Stage 3 and its relation to CH_4, Earth Planet. Sc. Lett., 243, 504–519.

Hughes, M.K., and Diaz, H.F., 1994. Was there a "Medieval Warm Period," and if so, where and when? Clim. Change, 26, 109-142.

Intergovernmental Panel on Climate Change, 2001. Climate Change 2001: The Scientific Basis, edited by J. T. Houghton et al., Cambridge Univ. Press, New York.

IPCC (Intergovernmental Panel on Climate Change), 1992. Climate Change 1992: The Supplementary Report to the IPCC Scientific Assessment, Houghton, J. T., Callander, B. A. and Varney, S. K. (eds). Cambridge University Press, Cambridge, UK, 198 pp.

Ito, A., and Inatomi, M., 2012. Use of a process-based model for assessing the methane budgets of global terrestrial ecosystems and evaluation of uncertainty. Biogeosciences, 9, 759–773.

Jain, A.K., Briegleb, B.P., Minschwaner, K. and Wuebbles, D.J., 2000. Radiative forcings and global warming potentials of 39 greenhouse gases. J. Geophys. Res. 105, 20773–20790.

Johnson, N. L., Kotz, S. and Balakrishnan, N., 1994. Continuous Univariate Distributions, vol. 1, John Wiley & Sons, New York, NY, USA.

Jouzel, J., Jouzel, N.I., Barkov, J.M., Barnola, M., Bender, J., Chappellaz, C., Genthon, V.M., Kotlyakov, V., Lipenkov, C., Lorius, J.R., Petit, D., Raynaud, G., Raisbeck, C., Ritz, T., Sowers, M., Stievenard, F., Yiou, F., Yiou, P., 1993. Extending the Vostok ice-core record of palaeoclimate to the penultimate glacial period. Nature 364, 407 – 412.

Jouzel, J., Lorius, C., Petit, J. *et al.*, 1987. Vostok ice core: a continuous isotope temperature record over the last climatic cycle (160,000 years). Nature 329, 403–408.

Kai, F. M., Tyler, S. C. and Randerson, J. T., 2010. Modeling methane emissions from rice agriculture in China during 1961–2007. J. Integr. Env. Sci. 7, 49–60.

Kai, F. M., Tyler, S. C., Randerson, J. T. and Blake, D. R., 2011. Reduced methane growth rate explained by decreased Northern Hemisphere microbial sources. Nature, 476, 194–197.

Kalman, R., 1960. A new approach to linear filtering and prediction problems, J. Basic Eng. (ASME), 82D, 35–45.

Kaminski, T., Heimann M. and Giering, R., 1999b. A coarse grid three dimensional global inverse model of the atmospheric transport, 2. Inversion of the transport of CO_2 in the 1980s, J . Geophys. Res., 104, 18,555-18,581.

Kaminski, T., Heimann, M. and Giering, R., 1999a. A coarse grid threedimensional inverse model of the atmospheric transport: 1. Adjoint model and Jacobian matrix, J. Geophys. Res., 104, 18,535– 18,553.

Kaminski, T., Rayner, P. J., Heimann, M., and Enting, I. G., 2001. On aggregation errors in atmospheric transport inversions, J. Geophys. Res. Atmos., 106, 4703–4715.

Kammen, D.M., and Marino, B.D., 1993. On the origin and magnitude of pre-industrial anthropogenic CO_2 and CH_4 emissions. Chemosphere 2, 6, 69-86.

Kaplan, J. O., 2002. Wetlands at the Last Glacial Maximum: Distribution and methane emissions. Geophys. Res. Lett., 29(6), 31-34.

Karlsdottir, S., Isaksen, I.S.A., 2000. Changing methane lifetime: possible cause for reduced growth. Geophys. Res. Lett. 27, 93–96.

Karmakar et al., 2015. Recent trends in global methane emissions inferred from 30-years of surface CH_4 and $\delta^{13}C$-CH_4 measurements. AGU Fall Meeting, 2015, San Francisco CA, 14-18 December 2015, https://agu.confex.com/agu/fm15/meetingapp.cgi/Paper/85278.

Kasibhatla, P., Arellano, A., Logan, J.A., Palmer, P.I. and P. Novelli, P., 2002. Top-down estimate of a large source of atmospheric carbon monoxide associated with fuel combustion in Asia, Geophys. Res. Lett., 29(19), 1900.

Kasibhatla, P., et al., 2000. Inverse Methods in Global Biogeochemical Cycles, Volume 114, published by the American Geophysical Union as part of the Geophysical Monograph Series, Volume 114.

Keeling, C.D., Piper, S.C. and Heimann, M., 1989b. A three dimensional model of atmospheric CO_2 transport based on observed winds, 4. Mean annual gradients and interannual variations, in Aspects of Climate Variability in the Pacific and the Western Americas [D. H. Peterson (ed.)]. Geophysical Monograph Series, Vol. 55. American Geophysical Union, Washington, D.C., pp. 305–363.

Keigwin, L.D., 1996. The Little Ice Age and Medieval Warm Period in the Sargasso Sea, Science 274, 1504-1508.

Keppler, F., Hamilton, J. T. G., Brass, M. and Rockmann, T., 2006. Methane emissions from terrestrial plants under aerobic conditions. Nature, 439, 187-191.

Khalil, M. A. K. and Shearer, M. J., 2006. In Greenhouse Gases and Animal Agriculture: An Update; Soliva, C. R., Takahashi, J., Kreuzer, M., Eds.; International Congress Series 1293, Elsevier: Amsterdam, The Netherlands, pp 33-41.

Khalil, M. A. K., Butenhoff, C. L., Rasmussen, R. A., 2007. Atmospheric methane: Trends and cycles of sources and sinks. Environ Sci Technol 41(7): 2131–2137.

Khalil, M. and Rasmussen, R., 1987. Atmospheric methane: trends over the last 10,000 years. Atmos. Environ. 21, 2445 – 2452.

Khalil, M. and Rasmussen, R., 1994a. Global emissions of methane during the last several centuries. Chemosphere 29, 833 – 842.

Khalil, M. and Rasmussen, R., 1994b. Trends in atmospheric methane. Pure and Applied Chemistry. 66, Special Report: Methane in the Atmosphere, Commission on Atmospheric Chemistry.

Khalil, M., and Rasmussen, R., 1993. Decreasing trend of methane: unpredictability of future concentrations. Chemosphere 26, 803–814.

Khalil, M.A.K., and Rasmussen, R.A., 1989. Climate-induced feedbacks for the global cycles of methane and nitrous oxide, Tellus, 4lB, 554-559.

Khalil, M.A.K., Rasmussen, R.A., 1985. Causes of increasing atmospheric methane: depletion of hydroxyl radicals and the rise of emissions. Atmos. Environ. 13, 397– 407.

Kirchgessner, D.A., 2000. Fossil fuel industries. In: Khalil, M. (Ed.), Atmospheric Methane: Its Role in the Global Environment. Springer-Verlag, New York, NY, pp. 263–279.

Kirschbaum, M. U. F., and Walcroft, A., 2008. No detectable aerobic methane efflux from plant material, nor from adsorption/desorption processes. Biogeosciences, 5, 1551–1558.

Kirschke S, et al., 2013. Three decades of global methane sources and sinks. Nat Geosci 6(10), 813–823.

Krol, M., van Leeuwen, P. and Lelieveld, J., 1998. Global OH trend inferred from methylchloroform measurements. J. Geophys. Res. 103, 10697– 10711.

Lamarque, J. F., et al., 2013. The Atmospheric Chemistry and Climate Model Intercomparison Project (ACCMIP): Overview and description of models, simulations and climate diagnostics. Geosci. Model Dev., 6, 179–206.

Langenfelds, R. L., Francey, R. J., Pak, B. C., Steele, L. P., Lloyd, J., Trudinger, C. M. and Allison, C. E., 2002: Interannual growth rate variations of atmospheric CO_2 and its $\delta^{13}C$, H_2, CH_4, and CO between 1992 and 1999 linked to biomass burning. Global Biogeochem. Cycles, 16, 1048.

Law, K.S. and Nisbet, E.G., 1996. Sensitivity of the CH4 growth rate to changes in CH4 emissions from natural gas and coal. J. Geophys. Res. 101, 14387– 14397.

Law, R., and Simmonds, I., 1996. The sensitivity of deduced CO_2 sources and sinks to variations in transport and imposed surface concentrations, Tellus, Ser. B, 48, 613–625.

Le Quéré, C., et al., 2014. Global carbon budget 2013, Earth Syst. Sci. Data, 6, 235–263.

Legrand, M., Lorius, C., Barkov, N., Petrov, V., 1988. Vostok (Antarctic ice core): atmospheric chemistry changes over the last climatic cycle (160,000 years). Atmos. Environ. 22, 317–331.

Lelieveld, J., Crutzen, P., Dentener, F., 1998. Changing concentration, lifetime and climate forcing of atmospheric methane. Tellus 50B, 128– 150.

Levin, I., et al., 2012. No inter-hemispheric $\delta^{13}CH_4$ trend observed. Nature, 486, E3–E4.

Levine, J. S., Coffer III, W. R. and Pinto, J. P., 2000. Biomass burning, in Atmospheric Methane: Its Role in Global Environment, edited by M. A. K. Khalil, Springer-Verlag, New York.

Li, C. S., et al., 2002. Reduced methane emissions from large-scale changes in water management of China's rice paddies during 1980–2000. Geophys. Res. Lett. 29, 1972.

Li, C., Qiu, J., Frolking, S., Xiao, X., Salas, W., Moore III, B., Boles, S., Huang, Y. and Sass, R., 2002. Reduced methane emissions from largescale changes in water management of China's rice paddies during 1980–2000, Geophys. Res. Lett., 29(20), 1972.

Lin, S. J. and Rood, R. B., 1996. Multidimensional flux form semi-Lagrangian transport schemes. Mon. Weather Rev., 124, 2046-2070.

Lorius, C., Jouzel, J., Ritz, C., Merlivat L., Barkov N. I., Korotkevich Y. S., Kotlyakov V. M., 1985. A 150,000-year climatic record from Antarctic ice. Nature 316, 591–596.

Loulergue, L., Schilt, A., Spahni, R., Masson-Delmotte, V., Blunier, T., Lemieux, B., Barnola, J.-M., Raynaud, D., Stocker, T. F., and Chappellaz, J., 2008. Orbital and millennial-scale features of atmospheric CH_4 over the past 800,000 years, Nature, 453, 383–386.

Lowe, D., Manning, M., Brailsford, G., Bromley, A., 1997. The 1991 – 1992 atmospheric methane anomaly: Southern Hemisphere ^{13}C increase and growth rate fluctuations. Geophys. Res. Lett. 24, 857–860.

Lowe, D.C., Brenninkmeijer, C.A.M., Brailsford, G.W., Lassey, K.R., Gomez, A.J., 1994. Concentration and 13C records of atmospheric methane in New Zealand and Antarctica: evidence for changes in methane sources. J. Geophys. Res. 99, 16913–16925.

Manning, M. R., Lowe, D. C., Moss, R. C., Bodeker, G. E. & Allan, W., 2005. Short-term variations in the oxidizing power of the atmosphere. Nature 436, 1001–1004.

Martini, A. M., Budai, J. M., Walter, L. M. and Schoell, M., 1996. Microbial generation of economic accumulations of methane within a shallow organic-rich shale. Nature, 383, 155–158.

Masarie, K. A., and Tans, P. P., 1995. Extension and integration of atmospheric carbon dioxide data into a globally consistent measurement record. J. Geophys. Res. Atmos., 100, 11593–11610.

Matsueda, H., Inoue, H.Y., Ishii, M. and Nogi Y., 1996. Atmospheric methane over the North Pacific from 1987 to 1993, Geochem. J. 30, 1-15.

Matthews, E. and Fung, I., 1987. Methane emissions from natural wetlands: Global distribution, area, and environmental characteristics of sources, Global Biogeochem. Cycles, 1, 61– 86.

Matthews, E., 1994. Assessment of methane sources and their uncertainties. Pure Appl. Chem. 66, 154–161.

Meirink, J. F., Bergamaschi, P. and Krol, M., 2008b. Four-dimensional variational data assimilation for inverse modelling of atmospheric methane emissions: Method and comparison with synthesis inversion, Atmos. Chem. Phys., 8, 6341–6353.

Melton, J. R., et al., 2013. Present state of global wetland extent and wetland methane modeling: conclusions from a model inter-comparison project (WETCHIMP), Biogeosciences, 10, 753–788.

Mieville, A., et al., 2010. Emissions of gases and particles from biomass burning during the 20th century using satellite data and an historical reconstruction. Atmos. Environ., 44, 1469–1477.

Mikaloff Fletcher, S. E., Tans, P. P., Bruhwiler, L. M., Miller, J. B. and Heimann M., 2004. CH_4 sources estimated from atmospheric observations of CH_4 and its $^{13}C/^{12}C$ isotopic ratios: 2. Inverse modeling of CH4 fluxes from geographical regions, Global Biogeochem. Cycles, 18, GB4005.

Mikaloff Fletcher, S.E., Tans, P.P., Bruhwiler, L.M., Miller, J.B., Heimann, M., 2004. CH_4 sources estimated from atmospheric observations of CH_4 and its $^{13}C/^{12}C$ isotopic ratios: 1. Inverse modeling of source processes. Global Biogeochem. Cycles, 18, GB4004.

Miller, J. B., Mack, K. A., Dissly, R., White, J.W.C., Dlugokencky, E. J. and Tans P. P., 2002. Development of analytical methods and measurements of $^{13}C/^{12}C$ in atmospheric CH_4 from the NOAA/CMDL global air sampling network, J. Geophys. Res., 107(D13), 4178.

Miller, S.M., et al., 2013. Anthropogenic emissions of methane in the United States. Proceedings of the National Academy of Sciences, 110 (50) 20018-20022. 10.1073/pnas.1314392110.

Mitchell, C., 1993. Methane emissions from the coal and natural gas industries in the UK. Chemosphere 26, 441– 446.

Möller, L., Sowers, T., Bock, M., Spahni, R., Behrens, M., Schmitt, J., Miller, H. and Fischer, H., 2013. Independent variations of CH_4 emissions and isotopic composition over the past 160,000 years, Nat. Geosci., 6, 885–890.

Monteil, G., et al., 2011. Interpreting methane variations in the past two decades using measurements of CH4 mixing ratio and isotopic composition. Atmos. Chem. Phys., 11(17), 9141-9153.

Montzka, S. A., Krol, M., Dlugokencky, E., Hall, B., Joeckel, P. and Lelieveld, J., 2011. Small interannual variability of global atmospheric hydroxyl. Science, 331, 67–69.

Mulquiney, J. E., and Norton, J.A., 1998. A new inverse method for trace gas flux estimation: State-space model identification and constraints, J. Geophys. Res., 103, 1417–1427.

Mulquiney, J. E., Taylor, J.A., Jakeman, A.J., Norton, J.P. and Prinn, R.G., 1998. A new inverse method for trace gas flux estimation: Application to tropospheric CFCl3 fluxes, J. Geophys. Res., 103, 1429–1442.

Myhre, G., et al., 2013. Radiative forcing of the direct aerosol effect from AeroCom Phase II simulations. Atmos. Chem. Phys., 13, 1853–1877.

Myhre, G., et al., 2013: Anthropogenic and Natural Radiative Forcing. In: Climate Change 2013. The Physical Science Basis. Contribution of Working Group I to the Fifth Assessment Report of the Intergovernmental Panel on Climate Change [Stocker, T.F., D. Qin, G.-K. Plattner, M. Tignor, S.K. Allen, J. Boschung, A. Nauels, Y. Xia, V. Bex and P.M. Midgley (eds.)]. Cambridge University Press, Cambridge, United Kingdom and New York, NY, USA.

Myhre, G., Highwood, E. J., Shine, K. P. and Stordal, F., 1998. New estimates of radiative forcing due to well mixed greenhouse gases. Geophys. Res. Lett., 25, 2715–2718.

Myhre, G., Highwood, E. J., Shine, K. P. and Stordal, F., 1998. New estimates of radiative forcing due to well mixed greenhouse gases. Geophys. Res. Lett., 25, 2715–2718.

Nakazawa, T., Machida, T., Tanaka, M., Fujii, Y., Aoki, S., Watanabe, O., 1993. Differences of the atmospheric CH4 concentration between the Arctic and Antarctic regions in preindustrial/ pre-agricultural era. Geophys. Res. Lett. 20, 943 – 946.

National Oceanic and Atmospheric Administration, 2001. GLOBALVIEW-CH4: Cooperative Atmospheric Data Integration Project- Methane [CD-ROM], report, Clim. Monit. and Diag. Lab., Boulder, Colo. (Also available at ftp.cmdl.noaa.gov, Path: ccg/ch4/GLOBALVIEW)

Neef, L., van Weele, M. and van Velthoven, P., 2010. Optimal estimation of the present day global methane budget. Global Biogeochem. Cycles, 24, GB4024.

Nisbet, E. G., Dlugokencky, E. J. and Bousquet, P., 2014. Methane on the rise - Again, Science, 343, 493–5.

Nisbet, E. G., et al., 2016. Rising atmospheric methane: 2007-2014 growth and isotopic shift, Global Biogeochem. Cycles, 30, 1356-1370.

Nisbet, R. E. R., et al., 2009. Emission of methane from plants. Proc. R. Soc. Ser. B, 276, 1347-1354.

Ohara, T. et al., 2007. An Asian emission inventory of anthropogenic emission sources for the period 1980–2020. Atmos. Chem. Phys., 7, 4419–4444.

Osborn, T. and Wigley, T., 1994. A simple model for estimating methane concentration and lifetime variations. Clim. Dyn. 9, 181– 193.

Ovando, J., Tomasella, J., Rodriguez, D. A., Martinez, J. M., Siqueira-Junior, J. L., Pinto, G. L. N., Passy, P., Vauchel, P., Noriega, L. and von Randow, C., 2015. Extreme flood events in the Bolivian Amazon wetlands, J. Hydrol. Reg. Stud., 5, 293–308.

Page, S. E., Siegert, F., Rieley, J. O., Boehm, H. D. V., Jaya, A. and Limin, S., 2002. The amount of carbon released from peat and forest fires in Indonesia during 1997. Nature, 420, 61–65.

Patra, P. K., et al., 2016. Regional methane emission estimation based on observed atmospheric concentrations (2002–2012), J. Met. Soc. Jpn., 94, 91-113.

Pavlov, A. A., Hurtgen, M. T., Kasting, J. F. and Arthur, M. A., 2003. Methane-rich Proterozoic atmosphere?. Geology, 31 (1), 87–90.

Peischl, J., et al., 2018. Quantifying Methane and Ethane Emissions to the Atmosphere From Central and Western U.S. Oil and Natural Gas Production Regions, JGR Atmospheres, 123(14), 7725-7740.

Petit, J., Jouzel, J., Raynaud, D., Barkov, N., Barnola, J. M., Basile, I., Bender, M., Chappellaz, J., Davis, M., Delaygue, G., Delmotte, M., Kotlyakov, V., Legrand, M., Lipenkov, V., Lorius, C., Pepin, L., Ritz, C., Saltzman, E., Stievenard, M., 1999. Climate and atmospheric history of the past 420,000 years from the Vostok ice core, Antarctica. Nature 399, 429– 436.

Peylin, P., Baker, D., Sarmiento, J., Ciais, P. and Bousquet, P., 2002. Influence of transport uncertainty on annual mean and seasonal inversions of atmospheric CO_2 data. J. Geophys. Res., 107(D19), 4385.

Pickett-Heaps, C. A., et al. 2011. Magnitude and seasonality of wetland methane emissions from the Hudson Bay Lowlands (Canada). Atmos. Chem. Phys., 11(8), 3773-3779.

Pison, I., Bousquet, P., Chevallier, F., Szopa, S. and Hauglustaine, D., 2009. Multi-species inversion of CH4, CO and H2 emissions from surface measurements. Atmos. Chem. Phys., 9, 5281–5297.

Plumb, R. A., and Zheng, X., 1996. Source determination from trace gas observations: An orthogonal function approach and results for long-lived gases with surface sources, J. Geophys. Res., 101, 18,569–18,585.

Prather, M. J., Holmes, C. D. and Hsu, J., 2012. Reactive greenhouse gas scenarios: Systematic exploration of uncertainties and the role of atmospheric chemistry. Geophys. Res. Lett., 39, L09803.

Prigent, C., Matthews, E., Aires, F., and Rossow, W. B., 2001. Remote sensing of global wetland dynamics with multiple satellite data sets, Geophys. Res. Lett., 28(24), 4631–4634.

Prinn, R. G. et al., 2001. Evidence for substantial variations of atmospheric hydroxyl radicals in the past two decades. Science 292, 1882–1888.

Prinn, R. G., et al., 2000. A history of chemically and radiatively important gases in air deduced from ALE/GAGE/AGAGE, J. Geophys. Res., 105(D14), 17,751– 17,792.

Prinn, R. G., et al., 2005. Evidence for variability of atmospheric hydroxyl radicals over the past quarter century. Geophys. Res. Lett., 32, L07809.

Prinn, R.G., Weiss, R.F., Miller, B.R., Huang, J., Alyea, F.N., Cunnold, D.M., Fraser, P.J., Hartley, D.E., Simmonds, P.G., 1995. Atmospheric trends and lifetime of CH3CCl3 and global OH concentrations. Science 269, 187–198.

Quay, P., Stutsman, J., Wilbur, D., Snover, A., Dlugokencky, E., Brown, T., 1999. The isotopic composition of atmospheric methane. Global Biogeochem. Cycles 13, 445– 461.

Quay, P.D., King, S.L., Lansdown, J.M., Wilbur, D.O., 1988. Isotopic composition of methane released from wetlands: implications for the increase in atmospheric methane. Global Biogeochem. Cycles 2, 385– 397.

Quay, P.D., King, S.L., Stutsman, J., Wilbur, D.O., Steele, L.P., Fung, I., Gammon, R.H., Brown, T.A., Farwell, G.W., Grootes, P.M. and Schmidt, F.H., 1991. Carbon isotopic composition of atmospheric CH4: fossil and biomass burning source strengths. Global Biogeochem. Cycles 5, 25– 47.

Rasmussen, R.A. and Khalil, M.A.K., 1984. Atmospheric methane in the recent and ancient atmospheres. J. Geophys. Res. 89, 11599-11605.

Rasmussen, R.A., Khalil, M.A.K., 1981. Atmospheric methane (CH_4): trends and seasonal cycles. J. Geophys. Res. 86, 9826–9832.

Raynaud, D., Jouzel, J., Barnola, J., Chapellaz, J., Delmas, R., Lorius, C., 1993. The ice record of greenhouse gases. Science 259, 926 – 934.

Rayner, P. J., Enting, I. G. and Trudinger, C. M., 1996. Optimizing the CO_2 observing network for constraining sources and sinks, Tellus, Ser. B, 48, 433–444.

Rayner, P. J., Enting, I. G., Francey, R. J. and Langenfelds, R. L., 1999. Reconstructing the recent carbon cycle from atmospheric CO_2, $\delta^{13}C$ and O_2/N_2 observations, Tellus Ser. B, 51, 213-232.

Rice, A. L., Butenhoff, C. L., Shearer, M. J., Teama, D., Rosenstiel, T. N. and Khalil M. A. K., 2010. Emissions of anaerobically produced methane by trees, Geophys. Res. Lett., 37, L03807.

Rice, A. L., Tyler, S. C., McCarthy, M. C., Boering, K. A. and Atlas, E., 2003. Carbon and hydrogen isotopic compositions of stratospheric methane: 1. High-precision observations from the NASA ER-2 aircraft. J. Geophys. Res., 108(D15).

Rice, A.L., Butenhoff, C.L, Teama, D.G., Roeger, F., Khalil, M.A.K, and Rasmussen, R.A., 2016. Atmospheric methane isotopic record favors fossil sources flat in 1980s and 1990s with recent increase, Proceedings of the National Academy of Sciences, 113, 10791-10796, 10.1073/pnas.1522923113.

Rice, D. D. and Claypool, G. E. 1981. Generation, accumulation, and resource potential of biogenic gas. American Association of Petroleum Geologists Bulletin, 65, 5–25.

Rigby, M., et al., 2008. Renewed growth of atmospheric methane. Geophys. Res. Lett., 35, L22805.

Röger, F., 2013. Inverse modeling of global methane emissions. Diploma Thesis (Karlsruhe Institite of Technology, Karlsruhe, Germany).

Sarmiento, J.L. and Sundquist, E.T., 1992. Revised budget for the oceanic uptake of anthropogenic carbon dioxide. Nature, 356, 589-593.

Sass, R. L., 1994. Short summary chapter for methane, in CH_4 and N_2O Global Emissions and Controls from Rice Fields and Other Agricultural and Industrial Sources, edited by K. Minami, A. Mosier, and R. Sass, pp. 1– 4, Natl. Inst. for Agro-Environ. Sci., Tsukuba, Japan.

Schaefer, H., et al., 2016. A 21st-century shift from fossil-fuel to biogenic methane emissions indicated by $^{13}CH_4$, Science, 352, 80–84.

Schauffler, S. and Daniel, J., 1994. On the effect of stratospheric circulation changes on trace gas trends. J. Geophys. Res. 99, 25747– 25754.

Schneider, H. R., Jones, D., McElroy, M. B. and Shi, G. Y., 2000. Analysis of residual mean transport in the stratosphere: 1. Model description and comparison with satellite data. J. Geophys. Res. 105(D15), 19991-20011.

Severinghaus, J. P., and Brook, E. J., 1999. Abrupt climate change at the end of the last glacial period inferred from trapped air in polar ice, Science, 286, 930–934.

Severinghaus, J., Sowers, T., Brook, E., Aley, R., Bender, M., 1998. Timing of abrupt climate change at the end of the Younger Dryas interval from thermally fractionated gases in polar ice. Nature 391, 141–146.

Shakhova, N., Semiletov, I., Salyuk, A., Yusupov, V., Kosmach, D. and Gustafsson, O., 2010. Extensive methane venting to the atmosphere from sediments of the East Siberian Arctic shelf. Science, 327, 1246–1250.

Shallcross, D. E., Khalil, M. A. K. and Butenhoff, C. L., 2007. The atmospheric methane sink. In: Greenhouse Gas Sinks [D. Reay (ed.)] CAB International, pp. 171-183.

Shindell, D. T., Faluvegi, G., Bell, N. and Schmidt G. A., 2005. An emissions-based view of climate forcing by methane and tropospheric ozone, Geophys. Res. Lett., 32, L04803.

Shine, K., Fuglestvedt, J., Hailemariam, K. and Stuber, N., 2005a. Alternatives to the global warming potential for comparing climate impacts of emissions of greenhouse gases. Clim. Change, 68, 281–302.

Simmonds, P. G., Manning, A. J., Derwent, R. G., Ciais, P., Ramonet, M., Kazan, V., and Ryall, D., 2005. A burning question. Can recent growth rate anomalies in the greenhouse gases be attributed to large-scale biomass burning events?, Atmos. Environ., 39, 2513–2517.

Simon, D. and Chia, T. L., 2002. Kalman filtering with state equality constraints. Aerospace and Electronic Systems, IEEE Transactions on 38(1), 128-136.

Simon, D., 2010. Kalman filtering with state constraints: a survey of linear and nonlinear algorithms. IET Control Theory & Applications, 4(8), 1303-1318.

Simpson, I. J., et al., 2012. Long-term decline of global atmospheric ethane concentrations and implications for methane. Nature 488, 490–494.

Simpson, I. J., Rowland, F. S., Meinardi, S. and Blake, D. R., 2006. Influence of biomass burning during recent fluctuations in the slow growth of global tropospheric methane. Geophys. Res. Lett., 33, L22808.

Simpson, I.J., et al., 2002. Implications of the recent fluctuations in the growth rate of tropospheric methane. Geophysical Research Letters, Vol. 29, no. 10, 1479.

Spahni, R., et al., 2005. Atmospheric Methane and Nitrous Oxide of the Late Pleistocene from Antarctic Ice Cores. Science, Vol. 310, Issue 5752, 1317-1321.

Spahni, R., et al., 2011. Constraining global methane emissions and uptake by ecosystems. Biogeosciences, 8, 1643-1665.

Sriskantharajah, S., Fisher, R. E., Lowry, D., Aalto, T., Hatakka, J., Aurela, M., Laurila, T., Lohila, A., Kuitunen, E. and Nisbet, E. G., 2012. Stable carbon isotope signatures of methane from a Finnish subarctic wetland, Tellus B, 64, 18818.

Stauffer, B., Fischer, G., Neftel, A. and Oeschger, H., 1985. Increase in atmospheric methane recorded in antarctic ice cores. Science 229, 1386-1388.

Steele, L., Dlugokencky, E., Lang, P., Tans, P., Martin, R., Masarie, K., 1992. Slowing down of the global accumulation of atmospheric methane during the 1980s. Nature 358, 313–316.

Stevens, C., 1993. Isotopic abundance in the atmosphere and sources. In: Khalil, M.A.K. (Ed.), Atmospheric Methane, Sources, Sinks and Role in Global Change. Springer-Verlag, New York, pp. 62–88.

Stevens, C.M. and Engelkemeir, A., 1988. Stable carbon isotopic composition of methane from some natural and anthropogenic sources. J. Geophys. Res. 93, 725–733.

Stevens, C.M. and Rust, F.E., 1982. The carbon isotopic composition of atmospheric methane. J. Geophys. Res. 87, 4879– 4882.

Subak, S., 1994. Methane from the House of Tudor and the Ming Dynasty: anthropogenic emissions in the sixteenth century. Chemosphere 29, 843– 854.

Tang, J. and Zhuang, Q., 2011. Technical Note: Propagating correlations in atmospheric inversions using different Kalman update smoothers. Atmos. Chem. Phys., 11(3), 921-929.

Tans, P.P., Fung, I.Y., and Takahashi, T., 1990a. Observational constraints on the global atmospheric CO_2 budget, Science, 247, 1431-1438.

Tarantola, A., 1987. Inverse Problem Theory, Methods for Data Fitting and Model Parameter Estimation, Elsevier, New York.

Tarantola, A., and Valette, B., 1982a. Inverse problems - quest of information, J. Geophys., 50, 159-170.

Tarantola, A., and Valette, B., 1982b. Generalized nonlinear inverse problems solved using the least squares criterion, Rev. Geophys., 20, 219-232.

Tarnocai, C., Canadell, J. G., Schuur, E. A. G., Kuhry, G. P., Mazhitova, G. and Zimov, S., 2009. Soil organic carbon pools in the northern circumpolar permafrost region. Global Biogeochem. Cycles, 23, Gb2023.

Teama, D. G., 2013. A 30-year record of the isotopic composition of atmospheric methane. Ph.D. Dissertation (Portland State University, Portland, Oregon).

Terazawa, K., Ishizuka, S., Sakata, T., Yamada, K. and Takahashi, M., 2007. Methane emissions from stems of Fraxinus mandshurica var. japonica trees in a floodplain forest. Soil Biology and Biochemistry, 39, 2689–2692.

The GEOS data used in this study/project have been provided by the Global Modeling and Assimilation Office (GMAO) at NASA Goddard Space Flight Center.

Thompson, A., 1992. The oxidizing capacity of the Earth's atmosphere: probable past and future changes. Science 256, 1157–1165.

Thompson, A., Chappellaz, J., Fung, I., Kucsera, T., 1993. The atmospheric CH_4 increase since the Last Glacial Maximum: 2. Interactions with oxidants. Tellus 45B, 242– 257.

Thompson, L.G., Mosley-Thompson, E., Davis, M.E., Lin, P.N., Henderson, K.A., Cole-Dai, J., Bolzan, J.F. and Liu, K.b., 1995. Late stage and Holocene tropical ice core records from Huascarán, Peru, Science 269, 46-50.

Thorpe, R., Law, K., Bekki, S., Pyle, J., Nisbet, E., 1996. Is methane-driven deglaciation consistent with the ice core record? J. Geophys. Res. 101, 28627– 28635.

Trampert, J. and Snieder, R., 1996. Model estimations biased by truncated expansions: Possible artifacts in seismic tomography, Science, 271, 1257-1260.

Tubiello, F. N., Salvatore, M., Rossi, S., Ferrara, A., Fitton, N. and Smith, P., 2013. The FAOSTAT database of greenhouse gas emissions from agriculture. Environmental Research Letters, 8, 015009.

Turner, A. J., Frankenberg, C., Wennberg, P. O., and Jacob, D. J., 2017. Ambiguity in the causes for decadal trends in atmospheric methane and hydroxyl, Proceedings of the National Academy of Sciences, 114, 5367-5372.

Tyler, S. C., Crill, P. M. and Brailsford, G. W., 1994. 13C/12C Fractionation of methane during oxidation in a temperate forested soil. Geochim. Cosmochim. Acta 58(6), 1625-1633.

Tyler, S. C., Rice, A. L., Ajie, H. O., 2007. Stable isotope ratios in atmospheric CH4: Implications for seasonal sources and sinks. J. Geophys. Res., 112 (D03303).

Tyler, S.C., 1986. Stable carbon isotope ratios in atmospheric methane and some of its sources. J. Geophys. Res. 91, 13232–13238.

Tyler, S.C., Ajie, H.O., Gupta, M.L., Cicerone, R.J., Blake, D.R. and Dlugokencky, E.J., 1999. Stable carbon isotopic composition of atmospheric methane: a comparison of surface level and free tropospheric air. J. Geophys. Res. 104, 13895–13910.

Tyler, S.C., Blake, D.R. and Rowland, F.S., 1987. $^{13}C/^{12}C$ ratio in methane from the flooded amazon forest. J. Geophys. Res. 92, 1044–1048.

U.S. Dept. of Energy Technology Laboratory, National Methane Hydrate Program, Methane: A Scientific Journey from Obscurity to Climate Super-Stardom by Gavin Schmidt, September 2004.

Uppala, S. M., et al., 2005. The ERA-40 reanalysis. Quarterly J. Roy. Meteorol. Soc. 131(612), 2961-3012.

US Environmental Protection Agency, 2013. Inventory of U.S. Greenhouse Gas Emissions and Sinks: 1990–2011, Technical Report EPA 430-R-13-001 (Environmental Protection Agency, Washington).

van Bodegom, P., Wassmann, R. and Metra Corton, T., 2001. A process- based model for methane emission predictions from flooded rice paddies, Global Biogeochem. Cycles, 15, 247–263.

van der Werf, G. R., et al., 2004: Continental-scale partitioning of fire emissions during the 1997 to 2001 El Nino/La Nina period. Science, 303, 73–76.

van der Werf, G. R., et al., 2010. Global fire emissions and the contribution of deforestation, savanna, forest, agricultural, and peat fires (1997–2009). Atmos. Chem. Phys., 10, 11707–11735.

van der Werf, G. R., Randerson, J. T., Giglio, L., Collatz, G. J., Kasibhatla, P. S., and Arellano Jr., A. F., 2006. Interannual variability in global biomass burning emissions from 1997 to 2004, Atmos. Chem. Phys., 6, 3423–3441.

van Huissteden, J., Berrittella, C., Parmentier, F. J. W., Mi, Y., Maximov, T. C. and Dolman, A. J., 2011. Methane emissions from permafrost thaw lakes limited by lake drainage. Nature Clim. Change, 1, 119–123.

Vigano, I., et al., 2008. Effect of UV radiation and temperature on the emission of methane from plant biomass and structural components, Biogeosci. Discuss., 5, 243-270.

Voulgarakis, A., et al., 2013. Analysis of present day and future OH and methane lifetime in the ACCMIP simulations. Atmos. Chem. Phys., 13, 2563–2587.

Walter Anthony, K. M., Anthony, P., Grosse, G. and Chanton, J., 2012. Geologic methane seeps along boundaries of Arctic permafrost thaw and melting glaciers. Nature Geosci., 5, 419-426.

Walter, B. P., Heimann, M. and Matthews, E., 2001. Modeling modern methane emissions from natural wetlands 2. Interannual variations 1982– 1993, J. Geophys. Res., 106(D24), 34,207–34,219.

Walter, K. M., Smith, L. C. and Chapin, F. S., 2007. Methane bubbling from northern lakes: Present and future contributions to the global methane budget. Philos. Trans. R. Soc. A, 365, 1657–1676.

Walter, K. M., Zimov, S. A., Chanton, J. P., Verbyla, D. and Chapin, F. S. I., 2006. Methane bubbling from Siberian thaw lakes as a positive feedback to climate warming. Nature, 443, 71–75.

Wang J.S., et al., 2004. A 3-D model analysis of the slowdown and interannual variability in the methane growth rate from 1988 to 1997. Global Biogeochem. Cycles 18(3).

Wang, C., Prinn, R., Sokolov, A., 1998. A global interactive chemistry and climate model: formulation and testing. J. Geophys. Res. 103, 3399– 3417.

Wang, Y., Jacob, D. J. and Logan, J. A., 1998a. Global simulation of tropospheric O3-NOx-hydrocarbon chemistry, 1. Model formulation. J. Geophys. Res., 103(D9), 10,713-10,726.

Wang, Z. P., Han, X. G., Wang, G. G., Song, Y. and Gulledge, J., 2008: Aerobic methane emission from plants in the Inner Mongolia steppe. Environ. Sci. Technol., 42, 62–68.

Wecht, K.J., et al., 2012. Validation of TES methane with HIPPO aircraft observations: implications for inverse modeling of methane sources. Atmos. Chem. Phys. 12(4), 1823-1832.

Whalen, M. and Reeburg, W., 1990. Consumption of atmospheric methane by tundra soils. Nature, 346, 160-162.

Whalen, S. C., Reeburgh, W. S. and Sandbeck, K. A., 1990. Applied and Environmental Microbiology, 56(11), 3405-3411.

White, J. W. C., Vaughn, B. H. and Michel, S. E., 2015. Stable Isotopic Composition of Atmospheric Methane (^{13}C) from the NOAA ESRL Carbon Cycle Cooperative Global Air Sampling Network, 1998-2014. (University of Colorado, Institute of Arctic and Alpine Research [INSTAAR], Boulder, CO).

Wikimedia Commons contributors, 'File:MethaneSinkPieChart.jpg', Wikimedia Commons, the free media repository, 15 October 2020, 07:30 UTC, <https://commons.wikimedia.org/w/index.php?title=File:MethaneSinkPieChart.jpg&oldid=490238977> [accessed 22 July 2021].

Worden, J., et al., 2013. El Niño, the 2006 Indonesian peat fires, and the distribution of atmospheric methane, Geophys. Res. Lett., 40, 4938–4943.

Wuebbles, D.J. and Hayhoe, K., 2002. Atmospheric methane and global change. Earth-Science Reviews 57, 177–210.

Yamada, K., et al., 2006. Hydrogen and carbon isotopic measurements of methane from agricultural combustion: Implications for isotopic signatures of global biomass burning sources. J. Geophys. Res., 111(D16), D16306.

Yang, J., Tian, H., Tao, B., Ren, W., Kush, J., Liu, Y. and Wang, Y., 2014. Spatial and temporal patterns of global burned area in response to anthropogenic and environmental factors: Reconstructing global fire history for the 20th and early 21st centuries, J. Geophys. Res. Biogeosci., 119.

Yevich, R. and Logan, J. A., 2003. An assessment of biofuel use and burning of agricultural waste in the developing world. Global Biogeochem. Cycles, 17, 1095.

Young, P., et al., 2013. Pre-industrial to end 21st century projections of tropospheric ozone from the Atmospheric Chemistry and Climate Model Intercomparison Project (ACCMIP). Atmos. Chem. Phys., 4, 2063–2090.

Zazzeri, G., et al., 2016. Carbon isotopic signature of coal-derived methane emissions to atmosphere: From coalification to alteration, Atmos. Chem. Phys. Discuss., doi:10.5194/acp-2016-235.

APPENDIX

Table A.1: List of a few* IDL routines used in this work.

Routine	Description
monthly_avg_CH42016_SK.pro	Processes the raw NOAA observation data to a form taking uncertainties into account which is input to the inversion. Includes the steps involved in processing the observational data for calculating the daily-averaged and consecutively monthly-averaged methane mixing ratios and associated total uncertainties and consequently creating concentration data-set to be used in the inversion.
Total_CH4_ResponseAdjIso_bpch_SK.pro	Generates plots the decay of emission of 1 Tg of total CH_4 mass over the entire model run time in the adjusted response function file for isotopes.
plot_H.pro	Generates plots comparing response functions i.e., H.bin files created in $4^0 \times 5^0$ and $2^0 \times 2.5^0$ grid resolution for lag months 0 to 11, using constant observation month of 07/2006 and also of 12/1980 for each source, for 20 sites distributed around the world.
plot_H_adj.pro	Generates plots comparing adjusted response functions i.e., H_adj.bin files created in $4^0 \times 5^0$ and $2^0 \times 2.5^0$ grid resolution for lag months, using constant observation month at the end of entire model run time for each source, for 20 sites distributed around the world.
plot_H_adjIso.pro	Generates plots comparing adjusted response functions for isotopes i.e., H_adjIso2_Strat.bin files created in $4^0 \times 5^0$ and $2^0 \times 2.5^0$ grid resolution, using constant observation month at the end of entire model run time for each source, for 20 sites distributed around the world.
compare_INVERSION_bpch_timeseries.pro	Compares the plots of INVERSION.bpch timeseries of 7 months, using observation month of 07/1980, 07/2006, 01/2013 and 01/2015 for each source, created from model run at $4^0 \times 5^0$ (red lines) and $2^0 \times 2.5^0$ (blue lines) grid resolution.
site_indices.pro	Reads in 'Concentration_data.txt' files for both $4^0 \times 5^0$ and $2^0 \times 2.5^0$ grid resolution and creates two output files named 'NOAA4x5Site_indices.txt' and 'NOAA2x25Site_indices.txt' printing names and corresponding grid indices of all observation sites.
Check_gridIndices.pro	Checks latitude and longitude coordinates of each observation site and also whether grid indices for each site were transformed from latitude and longitude coordinates correctly or not.
gv_SK_2016.pro	Reads in input text file 'processed_NOAA_CH4_2016_reduced.txt' and considers aggregation, mismatch error calculation, uncertainty assignments, correcting data from ocean transects and then generates output text file named 'NOAA_2016_OceanCorrect.txt'.

**Includes only new routines which are coded by me for this work, all other routines also used in previous work which are improved by me for this work are not included in this list.*